Department of Physics and Astronomy
School of Physical and Chemical Sciences

An Optical Study of Southern Gamma Doradus Stars

Including a detailed analysis of the modes of oscillation of five targets

Author
Rosemary Dorsey

Supervisor
Assoc. Prof. Karen Pollard

A thesis submitted for the degree of Master of Science in Astronomy

February 2020

"What is the universe? The universe is a symphony of vibrating strings... We are nothing but melodies. We are nothing but cosmic music played out on vibrating strings and membranes." – Michio Kaku

Abstract

This thesis aimed to perform a comprehensive analysis of the five target stars HD 10167*, HD 206481, HD 209295*, HD 214291* and HD 216910 to identify their pulsation modes.

High-precision space photometry from the Transiting Exoplanet Survey Satellite (TESS) and contemporaneous high-resolution High Efficiency and Resolution Canterbury University Large Échelle Spectrograph (HERCULES) spectra were utilized to classify their pulsation behaviour and therefore determine their pulsator class. Analyses were performed using SigSpec and FAMIAS to identify the photometric and spectroscopic frequencies for each target, with orbital solutions for the three binary systems (*) calculated using SpecBin.

This paper confirms that all targets are γ Dor pulsators, with HD 206481, HD 209295 and HD 214291 identified as hybrids of the γ Dor and δ Sct classes. Future work on these stars includes the further observation and identification of the origin of the absorption spikes observed in the spectral lines of HD 206481 and the dominant spectroscopic frequency of the secondary component of HD 214291, which is suspected by this thesis to be a degenerate star.

Contents

List of Figures

List of Tables

1. An Introduction to Asteroseismology

1.1 Asteroseismology

Asteroseismology is the study of stellar pulsations to infer the internal structure of different stellar classes (Aerts et al. 2010). It is impossible to directly observe stellar interiors due to their opaque nature (Lang 2013), and so it could be presumed that "the deep interior of the Sun and stars is less accessible to scientific investigation than any other region of the universe" (Eddington 1926). However, Eddington also suggests that the combination of the laws of physics and the observed conditions of a star's surface should allow for the determination of its structure; thus our mission to understand stellar interiors is not as impossible as it would appear.

Pulsations occur in stars which are not in hydrostatic equilibrium, such that the inward pressure of gravity and outward thermal pressure are not balanced within the star (Böhm-Vitense 1992). This imbalance causes the shape or size of the star to change and the brightness to increase and decrease periodically. The periodicity of this variation in brightness is maintained by excitation mechanisms inside the star. The different periodicities and excitation mechanisms within the stars are used to define the different classes of variable stars.

1.2 Variable Stars and the Hertzsprung-Russell Diagram

Variable stars are stars whose light output (or flux) varies with time. As shown by the Hertzsprung-Russell (H-R) diagram, there are many different classes of variable star, each of which occupies a specific region of the H-R diagram (Figure 1.1). There are two main categories of variable stars: intrinsic and extrinsic. Intrinsic variable stars are stars whose flux changes are due to physical changes within the star (i.e. pulsating or erupting stars), whereas extrinsic variable stars are stars whose observed flux changes are due to their perspective from Earth (i.e. eclipsing or rotating stars).

The instability strip is a renowned, near-vertical region of the H-R diagram which is occupied by select intrinsic variable pulsator classes such as Cepheid, RR Lyrae, Delta Scuti, rapidly oscillating Ap (roAp) and Gamma Doradus stars.

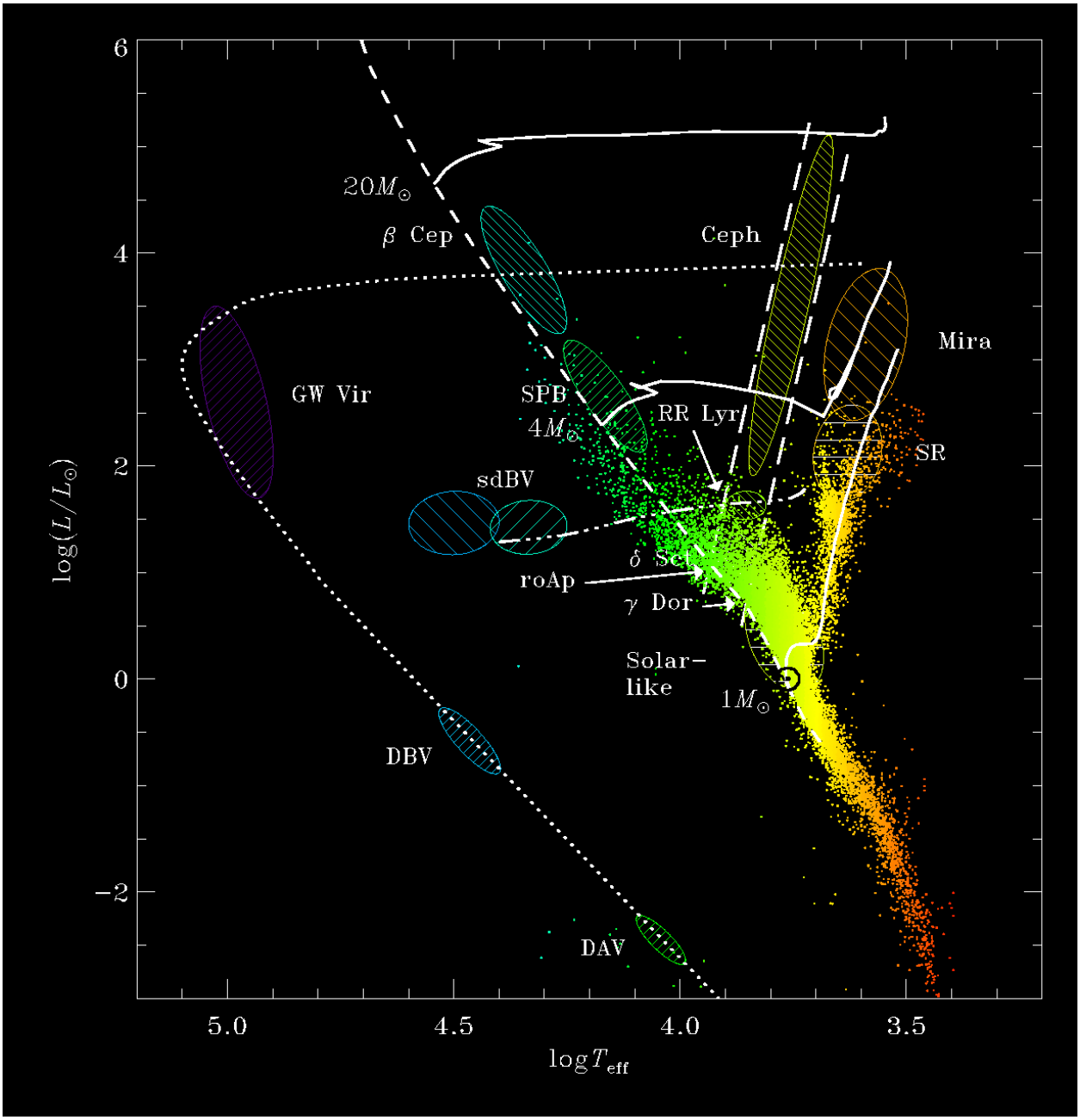

Figure 1.1: The Hertzsprung-Russell diagram. The parallel white dashed lines (top right) indicate the location of the instability strip. The ellipsoids indicate the regions occupied by particular classes of variable star. Image from Aerts (2007).

1.3 Pulsation Mechanisms

There are many types of pulsating stars, each of which is classified by the mechanism producing the pulsations and the resulting characteristic range of frequencies at which those stars may pulsate. This allows any variable star to be classified by comparing the pulsational frequencies present in its variable signal to those produced by the different pulsator classes.

There are four major processes which drive stellar pulsation: the κ-, γ- and ϵ-mechanisms and convective blocking (Handler 2012). All of these mechanisms involve a layer of the star regulating the transfer of energy within the star to some degree.

The κ-mechanism involves the opacity of a layer in the star varying to allow energy to be stored or released (Baker 1963). These driving layers are typically regions in the star where the partial or full ionization of hydrogen or helium occurs (Baker et al. 1962). When a layer undergoes a contraction, its density and thermal energy increases. Instead of heating the layer, the additional thermal energy is used to ionize the elements within it. This results in an increase in opacity, which means that less radiation is transferred through the layer from the star's core. As the radiation energy stored in the layer increases, the pressure below the layer also increases. At the point of maximum compression, the opacity is maximised and the pulsation is excited. This continues until the layer expands and cools, becoming less opaque as the elements recombine with the ionized electrons, and releases the radiation. The pressure below the layer decreases and the layer contracts again, repeating the cycle. This driving mechanism is important for the pulsations in Cepheids (Baker et al. 1962), RR Lyrae (Cox 1963) and Delta Scuti stars (Chevalier 1971).

The γ-mechanism (Cox et al. 1966) is a driving effect independent of opacity (Cox 1963) which increases the radiation stored in an ionized layer of the star. During the γ-mechanism, instability is increased due to a low value of the adiabatic exponent $\Gamma_3 - 1 = \left(\frac{d \log T}{d \log \rho}\right)_{ad}$ (Cox et al. 1966) in a region of ionization, which indicates that the temperature does not vary significantly during an increase in density associated with a compression. This results in a reduction of radiation flowing through the ionized layer. At the exact moment of maximum compression, the stored energy is absorbed by matter in the ionized layer to increase the pressure, temperature and rate of temperature increase in the subsequent expansion (Cox 1980). Despite this mechanism causing an observable increased local instability, Cox (1963) notes that globally the star is still pulsationally stable. Hence, it is suggested that the κ- and γ-mechanisms act together to provide the pulsation instability in stars, since Cox (1963) shows that most of the effects of the κ-mechanism can be attributed to the adiabatic exponent and therefore the γ-mechanism. Conversely, the effects of the γ-mechanism are not dependent on the κ-mechanism but on the ionization state of the layer (Cox et al. 1966).

Pulsations in stars are driven by the ϵ-mechanism when the nuclear reaction rate varies within the star (Rosseland et al. 1983). When a layer which is nuclear burning is compressed, it increases in temperature and therefore produces more energy. This energy increase causes the layer to expand, decreasing its pressure and temperature. This results in a reduction in the energy generated, the layer compresses and the process begins again. This mechanism is important for pulsations in the extremely massive stars ($M > 100 M_\odot$, where $M_\odot$ is one solar mass; Ledoux 1941) and pulsating white dwarfs (Marshall et al. 1973).

Convective blocking involves a convective zone in the star blocking the radiation from the stellar interior during a compression. It was theorised by Cox et al. (1966) as another possible excitation mechanism before being introduced by Pesnell (1987). Convective blocking occurs at the base of a convective zone where there is a sudden change from radiative to convective energy transfer (Guzik et al. 2000). If the convective timescale is the same or greater than the pulsation period, the convective luminosity remains constant and therefore cannot transport any additional luminosity at the base of the layer during a pulsation. This periodic blocking of the radiative energy drives the stellar pulsations. This mechanism is responsible for the pulsations in DA or DB type pulsating white dwarfs (Starrfield 1987) and γ Doradus stars (Guzik et al. 2000), and is potentially important for Cepheid and Mira stars (Handler 2012).

1.4 Spherical Harmonics

There are two different ways in which a star may pulsate: radially and non-radially. Radial pulsations preserve the spherical symmetry of the star's shape, whereas non-radial pulsations produce distortions in the stellar surface which change the shape of the star. Such distortions are described by spherical harmonics (see Figure 1.2), which can be mathematically described by the following two equations

$$Y_l^m(\theta,\phi) = N_l^m P_l^{|m|}(cos\theta)e^{im\phi} \tag{1.1}$$

$$P_l^m(x) = (-1)^m(1-x^2)^{m/2}\frac{d^m}{dx^m}P_l(x) \tag{1.2}$$

where θ is the angle from the polar axis, ϕ is the longitude, N_l^m is a normalisation constant, and $P_l^{|m|}$ is the associated Legendre polynomial for the given (l,m) values representing the spherical degree and the azimuthal order of the oscillation respectively (Handler 2012).

When the stellar surface becomes distorted by a pulsation, it becomes separated into areas of expansion and contraction. The lines where these areas connect are called nodal lines, as no radial motion occurs along them. The spherical degree l is the number of nodal lines on the surface of the star, which must be greater than or equal to zero ($l \geq 0$). In order for radial modes to preserve spherical symmetry, the pulsation is required to have $l = 0$. Subsequently, all modes with $l \neq 0$ are non-radial modes.

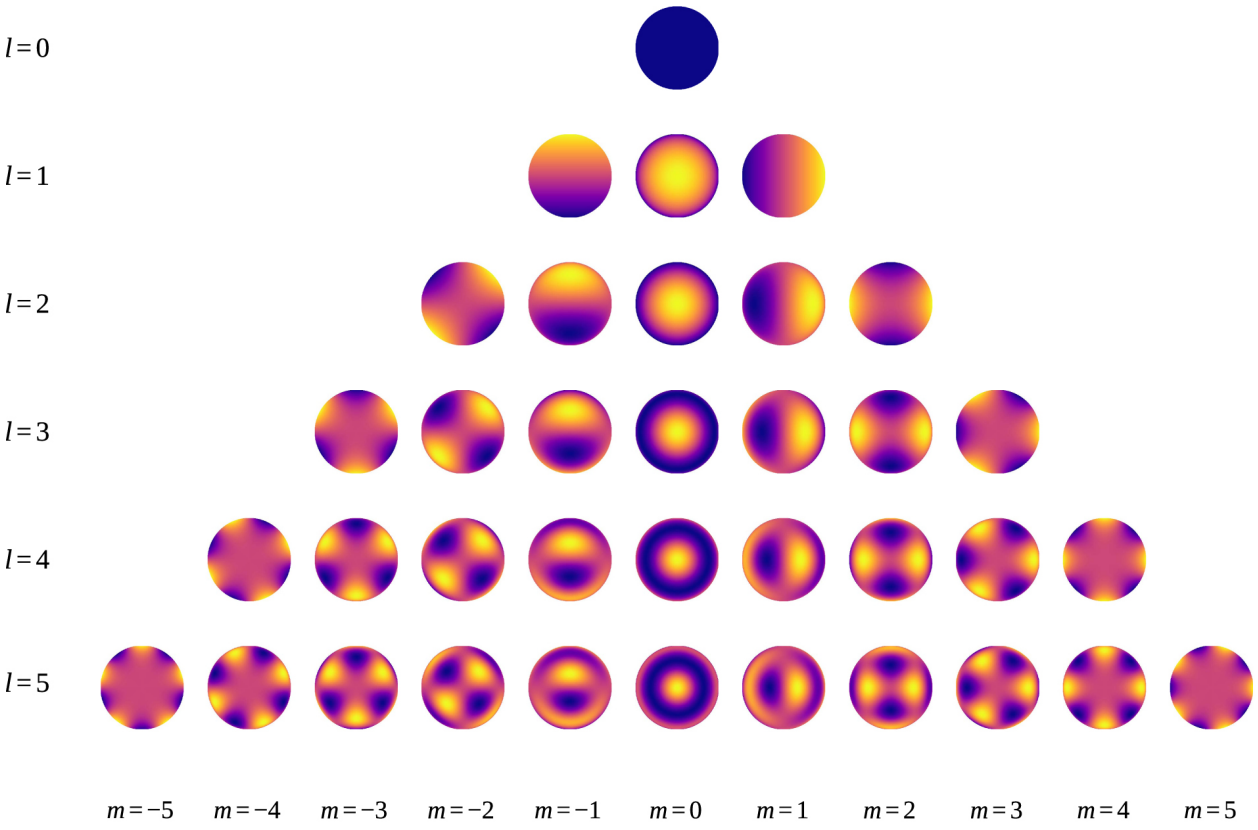

Figure 1.2: Diagram of the stellar surface distortions produced by pulsation modes of varying l and m values. Each stellar schematic is viewed from the perspective of the polar axis; i.e. from 'above' or 'below' the star. Image from Luger et al. (2019).

The azimuthal order m is the number of nodal lines that intersect the stellar equator, excluding those that are coincident with the equator. The value of m is restricted to the interval $[-l, +l]$. For modes with $m \neq 0$, the pulsations are travelling waves which propagate across the surface of the star. By convention, positive m values indicate a prograde pulsation which travels with the rotation of the star, and negative m values indicate a retrograde pulsation which travels against the rotation of the star.

1.5 Pressure and Gravity Modes

As previously stated, pulsations occur in stars which are not in hydrostatic equilibrium and thus act as a simple harmonic motion phenomenon (oscillating about an equilibrium but never achieving it). Just as for simple harmonic motion, a restoring force is required to produce the oscillation, the source of which depends on the type of pulsation occurring in the star. For pressure (p) or acoustic modes, pressure acts as the the restoring force against the gravity of the star to produce both radial ($l = 0$) and non-radial oscillations. For gravity (g) modes, gravity acts through buoyancy as the restoring force to produce non-radial oscillations. Whether an oscillation is a p-mode or g-mode in a specific region of a star is determined by two frequencies: the Lamb (or critical acoustic) frequency, defined by

$$S_l{}^2 = \frac{l\,(l+1)\,\Gamma_1 P}{r^2 \rho} \tag{1.3}$$

where Γ_1 is the heat capacity ratio, P is pressure, ρ is density; and the Brunt-Väisälä frequency, defined by

$$N^2 = -Ag \tag{1.4}$$

where A is a local convective stability criterion ($A > 0$ for convection zones and $A < 0$ for radiative zones) and g is the local gravity (Cox 1980). A pulsation with squared angular frequency $\sigma^2 > S_l{}^2, N^2$ is a p-mode restored by pressure and $\sigma^2 < S_l{}^2, N^2$ is a g-mode restored by gravity. For these cases, the pulsations are propagating standing waves. However for the mixed case where $S_l{}^2 < \sigma^2 < N^2$ or $N^2 < \sigma^2 < S_l{}^2$, pulsations are non-propagating, evanescent waves whose amplitude decreases exponentially. This is more obvious when visualised as a propagation diagram (Figure 1.3), which illustrates the relationship between pulsation frequency and dimensionless radius (ranging from 0 at the core to 1 at the surface).

As shown by Figure 1.3, the regions of the model which allow the propagation of p-modes or g-modes differ depending on the interior structure which in turn depends on the polytropic index n for the model. These regions also differ for varying values of spherical degree l. For pulsational waves confined to acoustic regions, modes with larger l values are more confined to the stellar surface (Ledoux 1978). This is due to the dependency of the Lamb frequency S_l on the term $[l(l+1)]^{\frac{1}{2}}$. Therefore, for main-sequence stars such as the Sun, p-modes generally propagate near the convective stellar surface whereas g-modes are restricted to radiative regions of the star, as shown schematically by Figure 1.4.

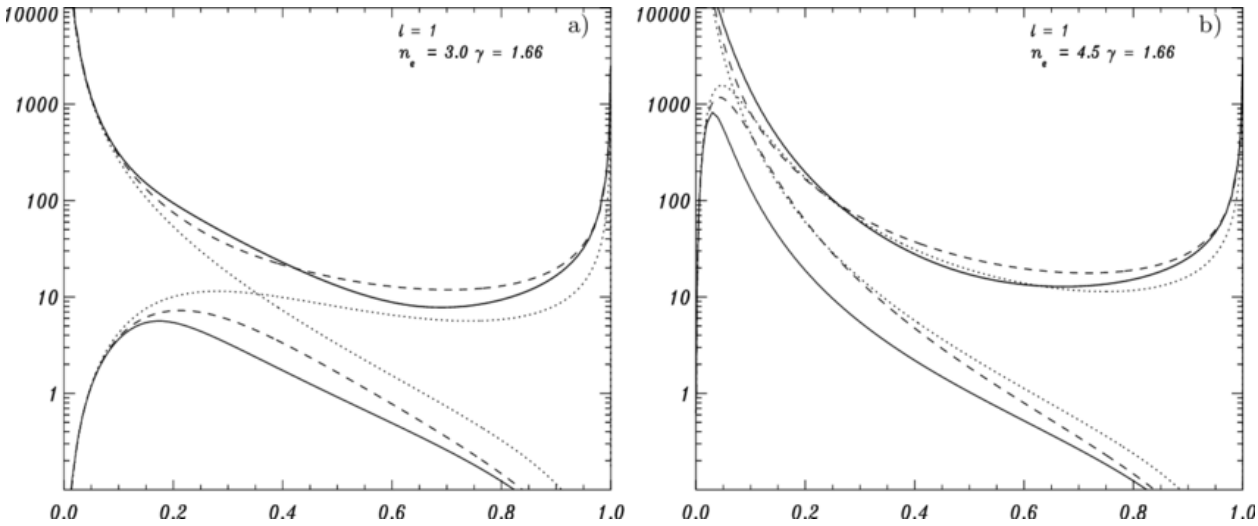

Figure 1.3: Propagation diagrams for the $l = 1$ mode for polytropic models with $\gamma = \frac{5}{3}$ and index $n = 3$ (left) or $n = 4.5$ (right). The dotted lines represent the Lamb (bottom) and Brunt-Väisällä (top) frequencies. The remaining dashed and solid lines are various Cowling approximations, explained in further detail by Lopes (2001). Image from Lopes (2001).

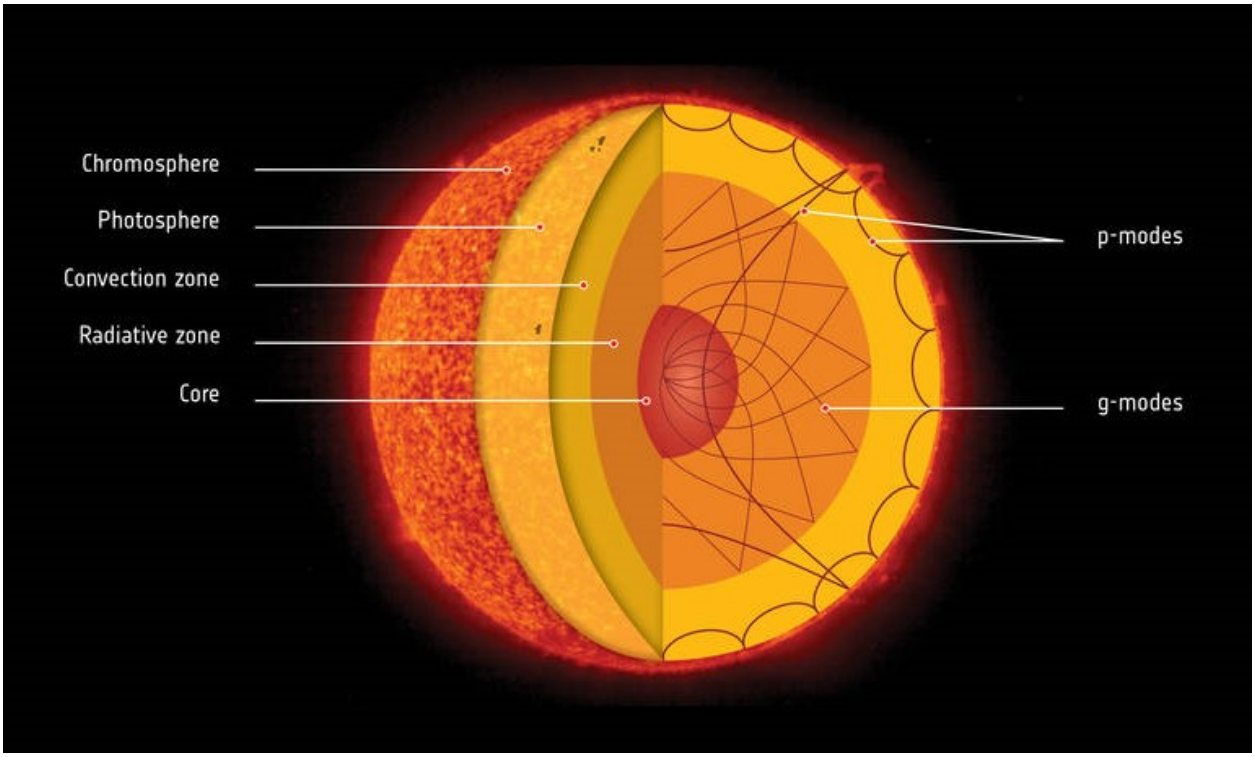

Figure 1.4: Locations of propagating p- and g-modes within the stellar interior. Image from Baldwin et al. (2017).

1.6 Gamma Doradus and Delta Scuti Stars

Gamma Doradus and Delta Scuti stars (hereafter referred to as γ Dor and δ Sct respectively) are two classes of pulsator which lie near the main-sequence in the instability strip. Prior to the *Kepler* and K2 missions, these stars were thought to differ in their pulsation frequencies, pulsation excitation mechanisms, interior structure and fundamental parameters. The release of *Kepler* data from its 2009–2013 campaign resulted an unprecedented shift in the direction of asteroseismology towards new models and theories, some of which are detailed in the following sections.

δ Sct stars were determined to be a separate class of pulsator in the mid 1900s after thorough analysis of the eponymous star δ Scuti. It was suggested by Sterne (1938) that the variations shown by δ Scuti were common among short-period Cepheids. Other stars, ρ Puppis and δ Delphini, were found to exhibit the same variability as δ Scuti (Eggen 1956a; Eggen 1956b) before the new pulsator class was defined by Baglin et al. (1973) with the following criteria: (1) the star must be situated in the Cepheid instability strip; and (2) the star must have a pulsation period less than one day (i.e. Population I star of spectral type A or F). The pulsations of δ Sct stars are explained by He II ionization through the κ-mechanism (Chevalier 1971) and are non-radial p- and g-mode oscillations with periods from 0.0125–0.25 days (Handler 2012).

γ Dor stars are a more recent addition to the existing pulsator classes. The variability of the eponymous γ Doradus was discovered by Cousins et al. (1963) but was unable to be classified until it was suggested that this star and others exhibiting similar variability may belong to a new class of pulsator whose variability is explained by non-radial g-mode pulsations (Mantegazza et al. 1994; Balona et al. 1994). This new class was defined by Kaye et al. (1999) to consist of early F-type stars with 1–5 periods of 0.4 to 3 days, all with amplitudes less than 0.1 mag in the Johnson V band. Such pulsations were later found to be produced by a convective blocking excitation mechanism (Guzik et al. 2000).

1.6.1 δ Sct/γ Dor Hybrids

Further analysis of the two pulsator classes led to questions of whether a 'hybrid' star exhibiting characteristics of both classes could possibly exist (Handler 1999). This question was answered when both δ Sct and γ Dor frequencies were detected for the binary HD 209295 by Handler et al. (2002b), which was previously found to lie outside the blue edge of the γ Dor instability strip but still within the δ Sct instability strip (Handler 1999). A study by Grigahcène et al. (2010) demonstrated the overlap of the theoretical and observed γ Dor and δ Sct instability strips and the positions of the four confirmed hybrids within their intersection. However, inspection of early *Kepler* data indicated that the majority of stars are hybrids rather than pure γ Dor or δ Sct pulsators. This led Grigahcène et al. (2010) to define new pulsator categories (δ Sct, γ Dor, δ Sct/γ Dor hybrid and γ Dor/δ Sct hybrid) by the pulsation range in which the majority of the detected frequencies lie. Despite the new categorisation, they found no clear or definitive separation between the categories and the theoretical edges of the instability strips no longer matched the observations. Contrary to this result, studies by Van Reeth et al. (2015) and Bowman et al. (2017) suggest that pure

γ Dor and δ Sct pulsators do still exist.

Xiong et al. (2016) continued examining the questions raised by Grigahcène et al. (2010) regarding the nature of hybrid stars and the individual γ Dor and δ Sct instability strips. Their paper found that the κ-mechanism provides the excitation for pulsations in the hotter δ Sct and γ Dor stars whereas the coupling of convective blocking and oscillations provides the excitation in the cooler stars. Thus, Xiong et al. (2016) hypothesized that δ Sct and γ Dor stars are p-mode and g-mode subgroups of one broad pulsator class which lies below the Cepheid instability strip. Such a theory would explain the number of hybrids which exhibit both p- and g-mode pulsations. This finding was supported by Balona (2018a) who used *Kepler* data to find that the γ Dor instability strip lies entirely within the δ Sct instability strip. This study also found that, despite existing at the exact same location on the H-R diagram (i.e. with the same effective temperature and luminosity), stars can still exhibit very different Fourier spectra. Results from a later study (Balona 2018b) indicated that neither the hypothesis from Xiong et al. (2016) of p-mode and g-mode subgroups nor different excitation mechanisms can explain the differences between δ Sct and γ Dor stars, as they showed that both classes, as well as non-pulsating stars from *Kepler*, are observed within the the γ Dor instability region (Figure 1.5). Additionally, it was found that more δ Sct stars occupied this region than γ Dor stars.

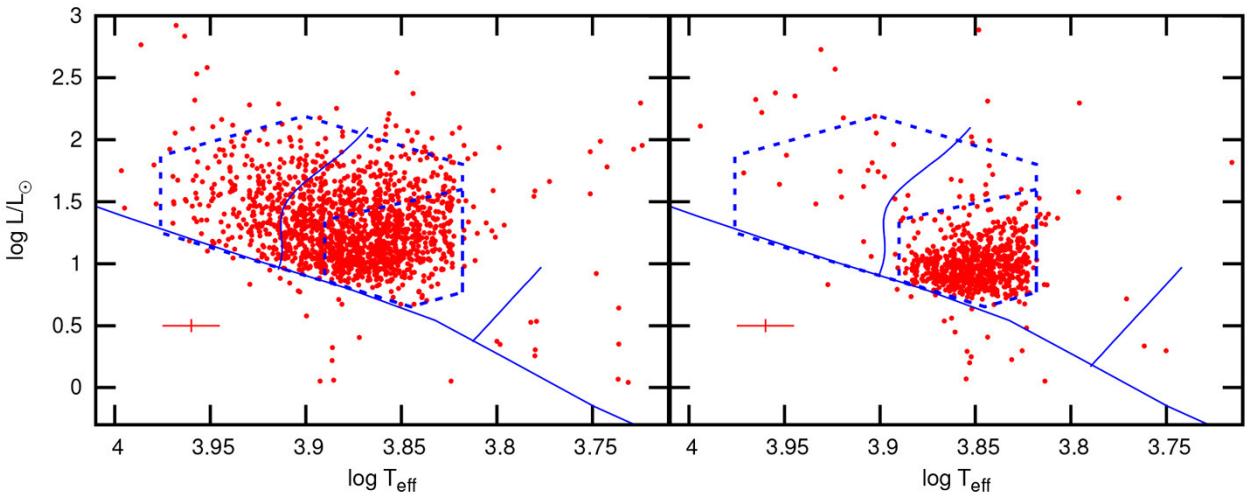

Figure 1.5: Locations of *Kepler* detected δ Sct stars (left) and γ Dor stars (right) on the H-R diagram. The long solid blue line indicates the main-sequence (Bertelli et al. 2008), the short solid blue lines indicate the width of the combined theoretical γ Dor/δ Sct instability strip (Xiong et al. 2016) and the dotted polygons (Balona 2018b) indicate the areas containing the majority of each pulsator class: δ Sct (larger box) and γ Dor (smaller box). Image from Balona (2018b).

1.6.2 Non-Pulsators in the Instability Strip

Several studies have been conducted to attempt to explain why non-pulsating stars exist within the instability strip. From the distribution of maximum detected amplitudes for *Kepler* δ Sct stars, Balona et al. (2011) found that 6.8% of these stars have a maximum

amplitude < 100 ppm. Adding non-pulsating stars to this distribution increases this proportion to 57.6%, which is an extreme jump from the 7–8% predicted from extrapolating the distribution of pulsating stars. Therefore this paper claims that there must be some mechanism present only in non-pulsating stars which prevents them from pulsating.

This finding was supported by a later analysis of the number and position of pulsating and non-pulsating stars within the δ Sct instability strip Balona (2018a). This study found that, even in the middle of the instability strip, only 60% of stars are pulsators. To determine whether the non-pulsators are simply pulsating below the current detectable amplitude level, they produced a distribution of the maximum amplitudes of their sample of *Kepler* δ Sct stars and discovered a discontinuity (similar to that found by Balona et al. 2011) which they believed to be non-physical. Therefore it is unlikely that the non-pulsators are pulsating below the detectable level. This paper also considered the possibility that the non-pulsating stars actually exist outside of the instability strip due to effective temperature errors. This hypothesis was rejected due to the statistical improbability that all 1782 non-pulsating stars found in the instability strip by Balona (2018a) actually exist outside it, and that many of the δ Sct stars would also be moved outside of the instability strip unless their effective temperatures were somehow much more accurate.

Another study using *Kepler* data was performed by Murphy et al. (2019) to determine the fraction of stars pulsating within the δ Sct instability strip. This paper found that the majority of δ Sct stars were located inside the theoretical instability strip derived by Dupret et al. (2005), but a significant number were located outside it. In contrast, the distribution of non-pulsators was found to centre on the red edge of the instability strip. They also determined the pulsator fraction as a function of temperature across the instability strip. This fraction varied from 25% just inside the red edge to a maximum of 60% in the middle of the instability strip, decreasing to 40% at the blue edge and 20% a few 100 K beyond it. The implication of this skewed distribution of pulsators is the potential for the instability strip to be redefined in terms of pulsator fraction, thus shifting it to a hotter region of the H-R diagram than current models predict. The other important implication is that there is a large fraction of non-pulsators which remains unexplained by observational uncertainties or chemically peculiar stars (Murphy et al. 2019).

1.6.3 Categories of γ Dor Stars

Further examination of light curves led Balona et al. (2011) to identify three categories of γ Dor stars. Balona (2018a) further improved their definitions to the following:

- GDORA - stars with large amplitude beating light variations where the maximum brightness variations are larger than those of minimum brightness (previously ASYM)
- GDORS - stars which present symmetric variations in maximum and minimum brightness in their beating light curves (previously SYM). This type is the most common
- GDORM - stars which show no beating but multiple frequencies of comparable amplitude (previously MULT)

During their analysis of *Kepler* γ Dor stars, Balona (2018a) found that the positions of GDORA, GDORS and GDORM γ Dor stars within the γ Dor instability strip are random rather than occupying specific regions. From their sample of 820 stars, they found 16.7% are GDORA, 54.45% are GDORS, 26.2% are GDORM and the remaining 2.6% are classified as GDOR as they were unable to be classified into these categories. In a subsequent study, Balona (2018b) investigated whether δ Sct stars within the γ Dor instability region also exhibited GDORA type light curves after significant frequencies above five cycles per day (5 d^{-1}) were removed. Their results showed that δ Sct stars do not show the same non-linearity as GDORA stars and therefore the non-linearities exhibited by γ Dor stars may indicate the mechanism which produces them, e.g. convective zones.

1.6.4 Correlation Between $v \sin i$ and Pulsation Parameters

A study of *Kepler* slow and moderately rotating γ Dor and hybrid stars by Tkachenko et al. (2013) shows a positive correlation between the spectroscopic $v \sin i$ and the photometric frequency, and a negative correlation between $v \sin i$ and photometric amplitude. The paper also notes that this correlation is even stronger when the few detected δ Sct frequencies are included. A comparison of the $v \sin i$ and photometric frequencies for a set of δ Sct stars however reveals a slight negative correlation. Since all independent frequencies (not just the dominant rotation frequency) show the same trends, Tkachenko et al. (2013) believe that these correlations are due to pulsation and not rotational modulation.

1.6.5 Present Day Status of γ Dor and δ Sct Stars

Our current knowledge of δ Sct and γ Dor stars is in the process of transitioning from the original theories, which defined these stars as quite separate pulsator classes, to new theories which will attempt to explain discrepancies such as the vast number of hybrid and non-pulsator stars, the mechanisms which excite the pulsations and the locations of the stars on the H-R diagram. It is hoped that the arrival of TESS data will provide enlightenment on the nature of these A- and F-type stars (Antoci et al. 2019).

1.7 Previous Studies of the Target Stars

This section details previous research performed on the five target γ Dor stars in this study.

1.7.1 HD 10167

The variability of HD 10167 was first discovered by Eyer et al. (2000) from the examination of Geneva photometry. Using a phase dispersion minimisation (PDM) technique, a frequency of 0.51258 d^{-1} was detected. Although this indicated γ Dor-type periodic behaviour, this frequency was close to the sampling frequency and therefore did not provide complete phase coverage for the PDM method used. Furthermore, correlation profiles from CORALIE spectra indicated that the star is a double star. Eyer et al. (2000) ultimately concluded that

the variability of HD 10167 was most likely due to its binary nature rather than a γ Dor component.

Eyer et al. (2002) reported that PDM and Fourier analysis of the photometric data obtained for HD 10167 at the South African Astronomical Observatory (SAAO) indicate that it is a mono-periodic γ Dor star. However, Eyer et al. (2002) also noted that stars of small amplitude variability with a small amount of available data are statistically more likely to be classified as mono-periodic rather than multi-periodic, which may or may not have been the case for HD 10167.

In the same year, Handler et al. (2002a) used Johnson B and V photometry from SAAO and Siding Springs Observatory (SSO) to determine that the B/V colour-amplitude ratio of 1.24 ± 0.12 found for HD 10167 met the criteria of typical photometrically observable γ Dor modes ($B/V = 1.2$ to 1.35), thus confirming that pulsation rather than binarity is the cause of its variation. They also failed to detect any δ Sct frequencies above an amplitude limit of 0.9 mmag in the V band. Handler et al. (2002a) therefore classified HD 10167 as a γ Dor candidate.

Table 1.1: Orbital solution determined by De Cat et al. (2006a) for HD 10167.

Parameter	Value
K_1 ($\mathrm{km\,s^{-1}}$)	39.7 ± 0.4
K_2 ($\mathrm{km\,s^{-1}}$)	41.8 ± 0.4
e	0.0
P (d)	9.3199 ± 0.0002
γ ($\mathrm{km\,s^{-1}}$)	5.2 ± 0.2
$a_1 \sin i$ (AU)	0.0340 ± 0.0003
$a_2 \sin i$ (AU)	0.0358 ± 0.0003
$M_1 \sin^3 i$ ($M_\odot$)	0.268 ± 0.011
$M_2 \sin^3 i$ ($M_\odot$)	0.254 ± 0.008
rms ($\mathrm{km\,s^{-1}}$)	0.99

1.7.2 HD 206481

This star was first classified as a 'prime' γ Dor candidate by Handler (1999) on the basis that, among other criteria, it showed multi-periodicity within the γ Dor frequency range. A period search of the star's *Hipparcos* light curve revealed two periods for HD 206481: 0.623 and 0.7 days (d), where the latter is an average of other possible extra periods. This was confirmed by Eyer et al. (2002) who determined from period searches using PDM and Fourier techniques that the star is a multi-periodic γ Dor star. HD 206481 was most recently analysed by Kahraman Aliçavuş et al. (2016), where the $v \sin i$ values was determined to be 86 ± 2 $\mathrm{km\,s^{-1}}$ from seven HARPS spectra.

1.7.3 HD 209295

The variability of this star was discovered by ESA (1997) and it was first classified as a γ Dor candidate when it was selected from the resulting *Hipparcos* photometry by Handler (1999) based on its spectral type, period and the resulting amplitude and brightness, among other criteria. A period search of the star's *Hipparcos* light curve resulted in four periods within the γ Dor frequency range: 0.885, 0.434, 0.388 and 0.853 d. A colour-magnitude diagram of all the candidates proposed by Handler revealed that HD 209295 is clearly positioned outside the blue edge of the γ Dor instability strip but still within the boundaries of the δ Sct instability strip. Despite this unexpected result, Handler (1999) was convinced that the star was indeed a γ Dor star as it was the only star for which four periods could be extracted from the *Hipparcos* photometry.

A period search performed by Eyer et al. (2002) on photometry obtained from SAAO confirmed that HD 209295 is a multi-periodic γ Dor star, and only months later Handler et al. (2002b) discovered δ Sct pulsation periods within its light curve, therefore establishing HD 209295 as the first γ Dor/δ Sct hybrid. The independent frequencies determined by Handler et al. (2002b) are shown in Table 1.2. The two highest amplitude photometric frequencies were also detected at a low level in the spectroscopic line profile variations. The mode identification performed by Handler et al. (2002b) for these frequencies results in $l = 1$, $|m| = 1$ for both. The paper also recognised that a number of the photometric frequencies were integer multiples of the orbital frequency, whose phases aligned near the periastron of the orbit of HD 209295; this synchronism was identified by Handler et al. (2002b) as possibly originating from a tidally-induced oscillation $l = 2$, $|m| = 2$ mode.

Further photometric and spectroscopic data obtained by Handler et al. (2002b) gave new insight into the dynamic nature of HD 209295. The object was determined to be a binary system after radial velocity variations > 100 km s^{-1} were measured. The secondary component's radial velocities were not visible; therefore it was classified as a single-lined spectroscopic binary (SB1). The orbit was found to have a period of 3.10575 d, eccentricity 0.35 and inclination $< 44°$, which indicates that the dark component of the binary has a mass > 0.98 $M_\odot$. Handler et al. (2002a) also commented that HD 209295 is a close binary.

Handler et al. (2002b) were unable to pinpoint the exact nature of the dark component of HD 209295: it lacked the infrared excess of a main-sequence star and exhibited an ultraviolet excess that could not be explained by a model with a hot component which is dark in the optical. The best explanation for the secondary component's nature that their paper could conjure is a neutron star, which agrees with the orbital eccentricity and mass constraint mentioned previously, but disagrees with the chemical composition, motion and lack of x-rays produced by the component.

Handler et al. (2002c) is a continuation of the analysis performed in Handler et al. (2002b). The paper determines a number of properties for the primary component of the system; $T_{\rm eff} = 7750 \pm 100$ K and $\log g = 4.10 \pm 0.05$ were obtained from the star's measured Strömgren indices, which in turn allowed for the calculation of its stellar radius $R_1 = 2.08 \pm 0.09$ $R_\odot$ (where $R_\odot$ is one solar radius) and mass $M_1 = 1.84 \pm 0.07$ $M_\odot$ using evolutionary tracks. By fitting a model of stellar rotation to a mean line profile, the star's $v \sin i$ value was determined for two different sets of line profile data to be 108 ± 10 and 98 ± 10 km s^{-1}.

Table 1.2: Independent photometric frequencies determined by Handler et al. (2002b) and Handler et al. (2002c) for HD 209295.

			Frequency (d^{-1})	
		Combination	Handler et al. (2002b)	Handler et al. (2002c)
γ Dor	f_1		1.12934 ± 0.00005	1.12934 ± 0.00005
	f_2		2.30217 ± 0.00006	2.30217 ± 0.00006
	f_3	$8f_{orb}$		2.57593 ± 0.00011
	f_4	$f_2 - f_1$		1.17283 ± 0.00004
	f_5	$9f_{orb} - f_1$		1.76859 ± 0.00005
	f_6	$7f_{orb}$		2.25394 ± 0.00011
	f_7	$3f_{orb}$		0.96597 ± 0.00011
	f_8	$5f_{orb}$		1.60996 ± 0.00011
	f_9	$9f_{orb}$		2.89792 ± 0.00011
δ Sct	f_1		25.9577 ± 0.0015	25.9577 ± 0.0015
	f_2		13.6873 ± 0.0018	
		f_{orb}	0.32199 ± 0.00011	0.32199 ± 0.00011

In terms of its classification, Handler et al. (2002c) stated that HD 209295 was the hottest known γ Dor star, since it lies in the middle of the temperature range for the δ Sct instability strip and is therefore also a prime δ Sct candidate. Multi-site photometric data from 2000 resulted in the detection of six significant γ Dor frequencies (shown as the first six frequencies listed in Table 1.2). In order to detect δ Sct pulsation frequencies, the data was prewhitened with the six γ Dor frequencies. One significant frequency was found (25.9577 ± 0.005 d^{-1}) and, after prewhitening with this frequency, several other prominent frequencies in the range of 12–25 d^{-1} were detected but not at a significant level. However, Handler et al. (2002c) believed that these frequencies may also be real after observing multi-periodic beating in the light curve and detecting similar signals in different subsets of the data.

The photometric data was further exploited for more frequencies using the software program Period 98 by fixing the frequencies of the six detected γ Dor pulsations and performing a least-squares fit before prewhitening the data. Three more γ Dor frequencies (0.96597, 1.60996 and 2.89792 d^{-1}, all with an error of 0.00011 d^{-1}) were detected as harmonics of the orbital frequency ($f_{\rm orb} = 0.32199 \pm 0.00011$), which was also determined from the light curve ($P_{\rm orb} = 3.1057 \pm 0.0010$ d). After prewhitening with all nine γ Dor frequencies and the single detected δ Sct frequency, the residual amplitude spectra still indicated the presence of further frequencies of both pulsation classes. Handler et al. (2002c) also searched for ellipsoidal variability in the residual light curve, but did not find any such signal greater than 2 mmag.

Handler et al. (2002c) attempted to identify high spherical (l) degree modes from line

profile variations which move across the correlated line profiles. The appearance and disappearance of such variations causes abrupt changes in the radial velocity which therefore indicate the spacing of the variations. From these spacings, Handler et al. (2002c) estimate that the high-degree modes are $l \approx 5$; however the frequencies of these modes were unable to be determined. This paper also used the Pixel-by-Pixel method (described in Section 3.3.3) to detect line profile variations due to pulsation. They were unable to detect any new pulsation frequencies but found traces of the first two photometric frequencies (1.1296 and 2.3024 d^{-1}) after deliberately searching for them. The mode identification for these frequencies was based on the phase changes of the frequencies and their first harmonics throughout the line profile. The modes were both determined to be $l = 1 \pm 1$, $m = 1 \pm 2$.

This paper also attempted mode identification on HD 209295 by comparing theoretical and observed amplitudes and phases of light variations in different wavebands. Only γ Dor frequencies were considered for this process. Applying this method to all wavebands simultaneously obtained no clear results, whereas application to two wavebands indicated that the photometric modes have $l = 1, 2$ and not $l = 3$.

Handler et al. (2002c) also believe that a number of the photometric frequencies are produced by tidal effects as they are exact harmonics of the orbital frequency and are therefore likely to be modes of $l = 2$, $|m| = 2$. The modes of these frequencies were unable to be identified. However, this paper also noted that tidally-forced oscillations should also be in phase when the tidal force is greatest (i.e. at periastron). An examination of the phases of the detected photometric frequencies shows some evidence of this.

More information on the orbit of HD 209295 was also able to be determined in this paper. Prewhitening the radial velocity data with trial frequencies indicated that the radial velocity curve was not sinusoidal. Fourier analysis suggested $f_{\mathrm{orb}} \approx 0.32$ d^{-1} but was hindered by aliasing in the data. Using a residualgram method and Period 98, the aliasing was reduced and the orbital frequency was refined to 0.32198 d^{-1}, which agrees with the result found from photometry. An orbital solution was determined for the binary (shown in Table 1.3) after an initial solution indicated that there was not a third object present in the system. There were also no significant pulsation frequencies found in the radial velocities once the orbital motion was corrected for.

The nature of the secondary star in the HD 209295 remains a mystery despite the efforts of Handler et al. (2002c) to investigate all types of electromagnetic radiation evidence.

By relating the secondary mass to the orbital inclination, they determined a lower limit for the companion's mass: $M_2 > 0.62\ M_\odot$. A companion of this minimum mass would cause the primary star to fill $\sim$90% of its Roche lobe at periastron. In order for the secondary star's spectra lines to be absent as a main-sequence star, it must have absolute magnitude $M_V > 4.4$, which would have spectral type G0 (or later) with mass $M_2 < 1.05\ M_\odot$. Since the light curve provides no evidence of eclipses, the inclination was refined to $i < 80°$. This type of star should be detectable in the infrared. To confirm this, Handler et al. (2002c) modelled the infrared range output of the primary star individually as a A7 to F0 star and with G0 and K5 type companions and compared the results to the observed infrared from HD 209295. Some infrared passbands suggested that a main-sequence star is present, another passband suggested the opposite and yet another had uncertainties too large to be meaningful. Therefore the paper concluded that the infrared result was too ambiguous to

Table 1.3: Orbital solutions determined by Handler et al. (2002c) and De Cat et al. (2006a) for HD 209295. Note that the units for $a_1 \sin i$ are different for each paper.

Parameter	Handler et al. (2002c)	De Cat et al. (2006a)
K_1 ($\mathrm{km\,s^{-1}}$)	54.2 ± 0.7	52.8 ± 0.3
e	0.352 ± 0.011	0.324 ± 0.005
ω (°)	31.1 ± 2.0	33 ± 1
P (d)	3.10575 ± 0.00010	3.10573 ± 0.00002
γ ($\mathrm{km\,s^{-1}}$)	-23.7 ± 0.4	-20.5 ± 0.2
T_0 (HJD)	2451771.864 ± 0.014	—
$a_1 \sin i$	3.11 ± 0.04 $R_\odot$	0.01426 ± 0.00008 AU
$f(M)$ ($M_\odot$)	0.042 ± 0.002	0.0401 ± 0.0007
rms ($\mathrm{km\,s^{-1}}$)	–	1.03

determine the nature of the secondary.

Additional evidence also suggested that the secondary is not a main-sequence star. A relation between the minimum orbital inclination and the secondary mass was determined by modelling the lack of ellipsoidal variability in the system and gave $i > \sim 41.5°$. In combination with the previous relation between inclination and secondary mass, this refined the secondary mass to $M_2 > 1.04\ M_\odot$, which is just below the maximum mass for a main-sequence companion. In addition, the eccentricity of the orbit is abnormal for a main-sequence binary as old as HD 209295. For a binary of the same age, the eccentricity is expected to be $e < 0.1$, whereas HD 209295 has $e = 0.352$. This evidence suggested that the secondary star is degenerate instead.

The next possibility entertained by Handler et al. (2002c) was a white dwarf companion. Such a star would have $M_2 > 1.04\ M_\odot$ but circularization of the orbit would also be expected for this type of binary due to the occurrence of previous mass transfer. This paper attempted to confirm the white dwarf nature of the secondary by comparing the UV flux measured by the TD-1 satellite to the predicted UV flux of the primary based on its measured *uby* magnitudes. A model with $T_{\rm eff} = 7750$ K and $\log g = 4.3$ was the best fit for the *uby* magnitudes. The UV flux produced by such a star was compared to the TD-1 UV measurements. There was a negligible amount of flux at 1565 Å but a clear UV excess at 1965 and 2365 Å. The shape of the UV excess could be explained by an object with $T_{\rm eff} \approx 15,000$ K. Handler et al. (2002c) then fit white dwarf models with a V magnitude of a star at the system's distance, $\log g = 8$ and $10,000 < T_{\rm eff} < 16,000$ K to the excess. According to Handler et al. (2002c), while the shape of the excess matched, a white dwarf would only have a luminosity capable of producing 0.1–0.2% of the UV excess observed in HD 209295. A hotter white dwarf could explain more of the excess but would not match the observed level of flux at 1565 Å. Thus the UV excess could not pinpoint the nature of the secondary star.

Finally, Handler et al. (2002c) considered the secondary as a neutron star. The high

eccentricity of the orbit would be explained by the secondary star's supernova event and circularization of the orbit would not have occurred during the main-sequence lifetime of the primary star. A comparison of the orbital parameters of HD 209295 to those of simulated x-ray binary populations showed reasonable agreement; thus the secondary could be a neutron star. However, this explanation also had its discrepancies. Previous evolutionary phases of the neutron star should be evident in the primary star's chemical composition, but its spectra appeared normal. A neutron star is also usually detectable in x-rays, but HD 209295 has not been detected by ROSAT or the Einstein Observatory. Lastly, the supernova kick experienced by the neutron star would have changed the motion of the binary system within the galaxy, but the system does not exhibit any abnormal velocities or proper motions. Thus Handler et al. (2002c) were unable to determine the nature of the secondary star.

Another orbital analysis of HD 209295 was performed by De Cat et al. (2006a). This paper provided a new description of the orbital parameters from the radial velocities of 61 CORALIE spectra (see Table 1.3), which includes the set of data used by Handler et al. (2002c). They found a $v \sin i$ value of 86 ± 3 km s^{-1} for the visible component of HD 209295. Clearly visible correlation profile variations in the spectra and the availability of *Hipparcos* photometric data allowed for the detection of 10 independent frequencies by De Cat et al. (2006a) as shown in Table 1.4. The paper notes that the 3$^{\rm rd}$, 6$^{\rm th}$, 8$^{\rm th}$, 9$^{\rm th}$ and 10$^{\rm th}$ periods are exact multiples of the orbital period and therefore possibly tidally induced, as found previously by Handler et al. (2002b). The first four periods were also detected by De Cat et al. (2006a) in the radial velocity variations after prewhitening with the orbital period.

The most recent analysis of HD 209295 was performed by Kahraman Aliçavuş et al. (2016), where $v \sin i$ was determined to be 89 ± 5 km s^{-1} from two HERCULES spectra.

Table 1.4: Independent photometric (denoted by ^{p}) and spectroscopic (^{s}) frequencies determined by De Cat et al. (2006a) for HD 209295.

	Period (d)	Resulting Frequency (d^{-1})
P_1^p	0.88529 ± 0.00002	1.12957
P_2^p	0.434363 ± 0.000006	2.30222
P_3^p	0.388230 ± 0.000008	2.57579
P_4^p	0.8519	1.17385
P_5^p	0.5659	1.76710
P_6^p	0.4430	2.25734
P_7^p	0.9246	1.08155
P_8^s	1.03523 ± 0.00012	0.96597
P_9^s	0.62113 ± 0.00004	1.60997
P_{10}^s	0.345075 ± 0.000013	2.89792

1.7.4 HD 214291

The binarity of HD 214291 has been confirmed as far back as the 1990s: the catalogue of Strömgren photometry of F- and G- stars (Olsen 1994) identifies two components for HD 214291; and the HIPPARCOS and TYCHO Catalogues present astrometric and photometric values for both components of the system (ESA 1997).

HD 214291 was classified as a candidate γ Dor star by Aerts et al. (1998) after the analysis of its *Hipparcos* light curve presented two periods, 0.8713 d and 6.6050 d, where the second was detected after prewhitening the data with the first. No attempts were made to find further frequencies as "the *Hipparcos* data are in general not suited to find very complicated variability patterns" (Aerts et al. 1998). It was determined that the combination of the two periods accounted for 84% of the star's variability. Aerts et al. (1998) also noted that the detection of a period of the order of days after the detection of a much shorter frequency (as is the case for this star) is possibly produced by the sampling of the data and the periods should be confirmed by obtaining follow-up data.

The most recent analysis of HD 214291 was presented by De Cat in two separate articles in 2006. The first (De Cat et al. 2006b) identified HD 214291 as a ellipsoidal, double-lined binary (SB2) from the examination of CORALIE spectra. The second (De Cat et al. 2006a) provided the first description of the orbital elements of the binary system from five CORALIE spectra (Table 1.5). Additionally, they found $v \sin i$ values of 67.6 ± 0.8 and 64.7 ± 0.7 km s^{-1} for the primary and secondary components respectively. As for HD 10167, De Cat et al. (2006a) state that the closeness of these values indicates the spin-alignment and synchronisation of the components, a conclusion which is supported by the binary's circular orbit. The previous classification of HD 214291 as an ellipsoidal variable in De Cat et al. (2006b) was confirmed in De Cat's second paper where twice the main *Hipparcos* period detected for the star matched the frequency at which the radial velocity varied.

Table 1.5: Orbital solution determined by De Cat et al. (2006a) for HD 214291.

Parameter	Value
K_1 (km s^{-1})	111 ± 14
K_2 (km s^{-1})	111 ± 14
e	0.0
P (d)	1.74247 ± 0.00002
γ (km s^{-1})	-13.9 ± 0.6
$a_1 \sin i$ (AU)	0.018 ± 0.002
$a_2 \sin i$ (AU)	0.018 ± 0.002
$M_1 \sin^3 i$ ($M_\odot$)	1.0 ± 0.5
$M_2 \sin^3 i$ ($M_\odot$)	1.0 ± 0.4
rms (km s^{-1})	0.67

1.7.5 HD 216910

This star was first classified as a candidate γ Dor star by Aerts et al. (1998) where periods 0.6935 and 0.6136 d were detected in its *Hipparcos* light curve, constituting 45% of its variability. As with HD 214291, the second period was detected after prewhitening the data with the first and there were no further attempts to detect periods due to the *Hipparcos* data quality. These periods were not able to be confirmed by a later study (Eyer et al. 2002) due to a lack of data.

However, more recent studies of HD 216910 confirmed that the star is a bona-fide γ Dor star (De Cat et al. 2006b). Furthermore, De Cat et al. (2006a) determined the $v \sin i$ value for HD 216910 to be 92 ± 3 km s^{-1} and identified clear correlated line profile variations in its 11 CORALIE spectra. They were unable to perform their own period search on their small amount of CORALIE data. However, they concluded from phasing their radial velocity data with the periods found by Aerts et al. (1998) that the photometric *Hipparcos* frequencies were not present in their spectroscopic data.

The most recent analysis of HD 216910 was performed by Kahraman Aliçavuş et al. (2016), where its $v \sin i$ value was found to be 95 ± 4 km s^{-1} from two HERCULES spectra.

1.8 Motivation for Thesis

This study aims to perform a comprehensive analysis of the selected target stars HD 10167, HD 206481, HD 209295, HD 214291 and HD 216910 by integrating high-precision TESS photometry with contemporaneous spectroscopic data from the High Efficiency and Resolution Canterbury University Large Échelle Spectrograph (HERCULES) in conjunction with the 1.0-m McLellan telescope at the University of Canterbury Mount John Observatory. The advantage of applying both photometric and spectroscopic analyses to the targets is the potential for the results of each method to support or confirm the results of the other.

The targets were selected primarily for the availability of their photometric and spectroscopic data (as detailed in Section 2) and secondarily for the lack of analysis performed on the targets, recent or otherwise. Even for HD 209295, which was thoroughly studied by Handler in multiple papers (Handler 1999; Handler et al. 2002a; Handler et al. 2002b; Handler et al. 2002c), the most recent individual analysis performed on any of the targets was by De Cat et al. (2006a) and De Cat et al. (2006b). It is also unfortunate that none of these targets were observed as part of the *Kepler* K2 campaigns from 2014–2018 which triggered advancements in asteroseismology. Therefore the recent NASA TESS campaign provides the first set of high-precision space photometric data for these targets and the ideal opportunity to revisit their analysis.

Additionally, this study aims to perform a photometric analysis of the University of Canterbury 'Mapping and Understanding Stellar Interiors through a Coordinated International Asteroseismology Network' (MUSICIAN) spectroscopic program stars for the purpose of providing a preliminary overview of their properties and identifying stars to reject as bonafide γ Dor stars.

The following chapter details the data collection for the targets and the required processing methods. Chapter 3 details the analytic methods, both photometric and spectroscopic, that were performed on the five target stars and the MUSICIAN stars. Chapters 4–8 provide summaries of the results of the analyses for each star and discussions of their implications. Chapter 9 details the analysis and results of the MUSICIAN program overview. Chapter 10 provides a summary of all results obtained by this thesis and their implications.

2. Data Collection and Processing

This optical study required both high-precision space photometry and high-resolution spectroscopic data in order to perform a detailed analysis of the target stars. Five targets (HD 10167, HD 206481, HD 209295, HD 214291 and HD 216910) were chosen for this study as they were observed as part of the MUSICIAN program and have Sector 1 or 2 data collected by the Transiting Exoplanet Survey Satellite (TESS).

In addition, most of the stars in the MUSICIAN program were analysed using TESS and *Gaia* data to produce an overview of the properties of these bonafide and candidate γ Dor stars. The list of targets for this analysis was restricted to the majority ($\sim$83%) of the MUSICIAN stars as there was no TESS and/or *Gaia* data available for some objects.

2.1 TESS Photometry

This study uses photometric data obtained by the National Aeronautics and Space Administration (NASA) satellite TESS. These data were very suitable for a detailed asteroseismological analysis and TESS data releases were planned during the timeline of this study.

TESS was launched on 18 April 2018 and made its first observations on 25 July 2018, with the first sector of data released by the TESS Asteroseismic Science Operations Center (TASOC; TASC n.d.) by the 13 October 2018 (Handberg et al. 2018). The purpose of the TESS mission is to perform a survey of 85% of the sky to detect exoplanets by the transit method (NASA 2019a). Compared to its predecessor *Kepler*, TESS observes 400 times more sky and 30 to 100 times brighter stars, with a limiting magnitude in the I band of $\sim$10–14 mag (Ricker et al. 2015). The TESS mission is scheduled to run for two years and observe 200,000 stars, with the first year (July 2018 - July 2019) observing Sectors 1–13 in the southern ecliptic hemisphere before observing Sectors 14–26 in the northern ecliptic hemisphere the following year (July 2019 - July 2020). Figure 2.1 presents the sky coverage of TESS up to Sector 21.

Currently, TESS's cameras have an exposure time of two seconds and the observations are stacked together to produce 120 or 1800 second cadence data products (NASA 2019b). Since each sector is observed for 27.4 days, a maximum of $\sim$19,700 individual measurements can be recorded by TESS for each target in a sector. Due to the nature of the TESS observations (large sky coverage, fine sampling rate and high photometric precision of $\sim$5 mmag for bright targets), the data collected by TESS is also of sufficient quality to enable asteroseismological analysis as well as its intended primary purpose of exoplanet detection and confirmation (Ricker et al. 2015).

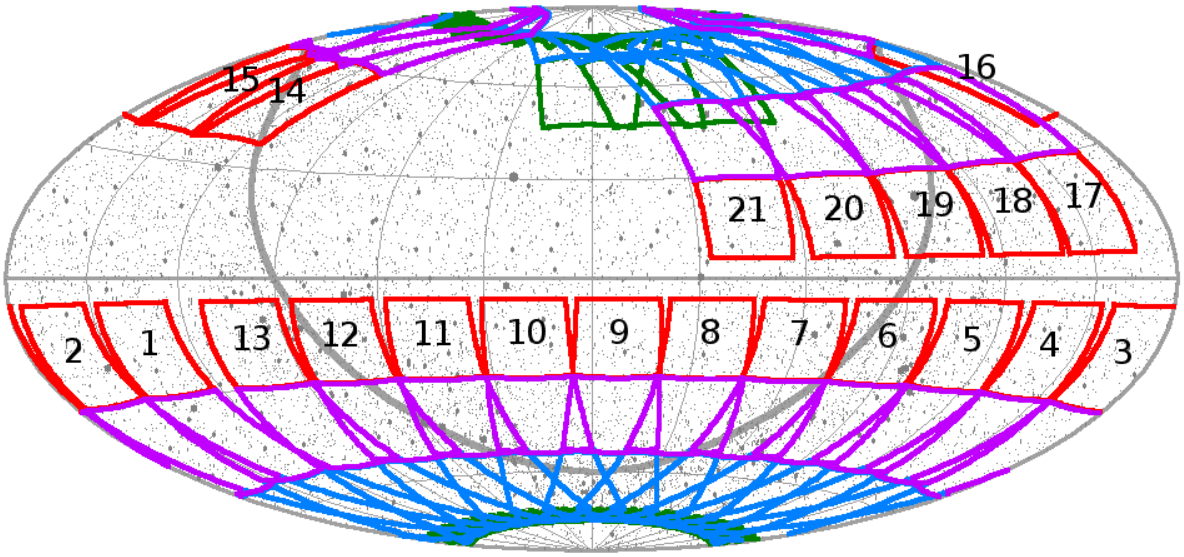

Figure 2.1: TESS sky coverage maps for Sectors 1–21, given in ecliptic coordinates. The thick grey and thin horizontal grey lines represent the galactic and ecliptic planes respectively. Each coloured square represents the field of view of one of TESS's four cameras. Sectors 1–13 were observed in the first year of the TESS mission. Image from MIT (2020).

2.1.1 Target TESS Data From TASOC and MAST

The data used in this study for the five target stars were obtained during observations of Sectors 1 and 2 of TESS's southern hemisphere campaign (Table 2.1).

The data products obtained via TASOC (TASC n.d.) for the targets are simple aperture photometry (SAP) light curves which have not been processed by the TASOC light curve correction pipeline, designed to correct for systematic errors with the purpose of preparing the data specifically for asteroseismological analysis. These data were used as the corrected light curves were not available from TASOC at the time.

Table 2.1: Sectors and observation time periods for the target stars in this study. Note TBJD stands for 'TESS Barycentric Julian Date' (BJD - 2457000) and UTC stands for 'Universal Time Coordinated'. Times retrieved from Handberg et al. (2019).

Target	Sector	Start Time (TBJD)	End Time (TBJD)	Start Time (UTC)	End Time (UTC)	# of Data Points
HD 10167	2	1354.11	1381.52	23-08-2018 14:32:48	20-09-2018 00:27:10	18,699
HD 206481 HD 209295 HD 214291 HD 216910	1	1325.30	1353.18	25-07-2018 19:09:59	22-08-2018 16:21:27	19,261

This study also uses TESS data available via the Barbara A. Mikulski Archive for Space Telescopes (MAST; STScI 2020) which contains data from all sectors observed to date. The difference between the MAST and TASOC data is the processing applied to the light curves which aim to prepare them for different analytical applications. Therefore it is possible that the MAST light curve correction pipeline removes real asteroseismological artefacts as it prepares the data for exoplanet detection or confirmation analysis. Although pre-search data conditioned SAP (PDCSAP) light curves are available from MAST for the five target stars, the data used from MAST are SAP light curves which will enable a direct comparison to the TASOC data and therefore the TASOC light curve correction pipeline.

2.1.2 MUSICIAN TESS Data From MAST

The data used in this study for the MUSICIAN program stars was obtained during observations of Sectors 3 - 13 of TESS's campaign. The data products obtained via MAST (STScI 2020) for these targets are PDCSAP light curves which have been de-trended by the TESS Science Processing Operations Center pipeline (Jenkins et al. 2016).

2.1.3 Light Curve Cleaning

TESS data includes data points which may not be accurate due to events such as movements of the satellite or incident cosmic rays. To prepare the datasets for analysis, these inaccurate data points must be removed.

Each data point in a TESS light curve is assigned a quality flag designed to indicate whether the data point has been affected by changes in the satellite's performance or other external influences (e.g. cosmic rays). The different quality flag values indicate the occurrence of a particular anomalous event and therefore the corresponding correction has been applied. Not all quality flags indicate a 'bad' data point; according to the TESS Archive Manual (Fleming 2018), only the flags 1–6, 8, 10 and 12 indicate a data point of lesser quality. Since the flags 7, 9 and 11 are not used in Sectors 1–13 data products (see Fausnaugh et al. (2018) for Data Release 1, and subsequent Data Releases 2–13 by these authors) and flag 0 indicates an 'ok' data point, all quality flags of a non-zero value present in the dataset indicate data of lesser quality. Hence, these data were removed from the TASOC and MAST light curves. An example of this is shown in Figure 2.2.

After the removal of lesser-quality flagged data, the light curves were further cleaned by manual removal of any outliers. For HD 10167, the dips in brightness occurring at $\sim$1355 and $\sim$1368 TBJD with a periodicity of $\sim$15 days were removed for two reasons: firstly, they behave similarly to light curve artefacts produced when the telescope is still cooling down to its operating temperature or the satellite is being re-oriented, and therefore could be erroneous data; and secondly, this study aimed to identify pulsation periods associated with γ Dor and δ Sct stars ($\leq$ 3 days) which are shorter than the period associated with the recurrence of these dips. The light curve was cropped to include only the relevant data by retaining data points after 1355 TBJD which have flux $> 3.865 \times 10^5$ $e^- s^{-1}$. The final TASOC and MAST light curves for the target stars are shown in Figure 2.3 and 2.4 respectively.

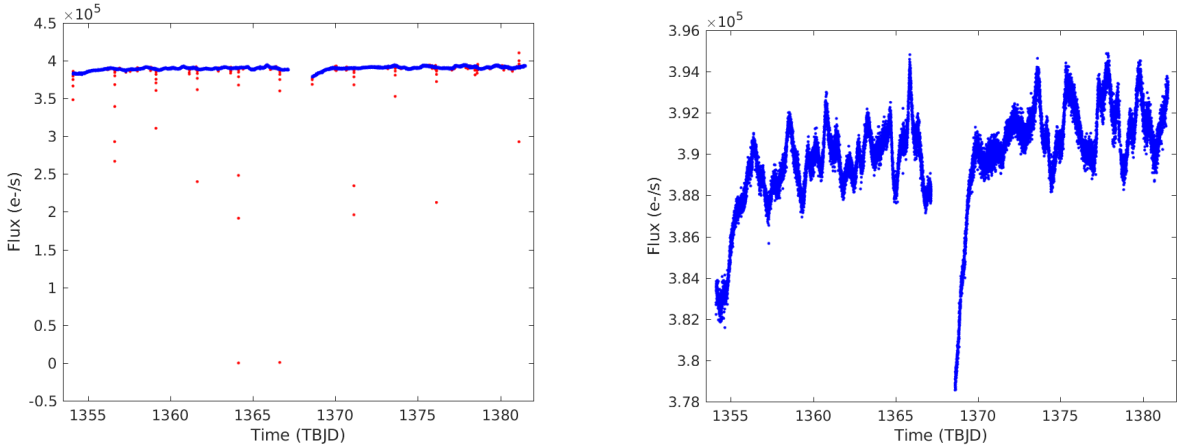

Figure 2.2: TESS light curves for target HD 10167 showing (a) the lesser-quality flagged data (red); and (b) the dataset with lesser-quality flagged data removed (blue).

No manual data removal was performed on the MAST light curves for the MUSICIAN stars. The final light curves for the MUSICIAN stars are shown in Chapter 9.

2.2 Échelle Spectroscopy

This study uses spectroscopic data observed by HERCULES in conjunction with the 1.0-m McLellan telescope at the University of Canterbury Mount John Observatory. Large amounts of spectroscopic data have been taken with the same instrument as part of the MUSICIAN collaboration monitoring campaign, which includes the target stars.

HERCULES is a spectrograph designed and built at the University of Canterbury and it has been operating at the Mount John Observatory since 2001. It receives light from the 1.0-m McLellan telescope via an optical fibre feed and operates over a wavelength range of 380–880 nm with a resolving power of R $\approx$ 41,000 (Hearnshaw et al. 2002). The spectrograph is designed to observe bright stars ($V \leq 9.1$) and achieves its high radial velocity precision (4–14 $\mathrm{m\,s^{-1}}$) through its thermally insulated and isolated location inside a vacuum tank.

There are three types of spectra taken during an observation of a star: flat fields, arcs and stellar images (see Figure 2.5). The first two are calibration images required to process the stellar spectra.

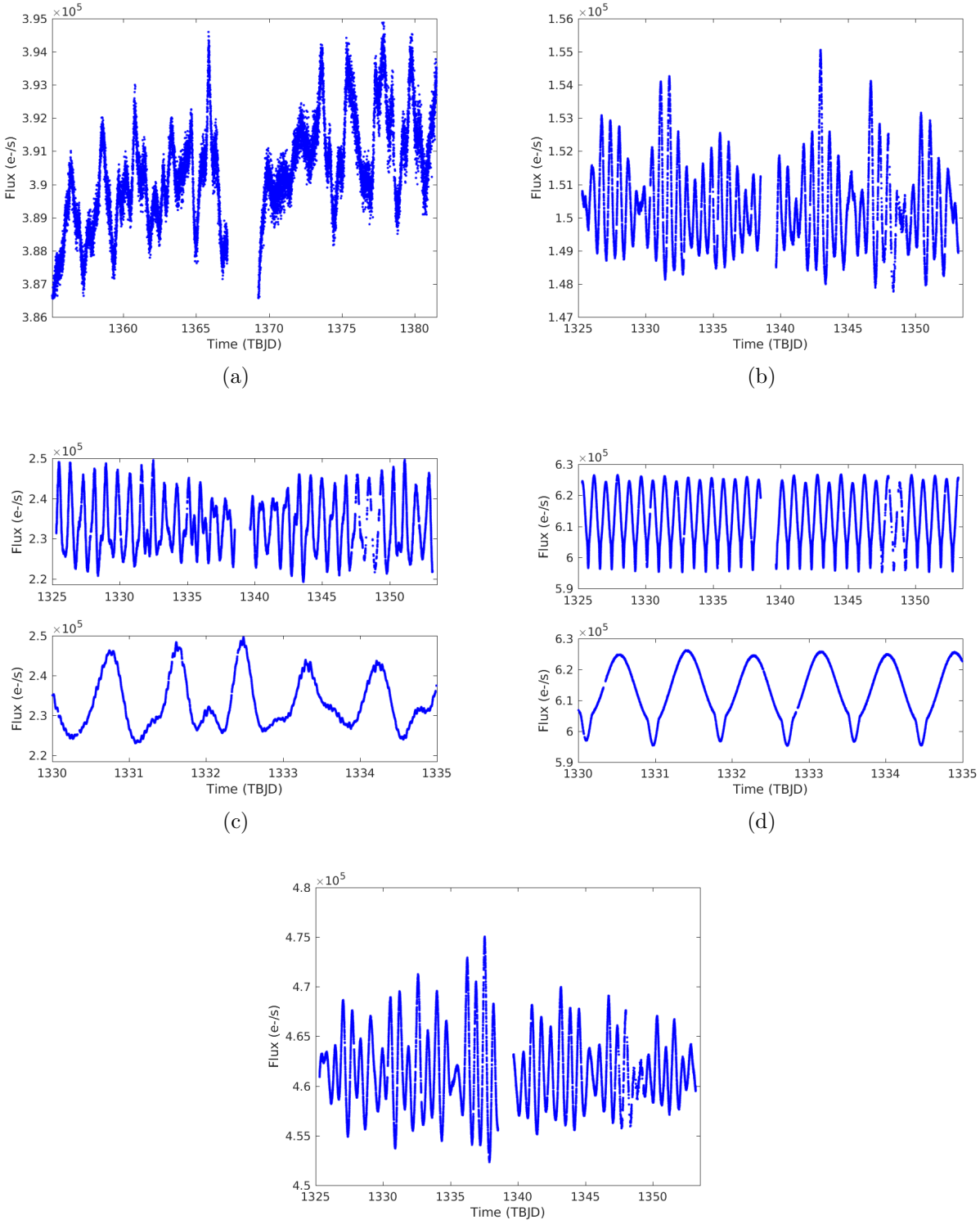

Figure 2.3: Cleaned SAP TASOC light curves for (a) HD 10167; (b) HD 206481; (c) HD 209295 full light curve (top) and a 15 day excerpt (bottom); (d) HD 214291 full light curve (top) and a 5 day excerpt (bottom); and (e) HD 216910.

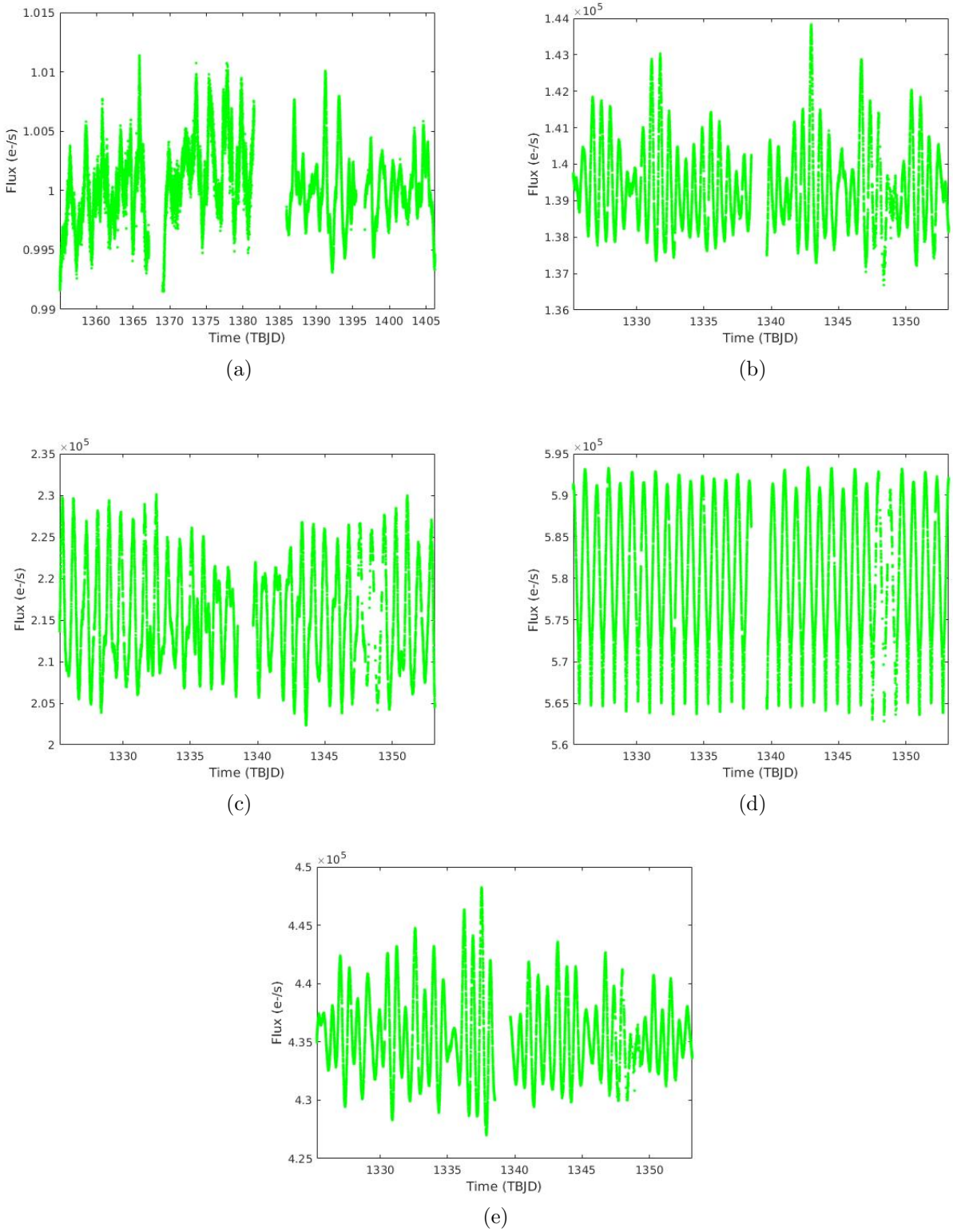

(a) (b) (c) (d) (e)

Figure 2.4: Cleaned SAP MAST light curves for (a) HD 10167; (b) HD 206481; (c) HD 209295); (d) HD 214291; and (e) HD 216910.

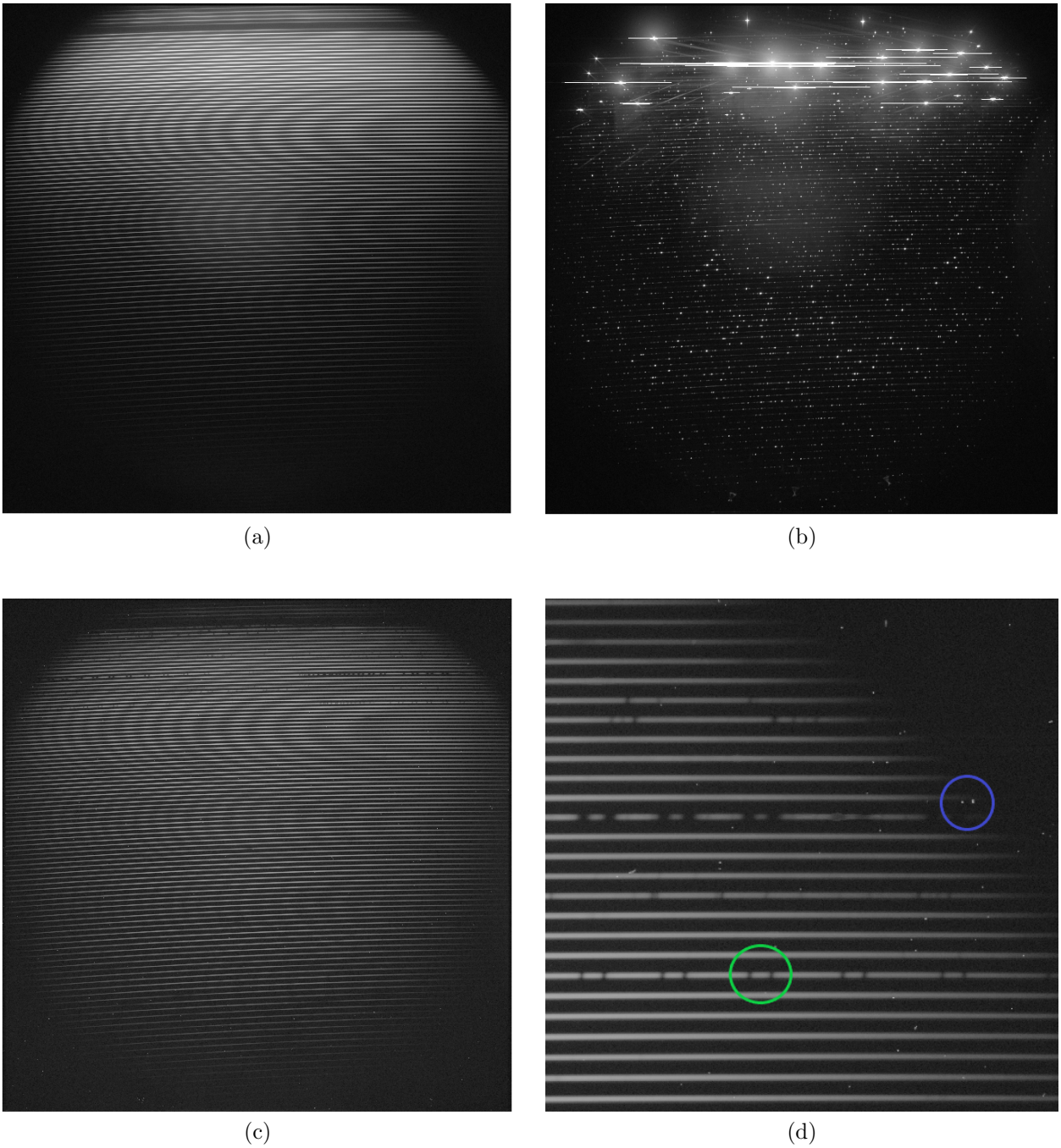

(a) (b)

(c) (d)

Figure 2.5: Examples of the three spectra types taken during a stellar observation: (a) flat field; (b) arc; (c) stellar spectrum of HD 10167; and (d) a close-up of the top right corner of (c) demonstrating the double absorption lines of this binary star system (green circle) and detected cosmic rays which appear as bright dots (blue circle).

Flat field (also known as white) images, as described by Bacon et al. (2017), are the "relative response of the instrument to a uniform illumination". The resulting spectrum maps the pixels of the Charged Coupled Device (CCD) camera which are over- or under-sensitive to any input light. This means that any systematic errors in the CCD can be taken into account before the stellar spectra are analysed. The white images are taken at the beginning and/or end of each observing night and at Mount John Observatory are recorded from the light output of a tungsten lamp. Due to their smooth blackbody emission, a tungsten lamp is the ideal source of light for a white image as it produces a spectrum with a high signal-to-noise ratio (S/N) (Bacon et al. 2017). White images are also used to correct for the blaze function of a spectrograph, which is a variation in the brightness along the spectral orders due to the specifications of the diffraction grating (Clayton 1996), by mapping the pixel positions of the échelle orders on the CCD.

Arcs are the mapping of the wavelength position to the pixels on the CCD. A reduced stellar spectrum is typically presented as a one-dimensional function of wavelength; however when the spectrum is observed by the CCD it is recorded two-dimensionally as a function of the pixel position on the CCD. As shown in Figure 2.5, an échellegram image consists of overlapping sections (called 'orders') of the full spectrum arranged vertically, from longer wavelengths (redder) at the top to shorter wavelengths (bluer) at the bottom. In order to determine where each wavelength in the observable wavelength range is positioned on the CCD, an arc is taken using a gas discharge lamp of an element with well-calibrated emission lines. The arcs are taken before and after the stellar spectra for each target and at least once per hour using a thorium-argon (Th-Ar) lamp.

Stellar images are the spectra taken when the telescope is observing a target star. The exposure time for a stellar spectrum varies depending on the magnitude or brightness of the star; brighter targets require less exposure time whereas fainter targets require a longer exposure time to allow more light to be gathered to increase the S/N of the resulting spectrum. The length of the exposure time does not affect the analysis of the spectra as the reduction pipeline is designed to account for varying exposure times.

2.2.1 Target Spectroscopic HERCULES Data

All the HERCULES observations used in this study were taken during the period of three years from July 2016 to July 2019. Due to the difficulties associated with ground-based observation (dependency on weather conditions and stellar position relative to the observer), the five targets were not observed in equal measure. Table 2.2 gives the exposure time for each stellar spectrum, time periods over which each star was observed, and the number of stellar spectra recorded. All white and arc spectra were taken with two- and five-second exposures respectively.

Table 2.2: Values for each target's observation parameters (apparent V magnitude and exposure time), dates of the first and last observations made, and the number of stellar spectra observed. V magnitudes retrieved from De Cat et al. (2006a) and Kahraman Aliçavuş et al. (2016).

Target	V Magnitude (mag)	Typical Exposure Time (s)	First Obs (dd-mm-yyyy)	Last Obs (dd-mm-yyyy)	# of Spectra
HD 10167	6.67	1200	15-07-2016	15-06-2019	131
HD 206481	7.86	1800	29-09-2017	21-07-2019	39
HD 209295	7.5	1800	04-06-2017	14-07-2019	66
HD 214291	6.54	1200	21-09-2018	21-07-2019	37
HD 216910	6.70	1200	13-07-2016	21-07-2019	193

2.2.2 Spectra Reduction

All spectral data was reduced using the MATLAB reduction pipeline *Megara* (V1.1) which was written by Dr E. Brunsden specifically for HERCULES spectra and is based on previously developed MATLAB codes by Drs D. Wright and E. Brunsden.

The following actions are performed during a typical reduction with *Megara*. All spectral data files (flats, arcs and stellars) are checked for the correct quality, size and image type and then reduced in monthly subsets. The flats are summed, the orders are traced, and the background is fitted and removed. The arc spectral emission lines are located and the arcs are calibrated to create a stellar wavelength template. The stellars are filtered for cosmic rays, the background is fitted and removed, and then calibrated using the summed flats and the two arcs either side of each stellar observation. All stellars are re-sampled on the same wavelength axis before a barycentric correction is applied. A continuum fit is applied before cosmic ray removal and the merging of the spectral orders. The result of the reduction is a one-dimensional spectrum as a function of wavelength for each observed stellar image.

As well as reducing spectra, *Megara* also produces a set of cross-correlation functions which demonstrate the line profile shape of absorption lines in the reduced spectra. Specific wavelength ranges, excluding the hydrogen and telluric lines which are influenced by other stellar and atmospheric phenomena, are extracted from the reduced spectra and the absorption lines are cross-correlated with a synthetic template spectrum to produce a representative line profile as a function of velocity. The cross-correlated line profiles (CCLPs) produced by *Megara* for this study's target stars are shown in Figure 2.6.

They were examined for low S/N line profiles to be removed and, for the single star targets, the continuum level of the line profile was normalised before further analysis. Line profiles for binary star targets were not normalised at this point as the line profiles of the individual components need to be disentangled before they can be analysed separately.

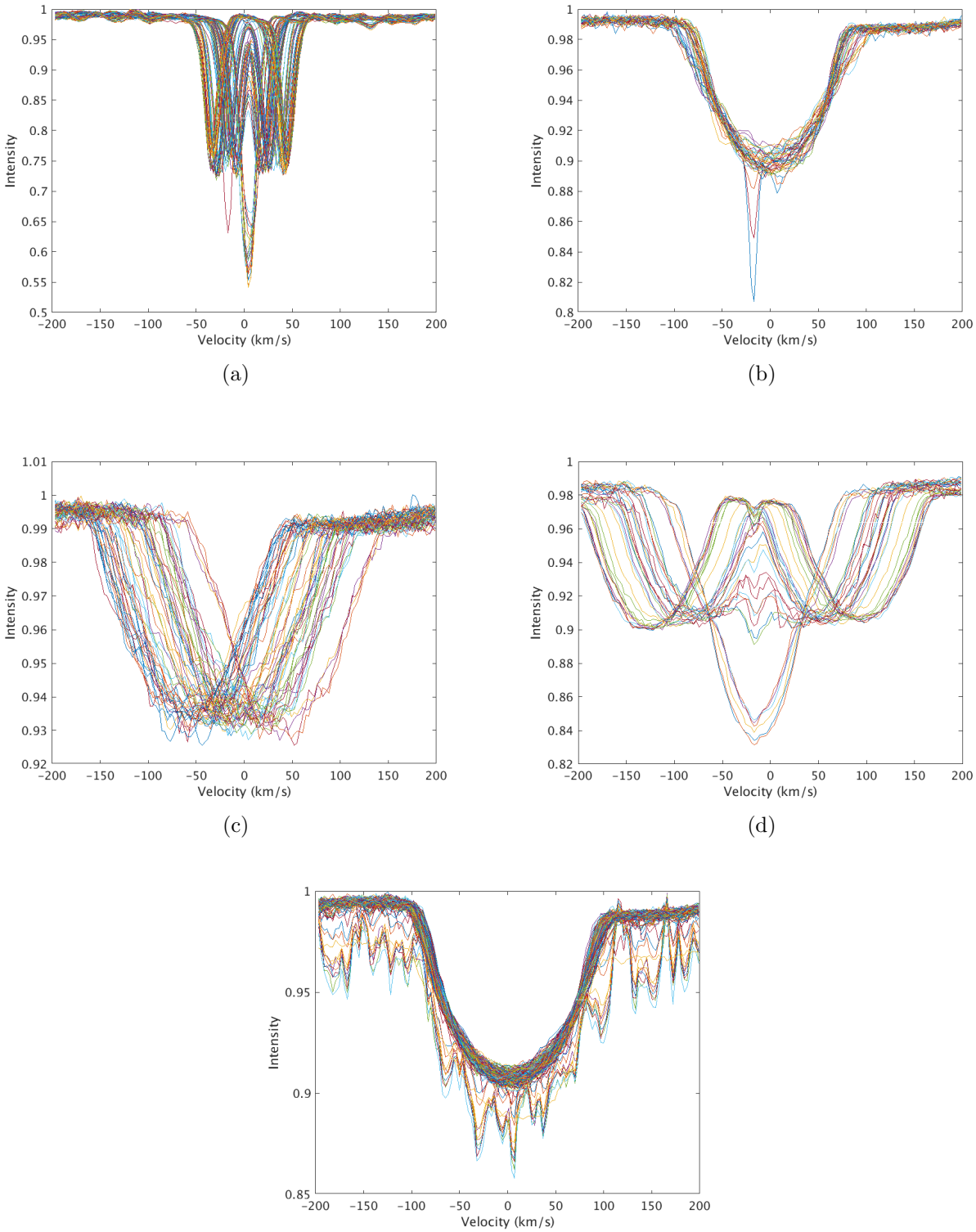

Figure 2.6: CCLPs produced by *Megara* for (a) HD 10167; (b) HD 206481; (c) HD 209295; (d) HD 214291; and (e) HD 216910.

For HD 10167, the CCLP with an atypically large absorption for one of the binary components at ∼(-20) km s^{-1} was removed. For HD 206481, the CCLPs with varying depths at ∼(-20) or ∼10 km s^{-1} were removed as they appear to be transient events of unknown origin. The remaining line profiles for this single star were continuum-normalised.

If the continuum on either side of the line profile does not have an intensity of 1, the results of any further analysis will be less accurate. To correct this, a mean line profile can be calculated by determining the average intensity at each sampled velocity. The points of the mean line profile which lie in the continuum are identified, to which a straight line is fitted. To apply the correction, each line profile is divided through by the normalising straight line (see Figure 2.7).

For HD 209295, no line profiles were removed. For HD 214291, three line profiles with noticeably lower S/N than the others were removed.

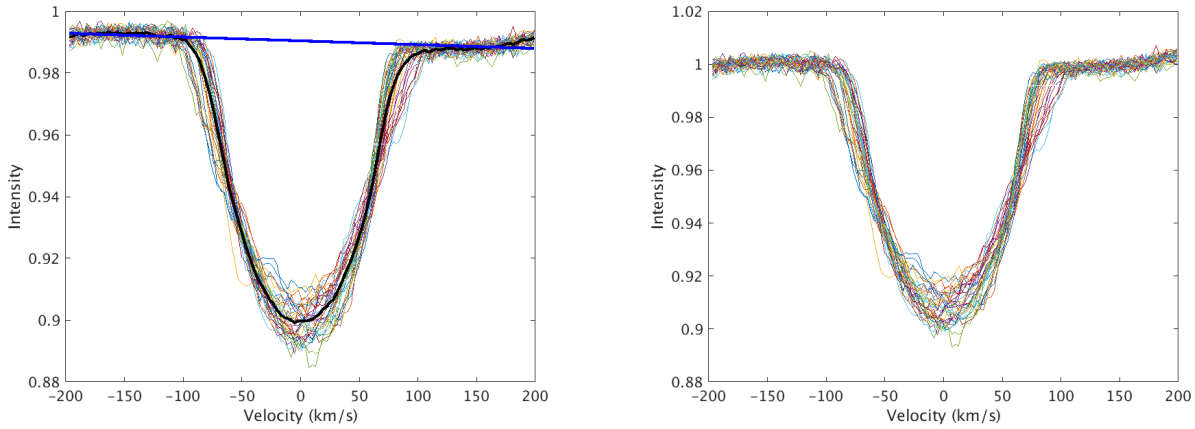

(a) (b)

Figure 2.7: Demonstrating the process of continuum flattening for target HD 206481. (a) CCLPs from *Megara* (multi-coloured lines) are used to calculate a mean line profile (black line) whose continuums are fitted with a straight line (blue line) which is used to correct all data points; and (b) continuum-flattened CCLPs.

For HD 216910, the set of line profiles with extremely low S/N were removed, as the absorptions with varying depths at the same velocities indicates a systematic error in the reduction of their stellar spectra. The set of low S/N stellar spectra were all identified to have been observed on the same night, 18 August 2018. When checked, the Th-Ar spectra taken on this night show significant variation compared to those taken on all other nights in the same month (see Figure 2.8). Despite re-reducing the spectra for this month separately for each night or reducing each observed stellar spectrum observed on 18 August 2018 separately, this issue was not resolved. Therefore, all of the stellar spectra observed on this night were removed before the line profiles were continuum-flattened for further analysis.

The final CCLPs used for further analysis are shown in Figure 2.9.

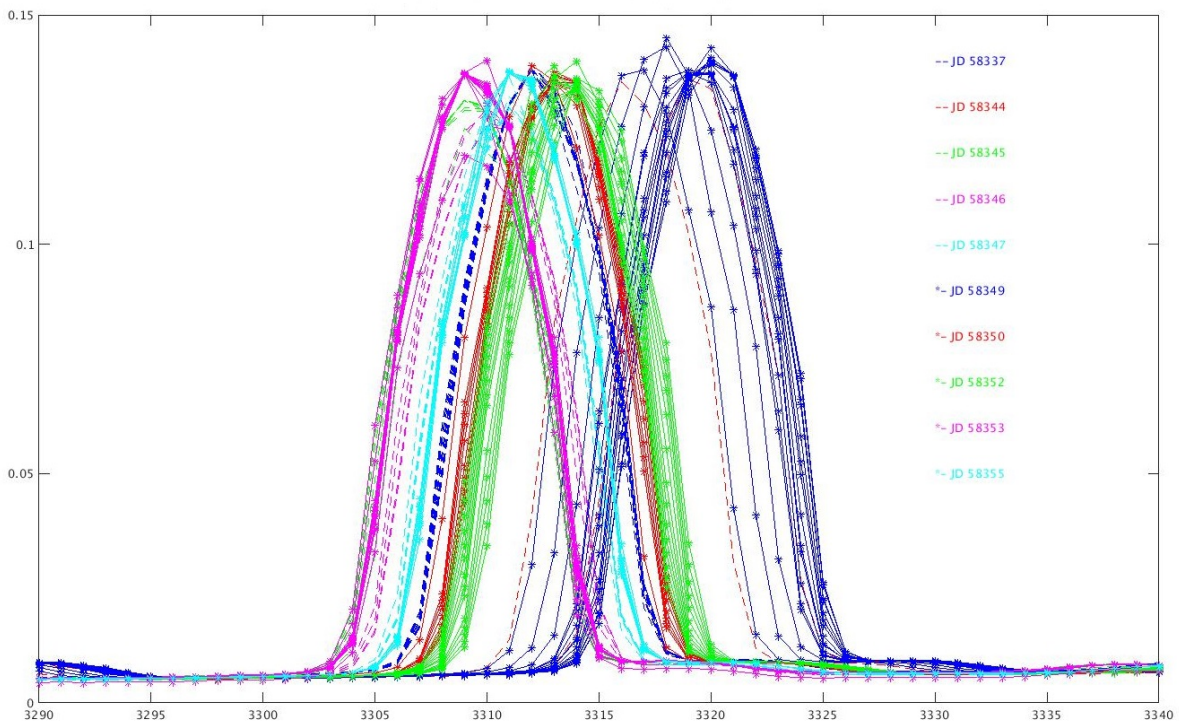

Figure 2.8: Movement of a specific wavelength range in the Th-Ar spectra taken during August 2018. Each line colour and style represents a different observing night. The blue -* lines (18 Aug) show the most variation.

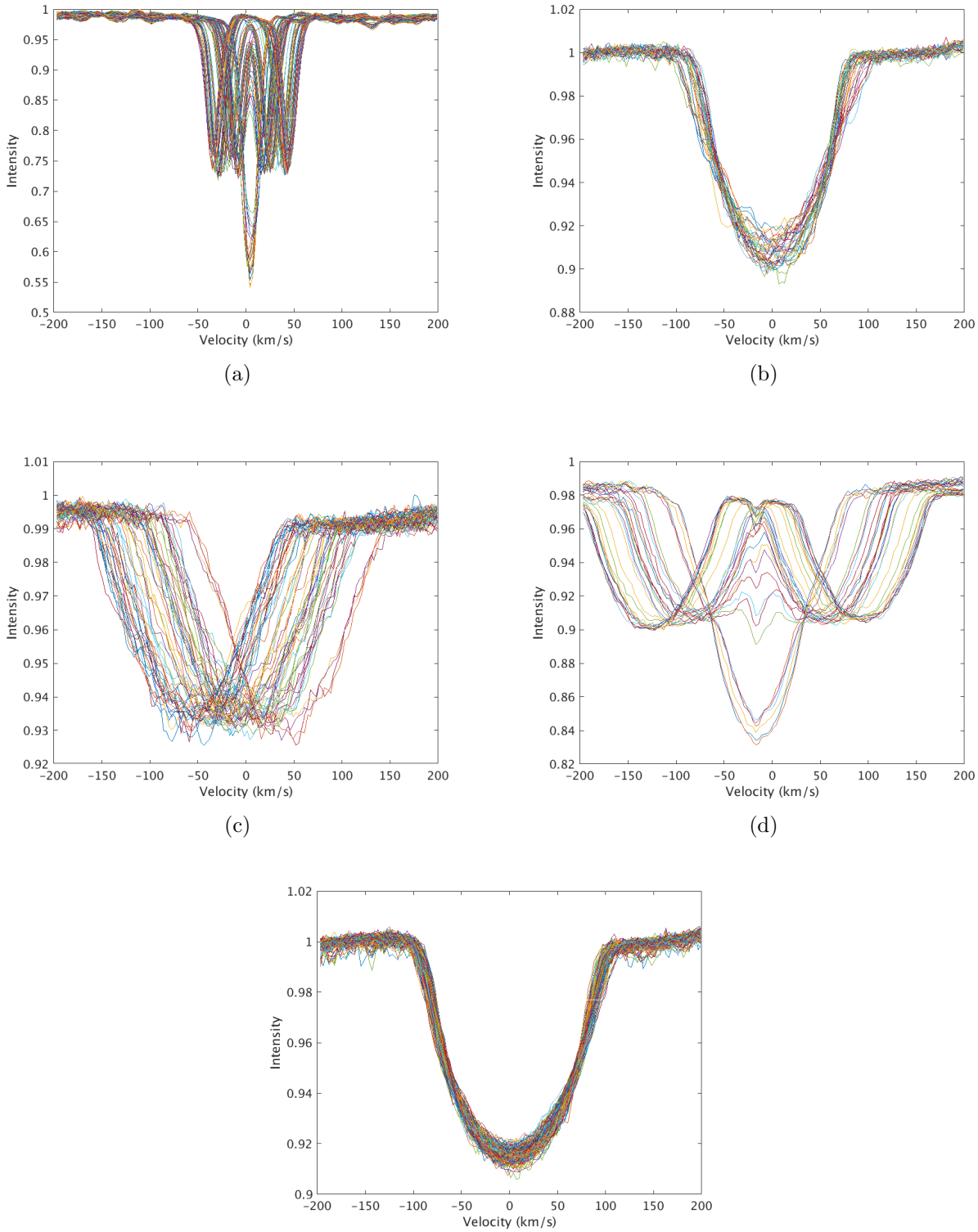

Figure 2.9: CCLPs used for further analysis for (a) HD 10167; (b) HD 206481; (c) HD 209295; (d) HD 214291; and (e) HD 216910.

2.3 *Gaia* Data

This study uses astrophysical parameters determined by the European Space Agency (ESA) satellite *Gaia* for the analysis of MUSICIAN stars. These data were selected due to the accuracy of the parallaxes measured by *Gaia* which allow for the production of high-quality H-R diagrams (Gaia Collaboration et al. 2016) since its estimates of stellar luminosity and radius depend on parallax as well as effective temperature (Andrae et al. 2018).

Gaia was launched on 19 December 2013 and took 26 days to reach the Earth's L_2 Lagrange point ($\sim$1.5 million km from Earth) around which it circles in a Lissajous-type orbit (Gaia Collaboration et al. 2016). This orbit provides the satellite with stable thermal conditions and ensures that the Sun, Earth and Moon are never in the field of view of its instruments. *Gaia* made its first observations on 25 July 2014 and the mission is designed to last five years (long enough for high-precision parallaxes to be measured) although the satellite may remain functional for up to 10 ± 1 years. The purpose of the *Gaia* mission is to measure the astrometric, photometric and astrophysical properties of a vast number of stars in our Galaxy in order to understand its formation, structure and evolution. Compared to its predecessor *Hipparcos*, which measured parallaxes for up to 117,955 objects (ESA 1997), *Gaia* is expected to measure 1 billion stars (Gaia Collaboration et al. 2016). As well as observing more stars, *Gaia* also improves on the milli-arcsecond (mas) accuracy of *Hipparcos* by observing the parallax of its faintest stars ($G \approx 20$ mag) to about 600 micro-arcseconds (μas) and its brightest stars ($G \lesssim 13$ mag) to less than 10 micro-arcseconds.

2.3.1 *Gaia* Data for MUSICIAN Targets

The data obtained from the *Gaia* Data Release 2 are effective temperature and stellar luminosity values for 30 MUSICIAN stars (Table 2.3). These values have typical uncertainties of 324 K and 10% respectively (Gaia Collaboration et al. 2018). Note that the luminosity value for HD 75202 was not available; therefore, any analyses related to luminosity do not include this star. This star was retained in the sample of MUSICIAN stars due to interesting features observed in its light curve (see Chapter 9).

Table 2.3: Effective temperature and stellar luminosity values obtained from the *Gaia* Data Release 2 for the 30 MUSICIAN stars.

HD	$T_{\rm eff}$ (K) (±324 K)	L ($L_\odot$) (±10%)	HD	$T_{\rm eff}$ (K) (±324 K)	L ($L_\odot$) (±10%)
10167	7013.5	12.606	85693	7000.3	7.939
14940	7070.25	5.821	86371	7008	11.365
17310	6898	6.539	103257	7050	6.855
27290	6906	6.999	109799	6904	6.441
27377	6899	9.585	112685	7135.97	5.28
32348	6764.71	9.972	112934	7031	5.603
34025	6697	8.449	149989	7003	6.268
40745	6891	9.943	153580	6481.5	4.407
41448	7145.55	6.049	172416	6363	11.813
41547	6922.75	11.291	187028	7154.45	6.073
46304	7441	8.957	189631	7137	6.13
48501	7070.38	6.054	206481	6989.54	5.647
49434	7164.17	6.447	209295	7697.9	12.764
55892	6934	5.74	214291	6129.75	18.124
75202	8068	-	216910	7003.93	8.286

3. Methodology

3.1 Fourier Analysis for Multiple Frequency Detection

The Fourier transform is a mathematical tool used to deconstruct a periodic signal as a function of time into the frequencies of the sinusoidals of which it is composed. The magnitude of the transform indicates the amplitude of the specific frequency found in the signal. For a signal containing multiple frequencies, a Fourier spectrum, which is a graph of the amplitude of the sinusoid in relation to its identified frequency, is used to display the various detected frequencies. This graph is also regularly known as a periodogram.

The Lomb-Scargle periodogram, introduced by Lomb (1976) and improved by Scargle (1982), is a least-squares frequency analysis used for unevenly spaced data and is therefore ideal for the purpose of analysing astronomical data which by nature is almost never equally spaced in time. When a signal is non-uniformly sampled, the resulting Fourier spectrum includes extra frequencies called aliases which are not inherent to the signal, but to the manner of its observation (Aerts et al. 2010). In order to identify multiple real frequencies in the signal, these aliases must be identified and removed by a process called prewhitening.

Prewhitening is the process between frequency detections where a sinusoidal function with the detected frequency is fitted and removed from the signal data before the Fourier transform is performed on the remaining signal (the residual). The best prewhitening strategy is to prewhiten the data after each frequency detection with a least-squares fit of all frequencies detected so far, where the frequencies, amplitudes and phases of the detected frequencies are allowed to vary. Frequency detection finishes once all frequencies above a specified significance level have been reached. Significance is determined by the ratio of the identified frequency's amplitude to the average amplitude of the surrounding frequency region. Breger et al. (1993) determined that a peak is statistically significant when such a ratio is greater than or equal to four (S/N$\geq$ 4), corresponding to a 99% confidence level of the frequency relating to the signal rather than noise; whereas S/N$\geq$ 3.6 indicates a 95% confidence level.

3.2 Photometric Fourier Analysis

3.2.1 Frequency Detection

This study uses FAMIAS (Zima 2008) and the ANSI-C program SigSpec (Reegen 2007) to perform a full Fourier analysis on the TASOC light curves. FAMIAS uses Fourier and non-linear least-squares fitting techniques to identify periodicities in photometric datasets (Zima

2008). Since prewhitening by varying the frequency significantly increased the computational time of FAMIAS, the detected frequencies were prewhitened by only varying their amplitudes and phases and not the frequency values themselves. SigSpec is specifically designed to overcome the problem of aliasing by prewhitening after every detected frequency using multi-sine least-squares fitting and determining a minimum residual fit (Reegen 2010). SigSpec is used to analyse the MAST light curves of the target stars (for a comparison to the TASOC data) and the MUSICIAN program stars. For all targets, the programs were set to detect frequencies from 0 to 50 d^{-1} with S/N$\geq$ 4.

3.2.2 Determining Dependent Frequencies

The frequencies detected by SigSpec in the TASOC data were checked for any aliasing and dependent frequencies. Dependent frequencies occur when a combination of multiple frequencies gives the same value as another detected frequency. The frequencies were checked for aliasing and frequency combinations using Equations 3.1 and 3.2 respectively

$$f_1 \pm p \approx f_2 \pm tol \tag{3.1}$$

$$pf_1 \pm q \approx rf_2 \pm tol \tag{3.2}$$

Coupling of frequencies was determined using Equation 3.3 with the additional condition given by Equation 3.4, which requires the phases of the coupled frequencies to relate in the same manner as the frequencies themselves

$$f_1 \approx f_2 \pm f_3 \pm tol \tag{3.3}$$

$$\phi_1 \approx \phi_2 \pm \phi_3 \pm tol \tag{3.4}$$

In these equations f_1, f_2 and f_3 are detected frequencies, p, q and r are integers in the range $[-10, +10]$ with $p, r \neq 0$, and tol is a chosen tolerance or accuracy value which was taken to be 0.0001 d^{-1} for all targets.

3.3 Spectral Analysis

The analysis of the spectroscopic data for each target depended on whether or not the target was in a binary system. In the case of a binary, the orbital parameters were determined in order to model the radial velocity variations present in the CCLPs. Once the radial velocity variations were determined for each binary component, they were applied to the individual cross-correlated line profiles to correct for the orbital motion. Following this, binary and single star targets were treated with the same pulsation frequency detection and mode identification using the software package FAMIAS (Zima 2008).

3.3.1 Radial Velocity Modelling

In order to determine the nature of the radial velocity variations of the binary components, the radial velocities of the components were measured. This was done by fitting a Gaussian

distribution to the inverted line profile of each component using the following equation

$$f(v) = a_1 exp\left(-\left[\frac{(v-b_1)}{c_1}\right]^2\right) + a_2 exp\left(-\left[\frac{(v-b_2)}{c_2}\right]^2\right) \tag{3.5}$$

where $f(v)$ indicates that the Gaussian is a function of velocity, $a_{1,2}$ are the heights of each peak, $b_{1,2}$ are the positions of the centre of each peak in velocity space and $c_{1,2}$ are the parameters which control the width of each peak. For each peak, the b value was recorded as the radial velocity shift of the component. This process was repeated for each observation of the target. The resulting sets of radial velocities and their observation times were then used to determine the orbital parameters of the binary. CCLPs containing a single combined line profile (representing the phase of the orbit where the components are moving perpendicular to the line of sight) were not used in this process as the results were less accurate due to the uncertainty of whether the two individual line profiles were partially or completely combined.

After determining the radial velocities for both components, the mass quotient q was found using

$$q = \frac{M_2}{M_1} = \frac{K_1}{K_2} \tag{3.6}$$

where M_1 and M_2 are the masses of the primary (more massive) and secondary star, respectively. Hence, by definition $q \leq 1$. The second equality, where K_1 and K_2 are the radial velocity semi-amplitudes of the primary and secondary components, follows due to the orbital motion about the centre of mass (CoM) of the binary system. The primary component is always closer to the CoM and therefore performs a smaller, lower velocity orbit around the CoM than the secondary component, but in the same amount of time (period) as it takes the secondary to perform its large, higher velocity orbit. Therefore, since the primary is the more massive of the two components, the secondary is the higher velocity component.

The mass quotient is determined by plotting the radial velocity of the secondary as a function of the radial velocity of the primary. The resulting graph is a scatter plot of radial velocities which form a straight line, the gradient of which gives q.

3.3.2 Binary Orbital Solutions and Disentanglement

The orbital solutions were determined using the collection of C programs SpecBin (Skuljan 2004), which uses radial velocity data and orbital parameter estimates as inputs to determine the set of orbital parameters which provide the best fit to the data. The parameters solved for are: radial velocity semi-amplitude (K), eccentricity (e), longitude of the periastron (ω), zero mean longitude passage time (T_0), period (P) and systemic velocity (γ). For solutions which failed to converge under the variation of multiple orbital parameters, convergence was achieved by keeping some parameters constant in order to determine others before performing a final run with all parameters variable.

Using the radial velocity solution, the orbital motion of each component was corrected for in the CCLPs which ideally shifts the line profiles until they are centred on $v = 0$. After the components were disentangled, the line profiles were continuum-flattened in preparation for pulsation frequency detection and mode identification.

3.3.3 Frequency Detection and Mode Identification

All spectroscopic frequency detection and mode identification results were obtained using the software package FAMIAS (Zima 2008). Frequency detection was performed using the Pixel-by-Pixel (PBP) method, which computes a Fourier spectrum of the intensity of each line profile pixel and averages them to produce a mean Fourier spectrum. According to Aerts et al. (2010), this method works best for stars rotating with $v \sin i \geq 50$ km s^{-1}; this criterion is met by all of the target stars in this study, with the exception of HD 10167. Performing a least-squares fit using the detected significant frequencies provides amplitude and phase variations across the line profile. These variations are dependent on the (l,m) values of the modes and the inclination of the star (Aerts et al. 2010).

The Fourier parameter fit (FPF) method was used to identify the pulsation modes of the detected frequencies. It was first presented by Zima (2006) as an improvement on previous mode identification methods by applying a χ^2 test to determine the significance of the best-fit models. This method assumes that the zero-point profile is independent of the stellar pulsations and therefore its defining parameters can be determined independently of the pulsation parameters. The zero-point profile parameters include:

- $v \sin i$ – stellar rotational velocity as observed along the line of sight to Earth
- Equivalent Width (EW) – the width of a rectangle of height 1 (from zero intensity to the normalised continuum level) having the same area as the line profile
- Intrinsic Width (σ) – the width of the line profile unbroadened by stellar rotation or pulsation (assumed to be symmetric and Gaussian for the FPF method)
- Radial velocity offset – the offset of the centre of the line profile peak from $v = 0$

The zero-point profile parameters are determined by fitting a rotationally broadened line profile to the observed zero-point profile, which provides reliable results for targets with $v \sin i > 20$ km s^{-1} (Zima 2008). The zero-point profile fit ('fit Z') requires input values for the effective temperature ($T_{\rm eff}$), surface gravity ($\log g$), metallicity and $v \sin i$. The values used for this study's targets are given in Table 3.1 and the metallicity of all targets was assumed to be zero. For $v \sin i$ values between 10 and 100 km s^{-1}, the value determined by the FPF method is accurate to 1 km s^{-1}. This accuracy decreases below 10 km s^{-1} due to increased uncertainty in the intrinsic width fit, and Zima (2006) recommends a lower limit of $v \sin i \approx 5$ km s^{-1} for the FPF method. This is approximately the same as the $v \sin i$ values for the components of HD 10167 (see Section 1.7.1).

Following the determination of the zero-point profile parameters, the pulsation parameters (radial velocity amplitude and phase across the line profile) are determined by fitting the observed Fourier parameters to theoretical models of various (l,m) values while optimising the calculated χ^2 value. There are two methods for fitting the amplitude and phase: AP and ZAP fitting. The AP method fits the velocity amplitude and phase to the observed variations across the line profile independently of the fit of the zero-point profile, whereas the ZAP method prioritises fitting the zero-point profile over the fitting of the velocity amplitude and phase. If the zero-point parameters are well-known, the AP fitting method should

Table 3.1: Initial stellar parameters used for the mode identification of each target star.

Target	$T_{\rm eff}$ (K)	$\log g$ (dex)	$v \sin i$ ($\mathrm{km\,s^{-1}}$)	Reference(s)
HD 10167	7079	4.0676	4.5	[1] [2] [3]
HD 206481	6900	4.1	86	[4]
HD 209295	7300	4.2	89	[4]
HD 214291	7079	4.0676	68	[2] [3]
HD 216910	7100	4.3	95	[4]

[1] Gaia Collaboration et al. (2018), [2] MUSICIAN Catalogue, [3] De Cat et al. (2006a), [4] Kahraman Aliçavuş et al. (2016).

produce good results for the zero-point, amplitude and phase (Zima 2008). However, if the AP method does not provide results where the zero-point profile is accurately modelled, the ZAP method can be used to force the FPF optimisation to fit the zero-point. The (l,m) values of the resulting best-fit modes can then be used as constraints for further AP fitting or other analysis.

Mode identification for multiple frequencies is ideally performed in two steps. The first step involves performing mode identification individually for each pulsation frequency to determine the optimal (l,m). This allows the results of the subsequent multi-mode identification to avoid computational issues and therefore produce better results. Simultaneous mode identification of all pulsation frequencies provides useful information about the pulsating star such as radius, mass and inclination which are stellar parameters common to all pulsations.

The range of values used by this study for the parameters optimised in this process are given in Table 3.2. Note that the lower limit for the inclination was set to 0°. While Zima (2008) states that this is unrealistic, as the implication is an infinite equatorial velocity if $v \sin i \neq 0$, $v \sin i$ for HD 10167 is very small due to a low rotational velocity and/or a low inclination. Thus the inclination range used for mode identification has been set to accommodate the possibility of a low inclination for HD 10167.

Tests run for low-degree modes ($l \leq 4$) by Zima (2006) showed that for modes with $l \leq 2$, m values are determined "unambiguously". For values higher than $m = 2$, the uncertainty increases to ± 1. In general, l was found to be accurate to ± 1 of its determined value.

Table 3.2: Range of values for each mode identification parameter used to compute theoretical pulsation models.

Parameter	Unit	Range
Radius	$R_\odot$	$[1, 10]$
Mass	$M_\odot$	$[1, 10]$
Inclination	$^\circ$	$[0, 90]$
Vel. Amp.	$\mathrm{km\,s^{-1}}$	$[0, 20]$
Phase	2π	$[0, 1]$
l	–	$[0, 3]$
m	–	$[-3, +3]$

4. HD 10167

This chapter presents the results of the photometric and spectroscopic analyses for the target HD 10167, which is a narrow spectral line-width SB2 star system with one or both components pulsating as a γ Dor star.

4.1 TESS Photometric Frequencies

An examination of the light curve for HD 10167 revealed that the binary system is either a GDORA or GDORM γ Dor star system, as defined by Balona (2018a). This categorization is based on the asymmetry between the maxima and minima of brightness (indicative of a GDORA star) and the absence of clear beating (indicative of a GDOR star) in the light curve.

It is important to note that HD 10167 is the only target for which the MAST light curve includes more than one sector of TESS data (see Table 2.1 and Figure 4.1). Therefore, the frequencies detected in the MAST light curve may be more significant and have better frequency resolution than those detected in the TASOC light curve due to the longer observation period. This is clearly seen in Figure 4.2 as a reduction in the noise level and therefore increase in the S/N of the detected peaks for the MAST Fourier spectrum.

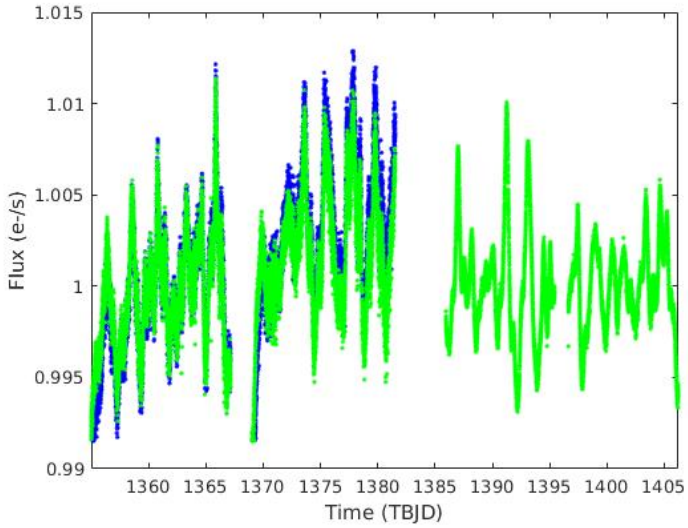

Figure 4.1: HD 10167 TASOC (blue) and MAST (green) SAP light curves normalised to a mean flux of 1 e^{-} s^{-1}.

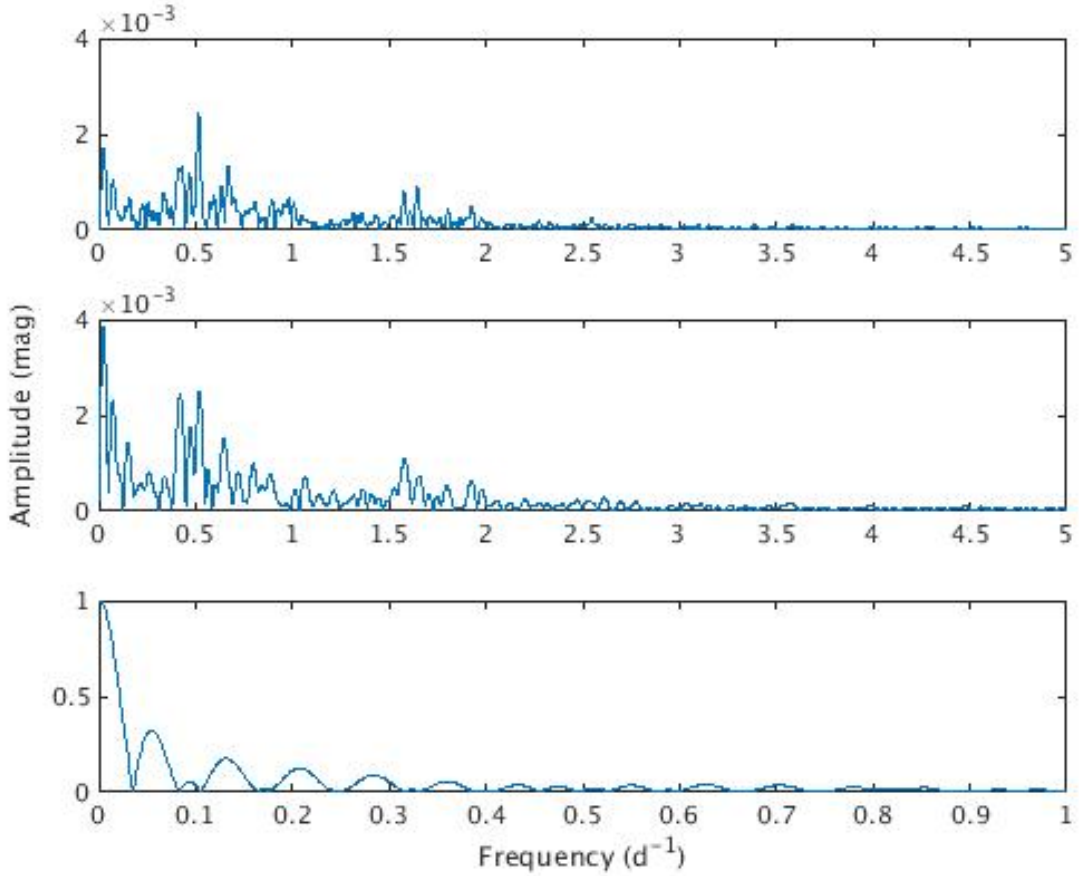

Figure 4.2: Fourier spectra for the HD 10167 light curve from MAST (top) and TASOC (middle) over the range 0–5 d^{-1}; and the TASOC light curve spectral window (bottom).

A comparison of the SigSpec (Reegen 2010) and FAMIAS (Zima 2006) TASOC Fourier spectra (Figure 4.2 and A.1) revealed extremely similar detected frequencies and their amplitudes.

The SigSpec Fourier analysis of the TASOC light curve produced 61 significant frequencies (S/N $\geq$ 4), 35 of which are within the γ Dor frequency range and 9 are within the δ Sct frequency range (Table B.1). Two frequency combinations ($-5f_8 + 1 \approx f_{44}$ and $-f_{49} + 6 \approx 2f_{61}$) and 12 frequency couplings (see the last column of Table B.1) were found within a tolerance of 0.0001 d^{-1}. Therefore it is likely that at least 14 of the 61 detected frequencies are not independent.

Table 4.1 presents the first 10 detected frequencies from the SigSpec and FAMIAS analyses of the TASOC and MAST light curves. While the MAST frequencies cannot be directly compared to the TASOC frequencies due to the different lengths of the light curves, only one of the frequencies match within 0.001 d^{-1}. However, a comparison of the two sets of TASOC frequencies only yields two matches within 0.001 d^{-1}. Therefore the SigSpec and FAMIAS analyses of the TASOC light curve provide somewhat different results.

Table 4.1: First 10 detected frequencies in the TASOC and MAST light curves for HD 10167, as detected by FAMIAS and SigSpec. All frequencies are listed in the order corresponding to their match to a SigSpec TASOC frequency. All figures have been rounded to 5 d.p.

Frequency (d^{-1})							
TASOC				MAST		Differences	
FAMIAS (1)		SigSpec (2)		SigSpec (3)		(1) & (2)	(2) & (3)
f_3	0.51896	f_1	0.50994	f_1	0.51483	0.00901	0.00489
f_2	0.42047	f_2	0.41346	f_3	0.41478	0.00701	0.00132
f_4	0.06440	f_3	0.08257	f_8	0.07588	0.01817	0.00649
f_1	0.02462	f_4	0.00531	f_2	0.02465	0.01931	0.01934
f_5	1.58149	f_5	1.57360	f_9	1.57764	0.00789	0.00404
f_7	0.13826	f_6	0.15123	f_6	0.43318	0.01297	0.28194
f_6	0.65343	f_7	0.63300	f_4	0.67445	0.02043	0.04145
f_9	0.23864	f_8	0.49859	f_5	0.47049	0.25995	0.02810
f_{10}	1.65536	f_9	1.65555	f_7	1.64427	0.00020	0.01128
f_8	0.88639	f_{10}	0.88548	f_{10}	0.88527	0.00091	0.00021

Despite our conclusion that the MAST frequencies are most likely more accurate than the frequencies determined from the TASOC light curve, the SigSpec TASOC frequency $f_1 = 0.50994$ d^{-1} provides the best match to the only frequency from previous studies; 0.51258 d^{-1} detected by Eyer et al. (2000). However, this paper also stated that this frequency was found using a PDM technique and since the frequency was close to the sampling frequency, the detected frequency had an incomplete phase coverage and therefore some uncertainty is associated with the value.

4.2 Orbital Solution

Orbital information, such as the mass quotient and the orbital solution for the two binary components, were determined by calculating the ratio of each component's radial velocities and using SpecBin to optimise orbital parameters from the radial velocities measured from the CCLPs for HD 10167.

The mass quotient for this binary system was determined to be $q = 0.96377$ (Figure 4.3). This means that the primary is more massive than the secondary by a factor of 1.0376.

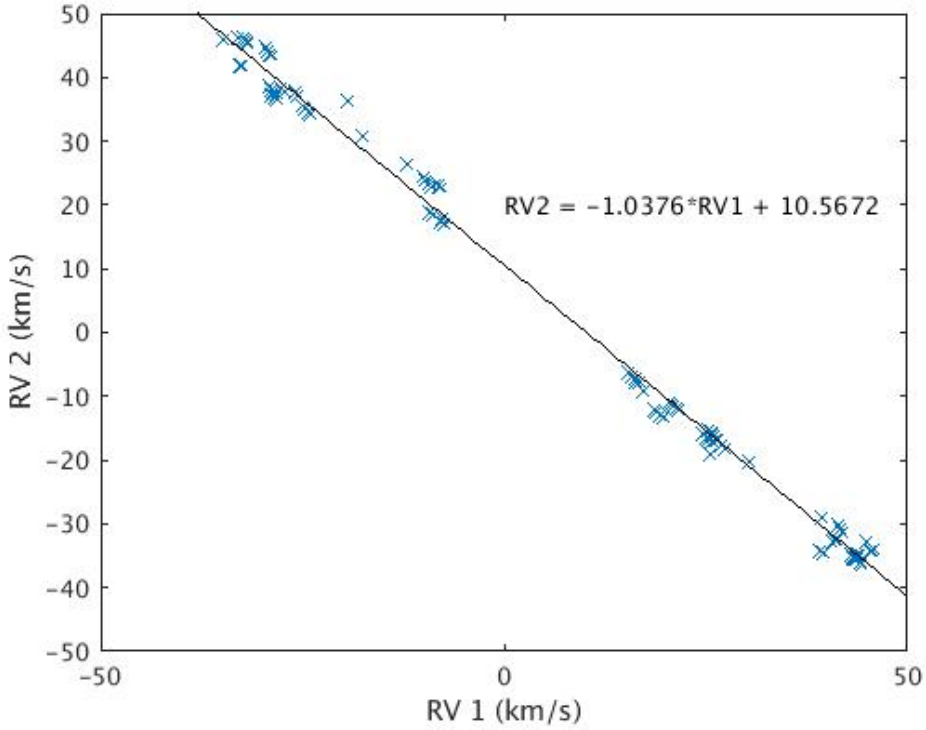

Figure 4.3: Radial velocity ratio for the components of HD 10167, where 1 and 2 indicate the primary and secondary stars respectively. The blue crosses are the radial velocity values and the black line is the best-fitting linear trend.

The radial velocity orbital solution for HD 10167 (Figure 4.4) was determined using SpecBin and has an *rms* of 2.61 $\mathrm{km\,s^{-1}}$ (Table 4.2). This value is higher than that of the solution found by De Cat et al. (2006a). Despite this result, the values found by this thesis for the primary radial velocity semi-amplitude, period and systematic velocity agree with those determined by De Cat et al. (2006a) within the given uncertainties. In addition, the 6^{th} harmonic of this thesis's orbital period (0.64379 $\mathrm{d^{-1}}$) is approximately a one day alias of the 9^{th} MAST photometric frequency (1.64427 $\mathrm{d^{-1}}$).

The orbital solution found by this thesis was applied to the radial velocities of the line profiles for each component to correct for the binary's orbital motion. However, despite this correction, the line profiles still showed a significant amount of variation from zero radial velocity (Figure 4.5). The maximum residual (difference between a radial velocity measurement and the value found from the orbital solution model) of the SpecBin radial velocity orbital solution was 4.22 $\mathrm{km\,s^{-1}}$ and the maximum standard error (equal to the standard deviation σ) was 2.22 $\mathrm{km\,s^{-1}}$. From Figure 4.5, most of the residual radial velocities are within 1σ and all of them are within 2σ of zero radial velocity. Therefore this variation could be due to the uncertainty in the orbital solution or pulsations in the star.

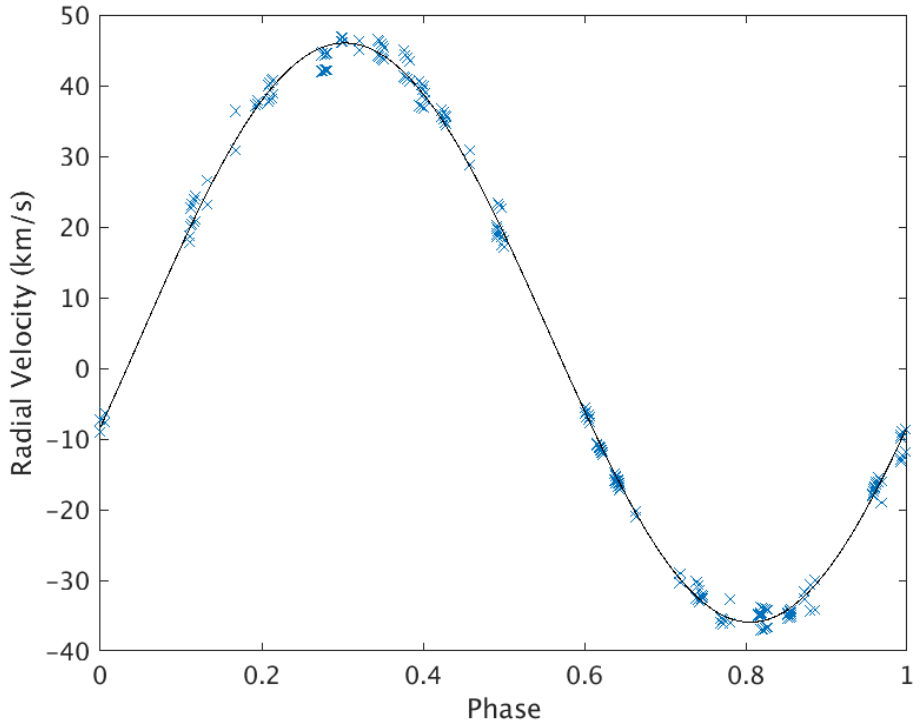

Figure 4.4: Radial velocity orbital solution for the primary component of HD 10167. The blue crosses are the phased radial velocity values and the black line is the best-fitting orbital solution.

Table 4.2: Radial velocity orbital solution parameters for HD 10167.

Parameter	This Thesis	De Cat et al. (2006a)
K_1 ($\mathrm{km\,s^{-1}}$)	39.5 ± 0.1	39.7 ± 0.4
K_2 ($\mathrm{km\,s^{-1}}$)	41.0 ± 0.1	41.8 ± 0.4
e	0.007 ± 0.004	0.0
ω (°)	34 ± 92	-
T_0 (MJD)	57583.216 ± 0.007	-
P (d)	9.3197 ± 0.0001	9.3199 ± 0.0002
γ ($\mathrm{km\,s^{-1}}$)	5.3 ± 0.1	5.2 ± 0.2
rms ($\mathrm{km\,s^{-1}}$)	2.61	0.99

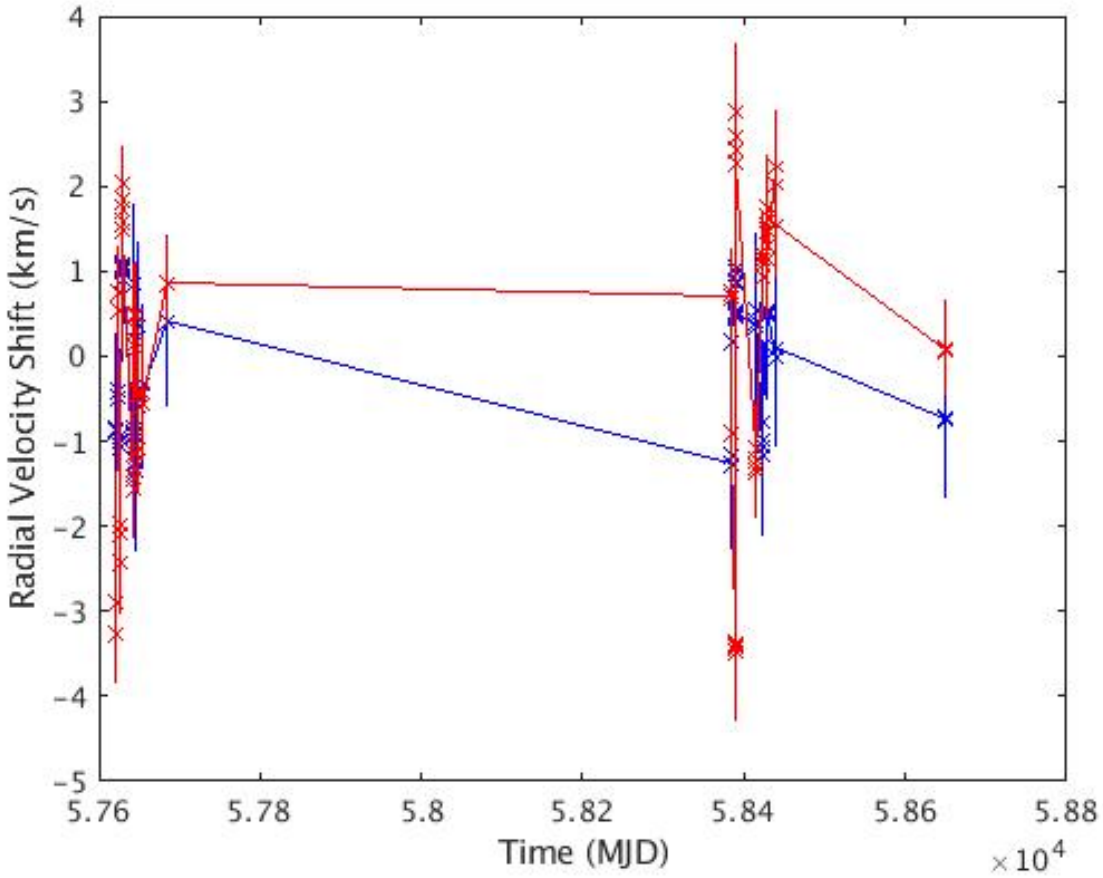

Figure 4.5: The residual radial velocity shifts of the line profiles of the components of HD 10167 as a function of Modified Julian Date (MJD) after the orbital solution was applied to the CCLPs. The blue and red crosses indicate the residual radial velocities for the primary and the secondary stars respectively (determined by fitting an inverted Gaussian to the line profiles) and the blue and red error bars indicate the error associated with the Gaussian fitting.

As the nature of this variation could not be determined with certainty, the spectroscopic frequency detection and the mode identification of the components of the binary were performed twice: once for the line profiles containing residual radial velocity variations and once for the line profiles where the residual radial velocity variations have been corrected for (Figure 4.6). The residual radial velocity variations were corrected for by fitting a Gaussian to the inverted line profile and measuring the velocity of the centre of the peaks. Performing the analysis twice may allow for the nature of these residual variations to be determined by comparing the best-fitting models obtained from each method.

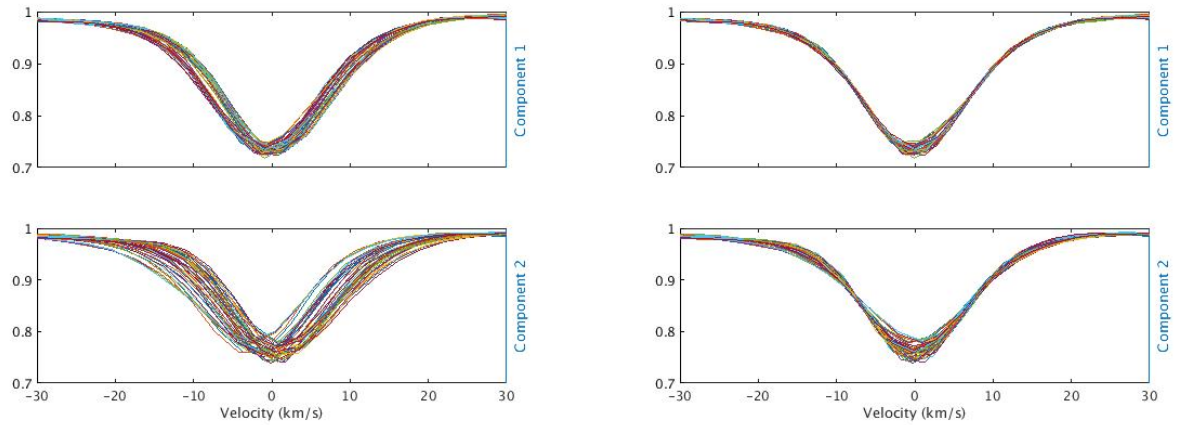

(a) (b)

Figure 4.6: Line profiles for the components of HD 10167 (a) after the orbital solution is applied to the CCLPs; and (b) after the CCLPs have been further corrected using the residual radial velocity values determined by the fitting of a Gaussian.

4.3 Mode Identification

Mode identification for the components of HD 10167 was performed twice (as explained in the previous section) using 56 resolved stellar spectra.

4.3.1 Unshifted

Component 1 (Primary)

The zero-point line profile was fitted to determine the pulsation-independent line parameters. The zero-point line profile for the primary star in HD 10167 was determined using FAMIAS to have a high χ^2 value of 175 (Table 4.3), which means that the fit is not very good. This is clear from Figure 4.7 which shows noticeable differences between the observed zero-point line profile and the model at the centre of the profile; specifically, the centres of the peaks appear to be offset slightly from each other. The $v \sin i$ value for this fit does not agree with the value 4.5 ± 0.5 km s^{-1} determined by De Cat et al. (2006a).

The PBP technique within FAMIAS in conjunction with individual and simultaneous mode identification was used to determine the dominant spectroscopic frequencies and their best-fitting modes of pulsation.

The frequency detection revealed five possible significant frequencies: 1.10907, 0.63450, 0.25353, 2.37577 and 0.48255 d^{-1}. None of these frequencies correspond to the first 10 detected photometric frequencies, with the exception of $f_5 = 0.48255$ d^{-1} which might correspond to the 8$^{\text{th}}$ SigSpec TASOC or MAST frequency. f_3 is possibly a sub-harmonic of the frequency 0.51258 d^{-1} detected by Eyer et al. (2000).

Table 4.3: The corresponding zero-point profile parameters for the unshifted primary component of HD 10167. All values have been rounded to 3 s.f.

Parameter	Value
$v \sin i$ ($\mathrm{km\,s^{-1}}$)	3.76
Equivalent width ($\mathrm{km\,s^{-1}}$)	4.60
Intrinsic width ($\mathrm{km\,s^{-1}}$)	7.27
Velocity offset ($\mathrm{km\,s^{-1}}$)	0.181
χ^2	175

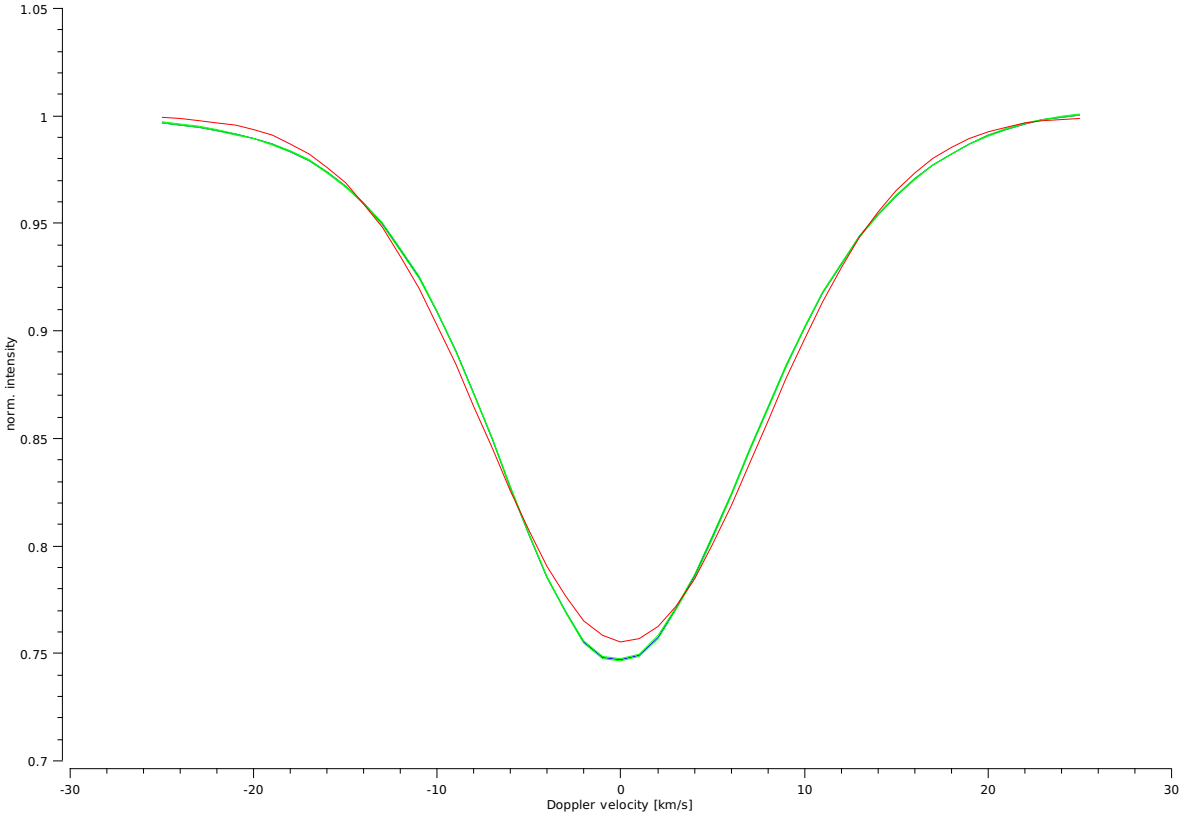

Figure 4.7: The zero-point for the unshifted primary component of HD 10167. The green and red lines indicate the observed zero-point line profile and the best-fitting theoretical model, respectively.

With the exception of f_1, most of the spectroscopic frequencies show asymmetric amplitude variations with respect to the centre of the zero-point profile. Mode identification was performed for each of the frequencies, where between 1–4 different modes were detected with similar χ^2 values (Table 4.4).

For f_1, three possible modes were found: (1,-1), (3,0) and (3,1), in order of increasing χ^2 (Figure 4.8). While the (3,0) mode is mathematically a better fit than the (3,1) mode, the fit to the phase variations is worse. Therefore f_1 is likely to be a (1,-1) mode.

Table 4.4: Parameters obtained from the mode identification of each individual pulsation frequency detected for the unshifted line profiles of Component 1 of HD 10167. All values except for the frequencies have been rounded to 3 s.f.

Parameters	Frequencies (d^{-1})						
	f_1 1.10907			f_2 0.63450			
Radius ($R_\odot$)	6.66	6.96	7.24	8.60	7.90	6.82	6.22
Mass ($M_\odot$)	9.96	4.86	4.19	1.01	3.71	8.22	2.21
i (°)	33.0	23.1	86.0	22.1	47.5	43.8	19.1
Mode (l,m)	(1,-1)	(3,0)	(3,1)	(1,-1)	(2,-2)	(3,-1)	(1,1)
Vel. Amp. ($km\,s^{-1}$)	3.23	2.58	3.87	5.81	1.94	0.645	4.52
Phase	0.771	0.772	0.780	0.937	0.953	0.929	0.441
χ^2	3.95	4.31	4.34	6.36	6.47	6.69	7.12

	f_3 0.25353			f_4 2.37577		f_5 0.48255	
Radius ($R_\odot$)	4.14	6.63	9.97	7.20	6.13	9.14	5.43
Mass ($M_\odot$)	5.57	4.42	7.59	5.66	4.26	4.04	6.89
i (°)	22.8	55.7	77.2	36.2	69.7	70.4	55.5
Mode (l,m)	(0,0)	(1,1)	(3,1)	(2,1)	(2,2)	(1,0)	(0,0)
Vel. Amp. ($km\,s^{-1}$)	1.94	1.29	4.52	1.29	1.29	0.645	0.645
Phase	0.961	0.220	0.724	0.228	0.724	0.811	0.795
χ^2	5.74	6.78	6.85	6.86	6.92	4.20	4.26

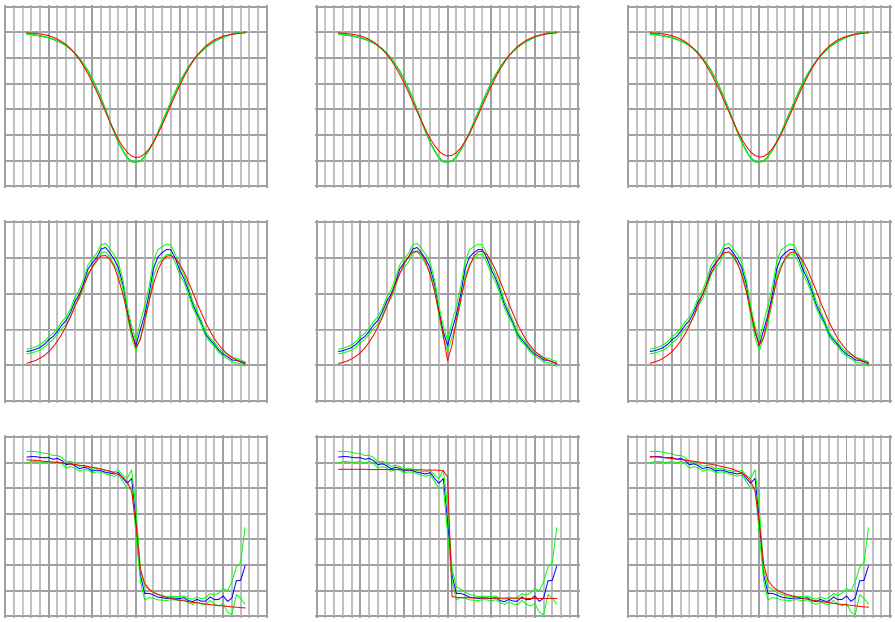

(a) (b) (c)

Figure 4.8: Zero-point (top row), amplitude (middle row) and phase (bottom row) diagrams of the mode identification of the HD 10167 unshifted Component 1 frequency $f_1 = 1.10907$ d^{-1} as (a) a (1,-1) mode; (b) a (3,0) mode; and (c) a (3,1) mode. The blue and green lines are the observed values and their uncertainties for the zero-point, amplitude and phase. The red lines are the theoretical models determined to best fit the observations.

For f_2, four possible modes were found: (1,-1), (2,-2), (3,-1) and (1,1) (Figure 4.9). While this frequency shows similar amplitude variations to f_1, its amplitude peaks are of unequal height and the dip between them is asymmetric and off-centre. The amplitude and phase fits for the first three modes are very similar, with the last mode differing from the others by the height of the fit to the amplitude variation peaks and the phase value is offset by approximately a factor of π compared to the first three modes (Table 4.4). f_2 was found to be a (1,-1) mode due to its low χ^2 value.

f_3 was found to be best fit by a radial (0,0) mode. Asymmetry in the observed amplitude variations for this frequency are in the form of a skewed amplitude distribution in the range of positive velocity (Figure 4.10). Although the modelled phase variations do not appear to fit the observations in the positive velocity space due to an offset of 2π between the model and the observation, the model still technically fits since phase is a periodic function with period 2π.

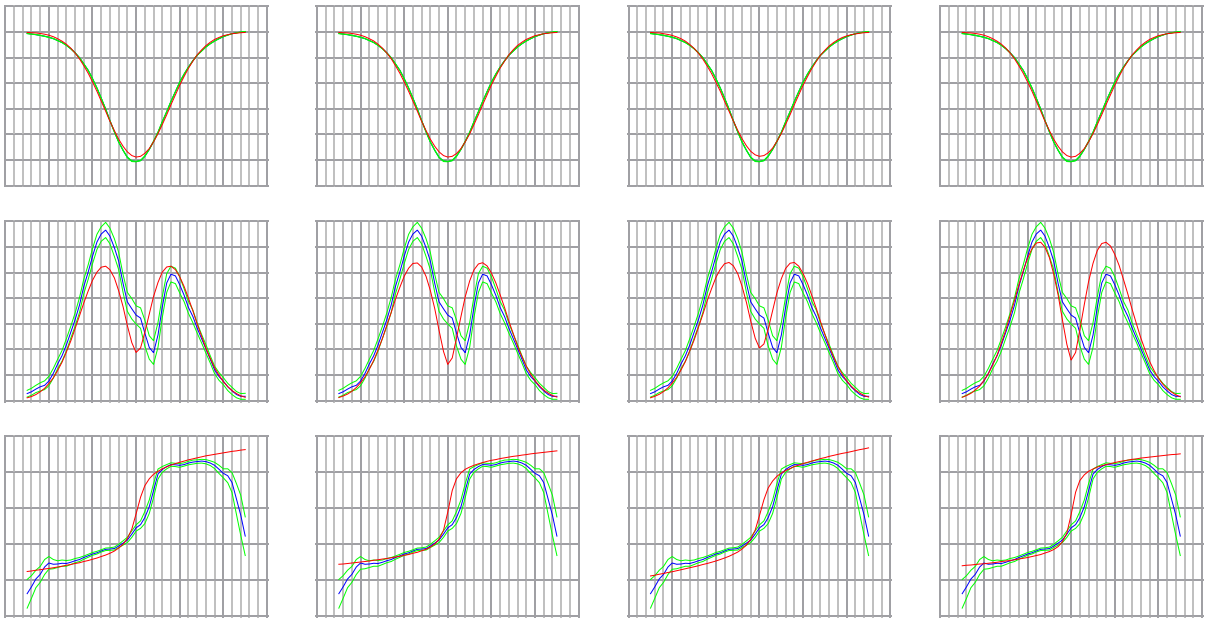

(a) (b) (c) (d)

Figure 4.9: Zero-point, amplitude and phase diagrams of the mode identification of the HD 10167 unshifted Component 1 frequency $f_2 = 0.63450$ d^{-1} as (a) a (1,-1) mode; (b) a (2,-2) mode; (c) a (3,-1) mode; and (d) (1,1) mode.

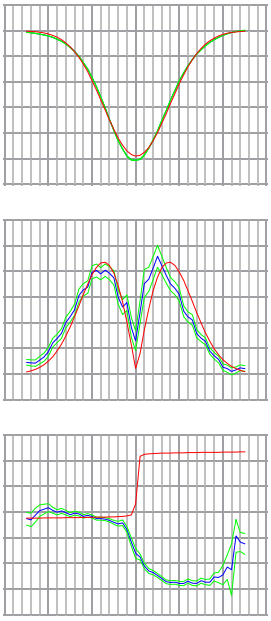

Figure 4.10: Zero-point, amplitude and phase diagrams of the mode identification of the HD 10167 unshifted Component 1 frequency $f_3 = 0.25353$ d^{-1} as a (0,0) mode.

For f_4, four possible modes were found: (1,1), (3,1), (2,1) and (2,2), which all indicate a prograde pulsation. The asymmetry in the observed amplitude variations are similar to those of f_2 except that the peaks for f_4 are noisier and rougher in shape (Figure 4.11). This frequency shows a 2π offset in the negative velocity space. There appear to only be subtle differences in the fit of the various modes, such as a greater amplitude peak height for the (1,1) mode and the slightly different phase fit between the (1,1) or (3,1) modes and the (2,1) or (2,2) modes. Contrary to this observed fit, the velocity amplitude values found from the fits of the (1,1), (2,1) and (2,2) modes are the same, and the phase values found from the fits of the (3,1) and (2,2) modes are the same (Table 4.4). f_4 was found to be a (1,1) mode due to its low χ^2 value.

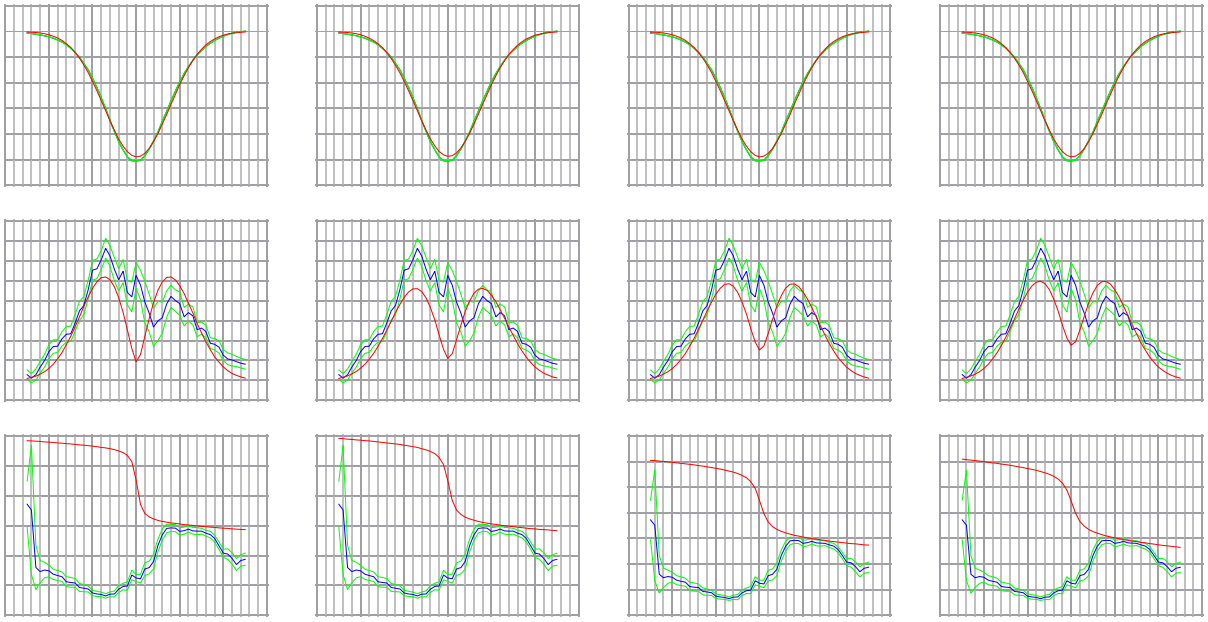

(a) (b) (c) (d)

Figure 4.11: Zero-point, amplitude and phase diagrams of the mode identification of the HD 10167 unshifted Component 1 frequency $f_4 = 2.37577$ d^{-1} as (a) (1,1) mode; (b) a (3,1) mode; (c) a (2,1) mode; and (d) a (2,2) mode.

For f_5, two possible modes were found: (1,0) and (0,0). These modes were both found to have the same velocity amplitude values and very similar phase values. Despite the reasonably low χ^2 values for these modes, the fit to the phase is relatively poor due to the noisy profile. (Figure 4.12). There are also issues with the amplitude fit. It could be argued that the amplitude variations form three peaks; however both modes are best fit with a model with two peaks in amplitude and have not been aided by the slight offset of the dip between the peaks from zero velocity. This frequency was the least significant of the five detected frequencies and so uncertainty in the fit is to be expected. f_5 was best fit by a (1,0) mode due to its low χ^2 value.

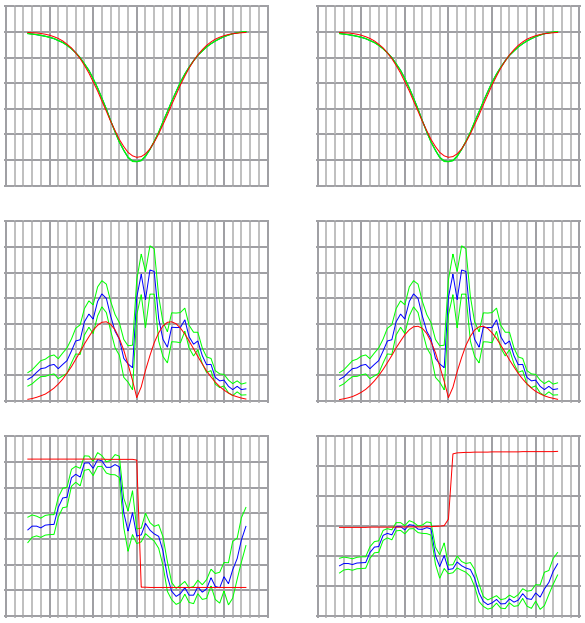

(a) (b)

Figure 4.12: Zero-point, amplitude and phase diagrams of the mode identification of the HD 10167 unshifted Component 1 frequency $f_5 = 0.48255$ d^{-1} as (a) (1,0) mode; and (b) a (0,0) mode.

A simultaneous mode identification of all five frequencies was then performed using the modes with the lowest χ^2 values for each frequency: f_1 = (1,-1), f_2 = (1,-1), f_3 = (0,0), f_4 = (1,1) and f_5 = (1,0). No models were found which fit the zero-point profile reasonably well while using the simultaneous amplitude and phase (AP) fitting method. Following this, an attempt was made to perform a simultaneous mode identification using the simultaneous zero-point, amplitude and phase (ZAP) fitting method; however no models were found which did not give a zero velocity amplitude for f_5. This indicates that f_5 may not be a significant spectroscopic frequency.

Component 2 (Secondary)

The zero-point line profile was fitted to determine the pulsation-independent line parameters. The zero-point profile for the secondary star in HD 10167 was determined using FAMIAS to have a χ^2 value of 68.3 (Table 4.5). While this is less than half of that of its companion, the fit could still be improved by reducing the differences between the observed zero-point and the model at the centre of the profile. The $v \sin i$ value found for this zero-point profile fit does not agree with the value 4.9 ± 0.6 km s^{-1} determined by De Cat et al. (2006a).

Table 4.5: The corresponding zero-point parameters for the unshifted secondary component of HD 10167. All values have been rounded to 3 s.f.

Parameter	Value
$v \sin i$ (km s^{-1})	0.652
Equivalent width (km s^{-1})	3.98
Intrinsic width (km s^{-1})	7.51
Velocity offset (km s^{-1})	-0.142
χ^2	68.3

The equivalent and intrinsic widths are similar to those found for the primary and the velocity offset of the profile is modelled to have the same size but different direction than the primary. This can be seen from Figure 4.13 where the centre of the modelled zero-point profile is offset to the left of the observed zero-point profile, whereas it was offset to the right for the primary component (Figure 4.7).

The PBP technique within FAMIAS in conjunction with individual and simultaneous mode identification was used to determine the dominant spectroscopic frequencies and their best-fitting modes of pulsation.

The frequency detection revealed five possible significant frequencies: 0.40376, 1.51979, 1.50146, 1.43585 and 3.12483 d^{-1}, none of which were detected in the primary component. In comparison to the first 10 detected MAST frequencies, the second or third spectroscopic frequency could be a one day alias to the first MAST frequency (0.51483 d^{-1}).

Similar to the primary component, the amplitude variations of the first frequency appear symmetrical with respect to zero velocity whereas the remaining four frequencies exhibit asymmetric amplitude variations. Mode identification was performed for each of the frequencies, where 1–2 different modes were detected with similar χ^2 values (Table 4.6).

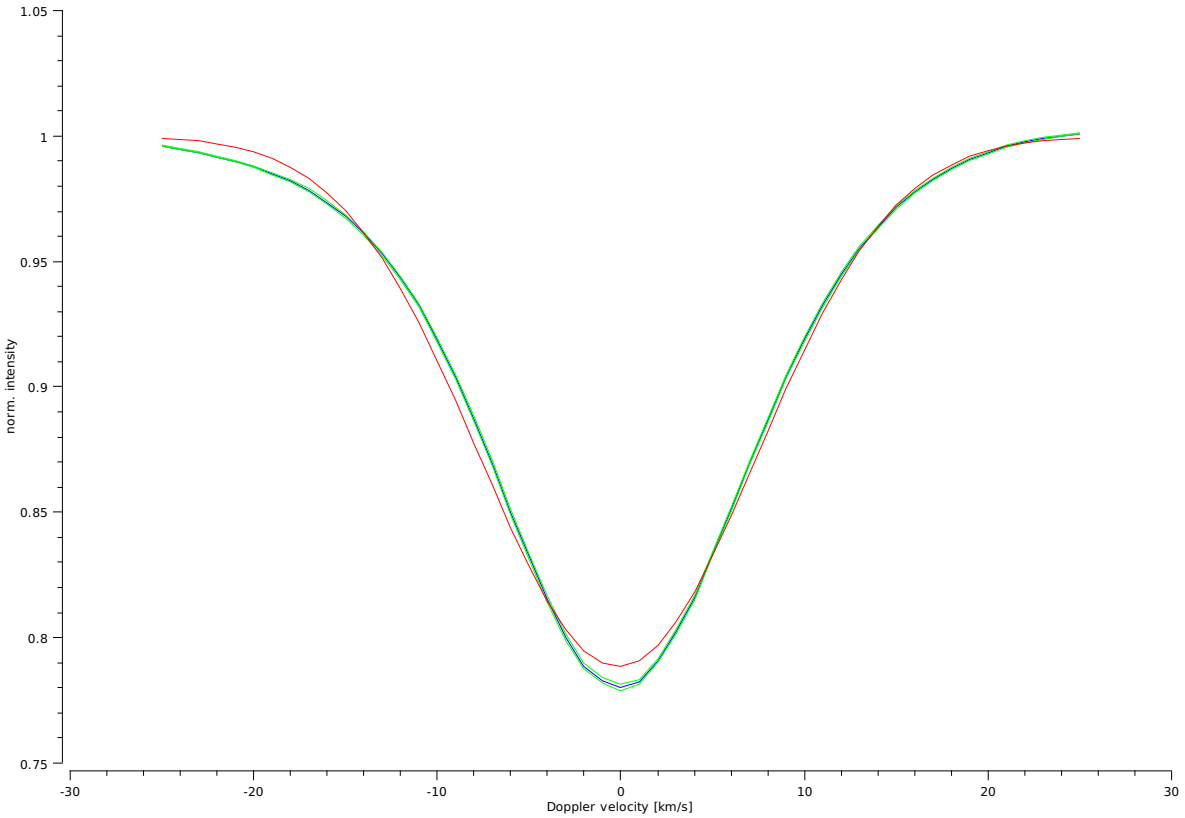

Figure 4.13: The zero-point for the unshifted secondary component of HD 10167.

Table 4.6: Parameters obtained from the mode identification of each individual pulsation frequency detected for the unshifted Component 2 of HD 10167. All values except frequencies have been rounded to 3 s.f.

Parameters	Frequencies (d^{-1})						
	f_1 0.40376		f_2 1.51979		f_3 1.50146	f_4 1.43585	f_3 3.12483
Radius ($R_\odot$)	9.86	9.86	6.81	8.23	5.82	6.88	4.54
Mass ($M_\odot$)	1.71	4.19	4.33	1.07	9.43	7.87	8.23
Inclination (°)	79.3	67.7	8.18	38.9	26.8	9.59	15.3
Mode (l,m)	(1,-1)	(1,0)	(2,-1)	(2,-2)	(3,2)	(3,1)	(3,2)
Vel. Amp. ($km\,s^{-1}$)	5.81	6.45	16.1	19.4	3.87	3.87	12.3
Phase	0.543	0.543	0.772	0.772	0.811	0.866	0.646
χ^2	7.57	7.63	2.84	3.44	2.65	1.97	4.81

For f_1, it was necessary to use the ZAP fitting method to determine the pulsation mode as the AP method did not result in any models fitting the zero-point profile. Two possible modes were found: (1,-1) and (1,0). These modes have the same stellar radius and phase value as determined by the fit. The fit to the amplitude and phase variations are indistinguishable except for the 2π phase offset in the positive velocity space for the (1,0) mode (Figure 4.14). f_1 was determined to be a (1,-1) mode due to its low χ^2 value.

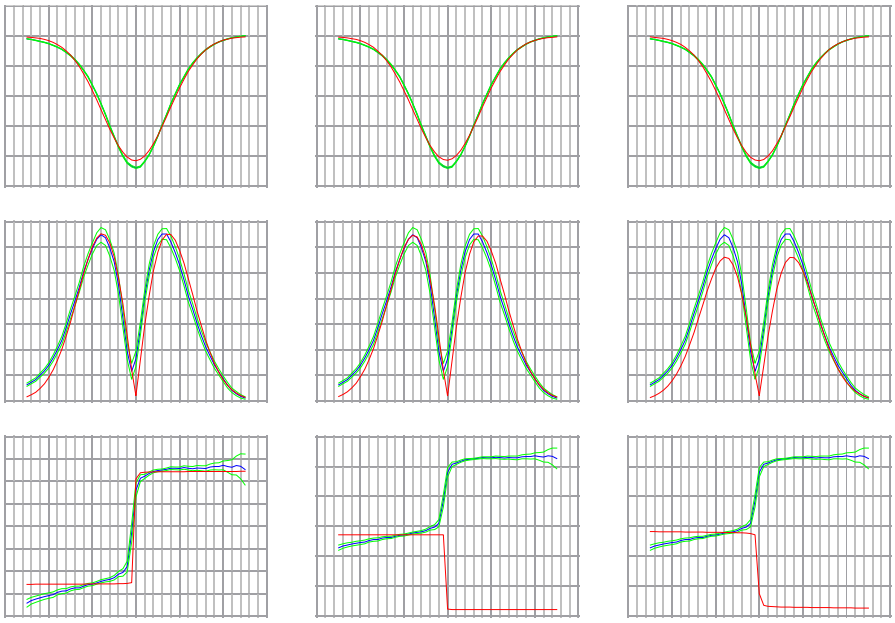

(a) (b) (c)

Figure 4.14: Zero-point, amplitude and phase diagrams of the mode identification of the HD 10167 unshifted Component 2 frequency $f_1 = 0.40376$ d^{-1} individually as (a) a (1,-1) mode and (b) a (1,0) mode; and (c) simultaneously with the other frequencies with f_1 as a (1,-1) mode and f_2 a (2,-1) mode.

As for f_1, the ZAP method was required in order to fit the zero-point profile during the mode identification for f_2. Two possible modes were found: (2,-1) and (2,-2), which both indicate a retrograde pulsation. The best-fitting (2,-2) mode was found to have a velocity amplitude of 20 km s^{-1} which is the maximum allowed value and therefore implies that the fit is failing to model the observations without reverting to extremely high velocity amplitudes. The model presented here is the first best-fitting (2,-2) mode which does not have a velocity amplitude of 20 km s^{-1}. Both the (2,-1) and (2,-2) modes are fitted using high velocity amplitudes and the same phase value (Table 4.6). The observed fit however shows that the (2,-1) mode fits the phase better while the height of the amplitude variation peaks is higher for the (2,-2) mode (Figure 4.15). It is also worth noting that the zero-point profile is fit marginally better by the (2,-2) mode. Ultimately, f_2 was found to be a (2,-1) mode due to its lower χ^2 value.

f_3 was found to be a (3,2) mode which is a prograde pulsation. While the amplitude variations have a smoother profile than that of f_2, there is a greater difference in the heights of the peaks (Figure 4.16).

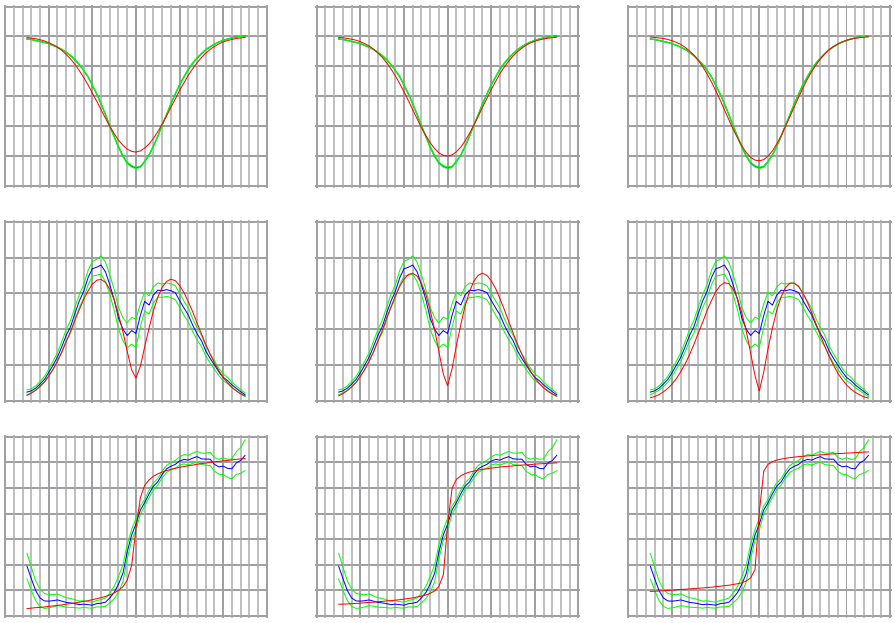

(a) (b) (c)

Figure 4.15: Zero-point, amplitude and phase diagrams of the mode identification of the HD 10167 unshifted Component 2 frequency $f_2 = 1.51979$ d^{-1} individually as (a) a (2,-1) mode and (b) a (2,-2) mode; and (c) simultaneously with the other frequencies with f_1 as a (1,-1) mode and f_2 a (2,-1) mode.

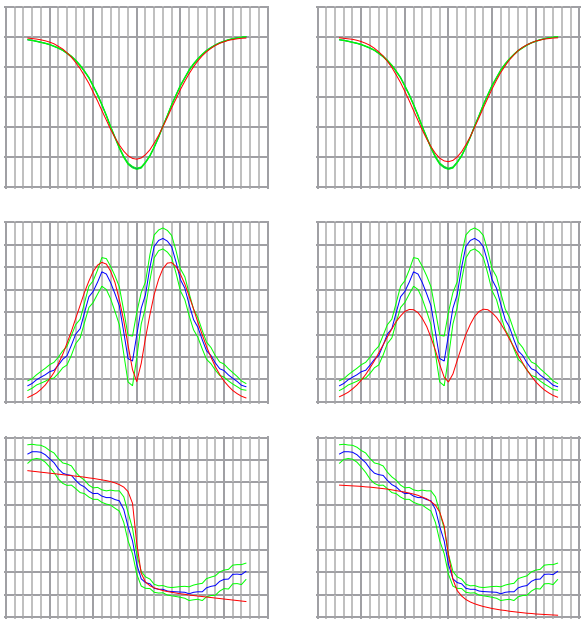

(a) (b)

Figure 4.16: Zero-point, amplitude and phase diagrams of the mode identification of the HD 10167 unshifted Component 2 frequency $f_3 = 1.50146$ d^{-1} (a) individually; and (b) simultaneously with the other frequencies with f_1 as a (1,-1) mode and f_2 a (2,-1) mode.

f_4 was found to be a (3,1) prograde pulsation mode. While this frequency has the same velocity amplitude and similar phase to f_3, the amplitude variations have a rougher profile and the overall phase variation is smaller (Figure 4.17).

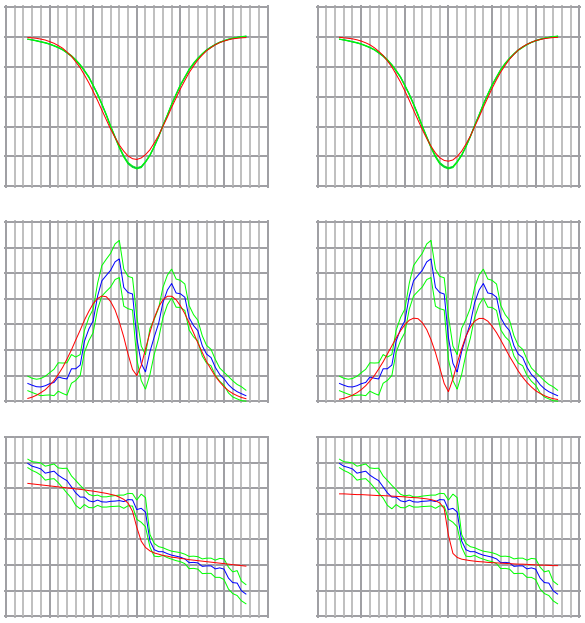

(a) (b)

Figure 4.17: Zero-point, amplitude and phase diagrams of the mode identification of the HD 10167 unshifted Component 2 frequency $f_4 = 1.43585$ d^{-1} (a) individually; and (b) simultaneously with the other frequencies with f_1 as a (1,-1) mode and f_2 a (2,-1) mode.

f_5 was found to be a (3,2) prograde pulsation mode. This frequency exhibits the most asymmetric amplitude variations, with a small peak offset to the left of a large, almost-centred peak (Figure 4.18).

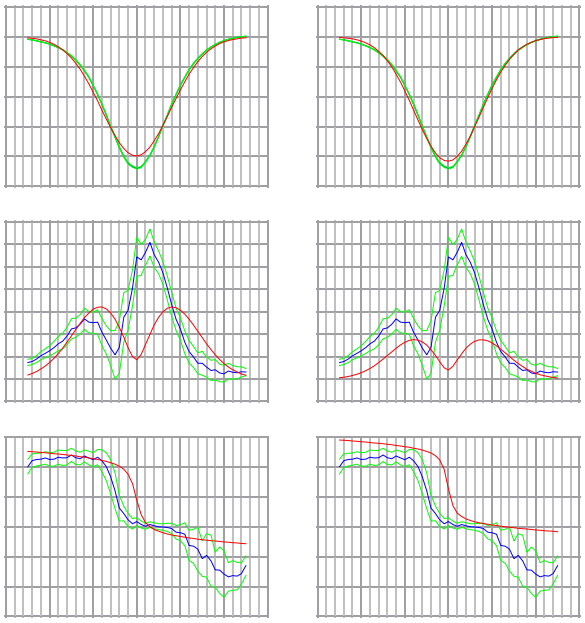

(a) (b)

Figure 4.18: Zero-point, amplitude and phase diagrams of the mode identification of the HD 10167 unshifted Component 2 frequency $f_5 = 3.12483$ d^{-1} (a) individually; and (b) simultaneously with the other frequencies with f_1 as a (1,-1) mode and f_2 a (2,-1) mode.

A simultaneous mode identification of all five frequencies was performed using the modes with the lowest χ^2 values for each frequency: f_1 = (1,-1), f_2 = (2,-1), f_3 = (3,2), f_4 = (3,1), f_5 = (3,2). The best-fitting model was found to have a stellar radius value of 10 $R_\odot$, which is the maximum allowed value, and therefore was discarded. The model presented in Table 4.7 is the best-fitting model with $R \neq 10\ R_\odot$.

Table 4.7: Parameters obtained from the simultaneous mode identification of all frequencies for the unshifted Component 2 of HD 10167. All values except frequencies have been rounded to 3 s.f.

Stellar Parameters			Frequency (d^{-1})					
Radius ($R_\odot$)	Mass ($M_\odot$)	Inclination ($^\circ$)	Pulsation Parameters	f_1 0.40376	f_2 1.51979	f_3 1.50146	f_4 1.43585	f_5 3.12483	χ^2
9.08	2.49	25.2	Mode	(1,-1)	(2,-1)	(3,2)	(3,1)	(3,2)	7.14
			Vel. Amp. ($km\,s^{-1}$)	10.3	7.74	17.5	4.52	8.39	
			Phase	0.559	0.819	0.748	0.827	0.724	

4.3.2 Shifted

Component 1

The zero-point line profile was fitted to determine the pulsation-independent line parameters. The zero-point profile for the primary star in HD 10167 was determined using FAMIAS to have a χ^2 value of 320 (Table 4.8). This value is approximately twice the value of the maximum zero-point fit χ^2 found for the unshifted line profiles. Similar to the unshifted zero-point profile for the primary, the model deviates from the observed profile in the centre and is slightly offset to the right of the observed centre (Figure 4.19). The $v \sin i$ value found from this zero-point profile fit does not agree with the value 4.5 ± 0.5 km s^{-1} determined by De Cat et al. (2006a).

Table 4.8: The corresponding parameters of the zero-point for the shifted primary component of HD 10167. All values have been rounded to 3 s.f.

Parameter	Value
$v \sin i$ (km s^{-1})	0.128
Equivalent width (km s^{-1})	4.52
Intrinsic width (km s^{-1})	7.35
Velocity offset (km s^{-1})	0.0582
χ^2	320

The PBP technique within FAMIAS in conjunction with individual and simultaneous mode identification was used to determine the dominant spectroscopic frequencies and their best-fitting modes of pulsation.

The frequency detection revealed two possible significant frequencies: 1.105785 and 1.177668 d^{-1}. In comparison to the frequencies detected in the unshifted primary line profiles, the first frequency could be the same as the first unshifted frequency (1.109068 d^{-1}) and the second could be a sub-harmonic of the 4$^{\text{th}}$ unshifted frequency (2.375767 d^{-1}). Mode identification of the first frequency using the ZAP and AP methods returned no viable results due to issues with fitting the zero-point and the amplitude variation profile respectively.

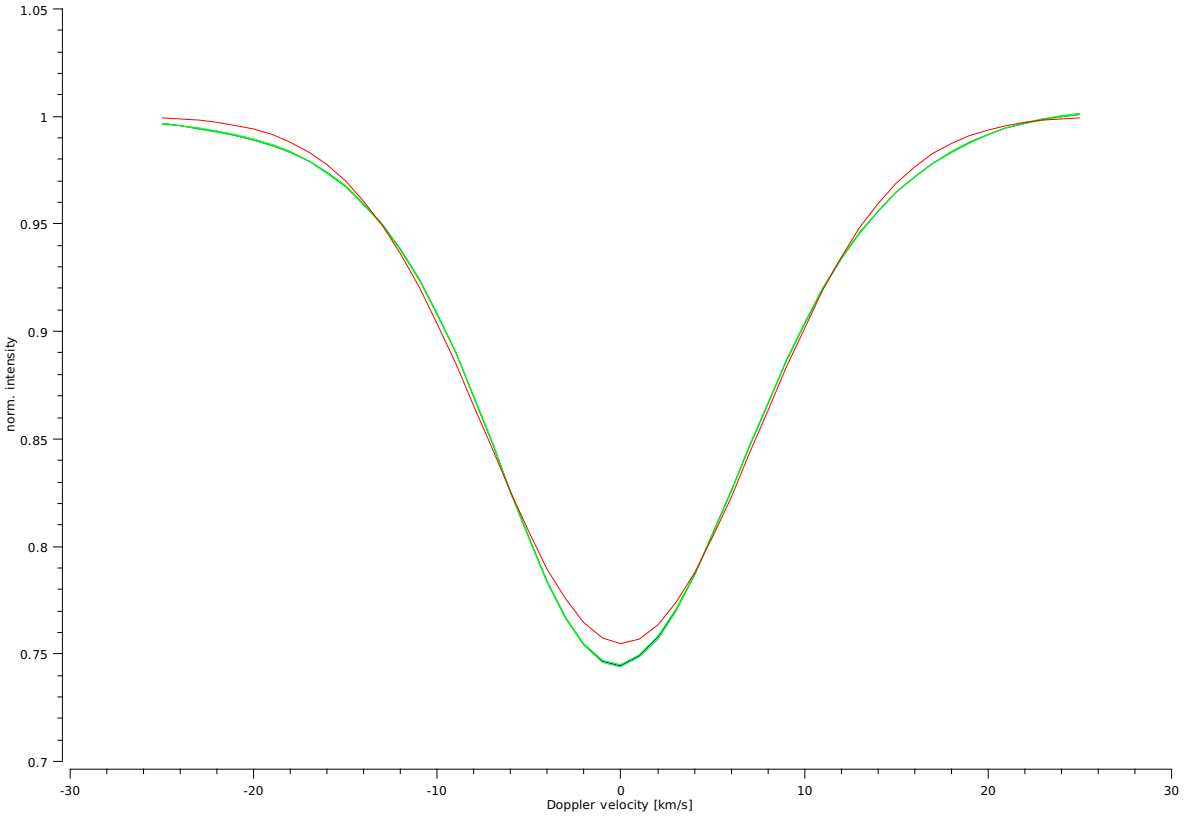

Figure 4.19: The zero-point profile for the shifted Component 1 of HD 10167.

Component 2

The zero-point line profile was fitted to determine the pulsation-independent line parameters. The zero-point profile for the secondary star in HD 10167 was determined using FAMIAS to have a χ^2 value of 325 (Table 4.9). Unlike the other zero-point models for the components of HD 10167, there is no visible offset from the centre of the observed zero-point line profile (Figure 4.20). The $v \sin i$ value found from the zero-point profile fit does not agree with the value 4.9 ± 0.6 km s^{-1} determined by De Cat et al. (2006a). The equivalent and intrinsic widths are similar to those found for all other zero-point models, shifted or unshifted.

Table 4.9: The corresponding zero-point parameters for the shifted Component 2 of HD 10167. All values have been rounded to 3 s.f.

Parameter	Value
$v \sin i$ ($\mathrm{km\,s^{-1}}$)	1.27
Equivalent width ($\mathrm{km\,s^{-1}}$)	3.93
Intrinsic width ($\mathrm{km\,s^{-1}}$)	7.30
Velocity offset ($\mathrm{km\,s^{-1}}$)	0.0147
χ^2	325

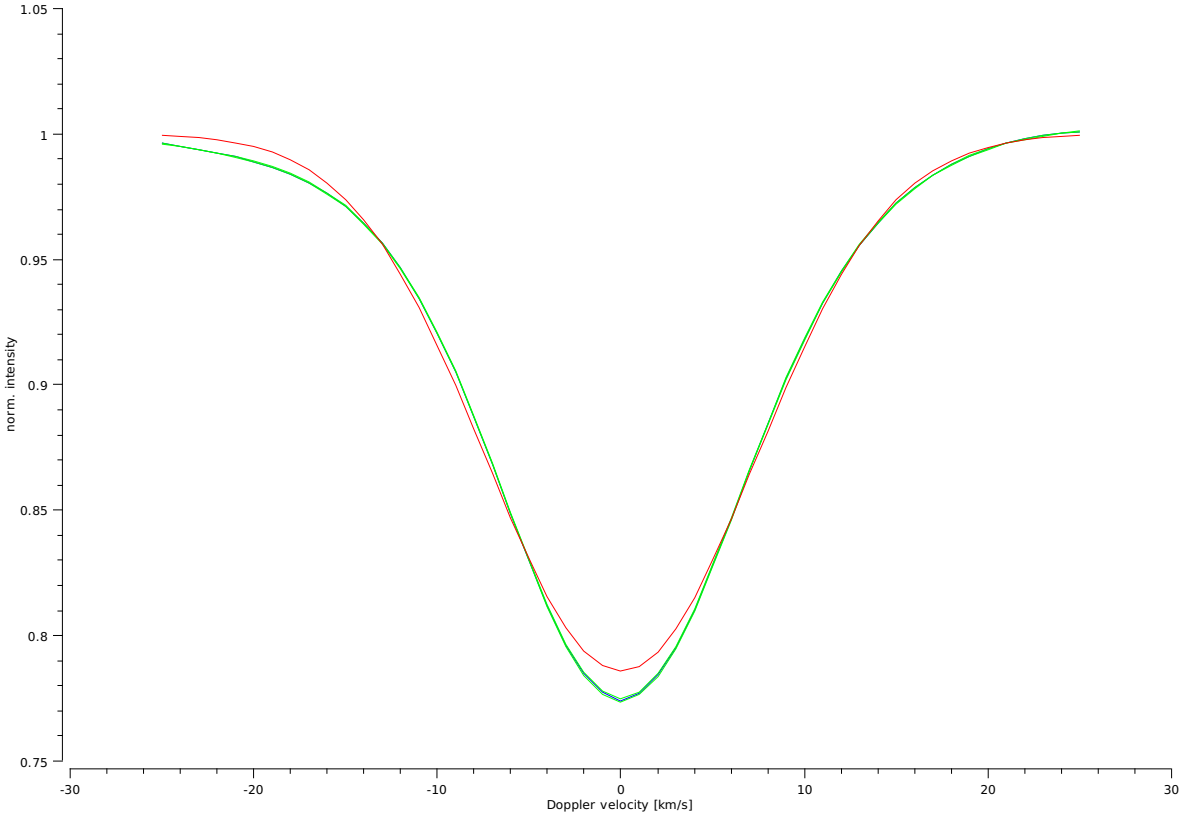

Figure 4.20: The zero-point line profile for the shifted component 2 of HD 10167.

The PBP technique within FAMIAS in conjunction with individual and simultaneous mode identification was used to determine the dominant spectroscopic frequencies and their best-fitting modes of pulsation.

The frequency detection revealed five possible significant frequencies: 1.53136, 1.17091, 1.60103, 0.80581 and 3.74968 $\mathrm{d^{-1}}$. The second of these frequencies could be the same as the second frequency of the shifted primary component (1.17767 $\mathrm{d^{-1}}$) and the third frequency could be a sub-harmonic of the fifth frequency of the unshifted secondary component (3.12483 $\mathrm{d^{-1}}$).

Some of the frequencies show symmetric amplitude variations but most show asymmetric variations about zero velocity. Mode identification was performed for each of the frequencies, where 1–2 different modes were detected with similar χ^2 values (Table 4.10).

f_1 was found to be a (3,-1) mode, which indicates a retrograde pulsation. This frequency shows the most symmetric amplitude variations of the five detected frequencies. Despite being the most significant frequency of the five detected, the fit for this frequency is one of the worst with a χ^2 value of 26.8. This is clear from the amplitude and phase variations (Figure 4.21) where the velocity amplitude does not match the variations in height and the phase is offset by a factor of 2π. Interestingly, the zero-point and amplitude fits improve during the simultaneous frequency mode identification.

Table 4.10: Parameters obtained from the mode identification of each individual pulsation frequency detected for the shifted Component 2 of HD 10167. All values except frequencies have been rounded to 3 s.f.

Parameters	Frequencies (d^{-1})			
	f_1 1.52126	f_2 1.17091		f_3 1.60103
Radius ($R_\odot$)	5.96	8.37	7.09	8.16
Mass ($M_\odot$)	8.44	9.72	2.91	3.06
Inclination (°)	61.3	0.176	0.0880	60.0
Mode (l,m)	(3,-1)	(3,-1)	(1,-1)	(3,1)
Vel. Amp. ($km\,s^{-1}$)	9.03	18.1	18.1	19.4
Phase	0.606	0.780	0.787	0.472
χ^2	26.8	7.57	7.61	27.3

	f_4 0.80581		f_5 3.74968	
Radius ($R_\odot$)	5.04	9.08	5.61	5.68
Mass ($M_\odot$)	9.93	5.18	1	9.43
Inclination (°)	1.14	0.616	61.1	38.4
Mode (l,m)	(1,-1)	(3,1)	(3,-1)	(3,0)
Vel. Amp. ($km\,s^{-1}$)	3.87	1.94	19.4	11.0
Phase	0.142	0.646	0.496	0.496
χ^2	9.85	9.99	6.01	6.32

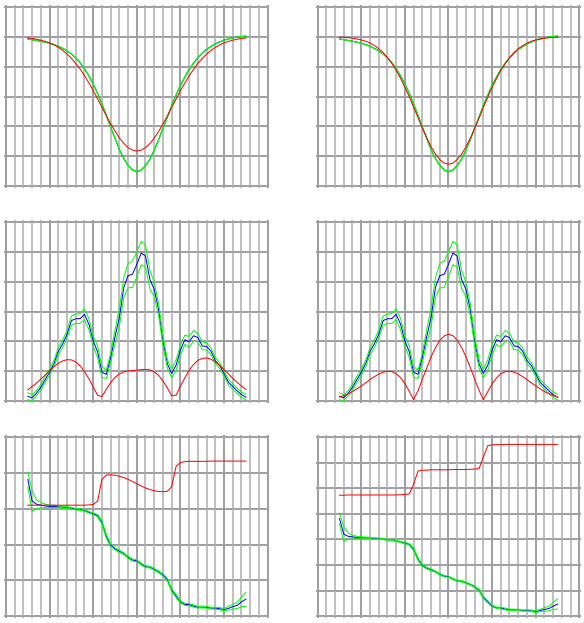

(a) (b)

Figure 4.21: Zero-point, amplitude and phase diagrams of the mode identification of the HD 10167 shifted Component 2 frequency $f_1 = 1.52126$ d^{-1} (a) individually; and (b) simultaneously with the other frequencies with f_2 as a (3,-1) mode, f_4 as a (1,-1) mode and f_5 a (3,-1) mode.

For f_2, two possible modes were found: (3,-1) and (1,-1), which both indicate a retrograde pulsation. The fits of these modes have exactly the same velocity amplitude and very similar phase values, which is also clear from their fit to the observed amplitude and phase variations (Figure 4.22). Despite their similarities, the (1,-1) mode was found to fit the zero-point profile slightly better and therefore the frequency was determined to be best modelled by this mode.

For f_3, the ZAP fitting method was required to determine that the frequency is a prograde (3,1) mode. This frequency shows asymmetric amplitude peak heights and a slight offset from zero velocity. This frequency has the worst fit of all of the frequencies, with a χ^2 value of 27.3. This is clear from the fit to the observed amplitude variations (Figure 4.23) where the model only fits one of the three observable peaks. The phase variations are affected by an offset of 2π. Just as for f_1, the zero-point and amplitude fits for this frequency improve during the simultaneous frequency mode identification.

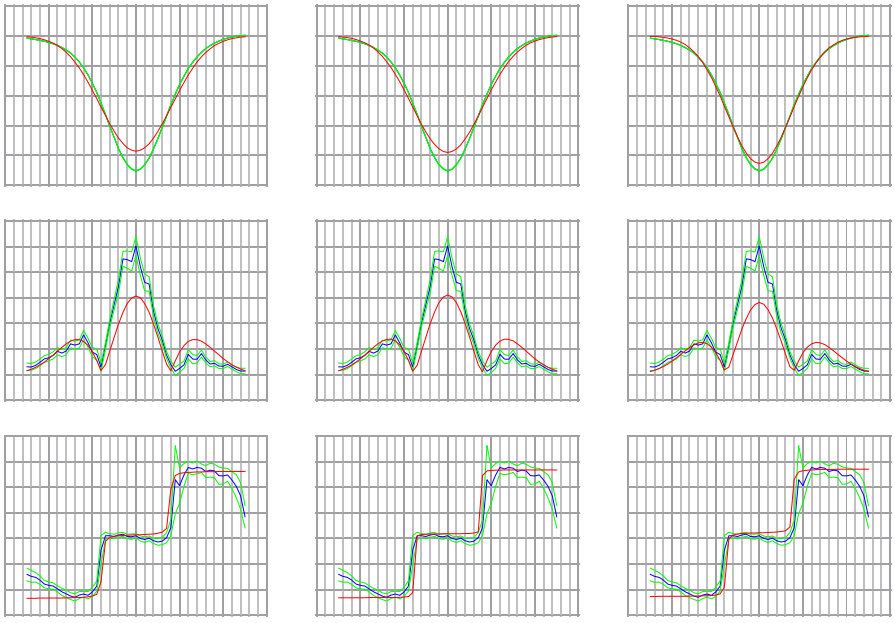

(a) (b) (c)

Figure 4.22: Zero-point, amplitude and phase diagrams of the mode identification of the HD 10167 shifted Component 2 frequency $f_2 = 1.17091$ d^{-1} individually as (a) a (3,-1) mode and (b) a (1,-1) mode; and (c) simultaneously with the other frequencies with f_2 as a (3,-1) mode, f_4 as a (1,-1) mode and f_5 a (3,-1) mode.

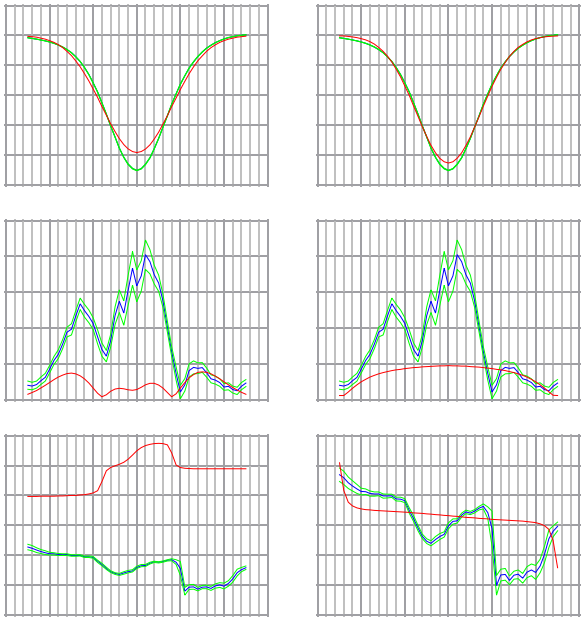

(a) (b)

Figure 4.23: Zero-point, amplitude and phase diagrams of the mode identification of the HD 10167 shifted Component 2 frequency $f_3 = 1.60103$ d^{-1} (a) individually; and (b) simultaneously with the other frequencies with f_2 as a (3,-1) mode, f_4 as a (1,-1) mode and f_5 a (3,-1) mode.

For f_4, two possible modes were found: (1,-1) and (3,1). The amplitude and phase variations are approximately symmetrical and show rough peak profiles. The fits are visually indistinguishable from each other. f_4 was determined to be a (1,-1) mode due to its low χ^2 value.

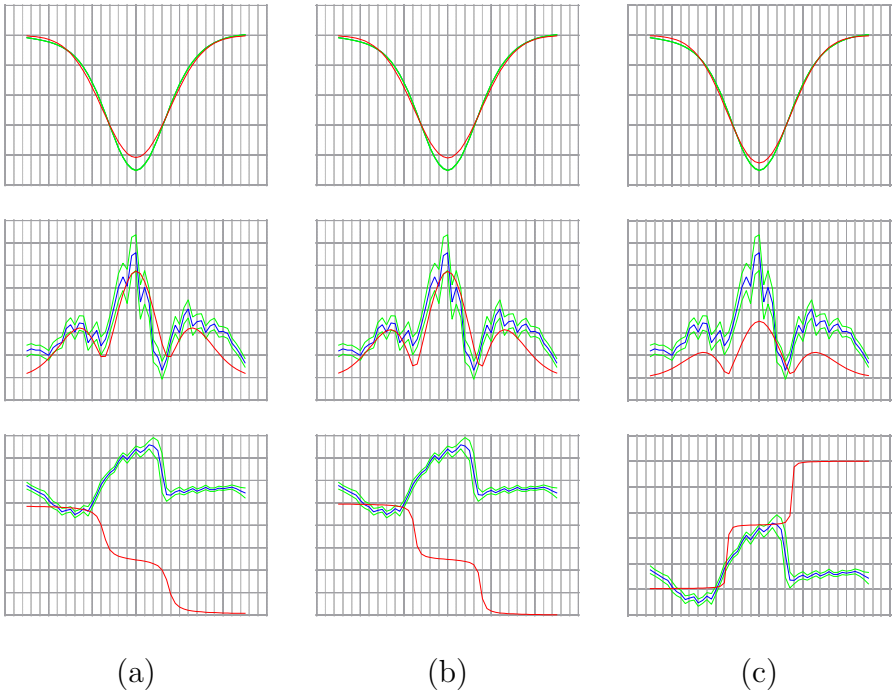

(a) (b) (c)

Figure 4.24: Zero-point, amplitude and phase diagrams of the mode identification of the HD 10167 shifted Component 2 frequency $f_4 = 0.80581$ d^{-1} individually as (a) a (1,-1) mode and (b) a (3,1) mode; and (c) simultaneously with the other frequencies with f_2 as a (3,-1) mode, f_4 as a (1,-1) mode and f_5 a (3,-1) mode.

For f_5, two possible modes were found: (3,-1) and (3,0). While the phase variations fit within a 2π offset, the fit to the amplitude variations fit the shape but not the height of the amplitude peaks. This is expected as this frequency was the last detected spectroscopic frequency. f_5 was determined to be a (3,-1) mode due to its low χ^2 value.

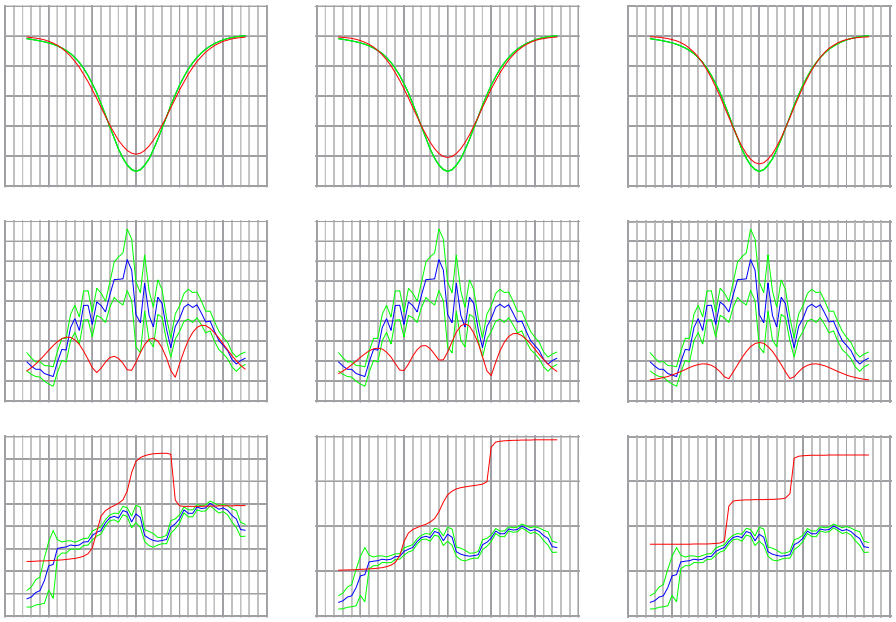

(a) (b) (c)

Figure 4.25: Zero-point, amplitude and phase diagrams of the mode identification of the HD 10167 shifted Component 2 frequency $f_5 = 3.74968$ d^{-1} individually as (a) a (3,-1) mode and (b) a (3,0) mode; and (c) simultaneously with the other frequencies with f_2 as a (3,-1) mode, f_4 as a (1,-1) mode and f_5 a (3,-1) mode.

A simultaneous mode identification of all five frequencies was performed using the following modes: f_1 = (3,-1), f_2 = (1,-1), f_3 = (3,1), f_4 = (1,-1), f_5 = (3,-1). The best-fitting model is presented in Table 4.11.

Table 4.11: Parameters obtained from the simultaneous mode identification of all frequencies for the shifted Component 2 of HD 10167. All values except frequencies have been rounded to 3 s.f.

Stellar Parameters			Frequency (d^{-1})					
Radius ($R_\odot$)	Mass ($M_\odot$)	Inclination ($^\circ$)	Pulsation Parameters	f_1 1.52126	f_2 1.17091	f_3 1.60103	f_4 0.80581	f_5 3.74968	χ^2
8.80	4.47	0.176	Mode	(3,-1)	(1,-1)	(3,1)	(1,-1)	(3,-1)	21.8
			Vel. Amp. ($km\,s^{-1}$)	18.7	19.4	16.1	7.74	3.23	
			Phase	0.110	0.795	0.614	0.654	0.0472	

4.4 Unshifted vs. Shifted Line Profiles

A number of aspects of the mode identification of the unshifted and shifted line profiles indicate that the unshifted line profiles show the true nature of the binary components. Firstly, the χ^2 values for the zero-point profile fits of the shifted components were both at least a factor of 1.8 larger than those of the unshifted components. Secondly, five significant spectroscopic frequencies were detected for both of the unshifted components compared to two and five frequency detections for the shifted primary and secondary components respectively. Lastly, mode identifications for the individual frequencies were able to be successfully performed for the unshifted components whereas the mode identification for the shifted primary was completely unsuccessful and the mode identification for the shifted secondary resulted in a few frequencies with poor-fitting amplitude variations and high χ^2 values. In addition to all of the residual radial velocity variations lying within a 2σ interval of zero velocity (Figure 4.5), these results indicate that the observed residual radial velocities are inherent to the binary components and not a residual from the orbital correction.

4.5 Discussion of HD 10167

Three orbital parameters (primary radial velocity semi-amplitude, period and systematic velocity) of the orbital solution obtained by this thesis agree with those determined by De Cat et al. (2006a) within the given uncertainties. Ultimately, the orbital solution provided a fit to the radial velocity data with a higher *rms* than the solution found by De Cat et al. (2006a).

The orbital period was detected as the 11^{th} photometric frequency, whereas several harmonics were in the first 10 detected photometric frequencies. This supports the hypothesis from De Cat et al. (2006a) that the components of this binary system are spin-aligned and synchronised.

A comparison of the detected frequencies for HD 10167 revealed that no definitive matches can be made between the spectroscopic frequencies of each component or between the photometric and spectroscopic frequencies. This was unexpected as the high-precision space photometry from TESS should allow for lower amplitude pulsation frequencies to be detected. An explanation for this could be that the 56 resolved spectra used for the frequency detection were insufficient to detect the same photometric frequencies to a high enough S/N ratio to be detected by FAMIAS. Alternatively, the lack of agreement between the photometric and spectroscopic frequencies could be due to the coarse velocity sampling of 3 $\mathrm{km\,s^{-1}}$ of the CCLPs produced by *Megara*. Combined with the narrow line-width of the absorptions produced by both components in the spectrum of HD 10167, this may have influenced the significance of the detected spectroscopic frequencies.

The final pulsation modes were (1,-1), (1,-1), (0,0), (1,1) and (1,0) for the primary component and (1,-1), (2,-1), (3,2), (3,1), and (3,2) for the secondary. All l values have an uncertainty of ± 1 and all m values were determined unambiguously, according to Zima (2006). Both components showed a combination of prograde and retrograde pulsations, with the primary component possessing the only radial (0,0) mode. Although five pulsation modes

were determined for each component, only the secondary component achieved a successful simultaneous mode identification. The resulting stellar parameters were $R = 2.49\ R_\odot$, $M = 9.08\ M_\odot$, and $i = 25.2°$. The value for the stellar radius agrees with the value $2.40^{+0.16}_{-0.08}\ R_\odot$ from the *Gaia* Data Release 2 (Gaia Collaboration et al. 2018) within its given uncertainty; although, it should be noted that the stellar mass and radius values are used during mode identification in FAMIAS to determine the ratio of the horizontal to vertical velocity of the pulsations rather than constraining the stellar parameters. The inclination implies a stellar equatorial velocity of 1.53 $\mathrm{km\,s^{-1}}$ from the $v \sin i$ found for the secondary component (Table 4.5). This result is unreliable, as Zima (2006) suggests a limit of $v \sin i \approx 5\ \mathrm{km\,s^{-1}}$ and the $v \sin i$ determined for both the primary and secondary by this paper are lower than this limit. Additionally, the velocity amplitudes of the pulsation frequencies range from moderate (4.52 $\mathrm{km\,s^{-1}}$) to high (17.4 $\mathrm{km\,s^{-1}}$). These high velocity amplitudes may have been influenced by the low inclination and $v \sin i$ values during their optimisation and therefore may also be unreliable.

Confirmation of the components as γ Dor stars is dependent on the resolved spectral data, as the photometric data was obtained from the observation of the entire binary system. Both stars have four γ Dor frequencies within their five detected spectroscopic frequencies. This suggests that both stars are γ Dor pulsators. While δ Sct frequencies were also detected in the photometry, they represent less than 15% of the detected frequencies; therefore there is potential for either of the components of HD 10167 to be a γ Dor/δ Scuti hybrid. This however needs confirmation, as no δ Sct frequencies were detected from the spectra for either component.

5. HD 206481

This chapter presents the results of the photometric and spectroscopic analyses for the target HD 206481, which is a single γ Dor star.

5.1 TESS Photometric Frequencies

A preliminary examination of the light curve of HD 206481 revealed that it is a GDORA star (as defined by Balona 2018a) due to the clear beating of the light curve and the asymmetry between the minima and maxima of its brightness.

Once normalised, the TASOC and MAST light curves (Figure 5.1) are identical except for a small region of the light curve at ∼1347.5 TBJD where a large proportion of the TESS data was flagged as being of lesser-quality. As there are more green than blue data points in this region, it is likely that the MAST pipeline was able to correct some of these flagged data points. A comparison of the SigSpec (Reegen 2010) and FAMIAS (Zima 2006) TASOC Fourier spectra (Figure 5.2 and A.2) reveals that both spectra show similar frequency features.

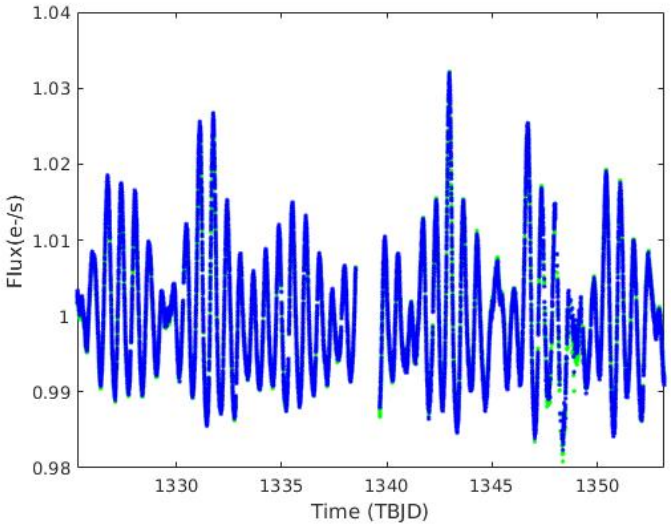

Figure 5.1: HD 206481 TASOC (blue) and MAST (green) SAP light curves normalised to a mean flux of 1 $e^{-}\,s^{-1}$.

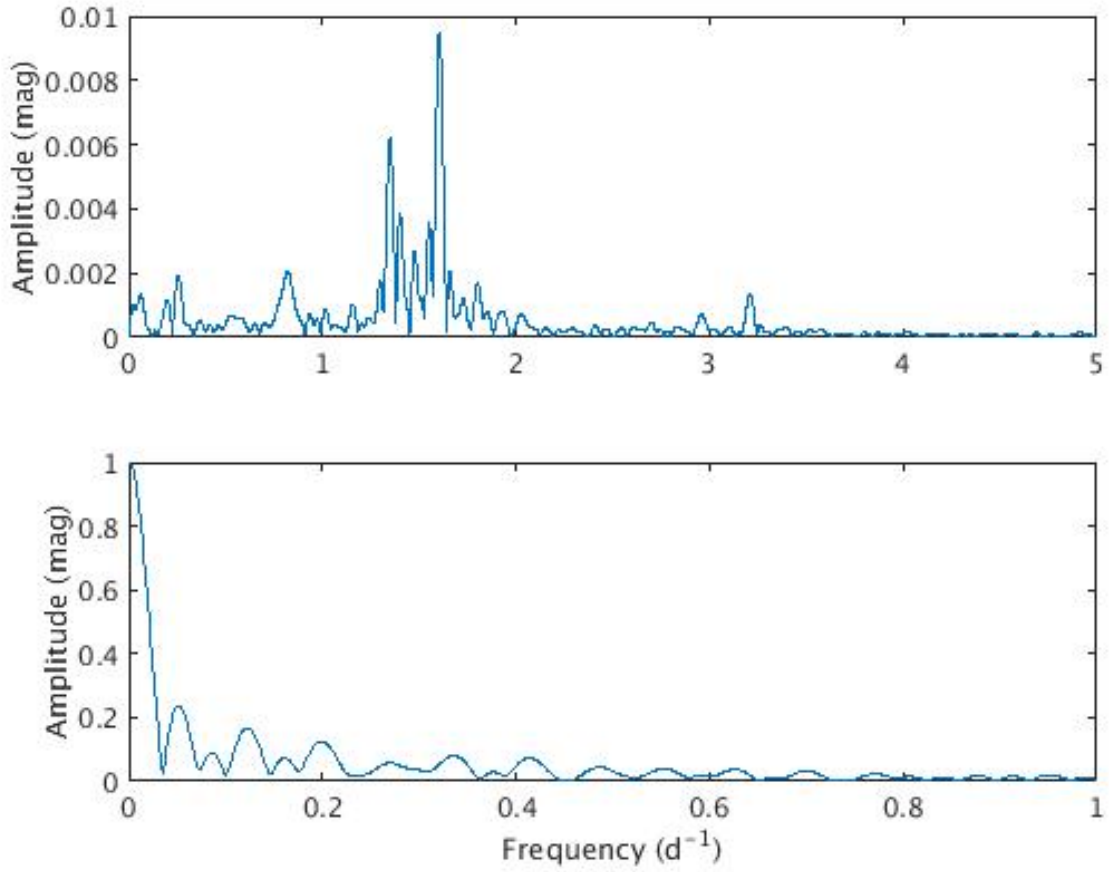

Figure 5.2: Fourier spectrum of the HD 206481 light curve from TASOC over the range 0–5 d^{-1} (top); and the corresponding spectral window, shown over the range 0–1 d^{-1} (bottom).

The SigSpec Fourier analysis of the TASOC light curve produced 146 significant frequencies (S/N $\geq$ 4), 41 of which are within the γ Dor frequency range and 74 are within the δ Sct frequency range (Table B.2). One aliasing event ($f_{79} + 8 \approx f_{140}$) and six frequency combinations (Table C.1) were found within a tolerance of 0.0001 d^{-1}. Therefore, it is likely that at least seven of the 146 detected frequencies are not independent.

Table 5.1 presents the first 10 detected frequencies from the SigSpec and FAMIAS analyses of the TASOC and MAST light curves. The order of the frequency detections for the SigSpec light curves are identical, whereas the FAMIAS analysis produces the same frequencies in a different order. Additionally, only one of the FAMIAS frequencies was found to agree with its associated SigSpec TASOC frequency within 0.001 d^{-1}, whereas seven of the MAST frequencies agree with the SigSpec TASOC frequencies within 0.001 d^{-1}.

Frequencies found previously for HD 206481 (Handler 1999) from *Hipparcos* photometry were 1.605 and 1.429 d^{-1}, where the latter is an average of other possible frequencies. The first frequency agrees with the first of the detected frequencies from this thesis's analysis whereas the second average frequency could be an average of the next three detected frequencies (f_2, f_3, f_4) where one day aliases of f_3 and f_4 are used. A phased MAST light curve using the MAST frequency 1.60835 d^{-1} confirms that this frequency produces a periodic sinusoidal effect in the star's light curve (Figure 5.3).

Table 5.1: First 10 detected frequencies in the TASOC and MAST light curves for HD 206481 as detected by FAMIAS and SigSpec. All frequencies are listed in the order corresponding to their match to a SigSpec TASOC frequency. All figures have been rounded to 5 d.p.

Frequency (d^{-1})							
TASOC				MAST		Differences	
FAMIAS (1)		SigSpec (2)		SigSpec (3)		(1) & (2)	(2) & (3)
f_1	1.60474	f_1	1.60809	f_1	1.60835	0.00336	0.00025
f_2	1.34834	f_2	1.34846	f_2	1.34873	0.00013	0.00026
f_6	0.79609	f_3	0.81071	f_3	0.80992	0.01462	0.00079
f_4	0.25640	f_4	0.25974	f_4	0.25940	0.00334	0.00034
f_5	1.41288	f_5	1.40896	f_5	1.40910	0.00392	0.00013
f_3	0.82299	f_6	0.83374	f_6	0.83478	0.01075	0.00104
f_8	3.20768	f_7	3.21179	f_7	3.21239	0.00411	0.00060
f_7	0.06455	f_8	0.05997	f_8	0.07043	0.00458	0.01045
f_9	1.49357	f_9	1.50450	f_9	1.50767	0.01093	0.00317
f_{10}	1.86651	f_{10}	1.86176	f_{10}	1.86169	0.00475	0.00007

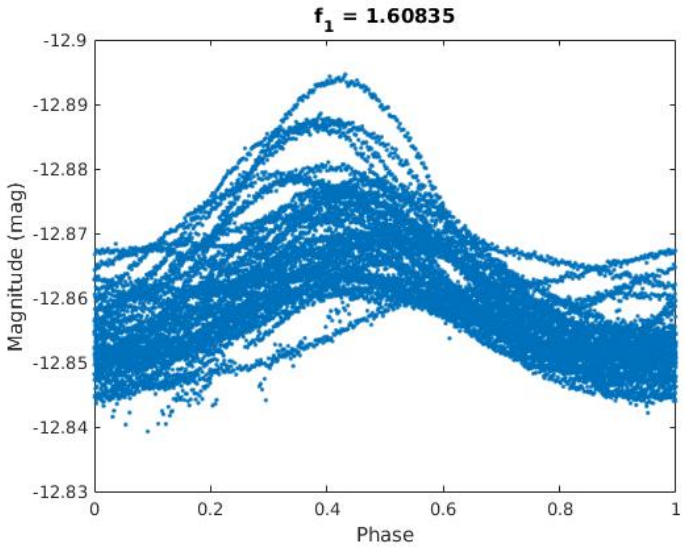

Figure 5.3: Phased MAST light curve for HD 206481 for the first detected MAST frequency, $f_1 = 1.60835$ d^{-1}.

5.2 CCLP Radial Velocity Features

As mentioned previously, the CCLPs for HD 206481 show evidence of several events which produce absorption spikes in the CCLPs at various velocities (Figure 5.4). The most extreme of these events occurs over a period of five days between MJD 58058 and 58062 (31 October to 4 Nov 2017). An interesting aspect of this event is the rate at which the absorption spike appears in the CCLPs; the dip is undetectable in the CCLP for MJD 58057 (30 October 2017) and very prominent in the next CCLP on 31 October. The spike appears to increase in depth to a minimum of 0.8 intensity relative to the continuum level intensity.

Similar features have been identified in the close binary system α Virginis studied by Harrington et al. (2016). Their paper finds multiple types of variable features in their CCLPs (such as wing shape, line profile shape, bumps and spikes), some of which they attribute to tidal effects. However, they identify 'quasi-stationary' strong absorption peaks in the CCLPs with a minimum relative intensity of 0.94 which appear for an interval of $\sim$2 hours with a period of $\sim$8 hours. Such short timescales can be attributed to the small separation of the binary and therefore short period of $\sim$4 days. The main difference with the spikes observed by Harrington et al. (2016) are that two absorption spikes are detected (one blue, one red) simultaneously at the same point in the orbit and are thought to be

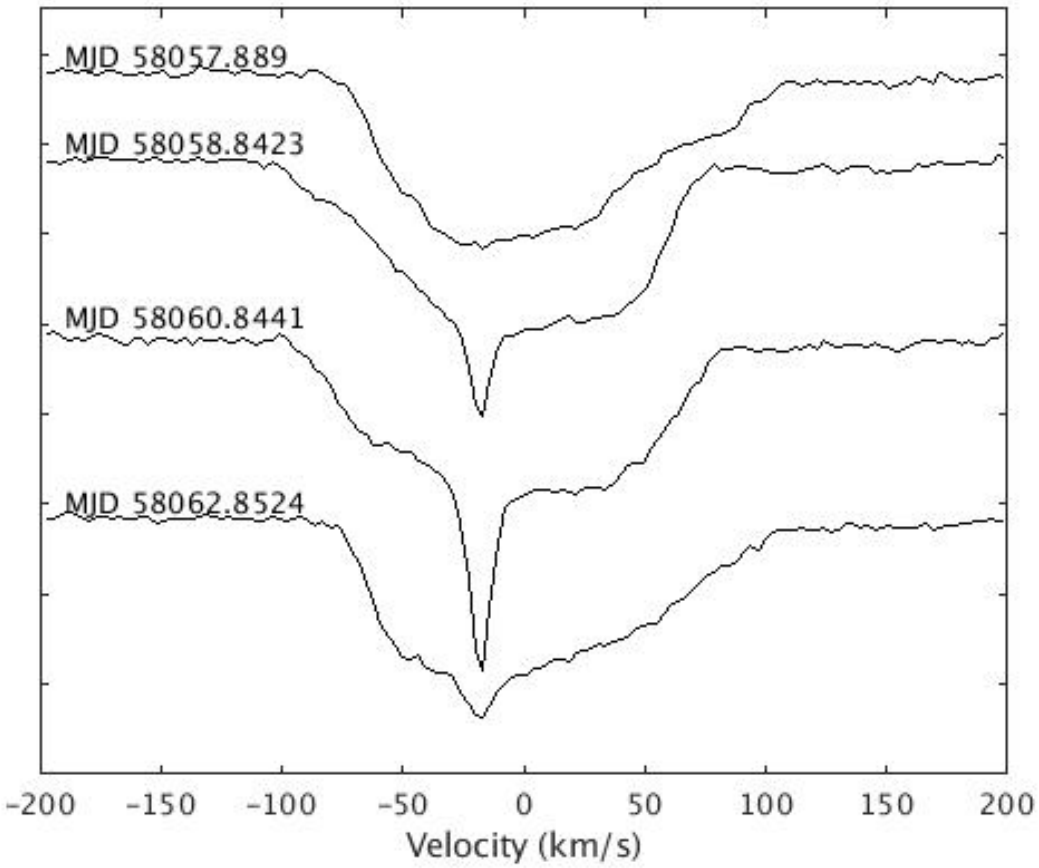

Figure 5.4: CCLPs for the time period around the peculiar radial velocity peak for HD 206481.

produced by a 'quasi-toroidal' tidally-induced mode. However, Harrington et al. (2016) also suggests that the behaviour of small features in the line profiles which do not vary with any orbital timescale may be influenced by internal pulsations or local hydrodynamical effects. Therefore it is possible that the similar events observed for HD 206481 are of an internal pulsation or local hydrodynamical nature; however, given the difference between the two systems, this conclusion needs to be tested.

A paper which may shed more light on the phenomena in the CCLPs of HD 206481 is the analysis of the Be star ω CMa by Maintz et al. (2003). They modelled non-radial pulsations in order to reproduce the absorption spikes observed in absorption line profiles of various elements (Si, S, Ne, C, Mg, and He). They found that as the non-radial pulsation amplitude increases, the absorption depth of the spike increases, the position of the spike is located closer to the centre of the line profile and the 'ramp' which broadens the wings of the line profile extends past the $v \sin i$ value of the non-pulsating model by the same value as the velocity amplitude of the pulsation.

There are some discrepancies between the explanation of the absorption spikes from Maintz et al. (2003) and what is observed for HD 206481. The first is that, although the 'ramp' feature is also present in the CCLPs of the event, it is the most prominent for MJD 58057 and MJD 58062 where the spike is not visible and becoming weaker respectively (Figure 5.4). The second discrepancy is that this theory for the origin of the absorption spike implies a periodic appearance of the spike. From our line profiles, two possible absorption spike events are observed: the aforementioned spike which occurs at $v \approx -20$ km s^{-1} and a smaller spike which occurs at $v \approx 10$ km s^{-1} at MJD 58653 (18 June 2019). Assuming that no other event has occurred between these, their temporal separation implies a period of $\sim$596 days or 1.6 years which would classify HD 206481 as a long-period variable rather than a γ Dor star. Additionally, it is uncertain as to whether the CCLPs of the second event are in fact an absorption spike since CCLPs directly before and after at MJD 58652 and MJD 58654 show no indication of the absorption. Thus the nature of the absorption spikes observed for HD 206481 remains unconfirmed.

5.3 Mode Identification

Mode identification for HD 206481 was performed using 34 stellar spectra.

The zero-point line profile was fitted to determine the pulsation-independent line parameters. The zero-point line profile fit for HD 206481 was determined using FAMIAS to have a χ^2 value of 6.60 (Table 5.2), which indicates a good fit to the observed profile. This is clear from Figure 5.5 where the main deviation of the model from the observation occurs near the wing and continuum level of the line profile in the positive velocity space. The $v \sin i$ value is close to the value 86 ± 2 km s^{-1} determined by Kahraman Aliçavuş et al. (2016).

The PBP technique within FAMIAS in conjunction with individual and simultaneous mode identification was used to determine the dominant spectroscopic frequencies and their best-fitting modes of pulsation.

Table 5.2: The zero-point line profile parameters for HD 206481. All values except frequencies have been rounded to 3 s.f.

Parameter	Value
$v \sin i$ ($\mathrm{km\,s^{-1}}$)	80.0
Equivalent width ($\mathrm{km\,s^{-1}}$)	10.9
Intrinsic width ($\mathrm{km\,s^{-1}}$)	11.9
Velocity offset ($\mathrm{km\,s^{-1}}$)	-0.425
χ^2	6.60

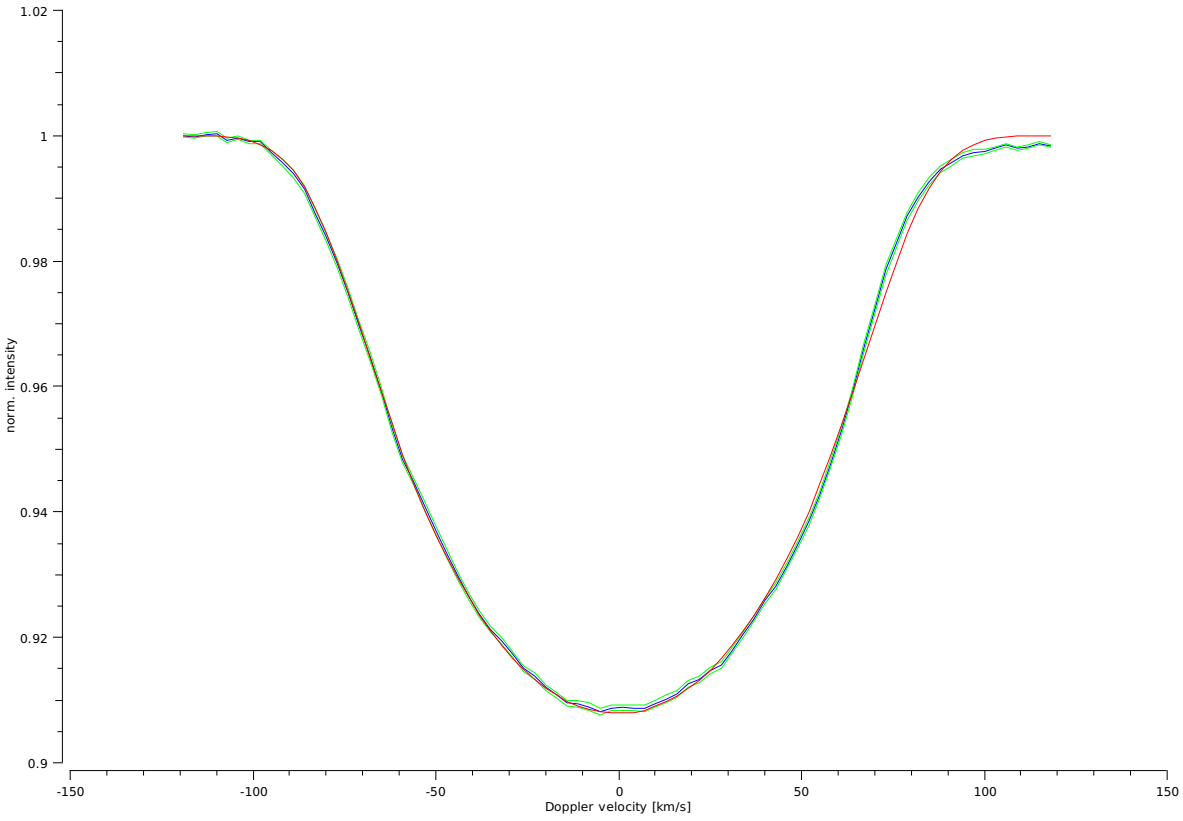

Figure 5.5: The zero-point line profile for HD 206481. The green and red lines indicate the observed zero-point line profile and the best-fitting theoretical model, respectively.

The frequency detection revealed three possible significant frequencies: 1.60636, 3.17918 and 5.8255 d^{-1}. The first is similar to the 1st detected photometric frequency (1.60809 d^{-1}) and the second is somewhat similar to the 7th detected photometric frequency (3.21179 d^{-1}).

All three spectroscopic frequencies show very similar symmetric amplitude variations and phase variations which decrease across the line profile. Mode identification was performed for each of the frequencies, where 1–2 different modes were detected with similar χ^2 values (Table 5.3).

Table 5.3: Parameters obtained from the mode identification of each individual pulsation frequency detected for HD 206481. All values except frequencies have been rounded to 3 s.f.

Parameters	Frequencies (d^{-1})				
	f_1 1.60636		f_2 3.17918	f_3 5.8255	
Radius ($R_\odot$)	4.04	3.07	3.41	2.04	3.40
Mass ($M_\odot$)	1.12	9.84	9.50	9.74	5.29
Inclination (°)	40.7	65.8	43.0	18.3	11.3
Mode (l,m)	(3,0)	(1,1)	(2,2)	(3,-2)	(1,-1)
Vel. Amp. ($km\,s^{-1}$)	18.1	1.47	1.94	3.87	5.81
Phase	0.843	0.866	0.913	0.535	0.543
χ^2	8.045	8.05	3.47	2.83	2.86

For f_1, two possible modes were found: (3,0) and (1,1). Despite the slightly lower χ^2 value for the fit of the (3,0) mode, the (1,1) mode appears to model the amplitude variations better with a similar phase fit as the (3,0) mode (Figure 5.6). The (1,1) mode also has a lower velocity amplitude compared to the more unrealistic 18.1 $km\,s^{-1}$ for the (3,0) mode. Therefore the (1,1) mode was taken to be the best-fitting mode for this frequency.

f_2 was found to be prograde (2,2) mode (Figure 5.7). Another possible mode was (3,1) which had a velocity amplitude equal to the maximum allowed value so it was discarded. Although symmetric, the amplitude variations for this frequency are variable throughout the centre of the line profile.

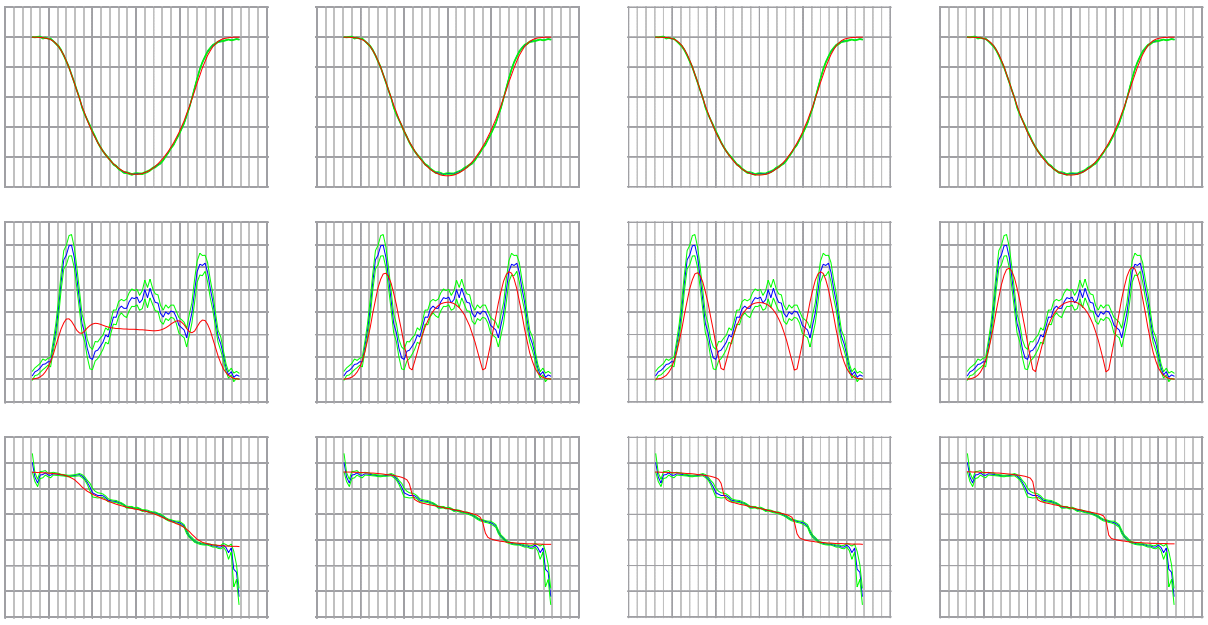

(a) (b) (c) (d)

Figure 5.6: Zero-point (top row), amplitude (middle row) and phase (bottom row) diagrams of the mode identification of the HD 206481 frequency $f_1 = 1.60636$ d^{-1} individually as (a) a (3,0) mode and (b) a (1,1) mode; and simultaneously with the other frequencies as a (1,1) mode with f_3 as (c) a (3,-2) mode; and (d) a (1,-1) mode. The blue and green lines are the observed values and their uncertainties for the zero-point, amplitude and phase. The red lines are the theoretical models determined to best fit the observations.

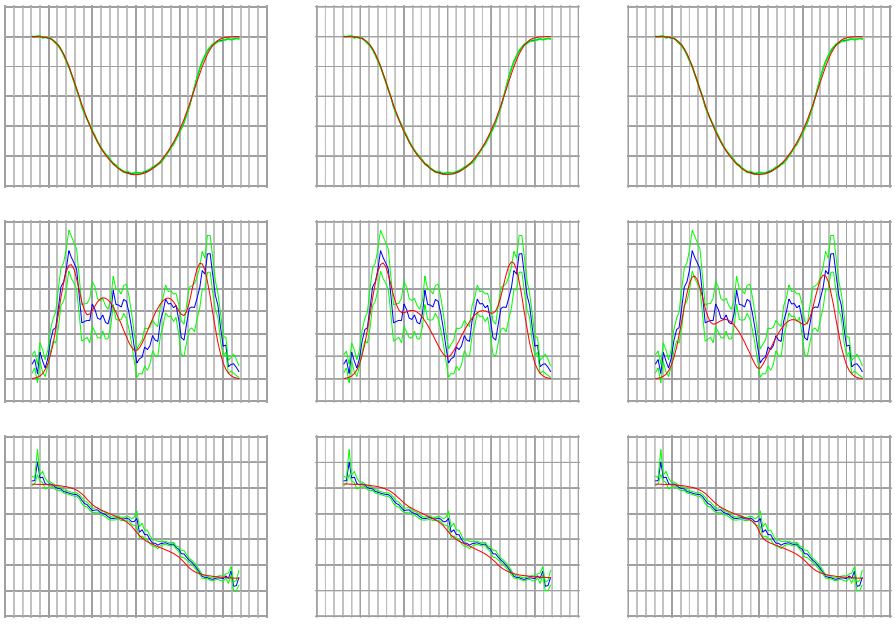

(a) (b) (c)

Figure 5.7: Zero-point, amplitude and phase diagrams of the mode identification of the HD 206481 frequency $f_2 = 3.17918$ d^{-1} (a) individually as a (2,2) mode; and simultaneously with the other frequencies, with f_3 as (b) a (3,-2) mode; and (c) a (1,-1) mode.

For f_3, the best fit for the amplitude and phase variations was found to be a (2,2) mode. However this mode did not fit the zero-point profile and was therefore discarded. There were two possible modes found for f_3 which fit the zero-point profile: (3,-2) and (1,-1), which both indicate a retrograde pulsation. Both modes present similar fits to the amplitude and phase variations, with similar phase values and χ^2 values (Table 5.3).

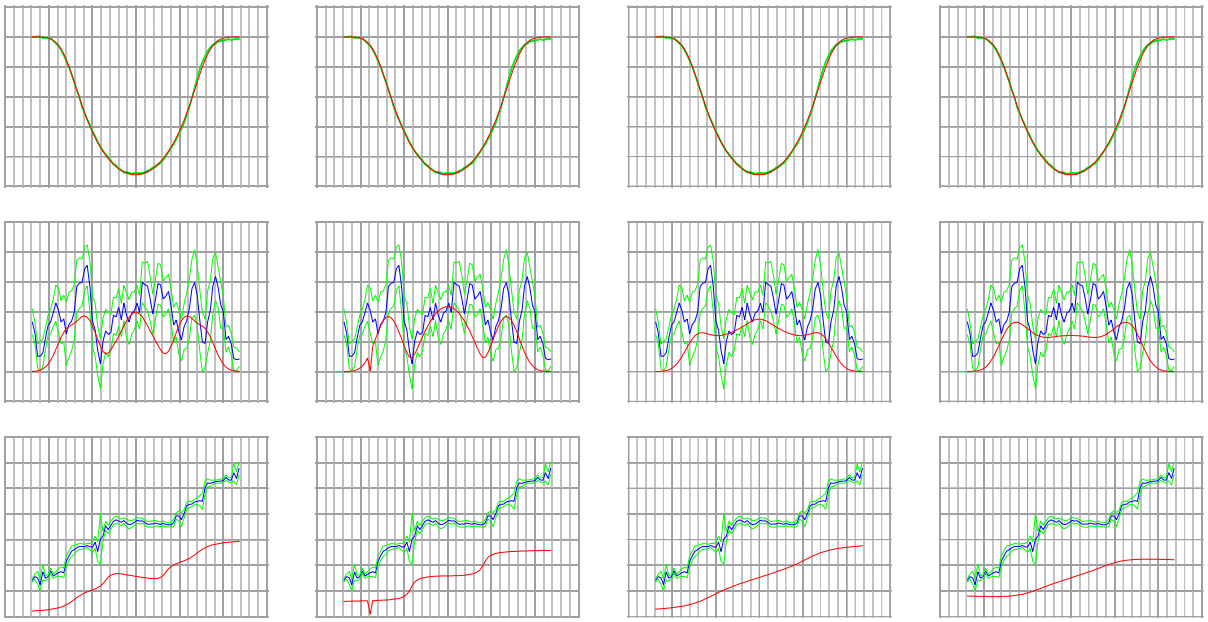

(a) (b) (c) (d)

Figure 5.8: Zero-point, amplitude and phase diagrams of the mode identification of the HD 206481 frequency $f_3 = 5.8255$ d^{-1} individually as (a) a (3,-2) mode and (b) a (1,-1) mode; and simultaneously with the other frequencies with f_3 as (c) a (3,-2) mode and (d) a (1,-1) mode.

A simultaneous mode identification of all three frequencies was performed twice with $f_1 = (1,1)$, $f_2 = (2,2)$ and $f_3 = (3,-2)$ or $f_3 = (1,-1)$. These models are presented in Table 5.4. The model with $f_3 = (3,-2)$ was determined to have a lower χ^2 value which is clear from the comparison of the amplitude and phase fits for the three individual frequencies (last two columns of Figures 5.6–5.8). This model gives an inclination of 49.0909° which implies a stellar rotational velocity of 105.87 km s^{-1}. Therefore the simultaneous mode identification with $f_3 = (3,-2)$ was determined to be the best model for the spectroscopic pulsation frequencies of HD 206481.

Table 5.4: Parameters obtained from the simultaneous mode identification of all frequencies for HD 206481 for the two cases where f_3 is a (3,-2) mode or a (1,-1) mode. All values except frequencies have been rounded to 3 s.f.

	Stellar Parameters			Frequency (d^{-1})				
	Radius ($R_\odot$)	Mass ($M_\odot$)	Inclination (°)	Pulsation Parameters	f_1 1.60636	f_2 3.71918	f_3 5.8255	χ^2
$f_3 = (3, -2)$	3.58	9.94	49.1	Mode	(1,1)	(2,2)	(3,-2)	4.90
				Vel. Amp. ($km\,s^{-1}$)	2.46	1.94	2.58	
				Phase	0.866	0.913	0.504	
$f_3 = (1, -1)$	3.70	9.97	47.3	Mode	(1,1)	(2,2)	(1,-1)	5.15
				Vel. Amp. ($km\,s^{-1}$)	2.95	2.58	3.87	
				Phase	0.879	0.929	0.488	

5.4 Discussion of HD 206481

A comparison of the detected frequencies for HD 206481 reveals that there are potentially two pairs of matching photometric and spectroscopic frequencies: 1.60809 and 1.60636 d^{-1}, and 3.21179 and 3.17918 d^{-1}.

A simultaneous mode identification of the three spectroscopic frequencies 1.60636, 3.17918 and 5.8255 d^{-1} was performed successfully. The best-fitting model was produced by the pulsation modes (1,1), (2,2) and (3,-2), where all l values have an uncertainty of ± 1 and all m values were determined unambiguously, according to Zima (2006). These modes include both prograde ad retrograde pulsations. The resulting stellar parameters were $R = 3.58\ R_\odot$, $M = 9.94\ M_\odot$ and $i = 49.1°$. The value for the stellar radius disagrees with the value $1.62^{+0.08}_{-0.04}\ R_\odot$ from the *Gaia* Data Release 2 (Gaia Collaboration et al. 2018) within its given uncertainty; although, it should be noted that the stellar mass and radius values are used during mode identification in FAMIAS to determine the ratio of the horizontal to vertical velocity of the pulsations rather than constraining the stellar parameters. The inclination implies a stellar equatorial velocity of 82.6 $\mathrm{km\,s^{-1}}$ from the $v \sin i$ value determined from the zero-point line profile fit (Table 5.2). This result is reasonable as it suggests that the star is a moderate rotator. Additionally, the velocity amplitudes of the pulsations frequencies are approximately the same, with a maximum of 2.58 $\mathrm{km\,s^{-1}}$. These are also reasonable values as the inclination indicates that the star is observed almost edge-on and therefore the observed velocity amplitudes should be small ($< 10\ \mathrm{km\,s^{-1}}$).

Confirmation of HD 206481 as a γ Dor star can be obtained from both the photometric and spectroscopic frequencies. Although there are no δ Sct frequencies detected in the first 10 photometric frequencies, there are almost twice as many δ Sct frequencies as γ Dor frequencies found in the light curve. Additionally, there is one frequency from each pulsator class detected in the spectroscopic frequencies (1.60636 and 5.8255 d^{-1}). This indicates that HD 206481 is a γ Dor/δ Sct hybrid pulsator.

6. HD 209295

This chapter details the results of the photometric and spectroscopic analysis of the target HD 209295, which is a γ Dor star in an SB1 star system.

6.1 Photometric Frequencies

A preliminary examination of the light curve of HD 209295 revealed that it is possibly a GDORS star system (as defined by Balona 2018b) based on the presence of beating and symmetric minima and maxima in brightness.

Just as for HD 206481, the normalised TASOC and MAST light curves are identical except for a section which had more quality-flagged data than the rest of the light curve (Figure 6.1). A comparison of the SigSpec (Reegen 2010) and FAMIAS (Zima 2006) TASOC Fourier spectra (Figure 6.2 and A.3) reveals that both show similar frequency features.

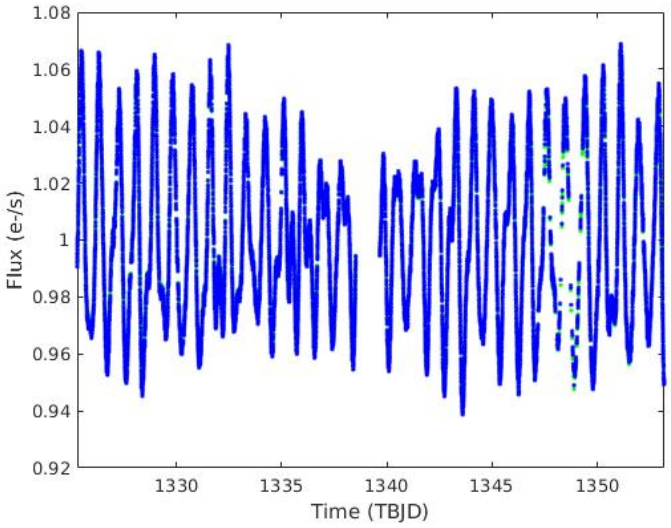

Figure 6.1: HD 209295 TASOC (blue) and MAST (green) SAP light curves normalised to a mean flux of 1 $e^{-}\,s^{-1}$.

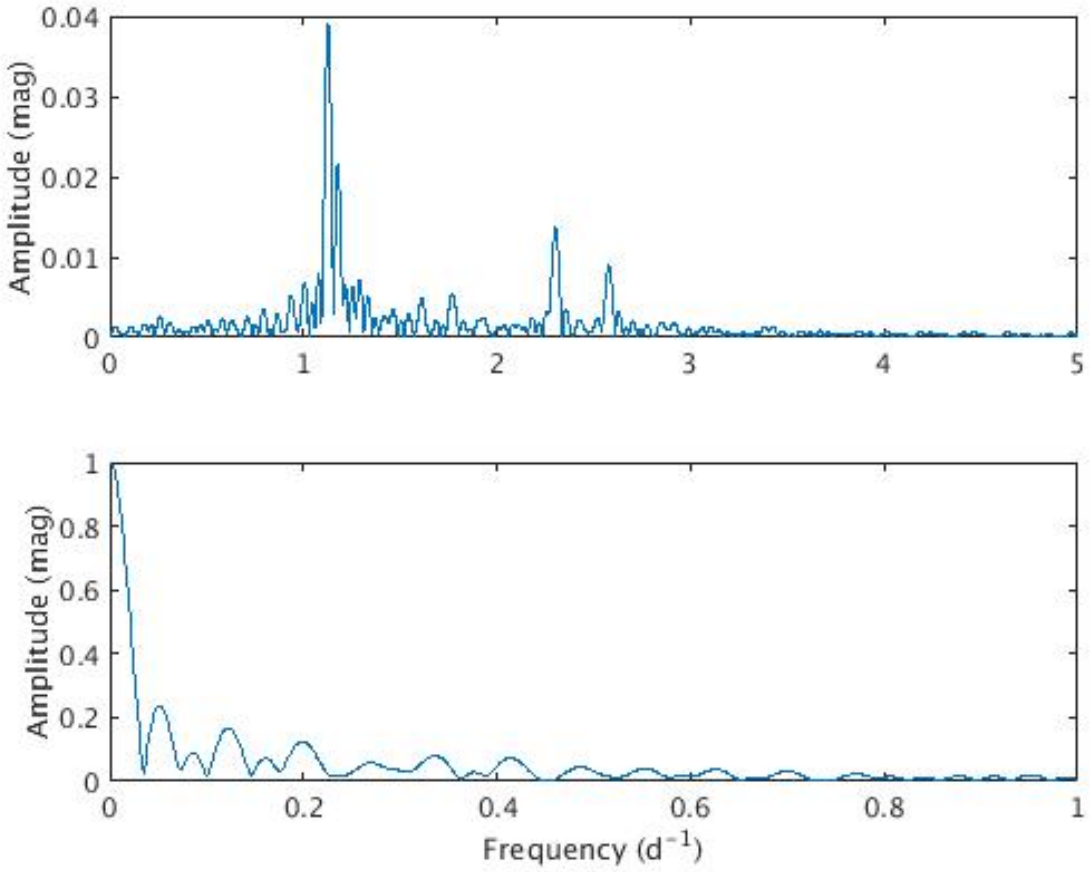

Figure 6.2: Fourier spectrum of the HD 209295 light curve from TASOC over the range 0–5 d^{-1}; and the corresponding spectral window, shown over the range 0 - 1 d^{-1}.

The SigSpec Fourier analysis of the TASOC light curve produced 643 significant frequencies (S/N $\geq$ 4), 38 of which are within the γ Dor frequency range and 573 are within the δ Sct frequency range (Table B.3). 40 aliasing events (Table C.2), 53 frequency combinations (Table C.3) and 94 frequency couplings (see the last column of Table B.3) were found within a tolerance of 0.0001 d^{-1}. Therefore, it is likely that at least 187 of the 643 detected frequencies are not independent.

Table 6.1 presents the first 10 detected frequencies from the SigSpec and FAMIAS analyses of the TASOC and MAST light curves. The order of the frequency detections for all methods are identical. Five of the FAMIAS frequencies are found to agree with the their associated SigSpec TASOC frequency within 0.001 d^{-1}; whereas nine of the MAST frequencies agree with the SigSpec TASOC frequencies, with the first four also agreeing within 0.0001 d^{-1}. The first four photometric frequencies agree with the periods found by Handler (1999) from the *Hipparcos* light curve for HD 209295 within < 0.003 d^{-1}. Frequencies f_5–f_8 from Handler et al. (2002c) are also present in the first 10 detected SigSpec TASOC frequencies. Additionally, the orbital frequency is detected as the 11$^{\text{th}}$ SigSpec TASOC frequency, where the 4$^{\text{th}}$, 6$^{\text{th}}$ and 8$^{\text{th}}$ frequencies are its harmonics. Despite the agreement between these results, the two δ Sct frequencies identified by Handler et al. (2002b) were not the first two δ Sct frequencies detected from the SigSpec TASOC light curve.

Table 6.1: First 10 detected frequencies in the TASOC and MAST light curves for HD 209295, as detected by FAMIAS and SigSpec. All frequencies are listed in the order corresponding to their match to a SigSpec TASOC frequency. All figures have been rounded to 5 d.p.

	Frequency (d^{-1})							
	TASOC				MAST		Differences	
	FAMIAS (1)		SigSpec (2)		SigSpec (3)		(1) & (2)	(2) & (3)
	f_1	1.12780	f_1	1.12808	f_1	1.12817	0.00029	0.00009
	f_2	2.30221	f_2	2.30455	f_2	2.30454	0.00234	0.00000
	f_3	1.17621	f_3	1.17509	f_3	1.17501	0.00111	0.00008
$8f_{\rm orb}$	f_4	2.57654	f_4	2.57642	f_4	2.57640	0.00012	0.00002
	f_5	1.76790	f_5	1.76732	f_5	1.76757	0.00058	0.00025
$3f_{\rm orb}$	f_6	0.96463	f_6	0.96652	f_6	0.96673	0.00189	0.00020
	f_7	1.61370	f_7	1.60881	f_7	1.60790	0.00489	0.00091
$4f_{\rm orb}$	f_8	1.28737	f_8	1.28657	f_8	1.28720	0.00081	0.00064
	f_9	2.26456	f_9	2.27029	f_9	2.27125	0.00573	0.00096
	f_{10}	0.64189	f_{10}	0.64263	f_{10}	0.64116	0.00073	0.00147

Phased MAST light curves using the first two detected MAST frequencies (1.12817 and 2.30454 d^{-1}) confirm that these frequencies produce periodic sinusoidal effects in the light curve of HD 209295 (Figure 6.3) and suggest that the frequency 2.30454 d^{-1} is close to a harmonic of the first, 1.12817 d^{-1}.

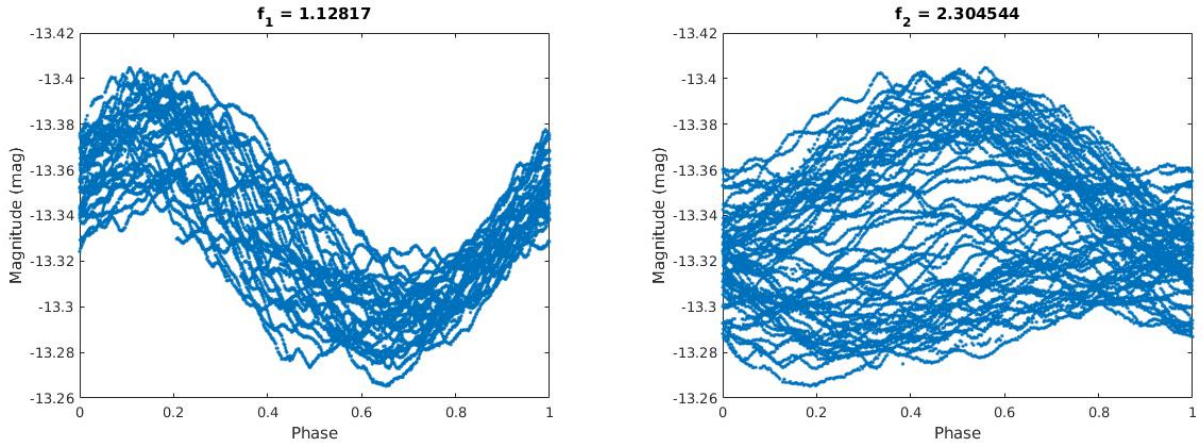

(a) (b)

Figure 6.3: Phased MAST light curves for HD 209295 for (a) the first ($f_1 = 1.12817$ d^{-1}) and (b) the second ($f_2 = 2.30454$ d^{-1}) detected MAST frequency.

6.2 Orbital Solution

The orbital solution for the visible binary component was determined using SpecBin to optimise orbital parameters from the radial velocities measured from the CCLPs for HD 209295. The mass quotient was unable to be determined for this system as it is an SB1 star system.

The radial velocity orbit for HD 209295 is presented in Figure 6.4. The orbital solution was determined using SpecBin and has an *rms* of 0.522 $\mathrm{km\,s^{-1}}$ (Table 6.2). This value is lower than that of the solution found by De Cat et al. (2006a) and is therefore mathematically the best-fitting solution. Most of the parameters determined by this thesis agree with the values from De Cat et al. (2006a) within the given uncertainties.

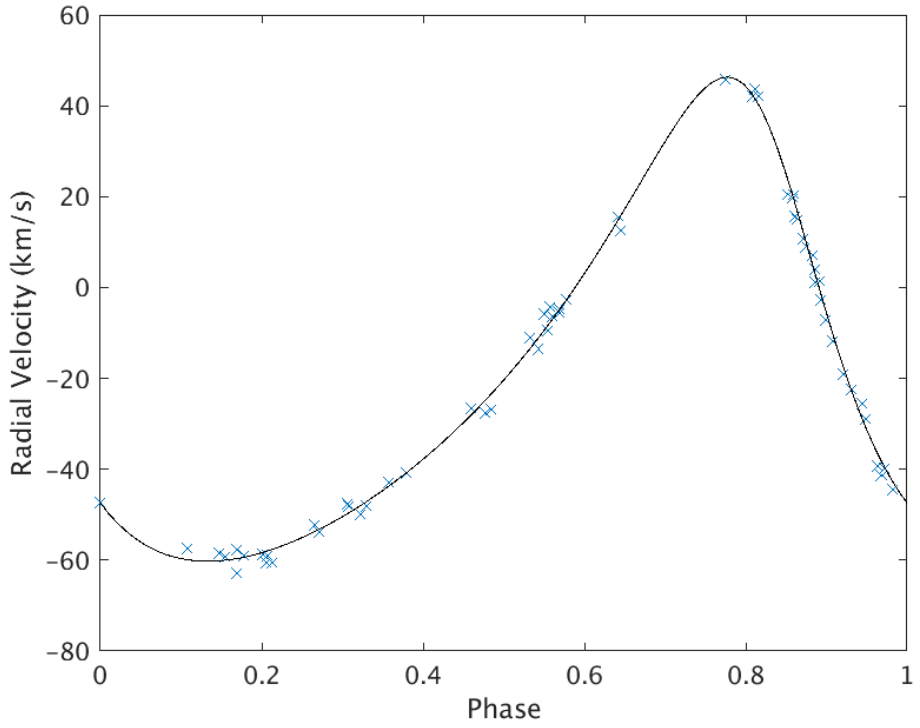

Figure 6.4: Radial velocity orbital solution for the visible component of HD 209295. The blue crosses are the phased radial velocity values and the black line is the best-fitting orbital solution.

Table 6.2: Radial velocity orbital solution parameters for HD 209295.

Parameter	This Thesis	De Cat et al. (2006a)
K_1 ($\mathrm{km\,s^{-1}}$)	53.3 ± 0.5	52.8 ± 0.3
e	0.330 ± 0.006	0.324 ± 0.005
ω (°)	-137.9 ± 1.5	33 ± 1
T_0 (MJD)	57909.947 ± 0.005	-
P (d)	3.10571 ± 0.00003	3.10573 ± 0.00002
γ ($\mathrm{km\,s^{-1}}$)	-20.0 ± 0.3	-20.5 ± 0.2
rms ($\mathrm{km\,s^{-1}}$)	0.522	1.03

6.3 Mode Identification

Mode identification for the visible component of HD 209295 was performed using 60 stellar spectra.

The zero-point line profile was fitted to determine the pulsation-independent line parameters. The zero-point profile for HD 209295 was determined using FAMIAS to have a χ^2 value of 10.2 (Table 6.3), which indicates a good fit to the observed profile. This is clear from Figure 6.5 where the theoretical zero-point profile does not deviate significantly from the observed zero-point at any point along the line profile. The $v \sin i$ value found from the zero-point line profile fit agrees with the values 86 ± 3 $\mathrm{km\,s^{-1}}$ and 89 ± 5 $\mathrm{km\,s^{-1}}$ determined by De Cat et al. (2006a) and Kahraman Aliçavuş et al. (2016) respectively.

This star is the only one of this thesis's targets which has previously had mode identification performed. Using spectroscopic data and prior knowledge from their photometry, Handler et al. (2002c) determined that the first two detected photometric frequencies (1.1296 and 2.3024 $\mathrm{d^{-1}}$) were $l = 1 \pm 1$, $m = 1 \pm 2$ modes. They were unable to detect any other frequencies.

Table 6.3: The zero-point line profile parameters for the visible component of HD 209295. All values have been rounded to 3 s.f.

Parameter	Value
$v \sin i$ ($\mathrm{km\,s^{-1}}$)	85.4
Equivalent width ($\mathrm{km\,s^{-1}}$)	7.48
Intrinsic width ($\mathrm{km\,s^{-1}}$)	16.05
Velocity offset ($\mathrm{km\,s^{-1}}$)	-1.84
χ^2	10.2

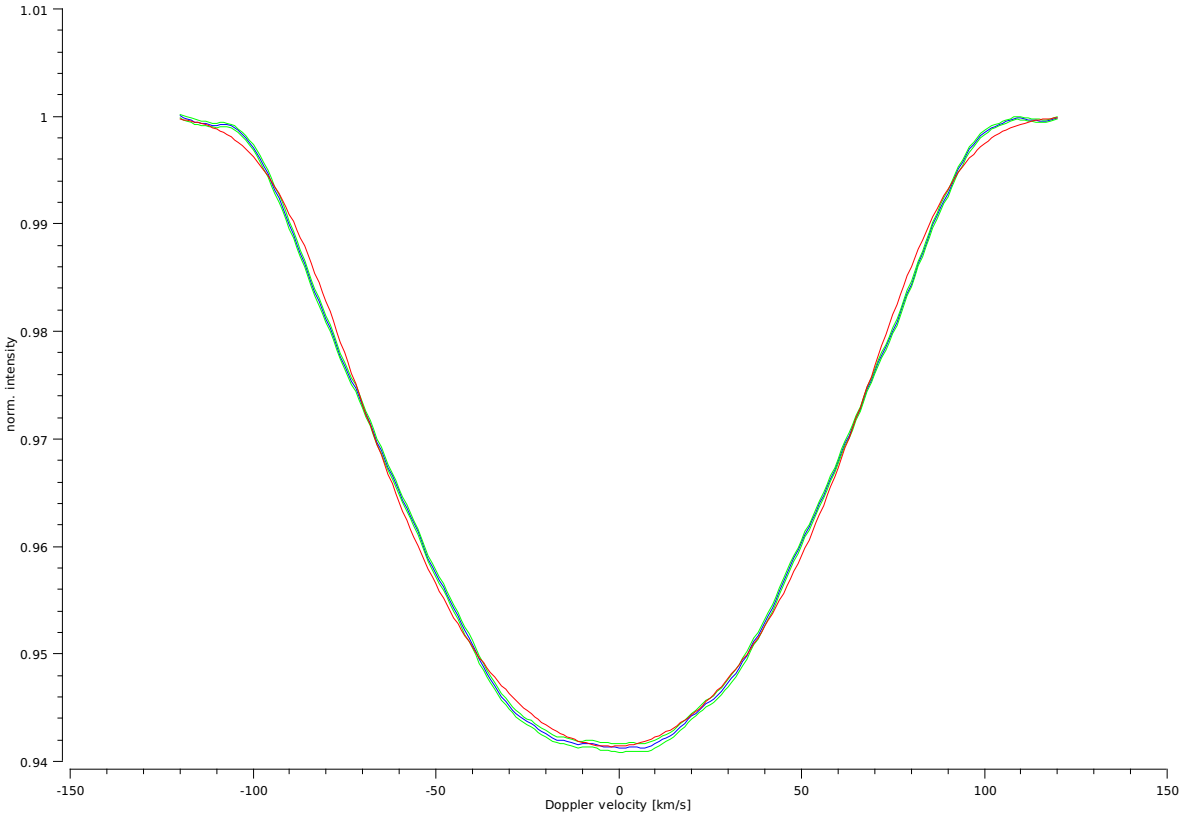

Figure 6.5: The zero-point for the visible component of HD 209295. The green and red lines indicate the observed zero-point line profile and the best-fitting theoretical model, respectively.

The PBP technique within FAMIAS in conjunction with individual and simultaneous mode identification was used to determine the dominant spectroscopic frequencies and their best-fitting modes of pulsation.

Despite our dataset of ∼60 spectra, the frequency detection only revealed one possible significant frequency of 1.17128 d^{-1}. This frequency is similar to the 3rd detected SigSpec TASOC photometric frequency and the 4th frequency detected by Handler et al. (2002c).

Mode identification was performed for this frequency using the ZAP method as the initial attempt using the AP method did not result in any modes fitting the zero-point profile. The frequency was found to be a (3,1) mode (Table 6.4). Despite achieving a low χ^2 value for the mode, the theoretical amplitude variations do not match those observed in the centre of the line profile (Figure 6.6). This frequency shows very asymmetric amplitude variations which are fitted well by the model on one side of the line profile and deviate on the other.

Table 6.4: Parameters obtained from the mode identification of the individual pulsation frequency $f_1 = 1.17128$ d^{-1} for the visible component of HD 209295. All values except the frequency have been rounded to 3 s.f.

Parameters	Frequency (d^{-1}) f_1 1.17128
Radius ($R_\odot$)	5.52
Mass ($M_\odot$)	1.01
Inclination (°)	55.8
Mode (l,m)	(3,1)
Vel. Amp. (km s^{-1})	6.13
Phase	0.629
χ^2	6.28

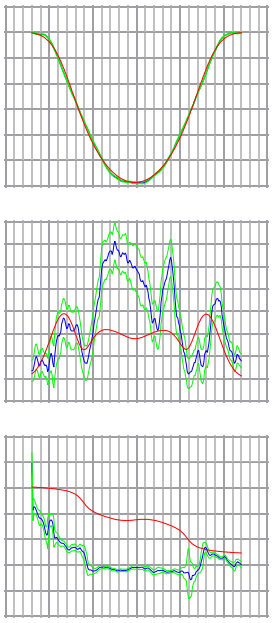

Figure 6.6: Zero-point (top row), amplitude (middle row) and phase (bottom row) diagrams of the mode identification of the HD 209295 frequency $f_1 = 1.17128$ d^{-1} as a (3,1) mode. The blue and green lines are the observed values and their uncertainties for the zero-point, amplitude and phase. The red lines are the theoretical models determined to best fit the observations.

6.4 Discussion of HD 209295

Four orbital parameters (primary radial velocity semi-amplitude, eccentricity, period and systematic velocity) of the orbital solution obtained by this thesis agree with those determined by De Cat et al. (2006a) within the given uncertainties. Additionally, this thesis's orbital solution provided a ∼50% smaller *rms* for the fit to the radial velocity data than the solution found by De Cat et al. (2006a).

A comparison of the detected frequencies for HD 209295 reveals a match between the spectroscopic frequency (1.17128 d^{-1}), the 3rd photometric frequency (1.17509 d^{-1}) and the 4th photometric frequency from Handler et al. (2002c).

The best-fitting model for the spectroscopic pulsation frequency was produced by the prograde pulsation mode (3,1), where all l values have an uncertainty of ±1 and all m values were determined unambiguously, according to Zima (2006). This mode was not detected by Handler et al. (2002c) in their analysis of HD 209295. The resulting stellar parameters were $R = 5.52\ R_\odot$, $M = 1.01\ M_\odot$ and $i = 55.8°$. The value for the stellar radius disagrees with the value $2.01^{+0.09}_{-0.16}\ R_\odot$ from the *Gaia* Data Release 2 (Gaia Collaboration et al. 2018) within its given uncertainty; although, it should be noted that the stellar mass and radius values are used during mode identification in FAMIAS to determine the ratio of the horizontal to vertical velocity of the pulsations rather than constraining the stellar parameters. The inclination implies a stellar equatorial velocity of 145 km s^{-1} from the $v \sin i$ value determined from the zero-point line profile fit (Table 6.3). This result is potentially reasonable as it suggests that the star is a rapid rotator. Additionally, the velocity amplitude of the pulsation frequency is 6.13 km s^{-1}, which is also reasonable, given the moderate inclination value.

Confirmation of HD 209295 as a γ Dor star can be obtained from both the photometric and spectroscopic frequencies. Although the first 10 detected photometric frequencies and the only detected spectroscopic frequency are in the γ Dor frequency range, there are ∼15 times as many δ Sct frequencies than γ Dor frequencies found in the light curve. This result may be due to harmonics of the orbital period (3.10571 d from this thesis) and combinations thereof which have frequencies within the δ Sct range. The ultimate conclusion of this thesis is that HD 209295 is a δ Sct/γ Dor hybrid pulsator.

7. HD 214291

This chapter details the results of the photometric and spectroscopic analyses of the target HD 214291, which is an SB2 star system with one or both components pulsating as a γ Dor star.

7.1 Photometric Frequencies

An examination of the light curve of HD 214291 revealed it is a GDORM star (as defined by Balona 2018a) due to the absence of beating in the light curve.

As for the previous two targets, the normalised TASOC and MAST light curves are identical except for the section from 1345 to 1350 TBJD which had a more significant proportion of quality-flagged data than the rest of the light curve (Figure 7.1). A comparison of the SigSpec (Reegen 2010) and FAMIAS (Zima 2006) TASOC Fourier spectra (Figure 7.2 and A.4) reveals that both spectra show similar frequency features.

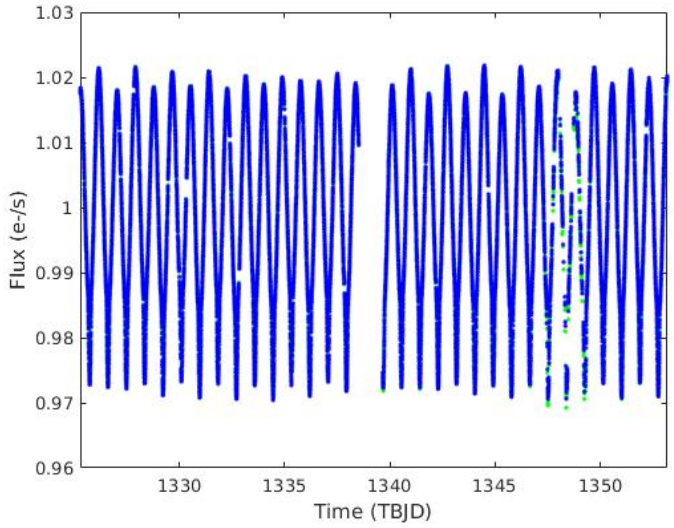

Figure 7.1: HD 214291 TASOC (blue) and MAST (green) SAP light curves normalised to a mean flux of 1 $e^{-}\,s^{-1}$.

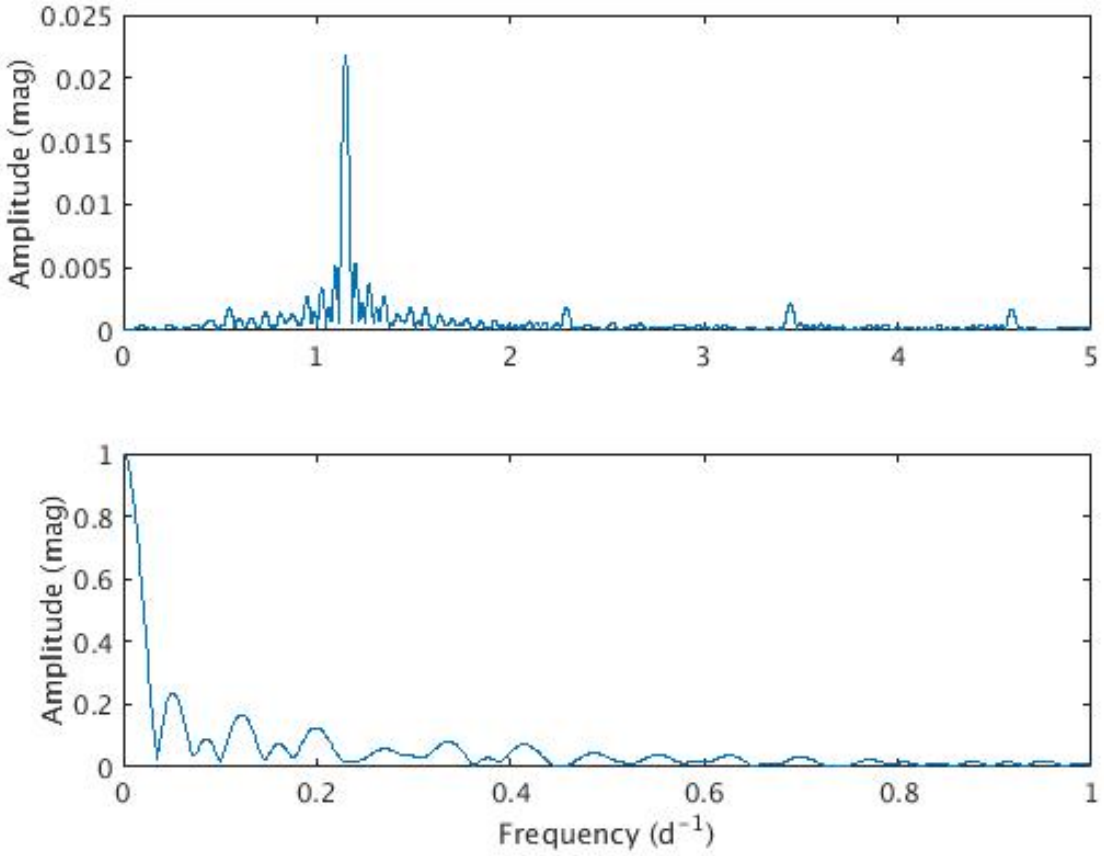

Figure 7.2: Fourier spectrum of the HD 214291 light curve from TASOC over the range 0 - 5 d^{-1}; and the corresponding spectral window, shown over the range 0 - 1 d^{-1}.

The SigSpec Fourier analysis of the TASOC light curve produced 134 significant frequencies (S/N $\geq$ 4), 37 of which are within the γ Dor frequency range and 73 are within the δ Sct frequency range (Table B.4). One aliasing event ($f_{79} + 17 \approx f_{46}$), 13 frequency combinations (Table C.4) and six frequency couplings (see the last column of Table B.4) were found within a tolerance of 0.0001 d^{-1}. Therefore, it is likely that at least 20 of the 134 detected frequencies are not independent.

Table 7.1 presents the first 10 detected frequencies from the SigSpec and FAMIAS analyses of the TASOC and MAST light curves. The order of the frequency detections for all methods are identical. Eight of the FAMIAS and MAST frequencies agree with their associated SigSpec TASOC frequency within 0.001 d^{-1}. The tenth FAMIAS frequency is the most inaccurate with a difference of 8.06181 d^{-1} between its SigSpec TASOC frequency.

The first SigSpec TASOC frequency agrees with the frequency 1.14771 d^{-1} found by Aerts et al. (1998), whereas their second frequency 0.15140 d^{-1} is similar to the 43rd SigSpec TASOC frequency or possibly an alias of f_1. However, in their paper Aerts et al. (1998) stated that the detection of this very low value frequency may have been influenced by the sampling frequency of their data. Therefore no conclusions can be drawn for this frequency. Most of the SigSpec TASOC frequencies are harmonics of the first frequency, with one possible sub-harmonic (f_9). These harmonics are confirmed by phased MAST light curves using the first four detected frequencies (Figure 7.3).

Table 7.1: First 10 detected frequencies in the TASOC and MAST light curves for HD 214291, as detected by FAMIAS and SigSpec. All frequencies are listed in the order corresponding to their match to a SigSpec TASOC frequency. All figures have been rounded to 5 d.p.

	Frequency (d^{-1})							
	TASOC				MAST		Differences	
	FAMIAS (1)		SigSpec (2)		SigSpec (3)		(1) & (2)	(2) & (3)
	f_1	1.14752	f_1	1.14784	f_1	1.14763	0.00032	0.00021
$3f_1$	f_2	3.44435	f_2	3.44369	f_2	3.44327	0.00016	0.00042
$2f_1$	f_3	2.29504	f_3	2.29506	f_3	2.29511	0.00002	0.00005
$4f_1$	f_4	4.59187	f_4	4.59119	f_4	4.59126	0.00068	0.00007
	f_5	0.54507	f_5	0.54576	f_5	0.54590	0.00069	0.00014
$5f_1$	f_6	5.73939	f_6	5.73890	f_6	5.73944	0.00049	0.00054
$6f_1$	f_7	6.88691	f_7	6.88683	f_7	6.88677	0.00008	0.00006
$7f_1$	f_8	8.03443	f_8	8.03438	f_8	8.03441	0.00005	0.00003
	f_9	0.59886	f_9	0.58797	f_9	0.58337	0.01090	0.00459
$8f_1$	f_{10}	1.120625	f_{10}	9.18244	f_{10}	9.18510	8.06181	0.00266

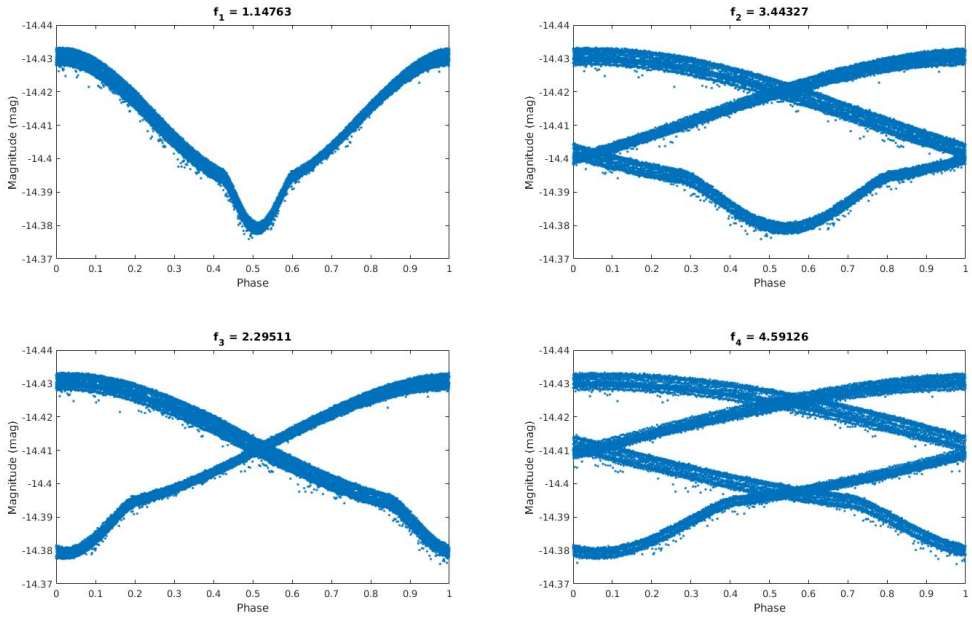

Figure 7.3: Phased MAST light curves for HD 214291 for the first four detected MAST frequencies.

7.2 Orbital Solution

Orbital information, such as the mass quotient and the orbital solution for the two binary components, were determined by calculating the ratio of each component's radial velocities and using SpecBin to optimise orbital parameters from the radial velocities measured from the CCLPs for HD 214291.

The mass quotient for this binary system was determined to be $q = 0.99142$ (Figure 7.4). This means that the primary star is more massive than the secondary star by a factor of 1.0087. The radial velocity orbit for HD 214291 is presented in Figure 7.5. The orbital solution was determined using SpecBin and has an *rms* of 1.05 $\mathrm{km\,s^{-1}}$ (Table 7.2). This value is higher than that of the solution found by De Cat et al. (2006a). The values found by this thesis for the primary and secondary semi-amplitudes agree with those determined by De Cat et al. (2006a) within their given uncertainties.

In addition, the orbital frequency is also present in the photometry as the ninth frequency. Therefore, since the first photometric frequency is twice this value, all the harmonics of the first frequency are also even harmonics of the orbital period. This confirms the ellipsoidal variability of the binary, previously detected by De Cat et al. (2006a).

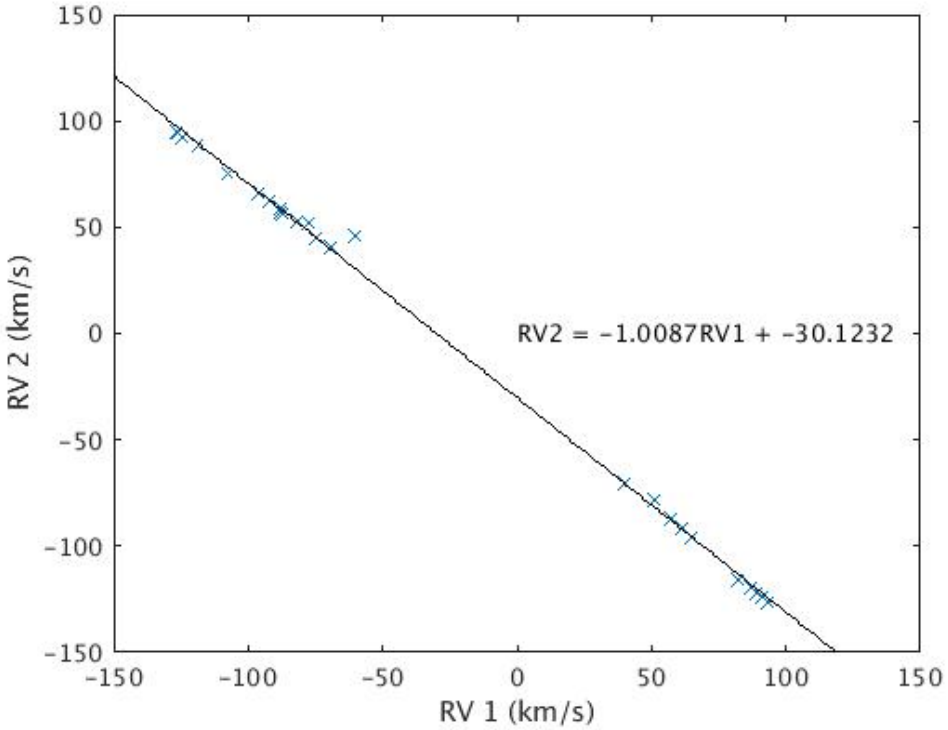

Figure 7.4: Radial velocity ratio for the components of HD 214291. The blue crosses are the radial velocity values measured from the CCLPs and the black line is the best-fitting linear trend.

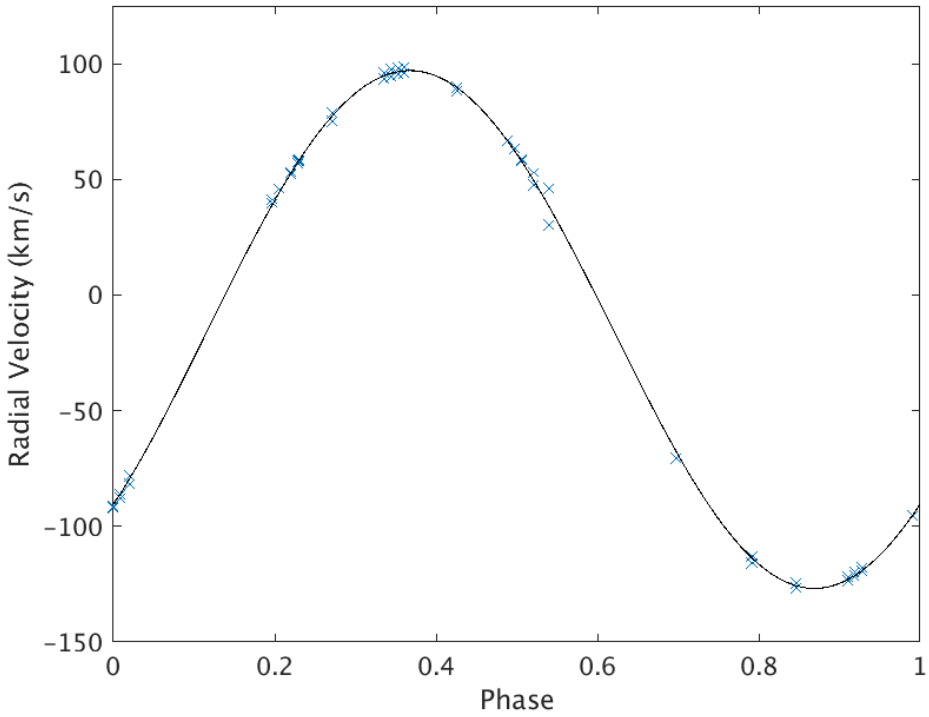

Figure 7.5: Radial velocity orbital solution for the primary component of HD 214291. The blue crosses are the phased radial velocity values and the black line is the best-fitting orbital solution from SpecBin.

Table 7.2: Radial velocity orbital parameters for HD 214291.

Parameter	This Thesis	De Cat et al. (2006a)
K_1 ($\mathrm{km\,s^{-1}}$)	110.9 ± 0.3	111 ± 14
K_2 ($\mathrm{km\,s^{-1}}$)	111.9 ± 0.3	111 ± 14
e	0.004 ± 0.006	0.0
ω (°)	38 ± 90	-
T_0 (MJD)	58682.521 ± 0.002	-
P (d)	1.74248 ± 0.00001	1.74247 ± 0.00002
γ ($\mathrm{km\,s^{-1}}$)	-14.5 ± 0.3	-13.9 ± 0.6
rms ($\mathrm{km\,s^{-1}}$)	1.05	0.67

7.3 Mode Identification

Mode identification for the components of HD 214291 was performed using 12 resolved stellar spectra. Due to the small sample of 12 resolved spectra for this binary, the expectations for the frequency detection and mode identification are low. Mode identification was performed only for the first frequency detected for each component as they had similar values. Both components required the ZAP fitting method in order to determine the best-fitting mode which also fits the zero-point profile.

7.3.1 Component 1 (Primary)

The zero-point line profile was fitted to determine the pulsation-independent line parameters. The zero-point profile for the primary component of HD 214291 was determined using FAMIAS to have a χ^2 value of 5.24 (Table 7.3). This value indicates a good fit which is clear from Figure 7.6 where the theoretical zero-point profile does not deviate significantly from the observed zero-point at any point along the line profile. The $v \sin i$ value found from the zero-point profile fit does not agree with the value 67.6 ± 0.8 km s^{-1} determined by De Cat et al. (2006a).

Table 7.3: The corresponding parameters of the zero-point line profile for the primary component of HD 214291. All values have been rounded to 3 s.f.

Parameter	Value
$v \sin i$ (km s^{-1})	66.7
Equivalent width (km s^{-1})	7.22
Intrinsic width (km s^{-1})	7.44
Velocity offset (km s^{-1})	-0.269
χ^2	5.24

The PBP technique within FAMIAS in conjunction with individual and simultaneous mode identification was used to determine the dominant spectroscopic frequencies and their best-fitting modes of pulsation.

The frequency detection for this component revealed two possible significant frequencies: 0.50171 and 9.23445 d^{-1}. Neither of these frequencies are present in the frequencies detected by Aerts et al. (1998); although, given the poor resolution of the spectroscopic frequencies, these frequencies are potential matches to the 9$^{\text{th}}$ and 10$^{\text{th}}$ SigSpec TASOC photometric frequencies.

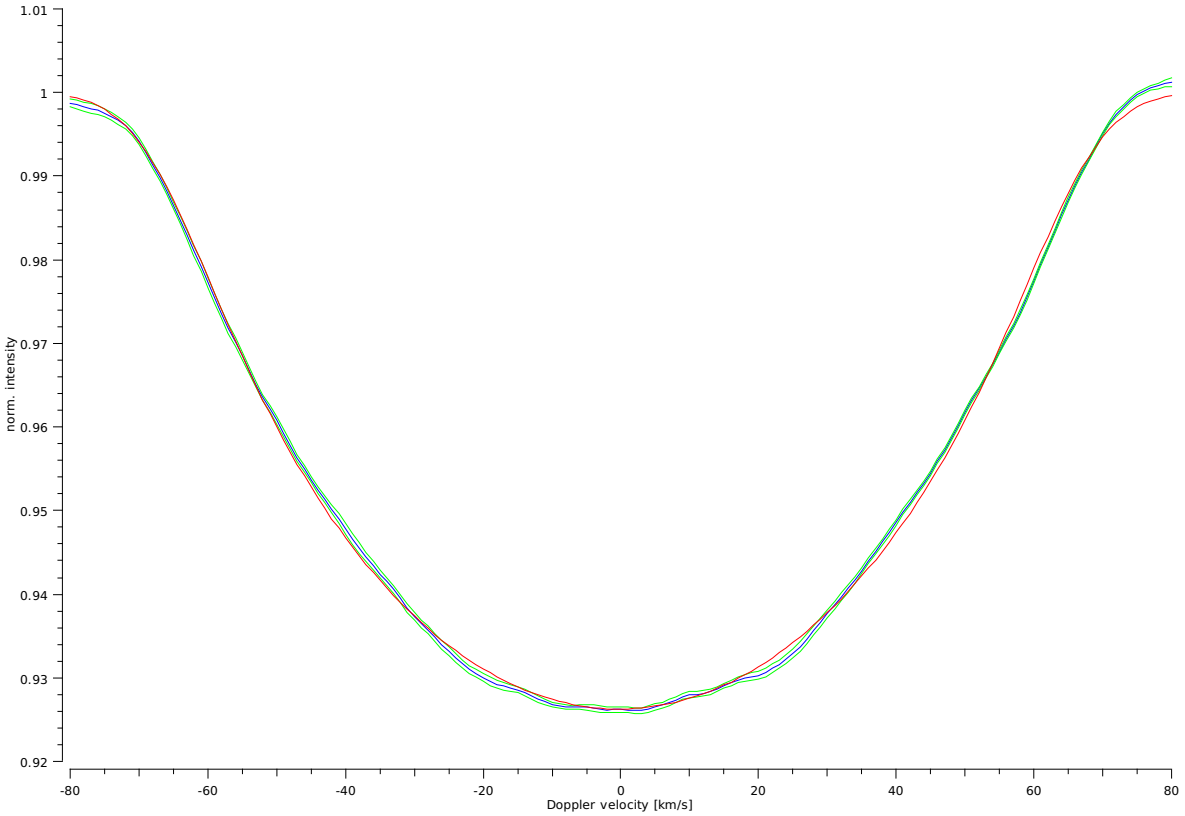

Figure 7.6: The zero-point line profile for the primary component of HD 214291. The green and red lines indicate the observed zero-point line profile and the best-fitting theoretical model, respectively.

Mode identification was performed for the first frequency. Two possible modes were found, (2,1) and (1,1), which both indicate a prograde pulsation. Despite their close χ^2 values, these modes were fit with very different stellar and pulsation parameters (Table 7.4). The amplitude variations for the spectroscopic frequency are asymmetric and show an off-centre main amplitude peak, which neither of the modes fits (Figure 7.7). f_1 was found to be a (1,1) mode due to its marginally better amplitude and phase fits.

Table 7.4: Parameters obtained from the mode identification of the individual pulsation frequency $f_1 = 0.50171$ d^{-1} for Component 1 of HD 214291 as a (2,1) and (1,1) mode. All values except the frequency have been rounded to 3 s.f.

Parameters	Frequency (d^{-1}) f_1 0.50171	
Radius ($R_\odot$)	9.08	9.86
Mass ($M_\odot$)	1.35	7.24
Inclination (°)	87.0	31.1
Mode (l,m)	(2,1)	(1,1)
Vel. Amp. (km s^{-1})	13.5	1.29
Phase	0.236	0.425
χ^2	3.21	3.21

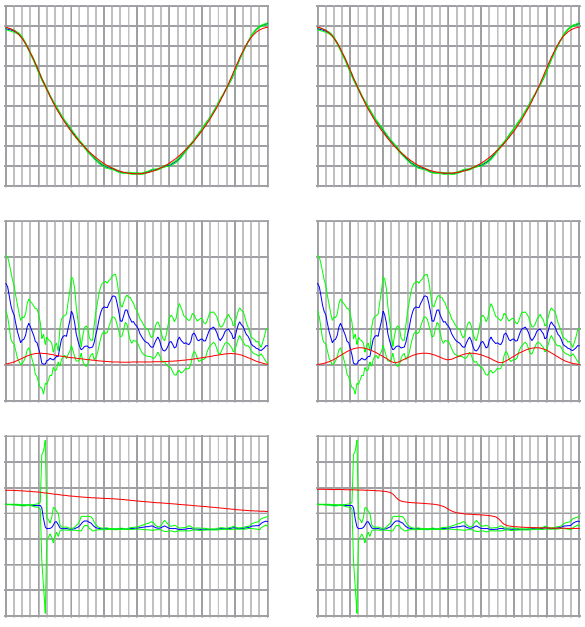

(a) (b)

Figure 7.7: Zero-point (top row), amplitude (middle row) and phase (bottom row) diagrams of the mode identification of the HD 214291 Component 1 frequency $f_1 = 0.50171$ d^{-1} as (a) a (2,1) mode and (b) a (1,1) mode. The blue and green lines are the observed values and their uncertainties for the zero-point, amplitude and phase. The red lines are the theoretical models determined to best fit the observations.

7.3.2 Component 2 (Secondary)

The zero-point line profile was fitted to determine the pulsation-independent line parameters. The zero-point profile for the secondary component of HD 214291 was determined using FAMIAS to have a χ^2 value of 2.18 (Table 7.5), which indicates a good fit. This is clear from Figure 7.8, where the theoretical zero-point does not deviate significantly from the observed zero-point at any point along the line profile. The $v \sin i$ value found from the zero-point profile fit agrees with the value 64.7 ± 0.7 km s^{-1} determined by De Cat et al. (2006a).

Table 7.5: The corresponding zero-point line profile parameters for the secondary component of HD 214291. All values have been rounded to 3 s.f.

Parameter	Value
$v \sin i$ (km s^{-1})	64.2
Equivalent width (km s^{-1})	6.90
Intrinsic width (km s^{-1})	7.08
Velocity offset (km s^{-1})	0.269
χ^2	2.18

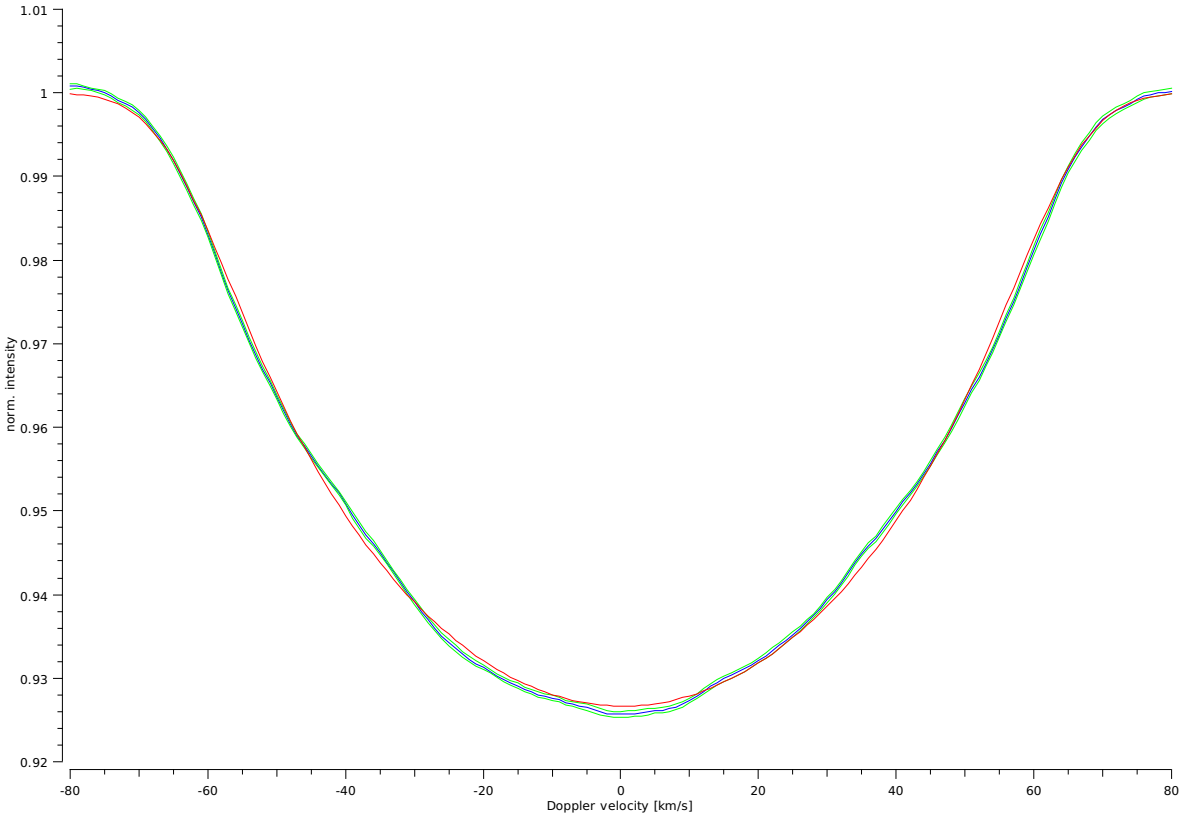

Figure 7.8: The zero-point line profile for the secondary component of HD 214291.

The PBP technique within FAMIAS in conjunction with individual and simultaneous mode identification was used to determine the dominant spectroscopic frequencies and their best-fitting modes of pulsation.

The frequency detection for this component revealed two possible significant frequencies: 0.50076 and 3.76593 d^{-1}. Neither of these frequencies are present in the SigSpec TASOC photometric frequencies or the frequencies detected by Aerts et al. (1998); although, given the poor resolution of the spectroscopic frequencies, the first frequency is a potential match to the 9th SigSpec TASOC photometric frequency.

Mode identification was performed for the first frequency. Two possible modes were found: (3,-3) and (3,-2). These retrograde pulsation modes indicate that the pulsation frequency $f_1 = 0.50076$ d^{-1} of the secondary star is not caused by the same pulsation in the primary star which produces the spectroscopic frequency $f_1 = 0.50171$ d^{-1} detected in this work. Despite their close χ^2 values, the (3,-3) and (3,-2) modes were fit with very different stellar and pulsation parameters except for the phase value (Table 7.6). The phase variations are fit similarly by both modes. f_1 is possibly a (3,-2) mode due to its marginally better fit to the minimally symmetric amplitude variations (Figure 7.9).

Table 7.6: Parameters obtained from the mode identification of the individual pulsation frequency $f_1 = 0.50076$ d^{-1} for Component 2 of HD 214291 as a (3,-3) and (3,-2) mode. All values except the frequency have been rounded to 3 s.f.

	Frequency (d^{-1})	
Parameters	f_1 0.50076	
Radius ($R_\odot$)	5.89	9.86
Mass ($M_\odot$)	1.57	5.46
Inclination (°)	73.8	80.2
Mode (l,m)	(3,-3)	(3,-2)
Vel. Amp. ($km\,s^{-1}$)	1.94	5.16
Phase	0.299	0.291
χ^2	5.94	5.96

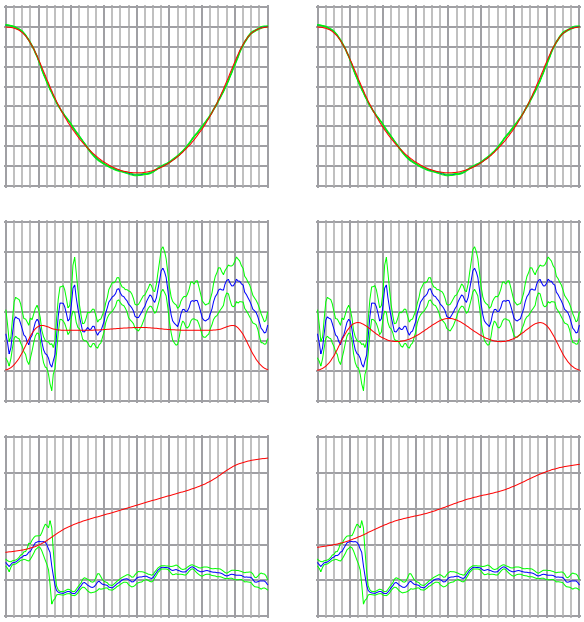

(a) (b)

Figure 7.9: Zero-point, amplitude and phase diagrams of the mode identification of the HD 214291 Component 2 frequency $f_1 = 0.50076$ d^{-1} as (a) a (3,-3) mode and (b) a (3,-2) mode.

7.4 Discussion of HD 214291

Five orbital parameters (primary and secondary radial velocity semi-amplitudes, eccentricity, period and systematic velocity) of the orbital solution obtained by this thesis agree with the values determined by De Cat et al. (2006a) within the given uncertainties. The orbital solution from this thesis had a higher *rms* value than that of the solution by De Cat et al. (2006a).

The solution obtained by De Cat et al. (2006a) also provides values for the separation of the binary components: $a_1 \sin i = a_2 \sin i = 0.018 \pm 0.002$ A. This is similar to the value $a_1 \sin i = 0.01426 \pm 0.00008$ AU found for HD 209295, which indicates that pulsations in HD 214291 may also be tidally-excited. This hypothesis is supported by the eight even harmonics of the orbital period which are present in the first 10 detected photometric frequencies. None of the detected spectroscopic frequencies for either component match any of these harmonics.

The final pulsation modes of the dominant detected spectroscopic frequencies of 0.50171 and 0.50076 d^{-1} for the primary and secondary components were (1,1) and (3,-2), where all l values have an uncertaint ofy of ± 1 and all m values were determined unambiguously, according to Zima (2006). Since these are prograde and retrograde pulsations respectively, they must be produced by different pulsations despite having similar pulsation frequencies (0.50171 and 0.50076 d^{-1}). Despite Handler et al. (2002c) stating that tidally-induced oscillations which produce frequencies of exact multiples of the orbital frequency are most likely produced by $l = 2$, $|m| = 2$ modes, no (2,$\pm$2) mode was detected in the spectra.

For the primary component, the resulting stellar parameters were $R = 9.08\ R_\odot$, $M =$

1.35 $M_{\odot}$, and $i = 87.0°$. The value for the stellar radius does not agree with the value $3.77^{+0.1}_{-0.1}$ $R_{\odot}$ from the *Gaia* Data Release 2 (Gaia Collaboration et al. 2018) within its given uncertainty; although, it should be noted that the stellar mass and radius values are used during mode identification in FAMIAS to determine the ratio of the horizontal to vertical velocity of the pulsations rather than constraining the stellar parameters. The inclination implies a stellar equatorial velocity of 66.8 km s^{-1} from the $v \sin i$ found by this thesis (Table 7.3). This result is reasonable as it suggest that the primary component is a moderate rotator. Despite the high inclination value, the velocity amplitude of the (1,1) pulsation is also high (13.5 km s^{-1}); however this result is plausible if the pulsation is tidally-induced, as other evidence has already suggested.

For the secondary component, the resulting stellar parameters were $R = 5.89$ $R_{\odot}$, $M = 1.57$ $M_{\odot}$, and $i = 73.8°$. The value for the stellar radius does not agree with the value $3.77^{+0.1}_{-0.1}$ $R_{\odot}$ from the *Gaia* Data Release 2 (Gaia Collaboration et al. 2018) within its given uncertainty; although, it should be noted that the stellar mass and radius values are used during mode identification in FAMIAS to determine the ratio of the horizontal to vertical velocity of the pulsations rather than constraining the stellar parameters. The inclination implies a stellar equatorial velocity of 66.9 km s^{-1} from the $v \sin i$ found by this thesis (Table 7.5). This result is reasonable as it suggest that, like the primary, the secondary component is a moderate rotator. Contrary to the result for the primary, the velocity amplitude of the (3,-2) is small (1.94 km s^{-1}). Due to the small separation of the binary system, if both stars are of similar spectral type (i.e. both F-type stars) then both components would be expected to exhibit tidally-induced pulsations, as is the case for the primary component. As the detected spectroscopic frequency for the secondary component has a velocity amplitude approximately seven times smaller than that of the pulsation in the primary component, it is likely that the detected frequency 0.50076 d^{-1} is not a pulsation frequency.

Confirmation of the components as γ Dor stars is dependent on the resolved spectral data, as the photometric data is obtained from the observation of the entire binary system. Both stars have one γ Dor and one δ Sct frequency detected in their spectra, with the γ Dor frequency as the more significant frequency. Although there is approximately an equal number of frequencies from each pulsator class in the first 10 detected photometric frequencies, there are twice as many δ Sct frequencies as γ Dor frequencies found in the system's light curve. This indicates that each component is a γ Dor/δ Sct or δ Sct/γ Dor hybrid pulsator. However, the velocity amplitude of the dominant spectroscopic frequency for the secondary star suggests an origin other than pulsation. Additionally, a comparison of the UV fluxes for HD 214291 and HD 209295 (whose dark companion is suspected to be degenerate) reveals that the UV flux of HD 214291 is the same magnitude in the 1565, 2365 and 2740 Å bands as HD 209295 and one magnitude smaller in the 1965 Å band (Thompson et al. 1978). This suggests that the secondary component of HD 214291 could be degenerate. Confirmation of this hypothesis is beyond the scope of this thesis.

8. HD 216910

This chapter details the results of the photometric and spectroscopic analyses of the target HD 216910, which is a single γ Dor star.

8.1 Photometric Frequencies

A preliminary examination of the light curve of HD 216910 revealed that it is most likely a GDORS star (as defined by Balona 2018a) as the majority of the light curve shows symmetric maxima and minima in brightness, with the exception of the section between 1335 and 1340 TBJD.

As for the previous three targets, the normalised TASOC and MAST light curves are identical except for the section between 1345 and 1350 TBJD which had a more significant proportion of quality-flagged data compared to the rest of the light curve (Figure 8.1). A comparison of the SigSpec (Reegen 2010) and FAMIAS (Zima 2006) TASOC Fourier spectra (Figure 8.2 and A.5) determined that both spectra show similar frequency features.

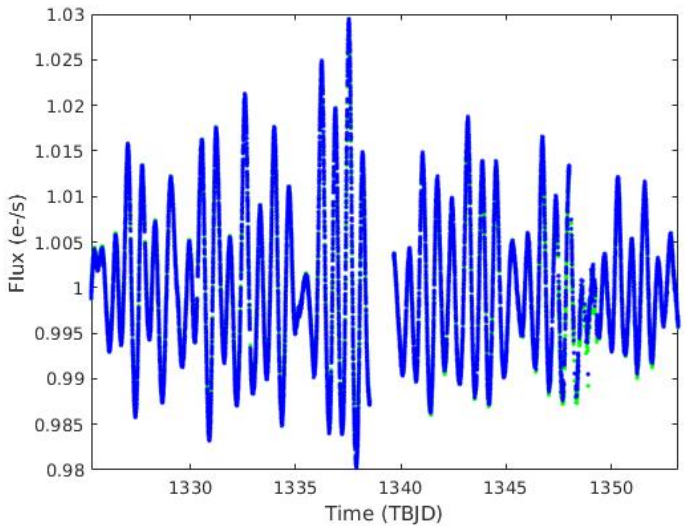

Figure 8.1: HD 216910 TASOC (blue) and MAST (green) SAP light curves normalised to a mean flux of 1 $e^{-}\,s^{-1}$.

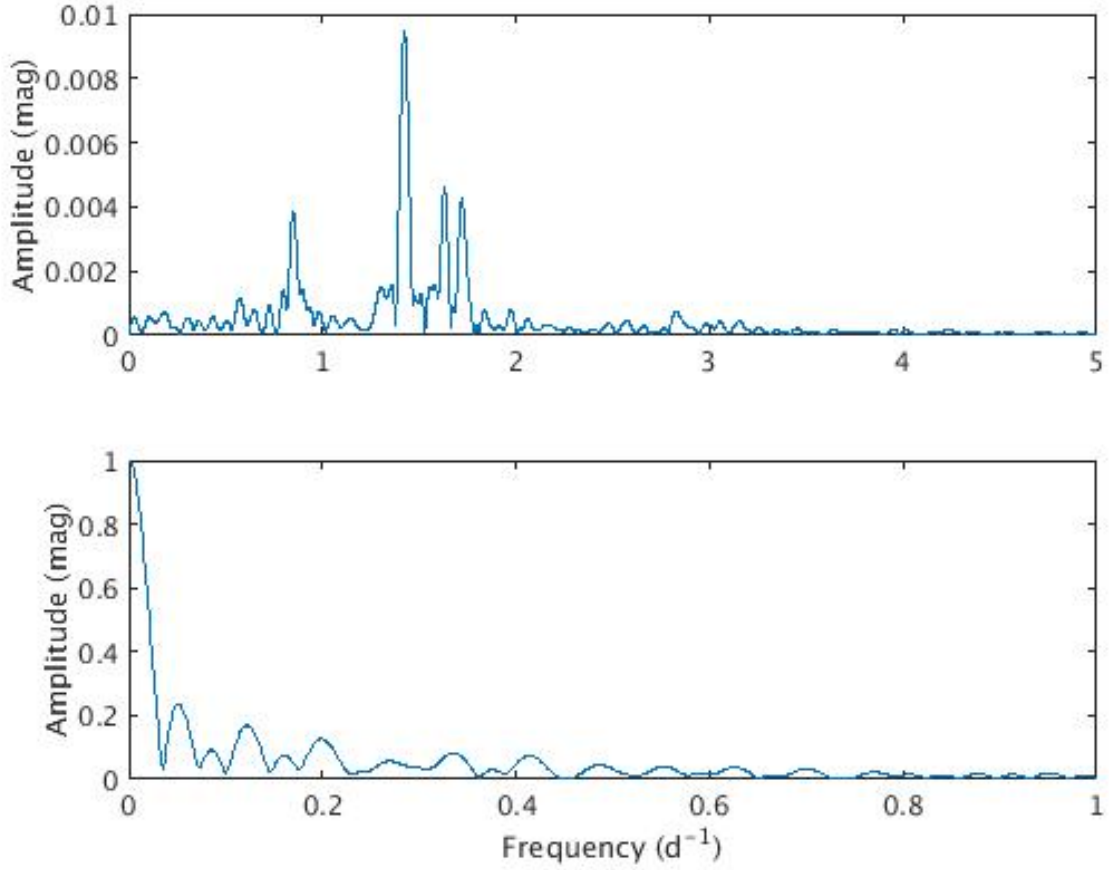

Figure 8.2: Fourier spectrum of the HD 216910 light curve from TASOC over the range 0–5 d^{-1} (top); and the corresponding spectral window, shown over the range 0–1 d^{-1} (bottom).

The SigSpec Fourier analysis of the TASOC light curve produced 126 significant frequencies (S/N $\geq$ 4), 40 of which are within the γ Dor frequency range and 54 are within the δ Sct frequency range (Table B.5). Nine frequency combinations (Table C.5) and one frequency coupling (see the last column of Table B.5) were found within a tolerance of 0.0001 d^{-1}. Therefore, it is likely that at least 10 of the 126 detected frequencies are not independent.

Table 8.1 presents the first 10 detected frequencies from the SigSpec and FAMIAS analyses of the TASOC and MAST light curves. The order of the SigSpec TASOC and MAST frequencies are identical, whereas the order of the FAMIAS frequencies is mixed. One of the FAMIAS frequencies matches its associated SigSpec TASOC frequency within 0.001 d^{-1} compared to three of the MAST frequencies which match their associated frequency within 0.001 d^{-1}. The 4$^{\text{th}}$ and 5$^{\text{th}}$ SigSpec TASOC frequencies agree with the frequencies 1.44196 and 1.62973 d^{-1} found by Aerts et al. (1998) from a *Hipparcos* light curve. A phased MAST light curve for the first detected MAST frequency 1.40754 d^{-1} (Figure 8.3) confirms that the frequency produces periodic sinusoidal effects in the light curve of HD 216910.

Table 8.1: First 10 detected frequencies in the TASOC and MAST light curves for HD 216910, as detected by FAMIAS and SigSpec. All frequencies are listed in the order corresponding to their match to a SigSpec TASOC frequency. All figures have been rounded to 5 d.p.

Frequency (d^{-1})							
TASOC				MAST		Differences	
FAMIAS (1)		SigSpec (2)		SigSpec (2)		(1) & (2)	(2) & (3)
f_6	1.39137	f_1	1.40590	f_1	1.40754	0.01454	0.00163
f_2	1.72128	f_2	1.72431	f_2	1.72256	0.00303	0.00174
f_3	0.85168	f_3	0.85547	f_3	0.84615	0.00380	0.00932
f_4	1.62984	f_4	1.62917	f_4	1.62952	0.00067	0.00035
f_5	1.45950	f_5	1.44129	f_5	1.44222	0.01822	0.00093
f_7	1.56708	f_6	1.57015	f_6	1.57133	0.00307	0.00117
f_8	0.88036	f_7	0.87546	f_7	0.89469	0.00491	0.01923
f_9	1.32682	f_8	1.31019	f_8	1.31000	0.01663	0.00018
f_1	1.42364	f_9	0.53448	f_9	0.57355	0.88916	0.03907
f_{10}	1.36089	f_{10}	0.29213	f_{10}	0.29976	1.06876	0.00763

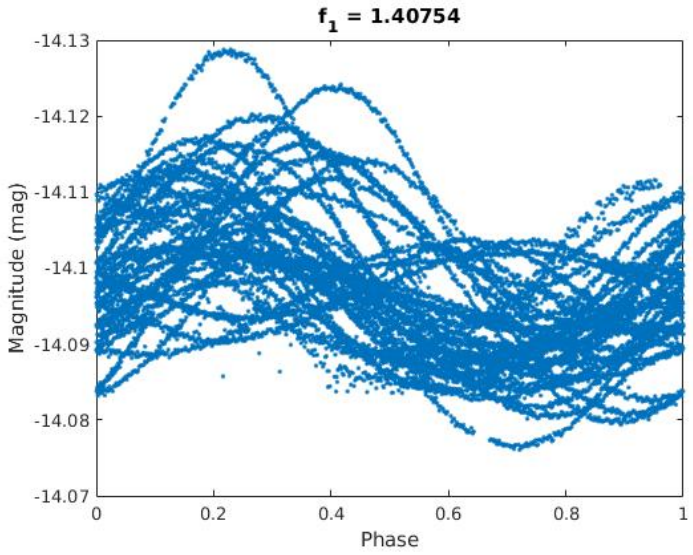

Figure 8.3: Phased MAST light curve for HD 216910 for the first detected MAST frequency, $f_1 = 1.40754$ d^{-1}.

8.2 Mode Identification

Mode identification for HD 216910 was performed using 156 stellar spectra.

The zero-point line profile was fitted to determine the pulsation-independent line parameters. The zero-point line profile was fitted to determine the pulsation-independent line parameters. The zero-point profile for HD 216910 was determined using FAMIAS to have a χ^2 value of 22.1 (Table 8.2). This value indicates a reasonable fit, which is clear from Figure 8.4 where the theoretical zero-point profile does not deviate significantly from the observed zero-point line profile. The $v \sin i$ value found from the zero-point profile fit agrees with the value 92 ± 3 km s^{-1} determined by De Cat et al. (2006a) and 95 ± 4 km s^{-1} determined by Kahraman Aliçavuş et al. (2016).

Table 8.2: The corresponding parameters for the zero-point line profile of HD 216910. All values have been rounded to 3 s.f.

Parameter	Value
$v \sin i$ (km s^{-1})	93.6
Equivalent width (km s^{-1})	11.6
Intrinsic width (km s^{-1})	8.87
Velocity offset (km s^{-1})	2.37
χ^2	22.1

The PBP technique within FAMIAS in conjunction with individual and simultaneous mode identification was used to determine the dominant spectroscopic frequencies and their best-fitting modes of pulsation.

The frequency detection revealed five possible significant frequencies: 1.62960, 1.71208, 2.40211, 1.43907 and 0.26596 d^{-1}. This result disagrees with the conclusion from De Cat et al. (2006a) that the frequencies detected by Aerts et al. (1998) were not present in the spectra, as up to four of the spectroscopic frequencies (with one as a possible alias) are identified in the first 10 detected photometric frequencies of this thesis, including the two frequencies from Aerts et al. (1998).

Mode identification was performed for each of the frequencies, where 1–2 different modes were detected with similar χ^2 values (Table 8.3). For most of the frequencies, the amplitude variations are symmetric and the phase variations decrease across the line profile.

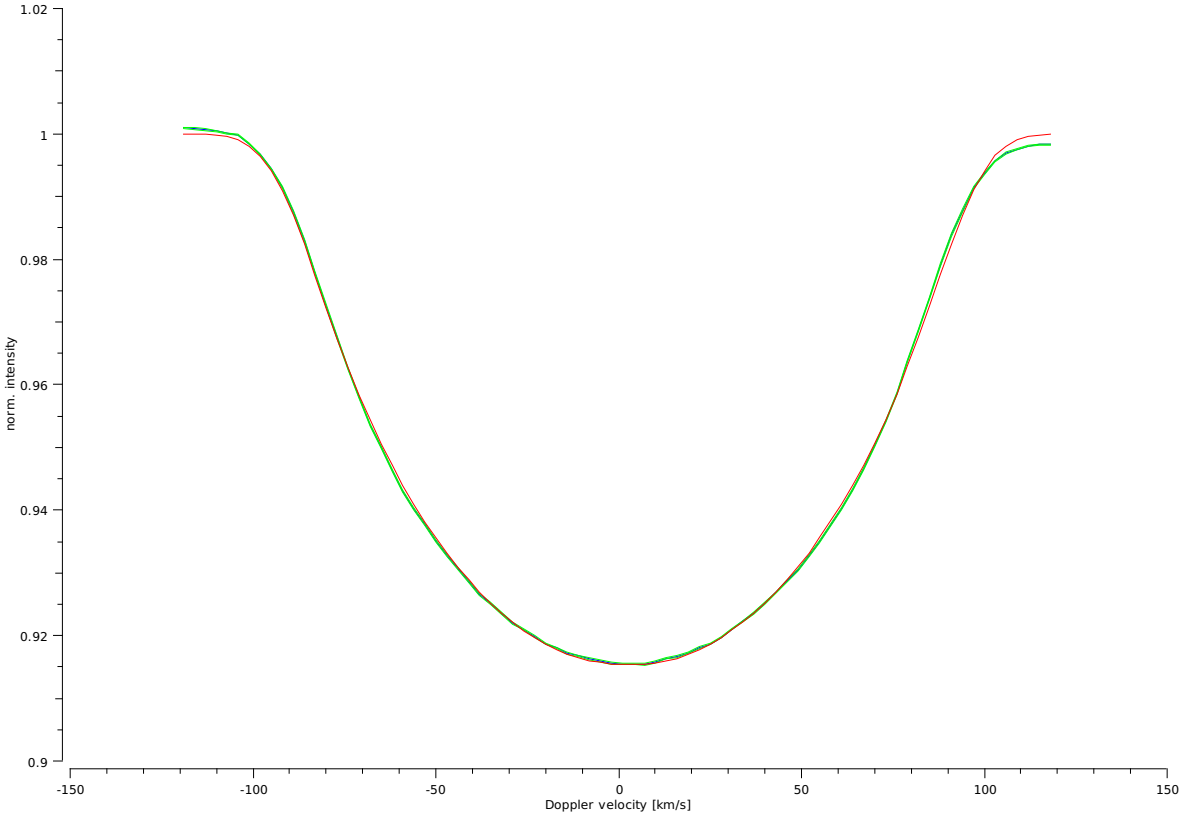

Figure 8.4: The zero-point line profile for HD 216910. The green and red lines indicate the observed zero-point line profile and the best-fitting theoretical model, respectively.

Table 8.3: Parameters obtained from the mode identification of each individual pulsation frequency for HD 216910. All values except frequencies have been rounded to 3 s.f.

	Frequencies (d^{-1})					
Parameters	f_1 1.62960	f_2 1.71208	f_3 2.40211	f_4 1.43907	f_5 0.26596	
Radius ($R_\odot$)	5.17	4.26	3.32	5.50	6.32	9.64
Mass ($M_\odot$)	1.94	1.02	1.11	1.69	8.38	8.35
Inclination (°)	49.1	50.2	49.1	53.2	18.8	88.5
Mode (l,m)	(3,0)	(3,0)	(3,0)	(3,0)	(3,-3)	(1,0)
Vel. Amp. ($km\,s^{-1}$)	10.3	7.74	7.74	7.74	7.10	8.39
Phase	0.150	0.189	0.0315	0.134	0.504	0
χ^2	2.10	1.111	4.12	1.86	3.09	3.09

The first four frequencies were all found to be (3,0) modes. The amplitude variations for f_1 are the most symmetric of the five frequencies (Figure 8.5). f_2 exhibits slight asymmetries in the amplitude variations as the two peaks in amplitude have different heights (Figure 8.6). f_3 shows the most asymmetry of all the frequencies with the amplitude variations in the centre of the line profile are skewed towards positive velocity (Figure 8.7). This asymmetry explains why this frequency has the highest χ^2 value of 4.12, as the theoretical models used by FAMIAS assume amplitude variations symmetric about zero radial velocity.

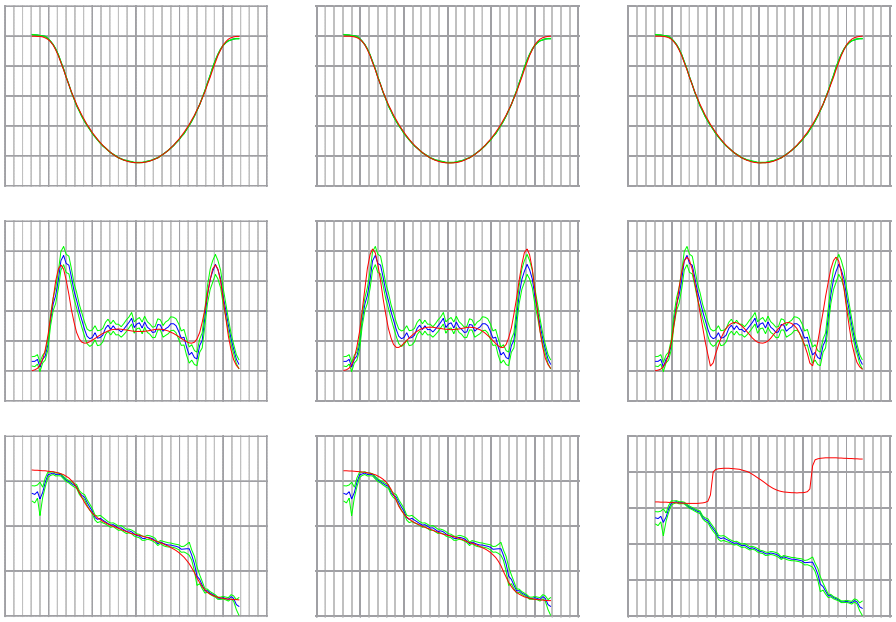

(a) (b) (c)

Figure 8.5: Zero-point (top row), amplitude (middle row) and phase (bottom row) diagrams of the mode identification of the HD 216910 frequency $f_1 = 1.62960$ d^{-1} (a) individually; and (b) simultaneously with the other frequencies with f_5 as a (3,-3) mode; and (c) as a (1,0) mode. The blue and green lines are the observed values and their uncertainties for the zero-point, amplitude and phase. The red lines are the theoretical models determined to best fit the observations.

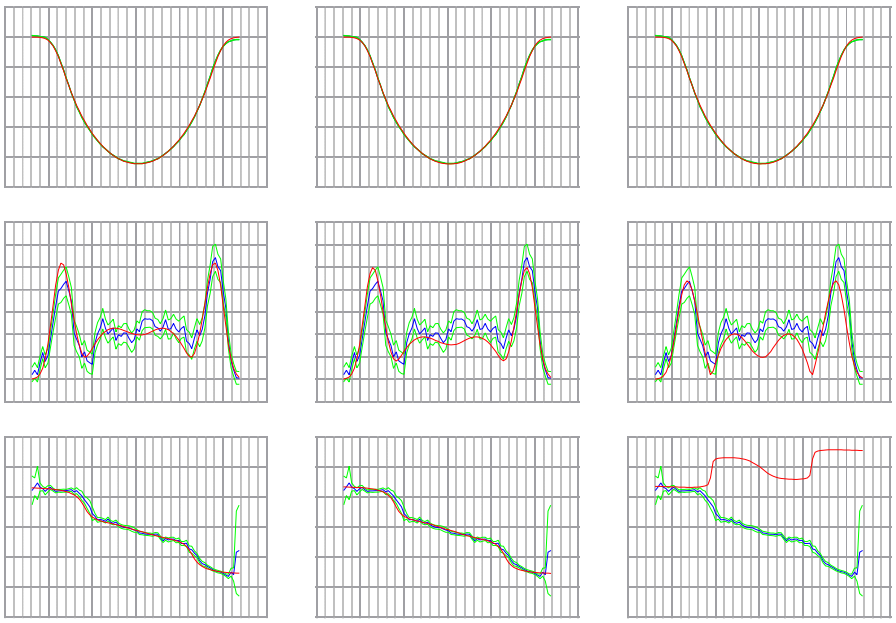

(a) (b) (c)

Figure 8.6: Zero-point, amplitude and phase diagrams of the mode identification of the HD 216910 frequency $f_2 = 1.71208$ d^{-1} (a) individually; and simultaneously with the other frequencies with f_5 as (b) a (3,-3) mode; and (c) as a (1,0) mode.

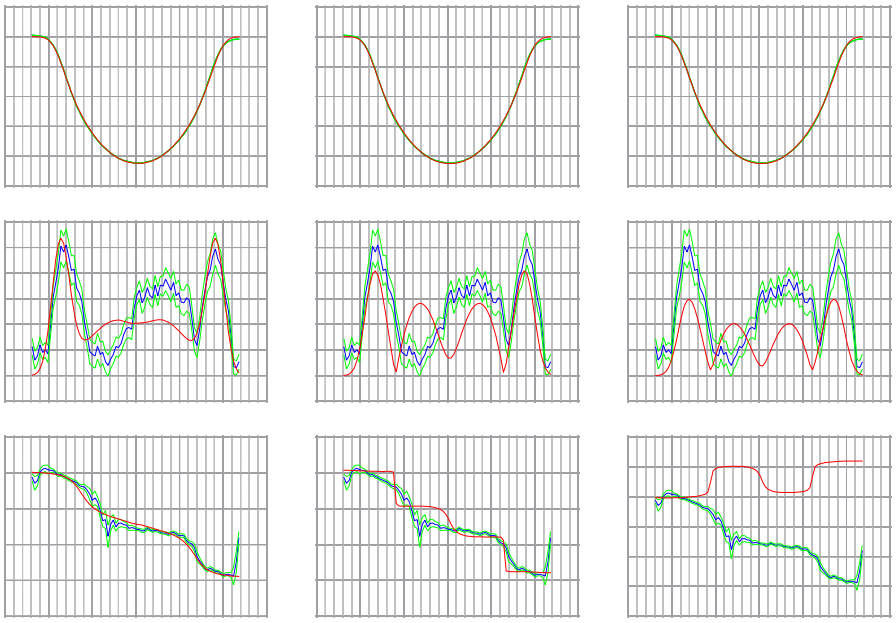

(a) (b) (c)

Figure 8.7: Zero-point, amplitude and phase diagrams of the mode identification of the HD 216910 frequency $f_3 = 2.40211$ d^{-1} (a) individually; and simultaneously with the other frequencies with f_5 as (b) a (3,-3) mode; and (c) as a (1,0) mode.

The amplitude and phase variations for f_4 are fit reasonably well, despite the 2π offset of the models from the observed phase variations (Figure 8.8).

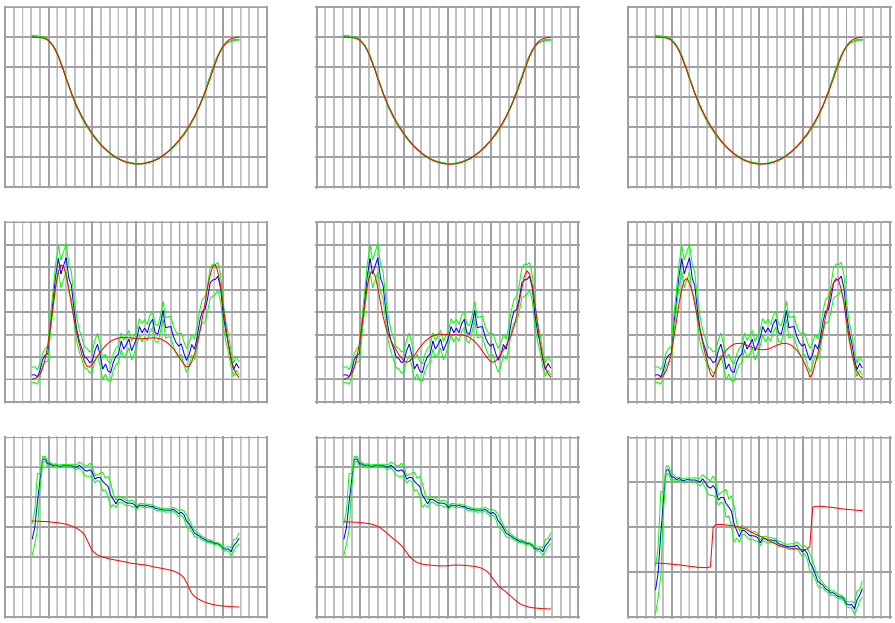

(a) (b) (c)

Figure 8.8: Zero-point, amplitude and phase diagrams of the mode identification of the HD 216910 frequency $f_4 = 1.43907$ d^{-1} (a) individually; and simultaneously with the other frequencies with f_5 as (b) a (3,-3) mode; and (c) as a (1,0) mode.

For f_5, two possible modes were found: (3,-3) or (1,0). Despite its slightly lower χ^2 value, the (3,-3) mode provides a worse fit to the observed amplitude variations than the (1,0) mode (Figure 8.9). However, ignoring the phase offset, the (1,0) mode provides a worse fit for both the zero-point profile and the phase variations.

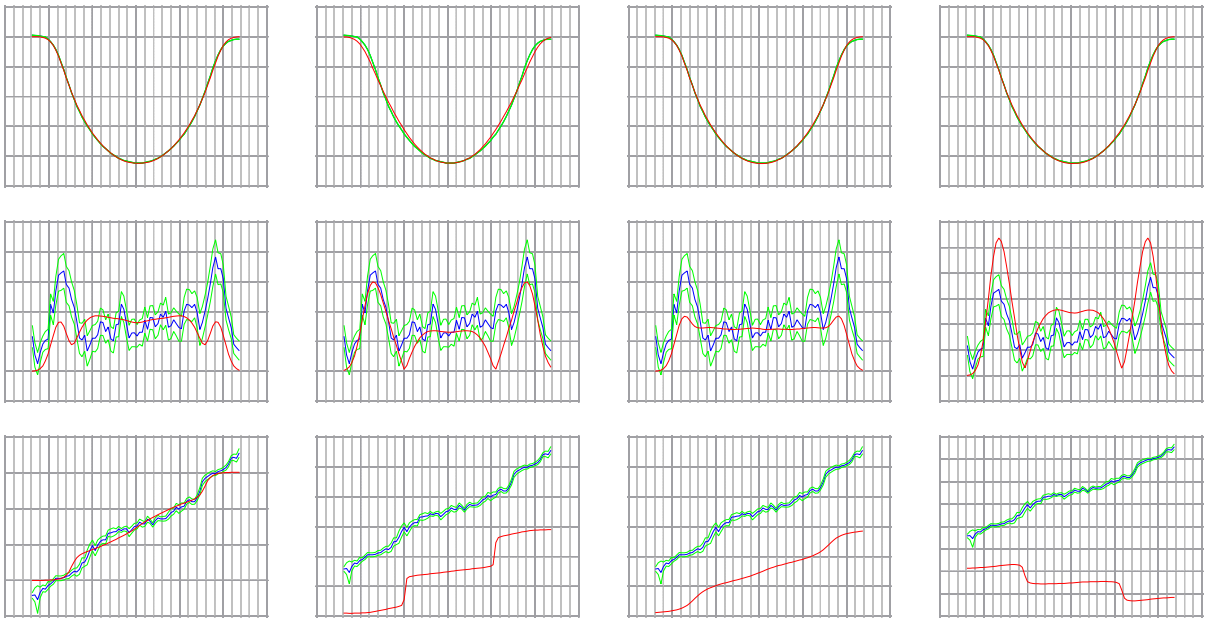

(a) (b) (c) (d)

Figure 8.9: Zero-point, amplitude and phase diagrams of the mode identification of the HD 216910 frequency $f_5 = 0.26596$ d^{-1} individually as (a) a (3,-3) mode and (b) a (1,0) mode; and simultaneously with the other frequencies with f_5 as (c) a (3,-3) mode and (d) a (1,0) mode.

A simultaneous mode identification of all five frequencies was performed twice with $f_1, f_2, f_3, f_4 = (3,0)$ and $f_5 = (3,-3)$ or $f_5 = (1,0)$. These models are presented in Table 8.4. The model with $f_5 = (3,-3)$ was determined to have a lower χ^2 value, which is clear from the comparison of the amplitude and phase fits for the five individual frequencies (last two columns of Figures 8.5–8.9). This model gives an inclination of 50.8° which implies a stellar rotational velocity of 121 km s^{-1} using the value of $v \sin i$ determined from the zero-point line profile. Therefore the simultaneous mode identification with $f_5 = (3,-3)$ was determined to be the best model for the spectroscopic pulsation frequencies of HD 216910.

Table 8.4: Parameters obtained from the simultaneous mode identification of all frequencies for HD 216910 for the two cases where f_5 is a (3,-3) mode or a (1,0) mode. All values except frequencies have been rounded to 3 s.f.

	Stellar Parameters			Frequency (d^{-1})					
	Radius ($R_\odot$)	Mass ($M_\odot$)	Inclination (°)	Pulsation Parameters	f_1 1.62960	f_2 1.71208	f_3 2.40211	f_4 1.43907	f_5 0.26596	χ^2
$f_5 = (3, -3)$	5.50	2.26	50.8	Mode	(3,0)	(3,0)	(3,0)	(3,0)	(3,-3)	3.89
				Vel. Amp. ($km\,s^{-1}$)	12.3	7.74	7.74	6.45	1.94	
				Phase	0.142	0.197	0.0709	0.110	0.496	
$f_5 = (1, 0)$	5.50	1.23	56.8	Mode	(3,0)	(3,0)	(3,0)	(3,0)	(1,0)	6.19
				Vel. Amp. ($km\,s^{-1}$)	14.2	8.39	6.45	7.74	0.645	
				Phase	0.134	0.228	0.0394	0.142	0.00	

8.3 Discussion of HD 216910

A comparison of the detected photometric and spectroscopic frequencies for HD 216910 reveals that there is one clear match (1.62917 and 1.62960 d^{-1}), two potential matches (1.72431 and 1.71208 d^{-1}; 1.44129 and 1.43907 d^{-1}) and one potential alias (1.40590 and 2.40211 d^{-1}).

A simultaneous mode identification of the five spectroscopic frequencies was performed successfully. The best-fitting model was produced by the pulsation modes (3,0) for four frequencies and (3,-3) for the last frequency, where all l values have an uncertainty of ± 1 and all m values were determined unambiguously, according to Zima (2006).

The resulting stellar parameters were $R = 5.50\ R_\odot$, $M = 2.26\ M_\odot$ and $i = 50.8°$. The value for the stellar radius disagrees with the value $1.95^{+0.14}_{-0.08}\ R_\odot$ from the *Gaia* Data Release 2 (Gaia Collaboration et al. 2018) within its given uncertainty; although, it should be noted that the stellar mass and radius values are used during mode identification in FAMIAS to determine the ratio of the horizontal to vertical velocity of the pulsations rather than constraining the stellar parameters. The inclination implies a stellar equatorial velocity of 121 $\mathrm{km\,s^{-1}}$ from the $v \sin i$ value determined from the zero-point line profile fit (Table 8.2). This result is reasonable as it suggests that the star is a moderately rapid rotator.

Confirmation of HD 216910 as a γ Dor star can be obtained from both the photometric and spectroscopic frequencies. The first 10 photometric frequencies and the five spectroscopic frequencies are in the γ Dor range, therefore the star is definitely a γ Dor pulsator. Contrary to this result, there are $\sim$1.4 times as many δ Sct frequencies as γ Dor frequencies found in the light curve. This indicates that HD 216910 is potentially a γ Dor/δ Sct hybrid pulsator.

9. MUSICIAN Overview

The purpose of this MUSICIAN program overview is to produce preliminary results and global properties for the γ Dor candidates in the program.

The MUSICIAN program consists of 98 southern stars of various variable star classes, of which the majority are (candidate) γ Dor stars. Of these stars, 38 have been observed during the first year of TESS observations of the southern ecliptic hemisphere (Sectors 1–13). Of these, only 30 had light curves available from MAST and luminosity and effective temperature measurements available from the second *Gaia* data release. This set of 30 stars, listed in Table 9.1, comprises the sample used for this overview and will hereafter be known as the MUSICIAN sample.

9.1 H-R Diagram

Classifications from the SIMBAD database (Wenger et al. 2000) and $T_{\rm eff}$ and luminosity values from *Gaia* (Gaia Collaboration et al. 2018) were used to present the known variable star classes of 29 of the candidate γ Dor MUSICIAN stars on a H-R diagram (Figure 9.1). HD 75202 was excluded for reasons explained in Section 2.3.1. The blue dashed polygon represents the region on the H-R diagram which is occupied by the majority of the *Kepler* γ Dor stars analysed by Balona (2018a). Of the 29 candidate γ Dor MUSICIAN stars in Figure 9.1, 26 are located within the γ Dor region of Balona (2018a), where six of these stars are located outside the blue edge of the theoretical γ Dor instability strip and two stars are located outside the red edge of the δ Sct theoretical instability strip. The remaining 18 stars in this region are located within both instability strips. From this information, it was hypothesised that this sample consists of both γ Dor stars and γ Dor/δ Sct hybrid stars.

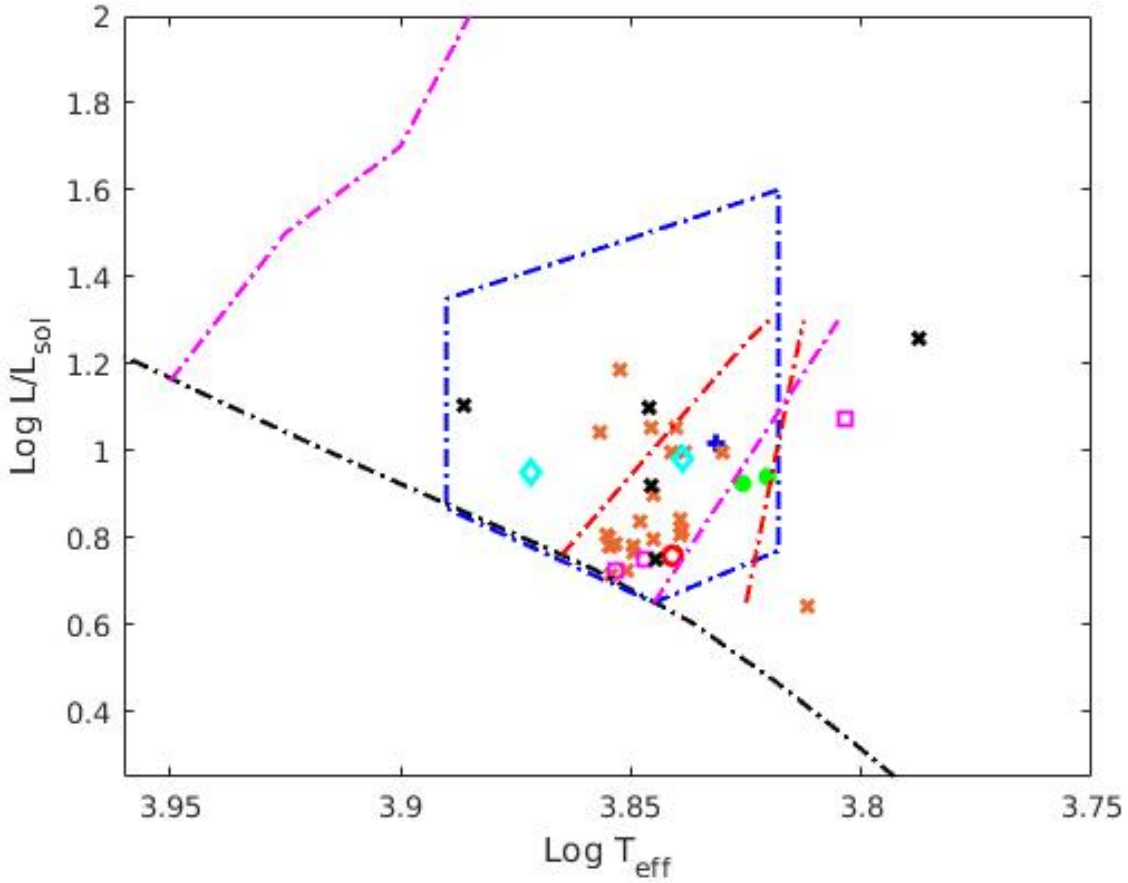

Figure 9.1: H-R diagram of 29 of the MUSICIAN stars analysed in this thesis, excluding HD 75202. The black dashed line is the main sequence (Bertelli et al. 2008), the pink dashed lines are the blue and red edges of the δ Sct instability strip (Pamyatnykh 2000; Dupret et al. 2005), the red dashed lines are the blue and red edges of the γ Dor instability strip (Dupret et al. 2005), and the blue dashed polygon is the γ Dor region from Balona (2018a), also shown in Figure 1.5. The symbols represent the classifications of the stars according to Simbad (Wenger et al. 2000) if any: Algol-type eclipsing binary (blue +), Alpha^2 Canum Venaticorum (α^2 CVn; red $\circ$), ellipsoidal variable (green *), high proper motion star (pink $\square$), γ Dor (orange $\times$) and unclassified (cyan $\Diamond$). The stars studied specifically by this thesis are represented by a black $\times$ (left: HD 209295; middle (top to bottom): HD 10167, HD 216910, HD 206481; right: HD 214291).

9.2 Frequencies of MUSICIAN Stars

Each of the 30 stars was analysed using SigSpec in order to determine the significant frequencies in their light curves. The light curves for these stars are presented in Figure 9.2. Note that the analysis of the MUSICIAN frequencies includes both independent and dependent frequencies.

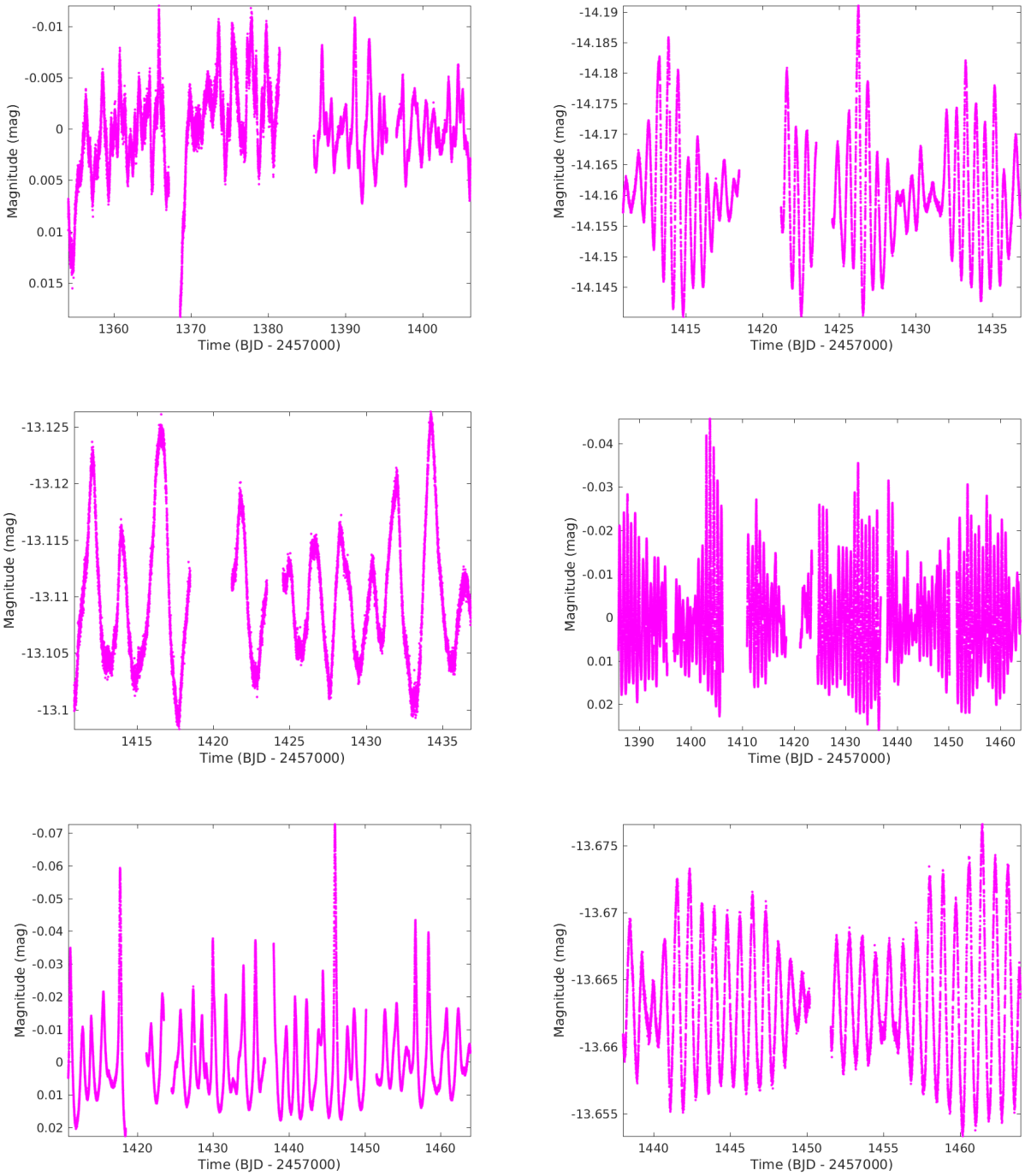

Figure 9.2: PDCSAP light curves for MUSICIAN stars. From top left to bottom right: HD 10167, HD 14940, HD 17310, HD 27290, HD 27377 and HD 32348.

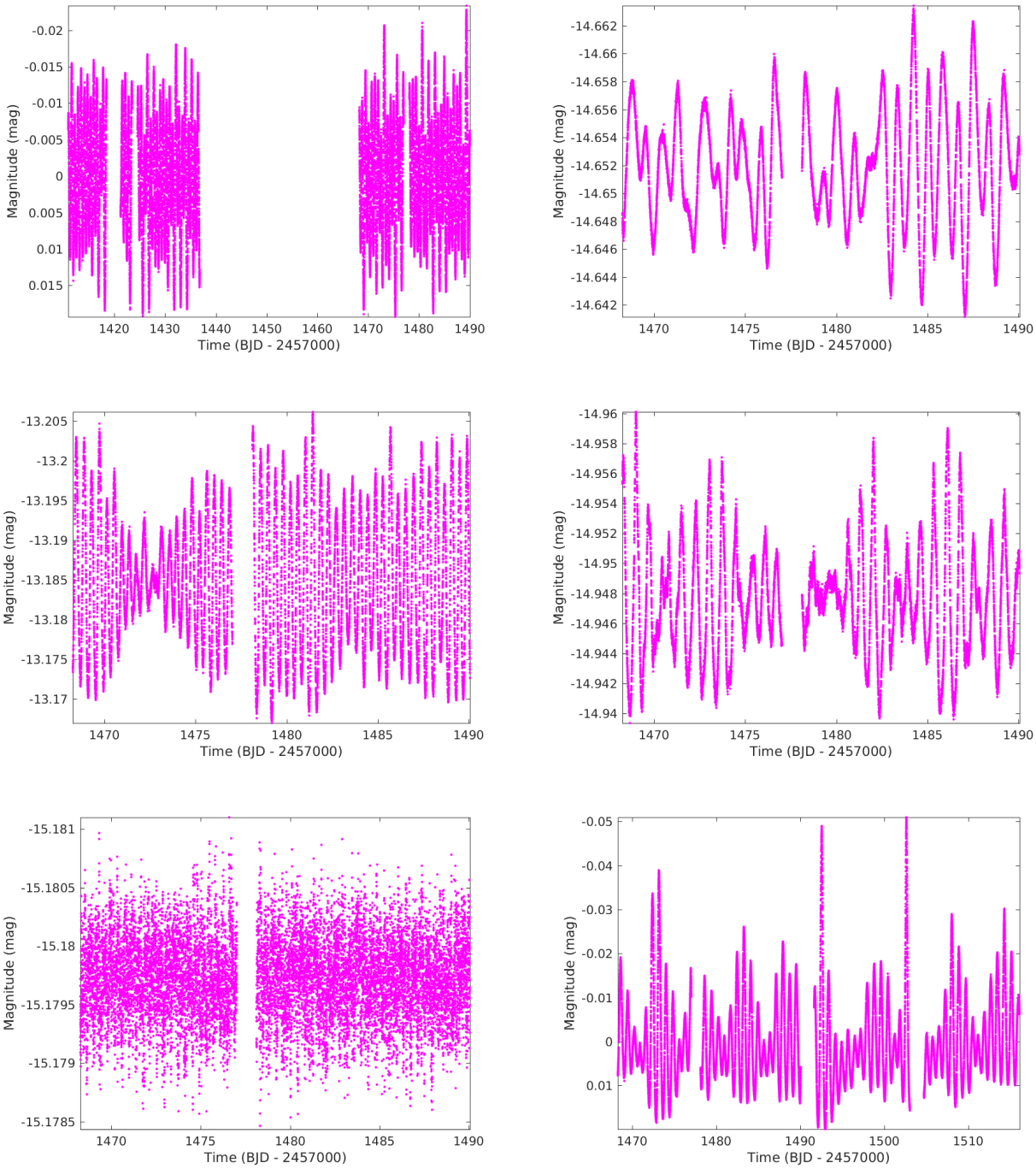

Figure 9.2: (Continued) PDCSAP light curves for MUSICIAN stars. From top left to bottom right: HD 34025, HD 40745, HD 41448, HD 41547, HD 46304 and HD 48501.

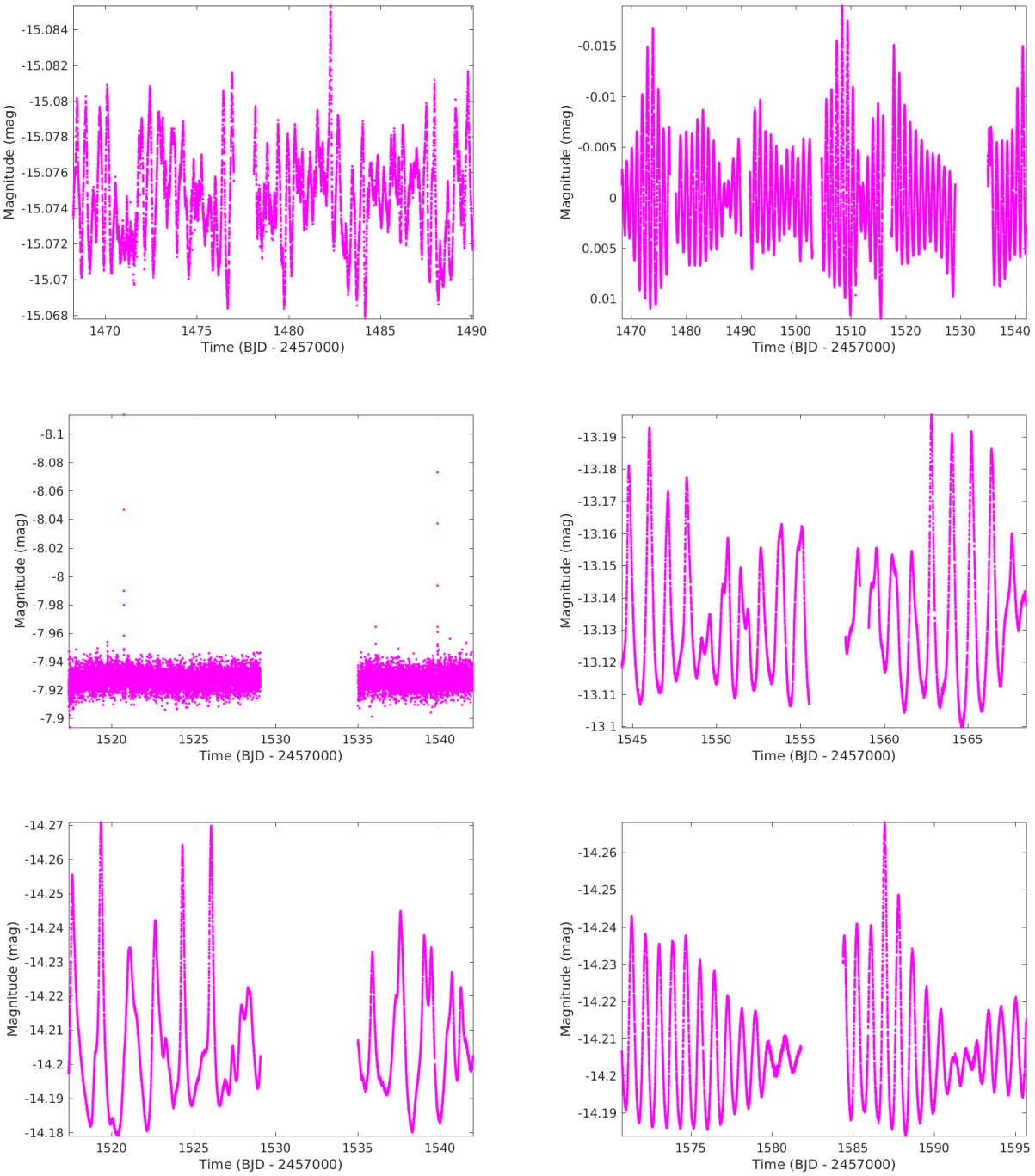

Figure 9.2: (Continued) PDCSAP light curves for MUSICIAN stars. From top left to bottom right: HD 49434, HD 55892, HD 75202, HD 85693, HD 86371 and HD 103257.

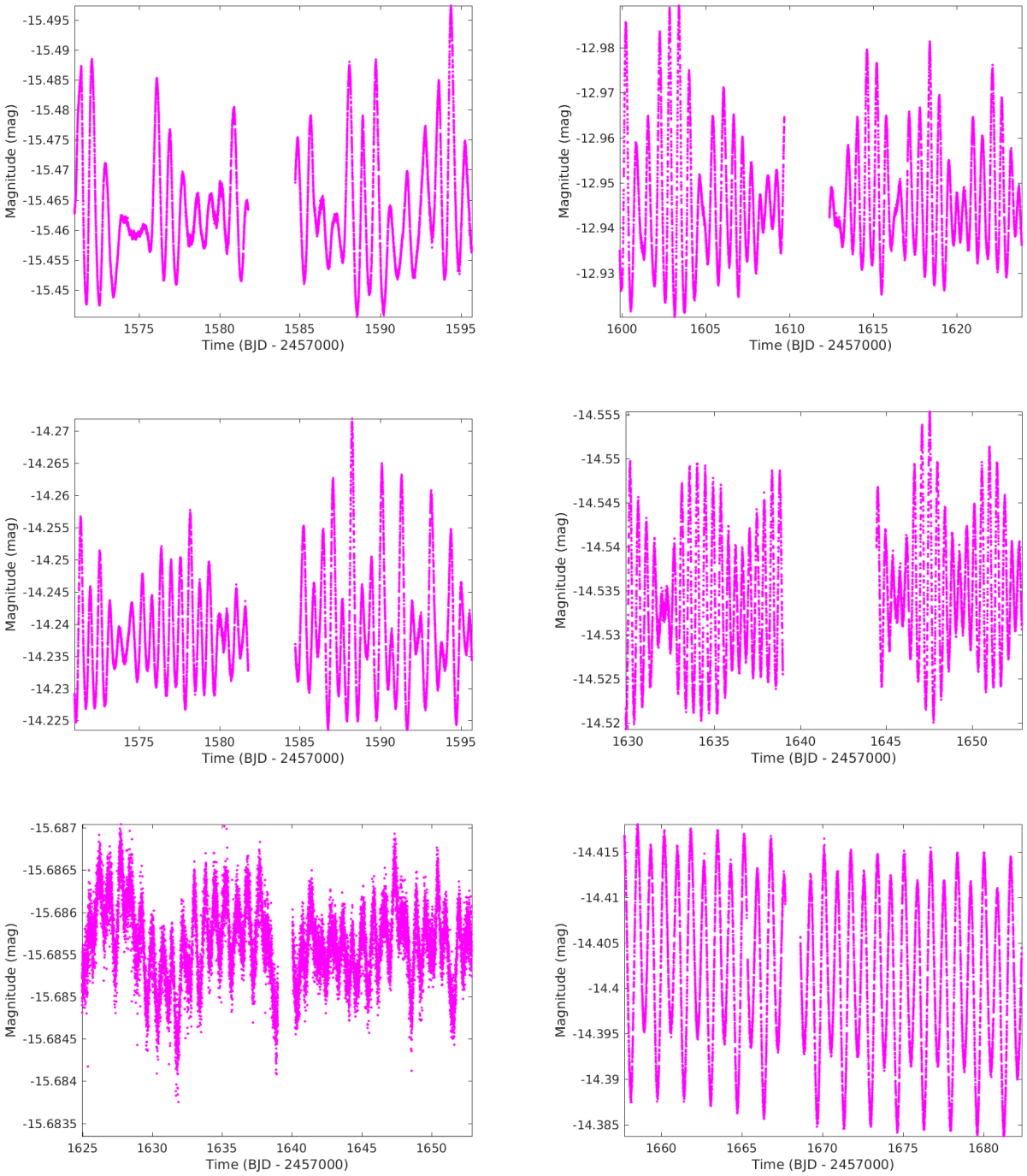

Figure 9.2: (Continued) PDCSAP light curves for MUSICIAN stars. From top left to bottom right: HD 109799, HD 112685, HD 112934, HD 149989, HD 153580 and HD 172416.

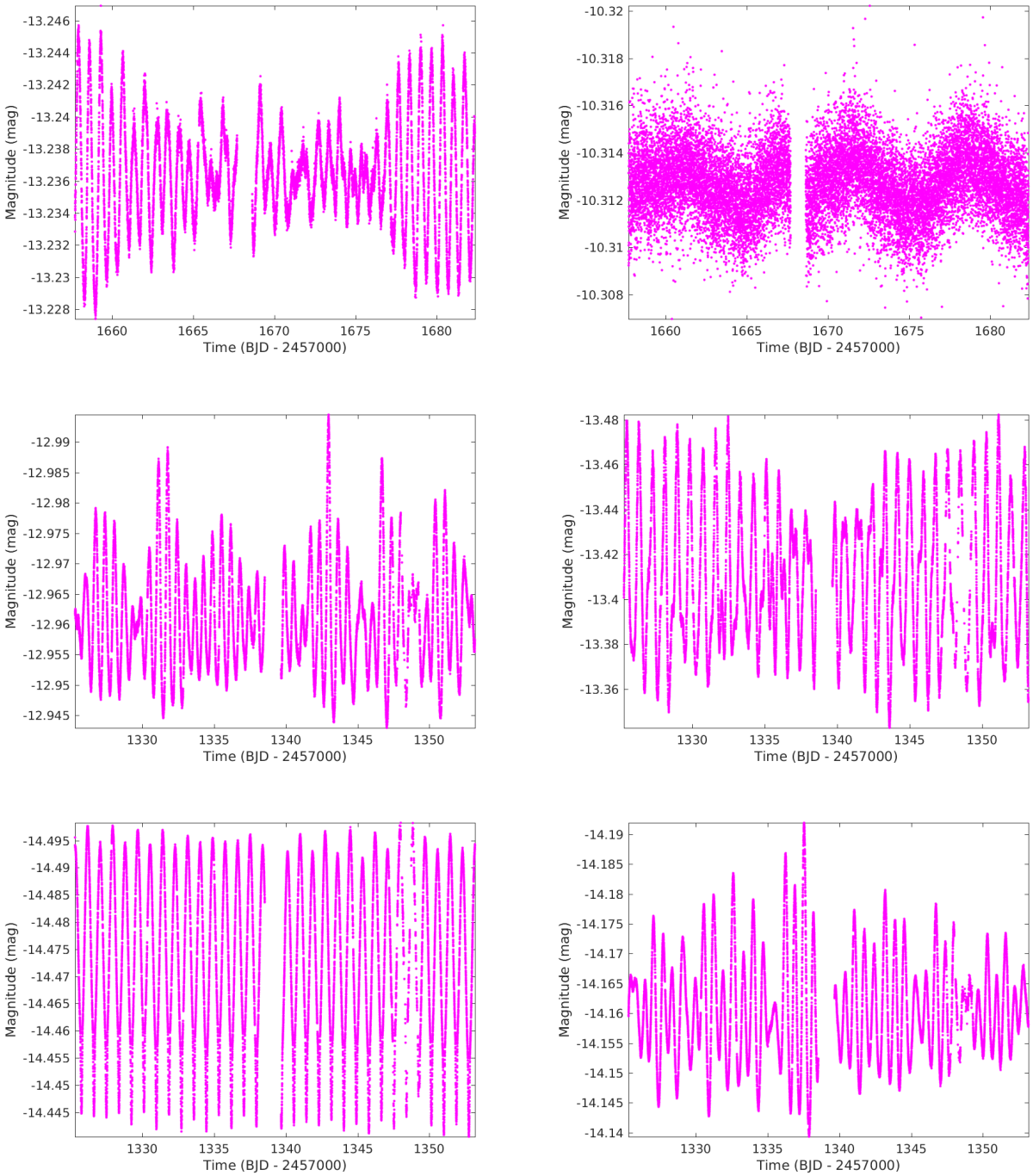

Figure 9.2: (Continued) PDCSAP light curves for MUSICIAN stars. From top left to bottom right: HD 187028, HD 189631, HD 206481, HD 209295, HD 214291 and HD 216910.

All detected frequencies for the sample of MUSICIAN stars are presented in Figure 9.3.

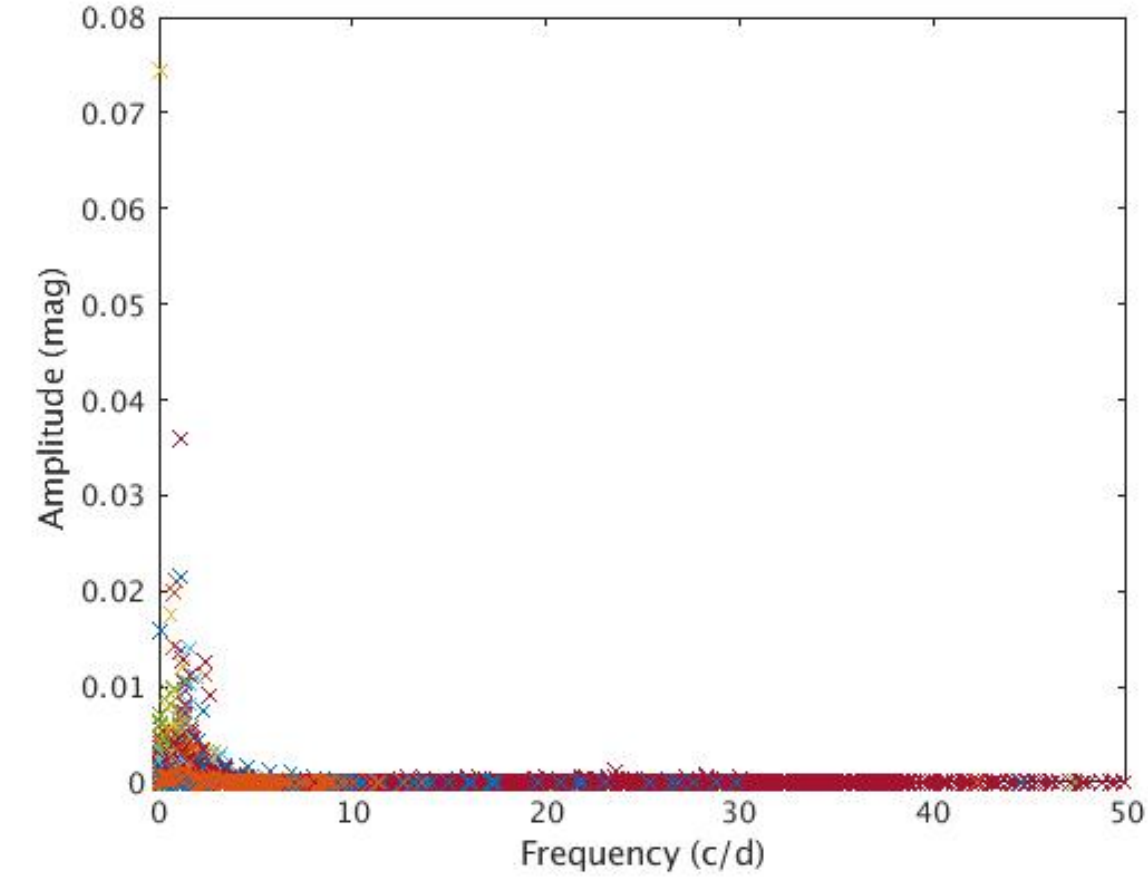

(a)

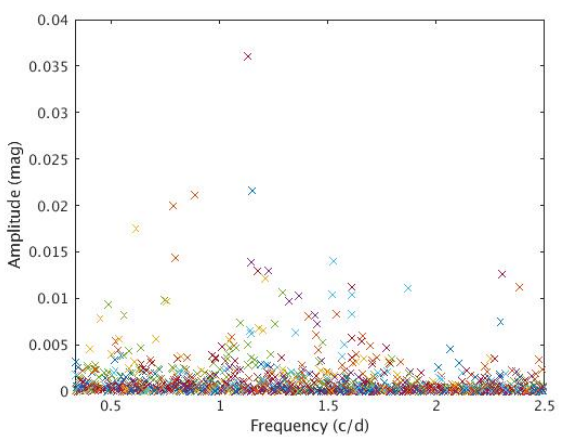

(b)

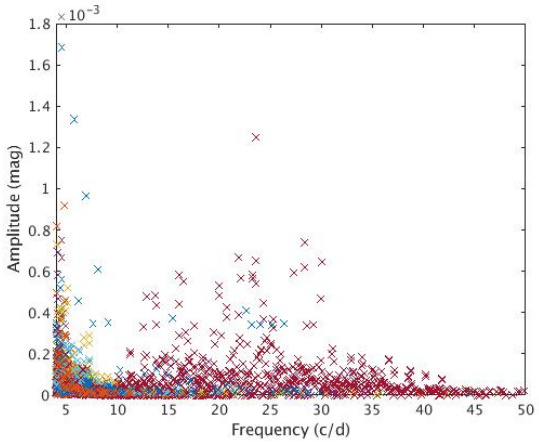

(c)

Figure 9.3: Combined Fourier spectrum from all 30 MUSICIAN stars for (a) all detected frequencies; (b) frequencies in the γ Dor range (0.33–2.5 d^{-1}); and (c) frequencies in the δ Sct range (4–50 d^{-1}). Different coloured data points indicate different stars.

Figure 9.3 also shows the distribution of the detected frequencies throughout the γ Dor and δ Sct frequency ranges. There is an even distribution of high amplitude frequencies throughout the γ Dor range, with the highest amplitude frequencies ranging between 0.5 and 1.5 d^{-1}. This trend is not observed in the δ Sct frequency range. An even distribution of high amplitude δ Sct frequencies is shown between 10 and 30 d^{-1}, but the highest amplitude δ Sct frequency is < 5 d^{-1}. This produces an observed local minimum in the amplitude value at $\sim$10 d^{-1}.

The distribution of the values of all the detected frequencies shows an approximately exponential decrease in the number of frequencies per frequency bin (Figure 9.4). An examination of the distribution of frequencies within the γ Dor frequency range shows that the number of frequencies per bin is roughly constant.

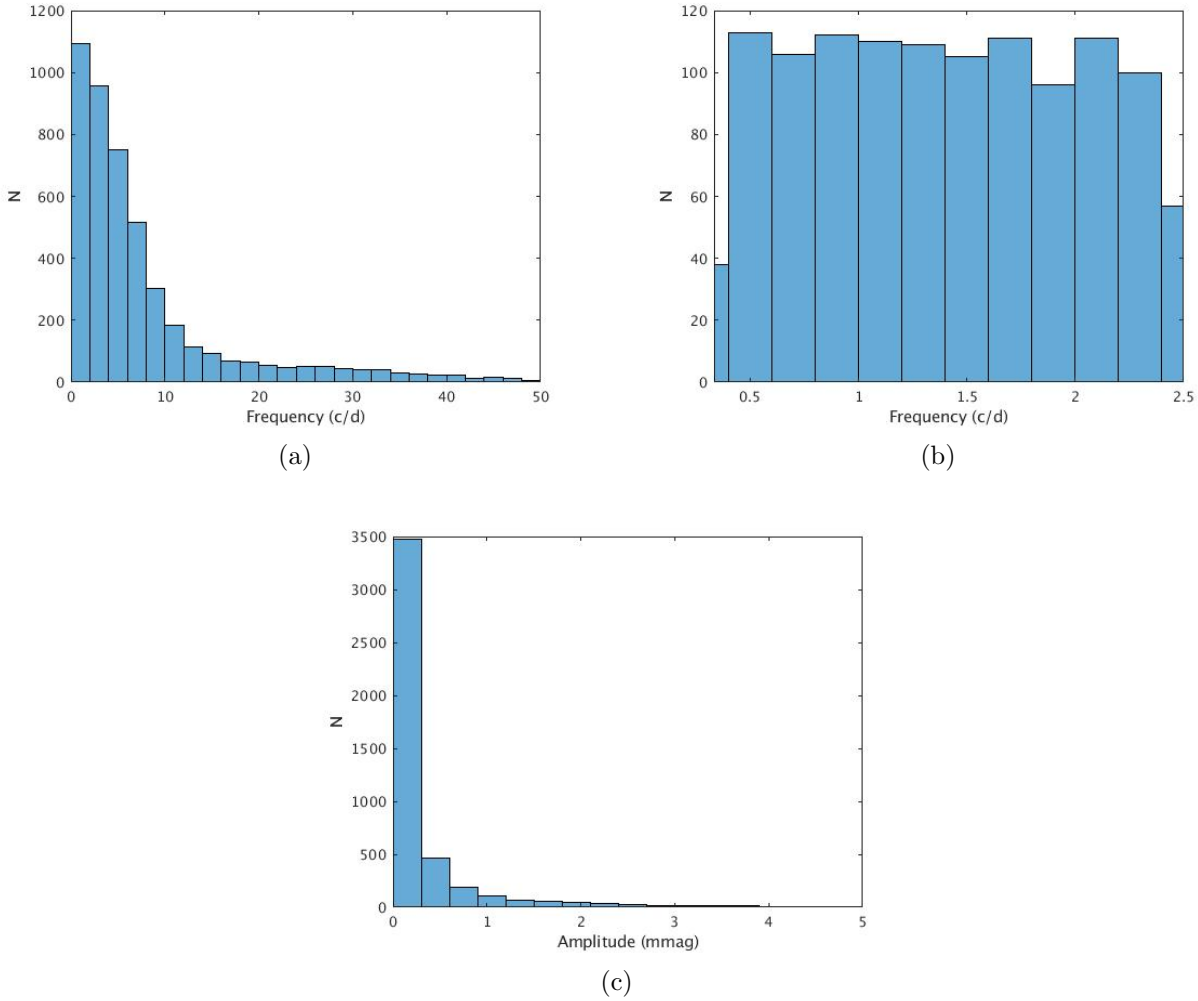

Figure 9.4: Distributions of (a) all detected MUSICIAN frequencies; (b) MUSICIAN frequencies within the γ Dor frequency range (0.33–2.5 d^{-1}); and (c) frequency amplitudes within the range 0–5 mmag. Of the 4,608 total detected frequencies, 58 have amplitudes of 5–80 mmag;

The distribution of amplitudes shows a more dramatic decrease in number with increasing amplitude value (Figure 9.4). Approximately 75% of the MUSICIAN frequencies have amplitude < 0.3 mmag while only 1.3% have amplitude > 5 mmag.

The first detected frequencies of the MUSICIAN stars (Figure 9.5) are all < 2.5 d^{-1}, with 28 frequencies in the γ Dor frequency range, except for the first frequency of HD 46304 (18.85 d^{-1}), which is a δ Sct frequency, and HD 189631 (0.1152 d^{-1}), which is neither a γ Dor nor a δ Sct frequency. The majority of the first detected frequencies are also the highest amplitude frequencies for each MUSICIAN star (Figure 9.5); however only 23 of these frequencies are within the γ Dor frequency range. Table 9.1 presents the first three detected frequencies for all 30 stars.

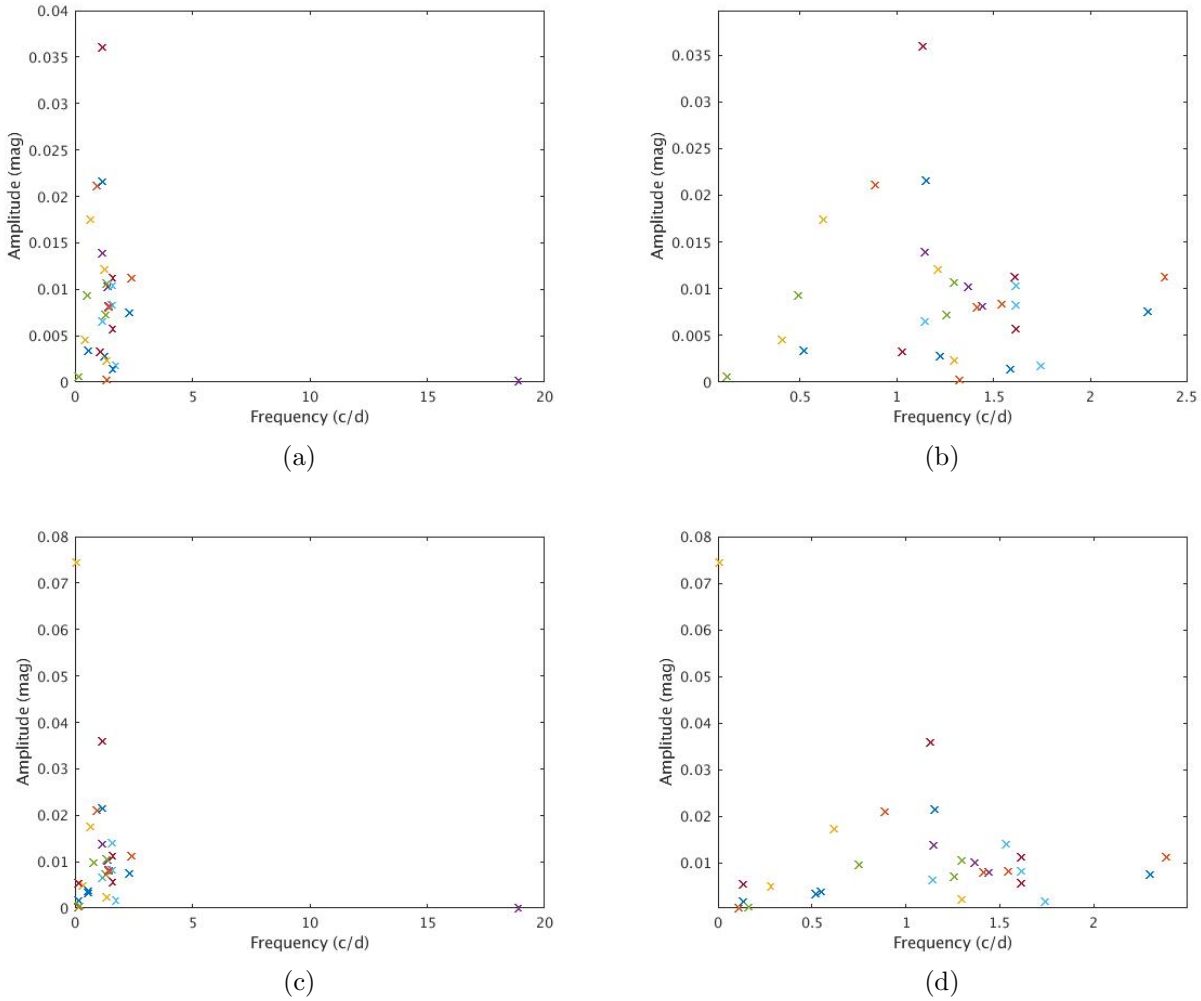

Figure 9.5: Combined MUSICIAN Fourier spectra from all stars for (a) the first detected frequency for each star; (b) the first detected frequencies within the range 0–2.5 d^{-1}; (c) the highest amplitude frequency for each star; and (d) the highest amplitude frequencies in the range 0–2.5 d^{-1}. Each coloured cross indicates a different star.

Table 9.1: The first three detected frequencies for all 30 MUSICIAN stars. Frequency, amplitude and S/N values have been rounded to 6 s.f., 2 s.f. and 3 s.f. respectively.

HD	Frequency (d^{-1})	Amplitude (mag)	S/N	HD	Frequency (d^{-1})	Amplitude (mag)	S/N
10167	0.515531	0.0034	1160	41547	1.29090	0.0024	1100
	0.0291128	0.0018	989		1.52975	0.0018	896
	0.411892	0.0020	861		1.23874	0.0022	848
14940	1.54072	0.0084	1400	46304	18.8509	0.00017	371
	1.69522	0.0050	1240		14.0730	0.00014	323
	1.45373	0.0045	1160		2.54084	0.00014	305
17310	0.400489	0.0046	1370	48501	1.29053	0.011	3480
	0.296969	0.0027	962		1.09218	0.0074	3130
	0.498705	0.0040	886		0.196283	0.0040	1210
27290	1.36309	0.010	4190	49434	1.73694	0.0018	711
	1.32095	0.0097	6500		0.236555	0.0014	579
	1.46969	0.0033	1370		2.53967	0.0011	562
27377	0.485206	0.0094	2040	55892	1.02271	0.0033	2650
	0.745624	0.0098	2440		0.978800	0.0037	3140
	0.560399	0.0082	1580		1.06769	0.0034	4160
32348	1.13836	0.0066	1580	75202	1.58517	0.0014	63.2
	1.26206	0.0026	1690		3.16610	0.0012	48.7
	1.21097	0.0029	1760		0.130242	0.0018	44.8
34025	1.60724	0.011	5440	85693	0.886065	0.021	2150
	0.805912	0.0036	2240		0.784806	0.020	1200
	0.683860	0.0031	3140		1.66040	0.00060	818
40745	1.21788	0.0028	981	86371	0.613223	0.018	1390
	0.546057	0.0039	1040		0.448468	0.0078	537
	1.18763	0.0030	1440		1.19917	0.0066	514
41448	2.38165	0.011	2390	103257	1.14328	0.014	1650
	2.47435	0.0034	1290		1.22548	0.013	2570
	2.58275	0.0025	866		0.0657850	0.0036	973

Table 9.1: (Continued) The first three detected frequencies for all 30 MUSICIAN stars. Frequency, amplitude and S/N values have been rounded to 6 s.f., 2 s.f. and 3 s.f. respectively.

HD	Frequency (d^{-1})	Amplitude (mag)	S/N	HD	Frequency (d^{-1})	Amplitude (mag)	S/N
109799	1.25306	0.0073	1250	187028	1.43851	0.0082	1842
	1.07250	0.0047	931		1.44876	0.0073	1540
	0.212397	0.0047	570		1.53128	0.0016	838
112685	1.60804	0.010	1310	189631	0.115204	0.00062	319
	1.86757	0.011	1800		0.157242	0.00062	225
	1.52646	0.014	928		0.250503	0.00022	72.5
112934	1.60813	0.0058	1200	206481	1.60856	0.0083	2160
	1.00898	0.0049	888		1.34834	0.0064	2360
	1.65448	0.0054	912		0.841966	0.0019	660
149989	2.29593	0.0075	1770	209295	1.12809	0.036	2890
	2.06116	0.0046	1550		2.30415	0.013	1190
	2.10306	0.0031	634		1.17524	0.013	1610
153580	1.31987	0.00031	1100	214291	1.14784	0.022	3780
	0.104450	0.00039	850		3.44329	0.0021	903
	0.121397	0.00033	637		2.29449	0.0018	942
172416	1.20891	0.012	3330	216910	1.40721	0.0081	2180
	0.607166	0.0032	2440		1.72224	0.0037	929
	-0.322851	0.000087	506		0.849508	0.0037	1060

The total number of frequencies detected for each star, as well as the proportion which fall into the γ Dor and δ Sct categories, are presented in Table 9.2. The stars with the highest proportion of γ Dor and δ Sct frequencies are HD 172416 (75.0%) and HD 209295 (88.8%) respectively. These are the best candidates for 'pure' γ Dor or δ Sct pulsators. The average proportion of γ Dor and δ Sct frequencies is 31.9% and 45.3% respectively.

Table 9.2 also presents the classifications of the 30 MUSICIAN stars by this thesis using criteria from Balona (2018a) and Grigahcène et al. (2010).

The classification of the stars as GDORA, GDORS, or GDORM type (Balona 2018a) was determined from examination of the MUSICIAN star light curves. This thesis found 16 GDORA stars (representing 53.3% of the sample), five GDORS stars (16.7%) and nine GDORM stars (30%). This result is contrary to the result from Balona (2018a), performed using the same analysis on a set of 820 target γ Dor stars. Their paper found approximately the same proportion of GDORM stars as found by this thesis. while the proportion of GDORA and GDORS stars was transposed (i.e. 16.7% and 54.45% respectively). This suggests that the set of 30 MUSICIAN stars is too small to accurately represent the different types of γ Dor stars.

The classification using the four pulsator classes (γ Dor, γ Dor/δ Sct, δ Sct/γ Dor and δ Sct) suggested by Grigahcène et al. (2010) was determined from the percentage of frequencies in the γ Dor and δ Sct ranges, using the following criteria imposed by this thesis:

- γ Dor stars have $< 15\%$ δ Sct frequencies in their light curve
- δ Sct stars have $< 15\%$ γ Dor frequencies in their light curve
- γ Dor/δ Sct have a % of γ Dor frequencies greater than their % of δ Sct frequencies
- δ Sct/γ Dor have a % of δ Sct frequencies greater than their % of γ Dor frequencies

The result of this classification was the identification of three γ Dor stars, two δ Sct stars, four γ Dor/δ Sct hybrids and 21 δ Sct/γ Dor hybrids.

An analysis of the proportions of γ Dor and δ Sct frequencies in the light curves of the MUSICIAN stars determined that there is a clear negative linear correlation between them (Figure 9.6). The best-fitting model for this relationship suggests that there is a maximum percentage of γ Dor or δ Sct frequencies present in the light curves of 'pure' pulsators: $\sim$65% and $\sim$87% respectively. It also suggests that a star with $\sim$40% of its light curve frequencies within the γ Dor range will also have $\sim$40% of its light curve frequencies within the δ Sct range.

Table 9.2: Number of detected γ Dor and δ Sct frequencies as compared to the total number of detected frequencies for the MUSICIAN stars.

	% of Frequencies			Classification	
HD	γ Dor	δ Sct	Total #	Balona (2018a)	Grigahcène et al. (2010)
10167	50.0	18.2	132	GDORM	γ Dor
14940	26.0	54.3	127	GDORA	δ Sct / γ Dor hybrid
17310	42.9	29.9	77	GDORM	γ Dor / δ Sct hybrid
27290	21.8	59.5	440	GDORA	δ Sct / γ Dor hybrid
27377	25.7	52.0	269	GDORA	δ Sct / γ Dor hybrid
32348	35.0	39.0	100	GDORS	δ Sct / γ Dor hybrid
34025	51.8	21.8	110	GDORS	γ Dor / δ Sct hybrid
40745	33.7	43.5	92	GDORS	δ Sct / γ Dor hybrid
41448	31.4	44.8	105	GDORS	δ Sct / γ Dor hybrid
41547	28.8	48.1	104	GDORA	δ Sct / γ Dor hybrid
46304	14.0	71.0	93	GDORM	δ Sct
48501	30.2	44.2	215	GDORA	δ Sct / γ Dor hybrid
49434	19.6	65.2	158	GDORM	δ Sct / γ Dor hybrid
55892	18.8	66.0	483	GDORA	δ Sct / γ Dor hybrid
75202	22.7	50.0	22	GDORM	δ Sct / γ Dor hybrid
85693	26.2	52.3	130	GDORA	δ Sct / γ Dor hybrid
86371	16.9	68.7	166	GDORA	δ Sct / γ Dor hybrid
103257	33.3	42.2	102	GDORA	δ Sct / γ Dor hybrid
109799	28.1	50.8	128	GDORA	δ Sct / γ Dor hybrid
112685	28.1	46.5	114	GDORA	δ Sct / γ Dor hybrid
112934	35.1	38.1	97	GDORA	δ Sct / γ Dor hybrid
149989	35.8	40.3	67	GDORA	δ Sct / γ Dor hybrid
153580	50.0	24.3	70	GDORM	γ Dor / δ Sct hybrid
172416	75.0	3.13	32	GDORM	γ Dor
187028	36.2	39.4	94	GDORS	δ Sct / γ Dor hybrid
189631	50.0	7.14	14	GDORM	γ Dor
206481	26.6	52.6	154	GDORA	δ Sct / γ Dor hybrid

Table 9.2: (Continued) Number of detected γ Dor and δ Sct frequencies as compared to the total number of detected frequencies for the MUSICIAN stars.

	% of Frequencies			Classification	
HD	γ Dor	δ Sct	Total #	Balona (2018a)	Grigahcène et al. (2010)
209295	5.99	88.8	634	GDORA	δ Sct
214291	27.3	53.8	143	GDORM	δ Sct / γ Dor hybrid
216910	29.4	44.9	136	GDORA	γ Dor / δ Sct hybrid

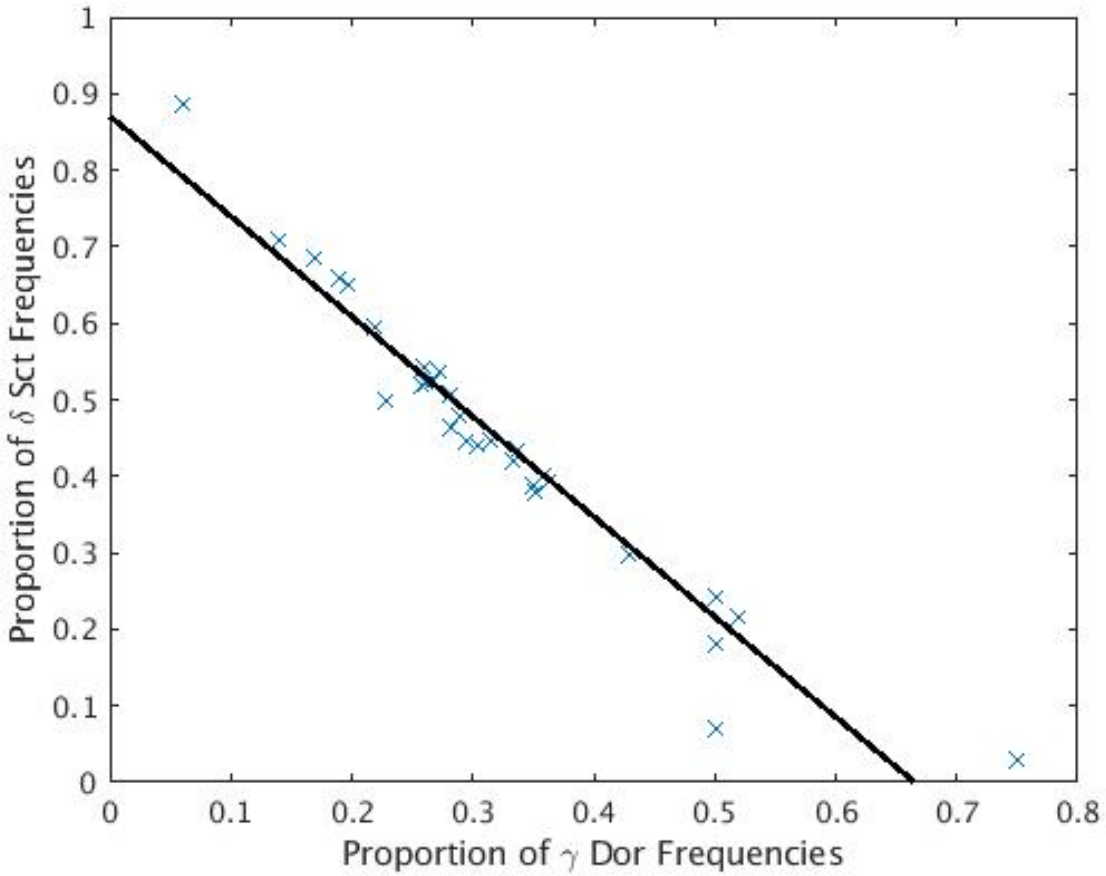

Figure 9.6: The relationship between the proportions of γ Dor and δ Sct frequencies present in the MUSICIAN star light curves. The blue crosses represent the observed proportions and the black line is the best-fitting linear model.

9.2.1 Interesting Fourier Spectra of MUSICIAN Stars

Three stars showed interesting γ Dor and δ Sct features in their spectra (Figure 9.7).

The first of these stars is HD 46304, whose highest amplitude frequency and first detected frequency 18.85 d^{-1} is a δ Sct frequency. Its spectrum of detected frequencies also shows that the majority of the high amplitude frequencies are in the δ Sct range.

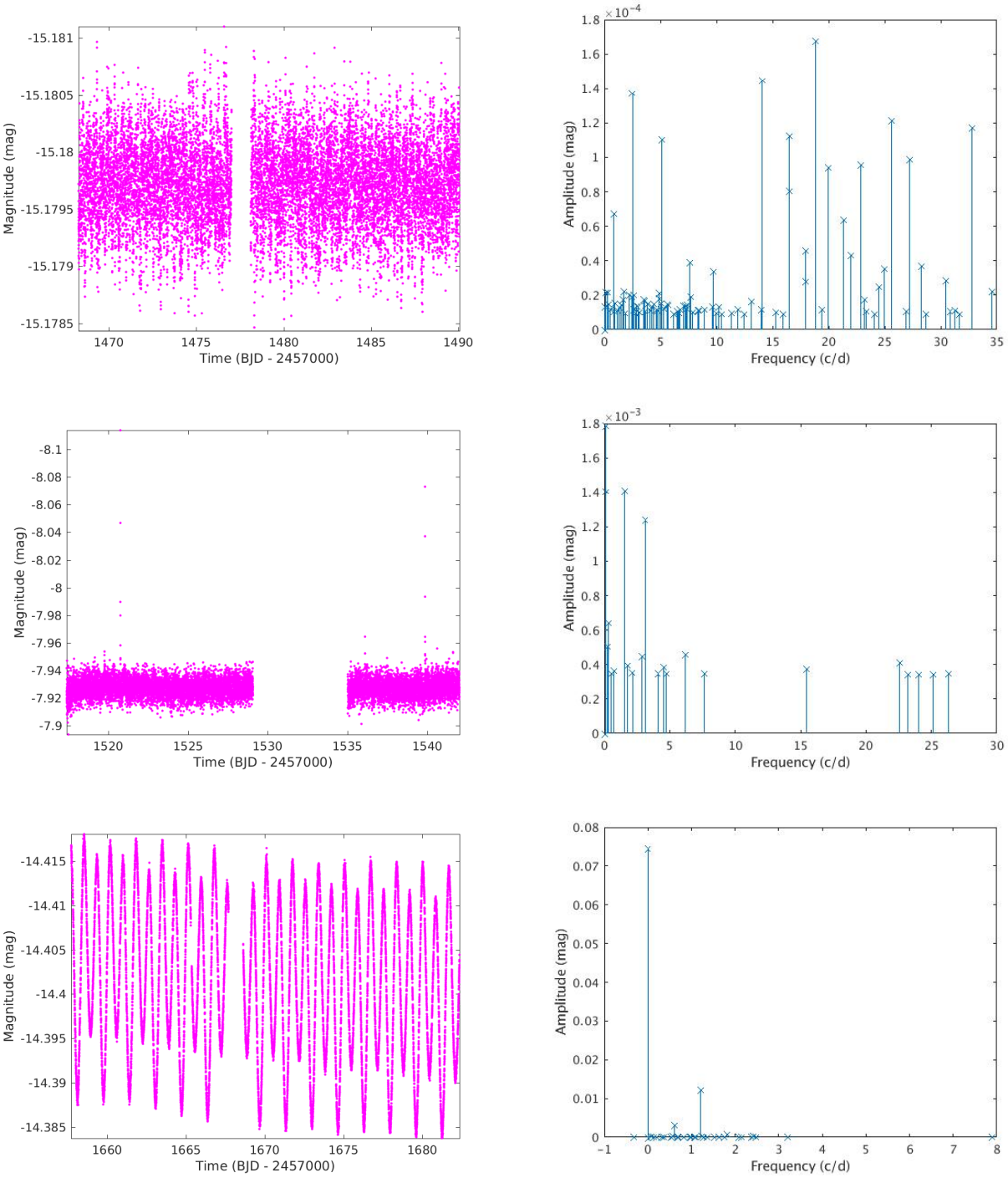

Figure 9.7: A selection of MUSICIAN star light curves with interesting detected frequencies. Top: HD 46304, middle: HD 75202, bottom: HD 172416.

The spectrum for HD 75202 shows three dominant frequencies with amplitude > 1 mmag. The remainder of the frequencies have amplitudes a factor of three smaller and are distributed between the γ Dor and δ Sct frequency ranges.

HD 172416 is a high proper-motion star and has the most interesting spectrum of all the sample MUSICIAN stars. This star has two negative frequencies, one of which is the highest amplitude frequency of all the frequencies detected for all 30 MUSICIAN stars. Negative frequencies are defined by Boutloukos et al. (2007) as equivalent to a positive frequency with a phase difference. Of its 32 detected frequencies, HD 172416 only has three frequencies with amplitude > 1 mmag.

9.3 Frequencies Related to Stellar Properties

The next step of the Fourier analysis of the MUSICIAN stars was to determine whether their stellar properties are related to the significant frequencies or their amplitudes.

Figure 9.8 presents the highest amplitude frequency for each star and the resulting amplitude as a function of effective temperature. There is no clear trend observed for either the frequencies or the amplitudes.

Figure 9.9 presents the first detected frequencies and the highest amplitudes of frequencies as a function of their position on the H-R diagram. The magnitude of the frequency or amplitude is indicated by the colour of the data point in the figure, where red represents the lowest values and blue represents the highest values. There is a small correlation between the first detected frequency and luminosity, shown by the location of the lower frequencies at higher luminosities, and the mid to high frequencies mostly located at lower luminosities. Additionally, most of the γ Dor frequencies (red to green colours) lie within the γ Dor instability strip. There appears to be no correlation between the values of the highest amplitudes and the positions of the stars on the H-R diagram.

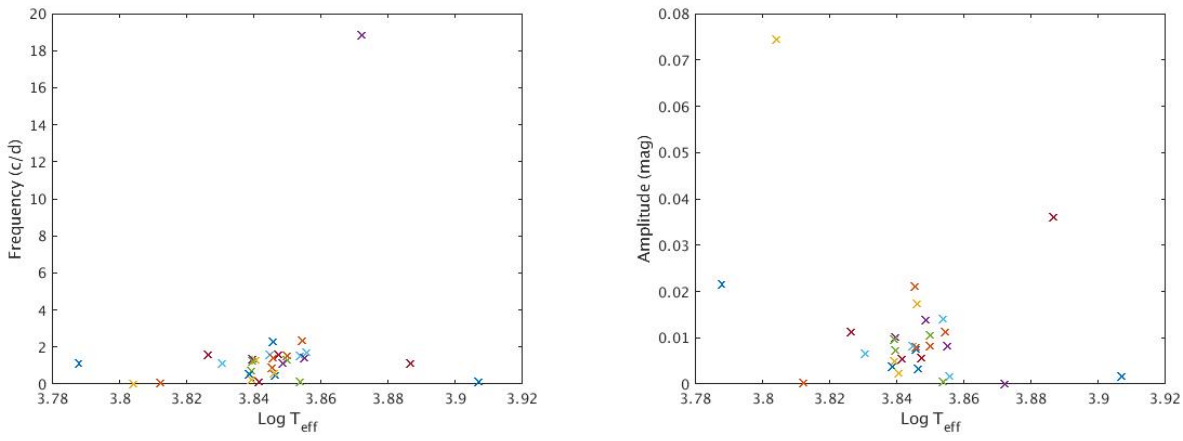

(a) (b)

Figure 9.8: (a) The frequencies with the highest amplitudes; and (b) the highest detected amplitude for each star in the MUSICIAN program are shown as a function of effective temperature ($T_{\rm eff}$).

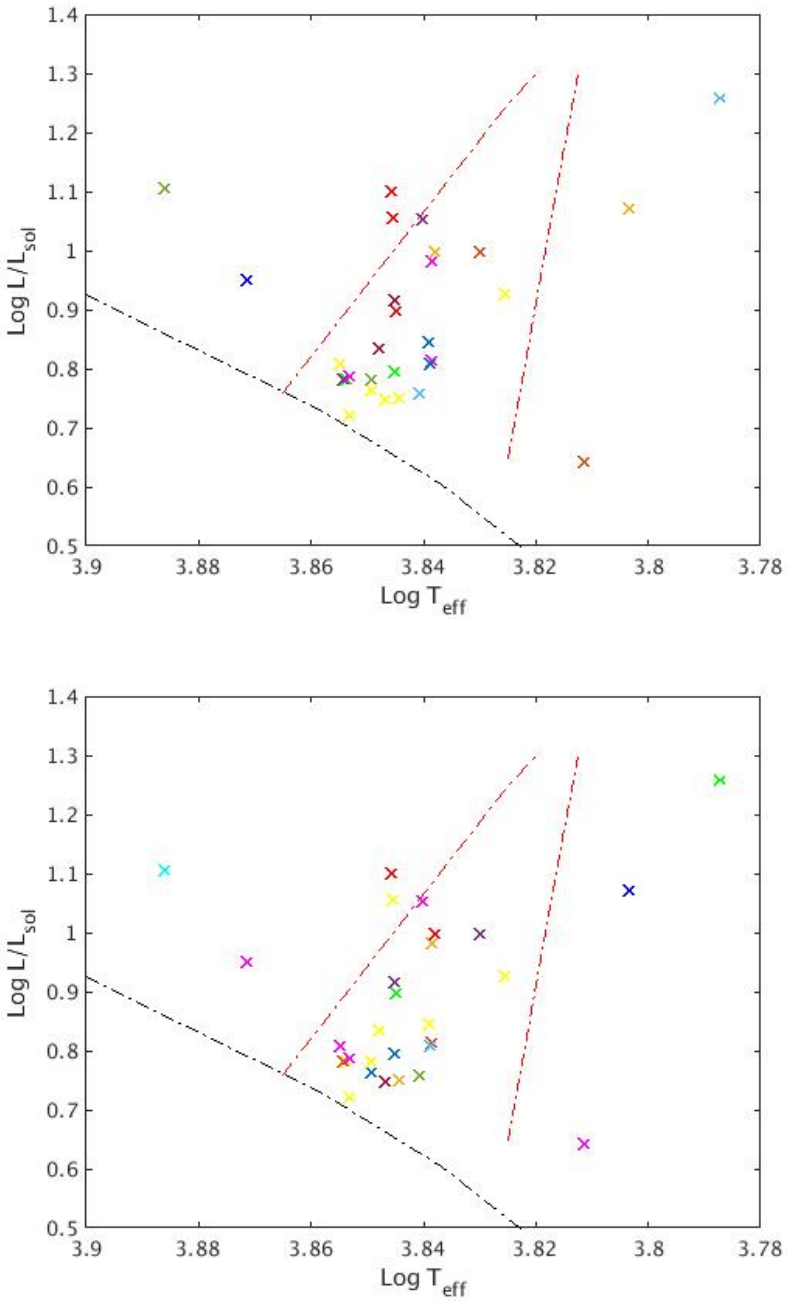

Magenta: $0 < f < 0.5$ d^{-1}
Red: $0.5 < f < 1$ d^{-1}
Orange: $1 < f < 1.5$ d^{-1}
Yellow: $1.5 < f < 2$ d^{-1}
Green: $2 < f < 2.5$ d^{-1}
Cyan: $2.5 < f < 3$ d^{-1}
Blue: $3 < f < 20$ d^{-1}

Magenta: $0 < A < 0.0025$ mag
Red: $0.0025 < A < 0.005$ mag
Orange: $0.005 < A < 0.01$ mag
Yellow: $0.01 < A < 0.02$ mag
Green: $0.02 < A < 0.03$ mag
Cyan: $0.03 < A < 0.04$ mag
Blue: $0.04 < A < 0.08$ mag

Figure 9.9: Distributions of first detected frequencies (top) and highest amplitudes (bottom) of the frequencies detected for 29 of the MUSICIAN stars (excluding HD 75202) on the H-R diagram. The colours indicate the frequency and amplitude values. The black dashed line indicates the main-sequence (Bertelli et al. 2008) and the red dashed lines indicate the γ Dor instability strip from Dupret et al. (2005).

Figure 9.10 presents the distribution of $v \sin i$ values for the single and binary stars of the MUSICIAN sample. $v \sin i$ values were obtained from Nordstrom et al. (1997), De Cat et al. (2006a), Gillon et al. (2006), Royer et al. (2007), Kahraman Aliçavuş et al. (2016), Schröder et al. (2009), Maisonneuve et al. (2011) and Fekel et al. (2016). Most of the stars are low to moderate rotators with $v \sin i < 150$ km s^{-1}, with the exception of HD 46304 which has $v \sin i \approx 240$ km s^{-1}.

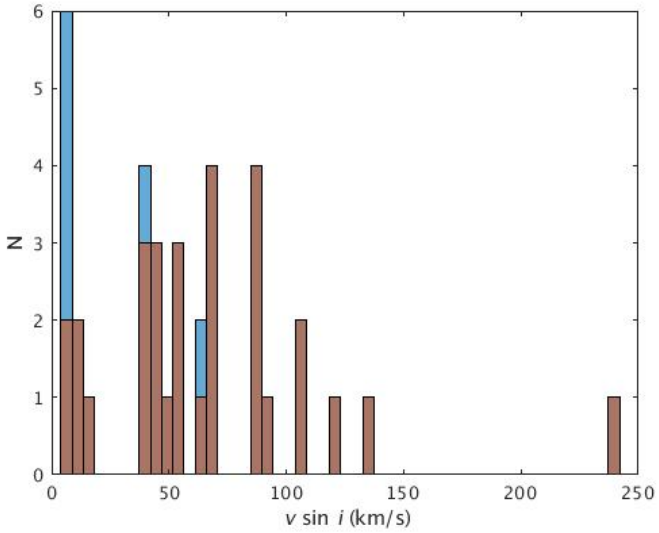

Figure 9.10: Distribution of MUSICIAN $v \sin i$ values, where the brown histogram shows single star values (including binaries for which only one component has a known $v \sin i$ value) and the blue histogram shows values for each binary component as well as the single stars.

Using these values, the independent pulsation frequencies and resulting amplitudes for the MUSICIAN stars were compared to their respective $v \sin i$ values to determine the correlation between them, as previously performed by Tkachenko et al. (2013) on a different set of stars. It was uncertain whether or not the components of the binary systems were included in their analysis, and therefore this thesis has performed the same analysis twice: once for the single stars and the binary components for which only one $v \sin i$ value was known, and once for all stars, both single and binary components. Since this analysis aims to determine properties of these γ Dor candidates, the star HD 46304 was removed from the sample for these analyses as the first detected frequency for this star was a δ Sct frequency which is unexpected for a true γ Dor star. Figure 9.11 presents the results of the analysis performed on the 4,515 detected MUSICIAN frequencies for this subset of stars, which are assumed to be independent of each other. Similar to the results of Tkachenko et al. (2013), a positive correlation was found between the pulsation frequencies and the $v \sin i$ values and a weak, negative correlation between amplitude and $v \sin i$. Interestingly, these correlations are stronger for the case where only single stars are analysed.

If it is now assumed that not all of the 4,515 frequencies are independent, this result will not be accurate. Therefore a second analysis only considering the first detected frequency for each star was performed. Figure 9.12 presents the results of this analysis.

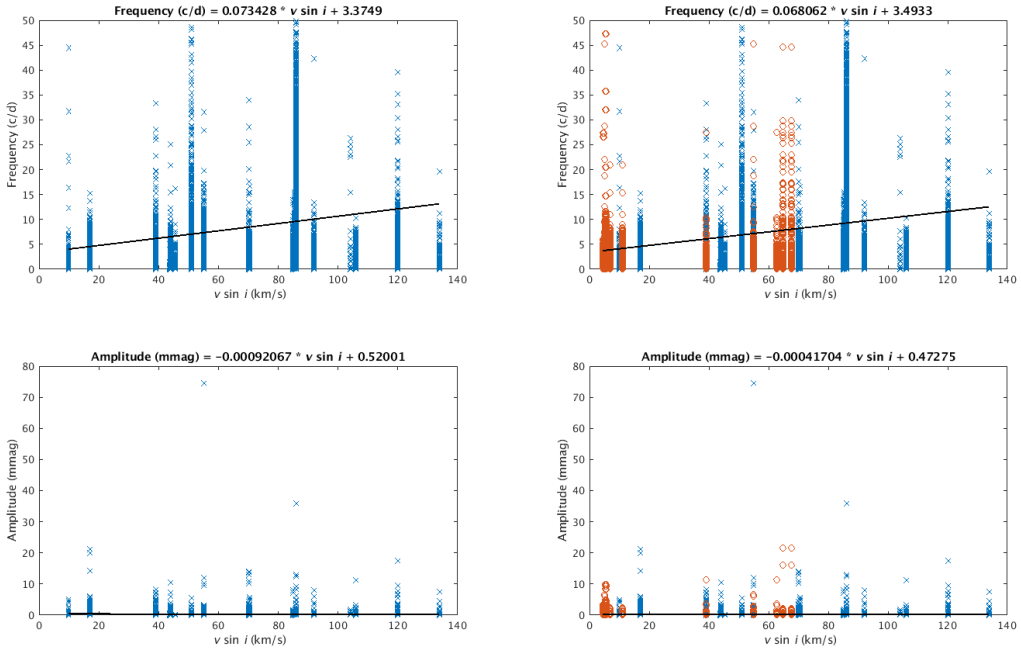

Figure 9.11: Correlations between $v \sin i$ and frequency (top row) and amplitude (bottom row) for all frequencies detected in MUSICIAN light curves for single stars, including binaries for which only one $v \sin i$ value is known (left column), and for both single stars (blue) and binary star components (red)(right column).

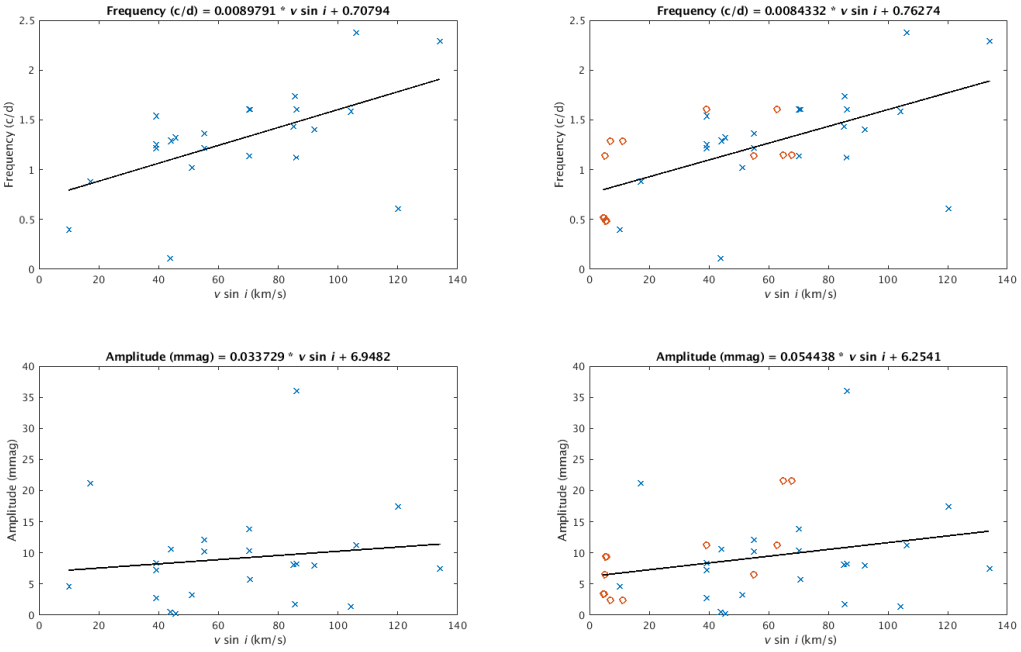

Figure 9.12: Correlations between $v \sin i$ and frequency (top row) and amplitude (bottom row) for the first detected frequencies of the MUSICIAN light curves for single stars, including binaries for which only one component has a known $v \sin i$ value (left column), and for both single stars (blue) and binary star components (red)(right column).

A clear positive correlation is observed between the frequency and $v \sin i$ values, but the correlation between amplitude and $v \sin i$ is now also clearly positive, which disagrees with the previous result and that of Tkachenko et al. (2013).

9.4 Global MUSICIAN Star Properties

The 30 stars in this thesis's sample of MUSICIAN stars occupy similar positions on the H-R diagram and most are contained within the theorised γ Dor instability strip and the *Kepler* γ Dor region defined by Balona (2018a). While the light curves of these stars demonstrate asymmetric and symmetric beating characteristic of a γ Dor star (Balona 2018a), most of the stars also exhibit a significant number of δ Sct frequencies in their Fourier spectra. This supports previous claims that most γ Dor stars are hybrids (Grigahcène et al. 2010).

This thesis observes a weak negative correlation between the first detected frequency of a star and its luminosity, where the lower frequencies are mostly located at higher luminosities. This result appears contradictory to the γ Dor classification of the MUSICIAN stars, as γ Dor stars are theoretically located in the cooler regions of the Cepheid instability strip compared to δ Sct stars; however, it is possibly indicative of the hybrid nature detected in most of the stars.

This work detects a positive correlation between the $v \sin i$ values of the MUSICIAN stars and their detected frequencies. This correlation is stronger when only single stars and binary systems with one known $v \sin i$ value are considered, and weaker when only the first detected frequency of each star is considered. A weak negative correlation is also identified between the $v \sin i$ values and the amplitudes of all the detected frequencies, which agrees with the results of Tkachenko et al. (2013). However, when only the amplitudes of the first detected frequencies are analysed in the same manner, a strong positive correlation is observed. These results suggest that a sample of 30 frequencies is insufficient to indicate an accurate correlation between $v \sin i$ and the frequencies or amplitudes of γ Dor stars. An alternative explanation is that all of the detected frequencies are independent, which would justify why the first analysis agreed with that of Tkachenko et al. (2013). However, such an explanation does not seem plausible given the low probability that none of the $\sim$5,000 detected frequencies are related by aliasing, combinations or coupling. Further analysis of the detected frequencies is required in order to identify which ones are independent in order to more accurate determine their correlation to the stellar $v \sin i$ values.

9.5 HD 75202

HD 75202 was identified as a star of interest after flare-like events were detected in its light curve (Figure 9.13). This is peculiar as A-type stars such as HD 75202 are theorised to be incapable of producing flares (Pedersen et al. 2017) due to the absence of an extensive convective zone.

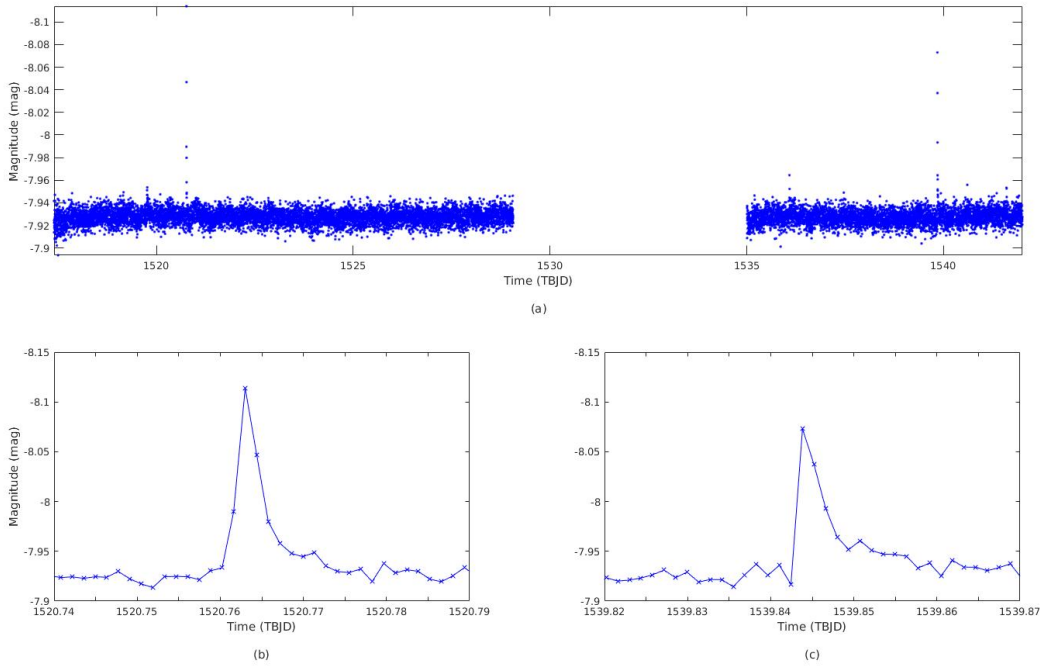

Figure 9.13: Light curve for HD 75202 (top) and the possible flare events which occur at ∼1520.7625 TBJD (bottom left) and ∼1539.844 TBJD (bottom right).

9.5.1 Fourier Analysis

The Fourier analysis of HD 75202 resulted in the detection of 22 frequencies (Figure 9.7). Of these, five were found to be γ Dor frequencies and 11 were found to be δ Sct frequencies (Table 9.2). From this thesis's classification criteria, HD 75202 is a GDORM δ Sct/γ Dor hybrid. None of the detected frequencies match the frequency associated with the time interval between the two flare events, the δ Sct period 0.291 d previously identified by Renson et al. (2009), or the orbital period 0.581 d detected by Avvakumova et al. (2013).

9.5.2 Flare Analysis

Photometric flares are observed as sudden increases in the brightness of a star, which then decay exponentially. Pedersen et al. (2017) defined multiple criteria for flare detection, including that the flare has at least three data points which show an exponential decay above a 3σ limit of the light curve scatter, and that it occurs over a period < 10 h. The 3σ limit is determined by the same process used by Pedersen et al. (2017). The light curve in the region of the flare but excluding the flare data points is modelled by a 4^{th} order polynomial (red lines in Figure 9.14). This is called the 'quiescent' light curve as it excludes the variability of the flare events. The observed flux (F) is corrected for the modelled quiescent flux (F_q) using

$$\frac{\Delta F}{F} = \frac{F - F_q}{F_q} \tag{9.1}$$

The standard deviation of the remaining residual flux is used to determine the 3σ limit for the first flare event criterion. Two flare parameters are determined using the term in

Equation 9.1. The photometric equivalent width (EW_{phot}) is equal to the time interval over which the star emits the same amount of energy as it emits during the flare interval. Although this value has units of time, it measures the energy of the flare and is equal to the integrated flux of the flare which is given as

$$EW_{phot} = \int \frac{\Delta F}{F}\, dt \tag{9.2}$$

The data point before the flare and the data points during the flare above the 3σ limits are used in this calculation. The flare amplitude (A) is the maximum relative increase in flux

$$A = \left(\frac{\Delta F}{F}\right)_{max} \tag{9.3}$$

As shown by Figure 9.14, the events of HD 75202 meet this criteria with a duration of 0.333 and 0.433 h respectively, where the duration is measured as the time interval between the data point before the flare and the data point where the brightness has approximately returned to the mean value of the relative flux.

The $\log(EW_{phot})$ was determined to be -1.7824 and -1.8196 h, indicating that the first event was the most energetic. Given these values and using the relationship found by Pedersen et al. (2017) between $\log(EW_{phot})$ and amplitude, the maximum value for the flare amplitude of either event is estimated to be $\sim$0.02. However, the observed amplitudes of the two flares were determined to be 0.1882 and 0.1442, which are one magnitude larger than the estimated value. The only difference between this thesis's data format and the data format used by Pedersen et al. (2017) is that the flux is measured in $e^{-}s^{-1}$ rather than parts per thousand. However since the flare parameters depend on the ratios between fluxes, the different units should not have any effect on the results.

A study by Günther et al. (2020) on flares in F- to M-type stars observed by TESS found that two separate stars in their sample produced the most energetic and largest amplitude flares. They theorised that the flare energy depends on the radius and effective temperature of the star. This result suggests that HD 75202 is not a A-type star like those analysed by Pedersen et al. (2017). Furthermore, Pedersen et al. (2017) found no A-type star for which the observed flaring could be not be reasonably explained by a theory other than intrinsic flaring, such as spots or binarity.

9.5.3 Classification of HD 75202

The object HD 75202 has a number of classifications. It has been classified as: a contact binary of A7V-type stars with RR Lyrae type variability (Pribulla et al. 2003); a system with δ Sct variability (P = 0.291 d), 0.3" angular separation and a 'doubtful' A3-type Am primary star (Renson et al. 2009); a RRC variable, which is a RR Lyrae star with a nearly symmetric light curve (Samus' et al. 2017); a low-mass contact binary, also known as W UMa stars (Eker et al. 2009); an eclipsing contact binary with detected period P = 0.581 d (Avvakumova et al. 2013); and an RR Lyrae, non-spectroscopic binary (Rainer et al. 2016).

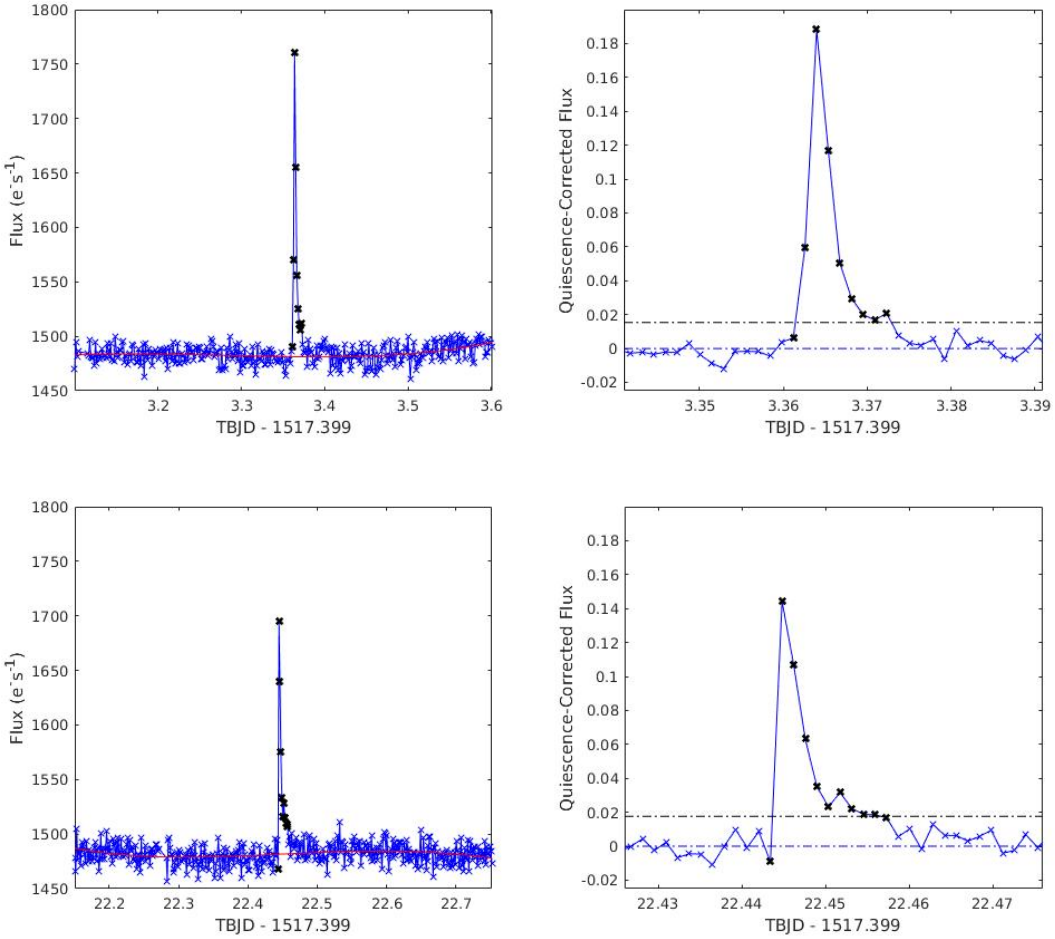

Figure 9.14: Confirmation of the light curve events of HD 75202 as flare events, using the criteria from Pedersen et al. (2017). The blue crosses indicate each data point in the light curve, where black crosses indicate suspected flare data points as well as the data point before the flare. The red line (left column) represents the modelled 'quiescent' light curve in the region of the flare, and the blue and black dashed lines (right column) represent the mean and 3σ levels for the remaining scatter after correcting for the quiescent light curve.

Several of these classifications indicate that the system is most likely a W UMa type binary, which commonly flare, with parameters such as its close orbit, period of ∼8 h, eclipsing events, and a harmonic period indicating possible ellipsoidal variability (Loeb et al. 2014). A-type stars are thought to possibly produce flares (if at all) due to star-spots or magnetic reconnection with a companion star (Balona 2012). Additionally, flares in binary or multiple systems are thought to be due to mass-transfer phenomena (Egge et al. 1983).

Due to the current ambiguity of the classification of HD 75202, it is not possible to confirm the nature of the system or the origin of the flare-like events in the photometric light curve. Further analysis of the $>$ 30 MUSICIAN HERCULES spectra of this target will be useful for any future work aiming to clarify the nature of the star system and its observing flaring events.

10. Conclusion

This thesis aimed to perform a comprehensive analysis of the five target stars HD 10167, HD 206481, HD 209295, HD 214291 and HD 216910 for the purposes of identifying their modes of oscillation. A summary of the results is presented in Table 10.1.

All stars were confirmed to be of the γ Dor pulsator class, with some stars pulsating as hybrids (HD 206481, HD 214291 and HD 216910).

The single star HD 206481 was observed to produce two possible absorption spikes in its cross-correlation line profiles. Previous work on absorption spikes in stellar spectra suggest that such periodic features are due to internal pulsations and local hydrodynamic effects (Harrington et al. 2016) or non-radial pulsations (Maintz et al. 2003). The absorption spikes for HD 206481 are only detected in five spectra over a period of $\sim$1.6 years. A pulsation of this period would imply that HD 206481 is a long-period variable rather than a γ Dor star. Further spectroscopic observations of this star are required in order to confirm or refute the origin of the absorption spikes.

Binary stars HD 214291 and HD 209295 exhibited photometric frequencies in their TESS light curves which are exact multiples of their orbital frequencies. This phenomenon is most likely due to tidally-locking which results in the excitation of numerous δ Sct frequencies. Furthermore, the radial velocity orbital solution determined by this thesis was found to have a $\sim$50% smaller *rms* value than the solution found by De Cat et al. (2006a).

A peculiar observation was the velocity amplitude of the only mode identified fro the secondary star of HD 214291, which was considerably smaller than that of its primary companion. This result was unexpected for binary stars with similar spectral classifications. Additionally, TD-1 UV flux observations of the system are generally of the same magnitude as the UV fluxes observed for HD 209295. This thesis proposes that the nature of the secondary component of HD 214291 is a degenerate star. The fact that this component is observed in the spectra indicates that it is not a 'dark' component, which will allow future analyses of this system to easily identify its nature.

Table 10.1: A summary of the modes of pulsation and subsequent variability classifications found by this thesis for the five target stars.

	Gaia Parameters			This Thesis's Results						
					Pulsation Parameters					
HD	$T_{\rm eff}$ (K) ±324 K	L ($L_\odot$) ±10%	R ($R_\odot$)	$v \sin i$ (km s^{-1})	i (°)	f (d^{-1})	Amp. (km s^{-1})	Mode (l,m)	Pulsator Class	Notes
10167	7013.5	12.606	$2.40^{+0.16}_{-0.08}$	3.76	33.0	1.10907	3.23	(1,-1)	γ Dor	C, [1]
					22.1	0.63450	5.81	(1,-1)		
					22.8	0.25353	1.94	(0,0)		
					55.7	2.37577	1.29	(1,1)		
					70.4	0.48255	0.645	(1,0)		
				0.652	79.3	0.40376	5.81	(1,-1)	γ Dor	
					8.18	1.51979	16.1	(2,-1)		
					26.8	1.50146	3.87	(3,2)		
					9.59	1.43585	3.87	(3,1)		
					15.3	3.12483	12.3	(3,2)		
206481	6989.54	5.647	$1.62^{+0.08}_{-0.04}$	80.0		1.60636	2.46	(1,1)	γ Dor/δ Sct hybrid	R, [2]
					49.1	3.71918	1.94	(2,2)		
						5.8255	2.58	(3,-2)		
209295	7697.9	12.764	$2.01^{+0.09}_{-0.16}$	85.4	55.8	1.17277	6.13	(3,1)	δ Sct/γ Dor hybrid	R, [3]

Table 10.1: (Continued) A summary of the modes of pulsation and subsequent variability classifications found by this thesis for the five target stars.

	Gaia Parameters			This Thesis's Results						
					Pulsation Parameters					
HD	$T_{\rm eff}$ (K) ±324 K	L ($L_\odot$) ±10%	R ($R_\odot$)	$v \sin i$ (km s^{-1})	i (°)	f (d^{-1})	Amp. (km s^{-1})	Mode (l,m)	Pulsator Class	Notes
214291	6129.75	18.124	$3.77^{+0.1}_{-0.1}$	66.7	31.1	0.50171	1.29	(1,1)	γ Dor/δ Sct hybrid	CR, [4]
				64.2	80.2	0.50076	5.16	(3,-2)	γ Dor/δ Sct hybrid	
216910	7003.93	8.286	$1.95^{+0.14}_{-0.08}$	93.6	50.8	1.62960	12.3	(3,0)	γ Dor	A, [5]
						1.71208	7.74	(3,0)		
						2.40211	7.74	(3,0)		
						1.43907	6.45	(3,0)		
						0.26596	1.94	(3,-3)		

Notes

Legend: C = Confirmed the classification by the reference; R = Refined the classification by the reference; A = Agreed with the classification by the reference.

References: [1] Handler et al. (2002a), [2] Eyer et al. (2000), [3] Handler et al. (2002b), [4] De Cat et al. (2006a), [5] De Cat et al. (2006b).

Acknowledgements

I would like to thank a number of people for their contributions to my completion of this thesis. My supervisor Karen, who sparked my interest in asteroseismology. Ruchita, who made this thesis year five stellar magnitudes more enjoyable with all the hours of chatting. My parents, Chris and Shirley, who are always interested to hear about my latest analysis or learned astrophysical concepts. And lastly, my partner Connor, for just always being there.

This work has made use of data from the European Space Agency (ESA) mission *Gaia* (`https://www.cosmos.esa.int/gaia`), processed by the *Gaia* Data Processing and Analysis Consortium (DPAC, `https://www.cosmos.esa.int/web/gaia/dpac/consortium`). Funding for the DPAC has been provided by national institutions, in particular the institutions participating in the *Gaia* Multilateral Agreement. This research has made use of the SIMBAD database, operated at CDS, Strasbourg, France. Mode identification results were obtained with the software package FAMIAS developed in the framework of the FP6 European Coordination Action HELAS (http://www.helas-eu.org/).

Bibliography

Aerts, C. (2007). *Lecture Notes*.

Aerts, C., Christensen-Dalsgaard, J., and Kurtz, D. W. (2010). *Asteroseismology*. Springer.

Aerts, C., Eyer, L., and Kestens, E. (1998). "The Discovery of New γ Doradus Stars From the HIPPARCOS Mission". In: *Astronomy & Astrophysics* 337.

Andrae, R., Fouesneau, M., Creevey, O., Ordenovic, C., Mary, N., Burlacu, A., Chaoul, L., Jean-Antoine-Piccolo, A. et al. (2018). "Gaia Data Release 2". In: *Astronomy & Astrophysics* 616. DOI: 10.1051/0004-6361/201732516.

Antoci, V., Cunha, M. S., Bowman, D. M., Murphy, S. J., Kurtz, D. W., Bedding, T. R., Borre, C. C., Christophe, S. et al. (2019). "The First View of δ Scuti and γ Doradus Stars with the TESS Mission". In: *Monthly Notices of the Royal Astronomy Society* 490. DOI: 10.1093/mnras/stz2787.

Avvakumova, E. A., Malkov, O. Yu., and Kniazev, A. Yu. (2013). "VizieR Online Data Catalog: Catalogue of Eclipsing Variables. Version 2 (Avvakumova+, 2013)". In: *VizieR Online Data Catalog*.

Bacon, R. and Monnet, G. (2017). *Optical 3-D Spectroscopy for Astronomy*. John Wiley & Sons.

Baglin, A., Breger, M., Chevalier, C., Hauck, B., Le Contel, J. M., Sareyan, J. P., and Valtier, J. C. (1973). "Delta Scuti Stars." In: 23.

Baker, N. H. (1963). "Pulsation Instability of Cepheid Models". In: *The Astrophysical Journal* 68. DOI: 10.1086/109004.

Baker, N. H. and Kippenhahn, R. (1962). "The Pulsations of Models of δ Cephei Stars. With 17 Figures in the Text". In: 54.

Baldwin, E. and Frazier, S. (2017). *ESA, NASA's SOHO Reveals Rapidly Rotating Solar Core*. URL: https://www.nasa.gov/feature/goddard/2017/esa-nasa-s-soho-reveals-rapidly-rotating-solar-core.

Balona, L. A. (2012). "Kepler Observations of Flaring in A-F type Stars". In: 423. DOI: 10.1111/j.1365-2966.2012.21135.x.

— (2018a). "Gaia Luminosities of Pulsating A-F Stars in the Kepler Field". In: *Monthly Notices of the Royal Astronomy Society* 479. DOI: 10.1093/mnras/sty1511.

— (2018b). "Pulsation in Intermediate-Mass Stars". In: *Frontiers in Astronomy and Space Sciences* 5. DOI: 10.3389/fspas.2018.00043.

Balona, L. A. and Dziembowski, W. A. (2011). "Kepler Observations of δ Scuti Stars". In: *Monthly Notices of the Royal Astronomy Society* 417. DOI: 10.1111/j.1365-2966.2011.19301.x.

Balona, L. A., Krisciunas, K., and Cousins, A. W. J. (1994). "Gamma Doradus: Evidence for a New Class of Pulsating Star." In: *Monthly Notices of the Royal Astronomy Society* 270. DOI: 10.1093/mnras/270.4.905.

Barbara A. Milkulski Archive for Space Telescopes (2020). URL: http://archive.stsci.edu/.

Bertelli, G., Girardi, L., Marigo, P., and Nasi, E. (2008). "Scaled Solar Tracks and Isochrones in a Large Region of the Z-Y Plane; I. From the ZAMS to the TP-AGB end for 0.15-2.5 $M_{\odot}$ stars". In: *Astronomy & Astrophysics* 484. DOI: 10.1051/0004-6361:20079165.

Böhm-Vitense, E. (1992). *Introduction to Stellar Astrophysics. Volume 3. Stellar Structure and Evolution*. Vol. 3.

Boutloukos, Stratos and Nollert, Hans-Peter (2007). "Eigenmode Frequency Distribution of Rapidly Rotating Neutron Stars". In: 75. DOI: 10.1103/PhysRevD.75.043007.

Bowman, D. M., Kurtz, D. W., Breger, M., Murphy, S. J., and Holdsworth, D. L. (2017). "Amplitude modulation in δ Sct stars: Statistics From an Ensemble of Kepler Targets". In: *European Physical Journal Web of Conferences*. Vol. 160. European Physical Journal Web of Conferences. DOI: 10.1051/epjconf/201716003008.

Breger, M. et al. (1993). "Non-Radial Pulsation of the Delta Scuti Star BU CANCRI in the Praesepe Cluster". In: *Astronomy & Astrophysics* 271.

Chevalier, C. (1971). "Short-Period Variables. VIII. Evolution and Pulsation of Delta Scuti Stars." In: 14.

Clayton, M. (1996). *Starlink Guide 9.2: Introduction to Echelle Spectroscopy*. Starlink Project.

Cousins, A. W. J. and Warren, P. R. (1963). "Variable Stars Observed During the Cape Bright Star Programme". In: *Monthly Notes of the Astronomical Society of South Africa* 22.

Cox, J. P. (1963). "On Second Helium Ionization as a Cause of Pulsational Instability in Stars." In: 138. DOI: 10.1086/147661.

— (1980). *Theory of Stellar Pulsation*.

Cox, J. P., Cox, A. N., Olsen, K. H., King, D. S., and Eilers, D. D. (1966). "Self-Excited Radial Oscillations in Thin Stellar Envelopes. I". In: 144. DOI: 10.1086/148702.

De Cat, P., Eyer, L., Cuypers, J., Aerts, C., Vandenbussche, B., Uytterhoeven, K., Reyniers, K., Kolenberg, K. et al. (2006a). "A Spectroscopic Study of Southern (Candidate) γ Doradus Stars - I. Time Series Analysis". In: *Astronomy & Astrophysics* 449. DOI: 10.1051/0004-6361:20053655.

De Cat, P., Goossens, K., Bouckaert, F., Eyer, L., Cuypers, J., De Ridder, J., Aerts, C., Dupret, M.-A. et al. (2006b). "Observational Results for Northern and Southern (Candidate) γ Doradus Stars". In: *Memorie della Societá Astronomica Italiana* 77.

Dupret, M.-A., Grigahcène, A., Garrido, R., Gabriel, M., and Scuflaire, R. (2005). "Convection-Pulsation Coupling. II. Excitation and Stabilization Mechanisms in δ Sct and γ Dor stars". In: 435. DOI: 10.1051/0004-6361:20041817.

Eddington, A. S. (1926). *The Internal Constitution of the Stars*. Cambridge University Press.

Egge, K. E. and Pettersen, B. R. (1983). "A Bright Spot and a Serendipitous Stellar Flare on the Contact-Binary VW CEP". In: *IAU Colloq. 71: Activity in Red-Dwarf Stars*. Ed. by Byrne, P. B. and Rodono, M. Vol. 102. Astrophysics and Space Science Library. DOI: 10.1007/978-94-009-7157-8_66.

Eggen, Olin J. (1956a). "ρ Puppis: A New Short-Period Variable Star". In: 68, p. 238. DOI: 10.1086/126922.

— (1956b). "Two New Bright Variable Stars: δ Delphini and δ Capricorni". In: 68, p. 541. DOI: 10.1086/126996.

Eker, Z., Bilir, S., Yaz, E., Demircan, O., and Helvaci, M. (2009). "New Absolute Magnitude Calibrations for W Ursa Majoris Type Binaries". In: *Astronomische Nachrichten* 330. DOI: 10.1002/asna.200811041.

The HIPPARCOS and TYCHO Catalogues. Astrometric and Photometric Star Catalogues Derived From the ESA HIPPARCOS Space Astrometry Mission (1997). Vol. 1200. ESA Special Publication.

Eyer, L. and Aerts, C. (2000). "A Search for new γ Doradus stars in the Geneva Photometric Database". In: *Astronomy & Astrophysics* 361.

Eyer, L., Aerts, C., Van Loon, M., Bouckaert, F., and Cuypers, J. (2002). "The γ Doradus Stars Campaign". In: *Observational Aspects of Pulsating B- and A Stars*. ASP Conference Series 256.

Fausnaugh, M. M., Caldwell, D. A., Jenkins, J. M., Smith, J. C., Twicken, J. D., Vanderspek, R., Doty, J. P., Li, J. et al. (2018). *TESS Data Release Notes - Sector 1, DR1*. Tech. rep.

Fekel, F. C., Henry, G. W., and Pourbaix, D. (2016). "The Spectroscopic Orbits of Five γ Doradus Stars". In: 151. DOI: 10.3847/0004-6256/151/2/26.

Fleming, S. (2018). *TESS Archive Manual*. URL: https://outerspace.stsci.edu/display/TESS/TESS+Archive+Manual.

Gaia Collaboration, Prusti, T., de Bruijne, J. H. J., Brown, A. G. A., Vallenari, A., Babusiaux, C., Bailer-Jones, C. A. L., Bastian, U. et al. (2016). "The Gaia Mission". In: *Astronomy & Astrophysics*. DOI: 10.1051/0004-6361/201629272.

Gaia Collaboration, Brown, A. G. A., Vallenari, A., Prusti, T., de Bruijne, J. H. J., Babusiaux, C., Bailer-Jones, C. A. L., Biermann, M. et al. (2018). "Gaia Data Release 2. Summary of the Contents and Survey Properties". In: *Astronomy & Astrophysics* 616. DOI: 10.1051/0004-6361/201833051.

Gillon, M. and Magain, P. (2006). "High Precision Determination of the Atmospheric Parameters and Abundances of the COROT Main Targets". In: 448. DOI: 10.1051/0004-6361:20053965.

Grigahcène, A., Antoci, V., Balona, L. A., Catanzaro, G., Daszyńska-Daszkiewicz, J., Guzik, J. A., Handler, G., Houdek, G. et al. (2010). "Hybrid γ Doradus-δ Scuti Pulsators: New Insights Into the Physics of the Oscillations From Kepler Observations". In: *The Astrophysical Journal Letters* 713. DOI: 10.1088/2041-8205/713/2/L192.

Günther, M. N., Zhan, Z., Seager, S., Rimmer, P. B., Ranjan, S., Stassun, K. G., Oelkers, R. J., Daylan, T. et al. (2020). "Stellar Flares From the First TESS Data Release: Exploring a New Sample of M Dwarfs". In: 159. DOI: 10.3847/1538-3881/ab5d3a.

Guzik, J. A., Kaye, A. B., Bradley, P. A., Cox, A. N., and Neuforge, C. (2000). "Driving the Gravity-Mode Pulsations in γ Doradus Variables". In: *The Astrophysical Journal* 542. DOI: 10.1086/312908.

Handberg, R. and Lund, M. N. (2018). *TESS Data Release Notes - Data Release 0 for TESS Sector 1*. Tech. rep. TESS Data for Asteroseismology (T'DA).

— (2019). *TESS Data Release Notes - Data Release 4 for TESS Sectors 1+2*. Tech. rep. TESS Data for Asteroseismology (T'DA).

Handler, G. (1999). "The Domain of γ Doradus Variables in the Hertzsprung-Russell Diagram". In: *Monthly Notices of the Royal Astronomy Society* 309. DOI: 10.1046/j.1365-8711.1999.03005.x.

— (2012). *Asteroseismology*.

Handler, G. and Shobbrook, R. R. (2002a). "On the Relationship Between the δ Scuti and γ Doradus Pulsators". In: *Monthly Notices of the Royal Astronomy Society* 333. DOI: 10.1046/j.1365-8711.2002.05401.x.

Handler, G., Balona, L. A., Shobbrook, R. R., Koen, C., Bruch, A., Romero-Colmenero, E., Pamyatnykh, A. A., Willems, B. et al. (2002b). "Asteroseismology and Force Oscillations of the Simultaneous p-Mode and g-Mode Pulsator HD 209295". In: *Radial and Non-Radial Pulsations as Probes of Stellar Physics*. ASP Conference Series 259.

— (2002c). "Discovery and Analysis of p-Mode and g-Mode Oscillations in the A-Type Primary of the Eccentric Binary HD 209295". In: *Monthly Notices of the Royal Astronomy Society* 333. DOI: 10.1046/j.1365-8711.2002.05295.x.

Harrington, D., Koenigsberger, G., Olgun, E., Ilyin, I., Berdyugina, S. V., Lara, B., and Moreno, E. (2016). "Alpha Virginis: Line-Profile Variations and Orbital Elements". In: 590. DOI: 10.1051/0004-6361/201526507.

Hearnshaw, J. B., Barnes, S. I., Kershaw, G. M., Frost, N., Graham, G., Ritchie, R., and Nankivell, G. R. (2002). "The Hercules Échelle Spectrograph at Mt John". In: *Experimental Astronomy* 13. DOI: 10.1023/A:1023770225275.

Jenkins, J. M., Twicken, J. D., McCauliff, S., Campbell, J., Sanderfer, D., Lung, D., Mansouri-Samani, M., Girouard, F. et al. (2016). "The TESS Science Processing Operations Center". In: vol. 9913. Society of Photo-Optical Instrumentation Engineers (SPIE) Conference Series. DOI: 10.1117/12.2233418.

Kahraman Aliçavuş, F., De Cat, P., Soydugan, E., Kolaczkowski, Z., Ostrowski, J., Telting, J. H., Uytterhoeven, K., Poretti, E. et al. (2016). "Spectroscopic Survey of γ Doradus Stars - I. Comprehensive Atmospheric Parameters and Abundance Analysis of γ Doradus Stars". In: *Monthly Notices of the Royal Astronomy Society* 458. DOI: 10.1093/mnras/stw393.

Kaye, A. B., Handler, G., Krisciunas, K., Poretti, E., and Zerbi, F. M. (1999). "Gamma Doradus Stars: Defining a New Class of Pulsating Variables". In: 111. DOI: 10.1086/316399.

Lang, K. R. (2013). *The Life and Death of Stars*. Cambridge University Press.

Ledoux, P. (1941). "On the Vibrational Stability of Gaseous Stars." In: 94. DOI: 10.1086/144359.

— (1978). "Stellar Stability." In: *Theoretical Principles in Astrophysics and Relativity*.

Loeb, A., Shvartzvald, Y., and Maoz, D. (2014). "Fast Radio Bursts May Originate From Nearby Flaring Stars." In: 439. DOI: 10.1093/mnrasl/slt177.

Lomb, N. R. (1976). "Least-Squares Frequency Analysis of Unequally Spaced Data". In: *Astrophysics and Space Science* 39. DOI: 10.1007/BF00648343.

Lopes, I. P. (2001). "Non-Radial Adiabatic Oscillations of Stars. Mode Classification of Acoustic-Gravity Waves". In: 373. DOI: 10.1051/0004-6361:20010130.

Luger, R., Agol, E., Foreman-Mackey, D., Fleming, D. P., Lustig-Yaeger, J., and Deitrick, R. (2019). "Starry: Analytic Occultation Light Curves". In: *The Astronomical Journal* 157. DOI: 10.3847/1538-3881/aae8e5.

Maintz, M., Rivinius, Th., Štefl, S., Baade, D., Wolf, B., and Townsend, R. H. D. (2003). "Stellar and Circumstellar Activity of the Be Star Omega CMa. III. Multiline Non-Radial Pulsation Modeling". In: 411. DOI: 10.1051/0004-6361:20031375.

Maisonneuve, F. et al. (2011). "Frequency Analysis and Pulsational Mode Identification of Two γ Doradus Stars: HD 40745 and HD 189631". In: 415. DOI: 10.1111/j.1365-2966.2010.17918.x.

Mantegazza, L., Poretti, E., and Zerbi, F. M. (1994). "Unusual Variability Among Early F-Type Stars: HD 224638 and HD 224945." In: *Monthly Notices of the Royal Astronomy Society* 270. DOI: 10.1093/mnras/270.2.439.

Marshall, M. P. and van Horn, H. M. (1973). "Radial Pulsations of Pre-White Stars. II. Pulsational Stability of 12C Shell-Burning Stars". In: 182. DOI: 10.1086/152191.

Murphy, S. J., Hey, D., Van Reeth, T., and Bedding, T. R. (2019). "Gaia-Derived Luminosities of Kepler A/F Stars and the Pulsator Fraction Across the δ Scuti Instability Strip". In: *Monthly Notices of the Royal Astronomy Society* 485. DOI: 10.1093/mnras/stz590.

National Aeronautics & Space Administration (NASA) (2019a). *Mission Objectives*. URL: https://heasarc.gsfc.nasa.gov/docs/tess/objectives.html.

— (2019b). *Operations*. URL: https://heasarc.gsfc.nasa.gov/docs/tess/operations.html.

Nordstrom, B., Stefanik, R. P., Latham, D. W., and Andersen, J. (1997). "Radial Relocities, Rotations, and Duplicity of a Sample of Early F-Type Dwarfs". In: 126. DOI: 10.1051/aas:1997248.

Olsen, E.H. (1994). "Strömgren Photometry of F- and G-Type Stars Brighter Than V = 9.6. I. UVBY Photometry". In: *Astronomy & Astrophysics* 106.

Pamyatnykh, A. A. (2000). "Pulsational Instability Domain of δ Scuti Variables". In: *Delta Scuti and Related Stars*. Vol. 210. Astronomical Society of the Pacific Conference Series.

Pedersen, M. G., Antoci, V., Korhonen, H., White, T. R., Jessen-Hansen, J., Lehtinen, J., Nikbakhsh, S., and Viuho, J. (2017). "Do A-Type Stars Flare?" In: 466. DOI: 10.1093/mnras/stw3226.

Pesnell, W. D. (1987). "A New Driving Mechanism for Stellar Pulsations". In: 314. DOI: 10.1086/165089.

Pribulla, T., Kreiner, J. M., and Tremko, J. (2003). "Catalogue of the Field Contact Binary Stars". In: *Contributions of the Astronomical Observatory Skalnate Pleso* 33.

Rainer, M., Poretti, E., Mistò, A., Panzera, M. R., Molinaro, M., Cepparo, F., Roth, M., Michel, E. et al. (2016). "The SpaceInn-SISMA Database: Characterization of a Large Sample of Variable and Active Stars by Means of Harps Spectra". In: 152. DOI: 10.3847/0004-6256/152/6/207.

Reegen, P. (2007). In: *Astronomy & Astrophysics* 467. DOI: 10.1051/0004-6361:20066597.

— (2010). *SigSpec's User Manual*.

Renson, P. and Manfroid, J. (2009). "Catalogue of Ap, HgMn and Am stars". In: 498. DOI: 10.1051/0004-6361/200810788.

Ricker, G. R., Winn, J. N., Vanderspek, R., Latham, D. W., Bakos, G. Á., Bean, J. L., Berta-Thompson, Z. K., Brown, T. M. et al. (2015). "Transiting Exoplanet Survey Satellite (TESS)". In: *Journal of Astronomical Telescopes, Instruments, and Systems* 1. DOI: 10.1117/1.JATIS.1.1.014003.

Rosseland, S. and Randers, G. (1983). "On the Stability of Pulsating Stars". In: *Astrophysica Norvegica* 3.

Royer, F., Zorec, J., and Gómez, A. E. (2007). "Rotational Velocities of A-Type Stars. III. Velocity Distributions". In: 463. DOI: 10.1051/0004-6361:20065224.

Samus', N. N., Kazarovets, E. V., Durlevich, O. V., Kireeva, N. N., and Pastukhova, E. N. (2017). "General Catalogue of Variable Stars: Version GCVS 5.1". In: *Astronomy Reports* 61. DOI: 10.1134/S1063772917010085.

Scargle, J. D. (1982). "Studies in Astronomical Time Series Analysis. II. Statistical Aspects of Spectral Analysis of Unevenly Spaced Data." In: *The Astrophysical Journal* 263. DOI: 10.1086/160554.

Schröder, C., Reiners, A., and Schmitt, J. H. M. M. (2009). "Ca II HK Emission in Rapidly Rotating Stars. Evidence for an Onset of the Solar-Type Dynamo". In: 493. DOI: 10.1051/0004-6361:200810377.

Skuljan, J. (2004). *Specbin: A Software Package for the Analysis of Radial-Velocity Curves of Spectroscopic Binary Stars*.

Starrfield, S. (1987). "Non-Radial Pulsations of Hot Evolved Stars". In: *IAU Colloq. 95: Second Conference on Faint Blue Stars*.

Sterne, T. E. (1938). "The Secondary Variation of δ Scuti". In: 87. DOI: 10.1086/143913.

Technology (MIT), Massachusetts Institute of (2020). *TESS Observations*. URL: https://tess.mit.edu/observations/.

TESS Asteroseismic Science Consortium (TASC) (n.d.). *TESS Asteroseismic Science Operations Center*. URL: https://tasoc.dk.

Thompson, G. I., Nandy, K., Jamar, C., Monfils, A., Houziaux, L., Carnochan, D. J., and Wilson, R. (1978). *Catalogue of Stellar Ultraviolet Fluxes: A Compilation of Absolute Stellar Fluxes Measured by the Sky Survey Telescope (S2/68) Aboard the ESRO Satellite TD-1 /*.

Tkachenko, A., Aerts, C., Yakushechkin, A., Debosscher, J., Degroote, P., Bloemen, S., Pápics, P. I., de Vries, B. L. et al. (2013). "Detection of a Large Sample of γ Doradus Stars From Kepler Space Photometry and High-Resolution Ground-Based Spectroscopy". In: 556. DOI: 10.1051/0004-6361/201220978.

Van Reeth, T., Tkachenko, A., Aerts, C., Pápics, P. I., Triana, S. A., Zwintz, K., Degroote, P., Debosscher, J. et al. (2015). "Gravity-mode Period Spacings as a Seismic Diagnostic for a Sample of γ Doradus Stars from Kepler Space Photometry and High-resolution Ground-based Spectroscopy". In: 218. DOI: 10.1088/0067-0049/218/2/27.

Wenger, M., Ochsenbein, F., Egret, D., Dubois, P., Bonnarel, F., Borde, S., Genova, F., Jasniewicz, G. et al. (2000). "The SIMBAD Astronomical Database. The CDS Reference Database for Astronomical Objects". In: 143. DOI: 10.1051/aas:2000332.

Xiong, D. R., Deng, L., Zhang, C., and Wang, K. (2016). "Turbulent Convection and Pulsation Stability of Stars. II. Theoretical Instability Strip for δ Scuti and γ Doradus Stars". In: *Monthly Notices of the Royal Astronomical Society* 457. DOI: 10.1093/mnras/stw047.

Zima, W. (2006). "A New Spectroscopic Mode Identification Method". In: *Communications in Asteroseismology* 147. DOI: 10.1553/cia147s56.

— (2008). *Frequency Analyis and Mode Identification for Asteroseismology (FAMIAS).*

Appendix A. FAMIAS Fourier Spectra

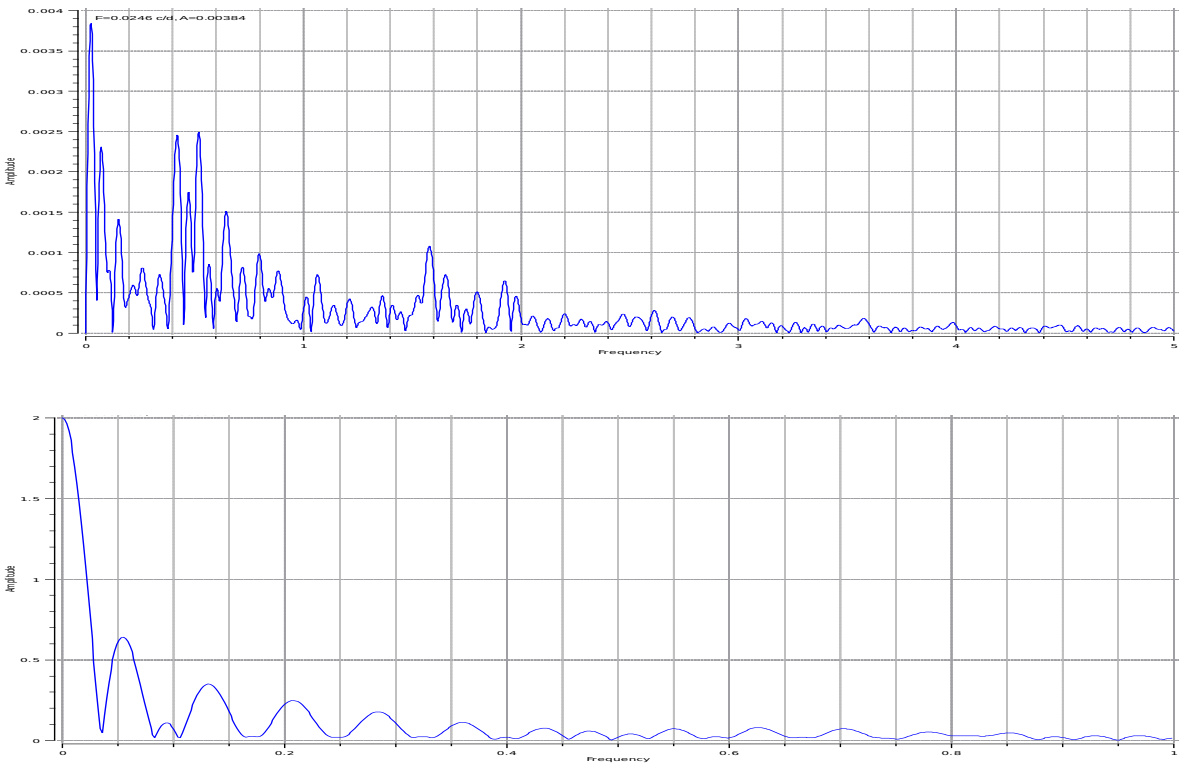

(b)

Figure A.1: Fourier spectrum from FAMIAS for the HD 10167 light curve for 0–5 d^{-1} (top) and the spectral window from 0–1 d^{-1} (bottom).

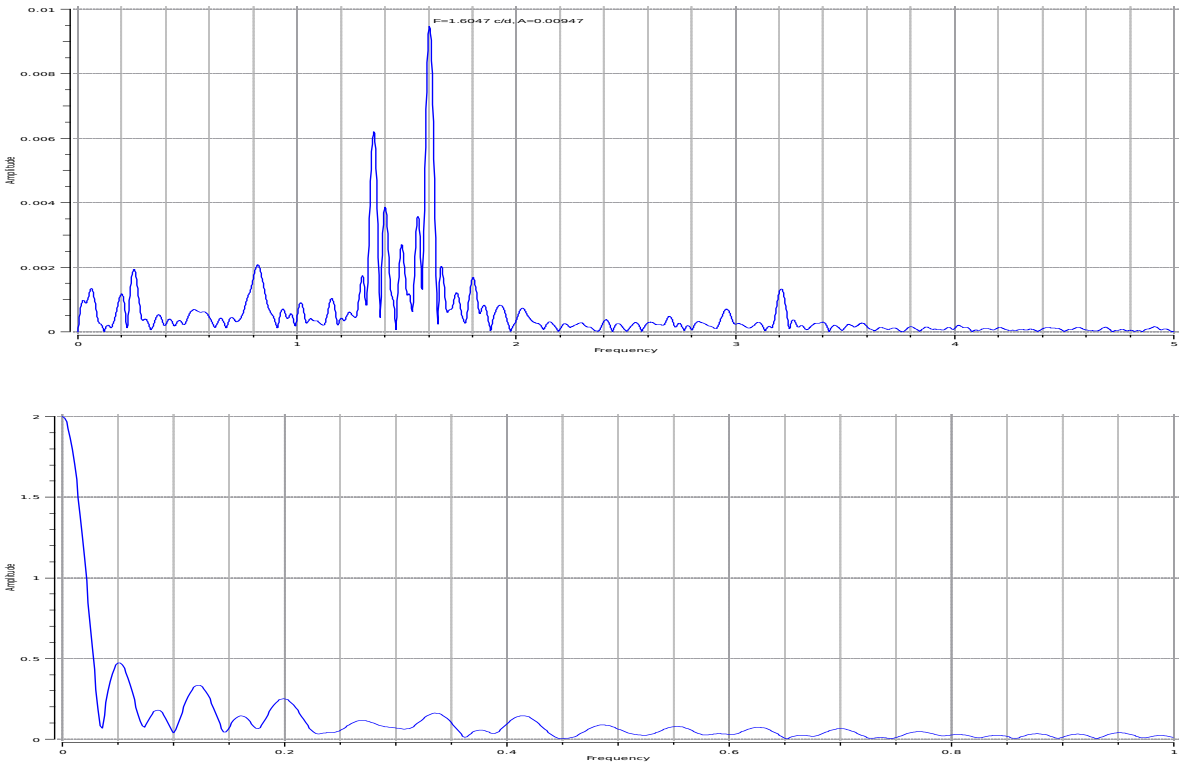

Figure A.2: Fourier spectrum from FAMIAS for the HD 206481 light curve for 0–5 d^{-1} (top) and the spectral window from 0–1 d^{-1} (bottom).

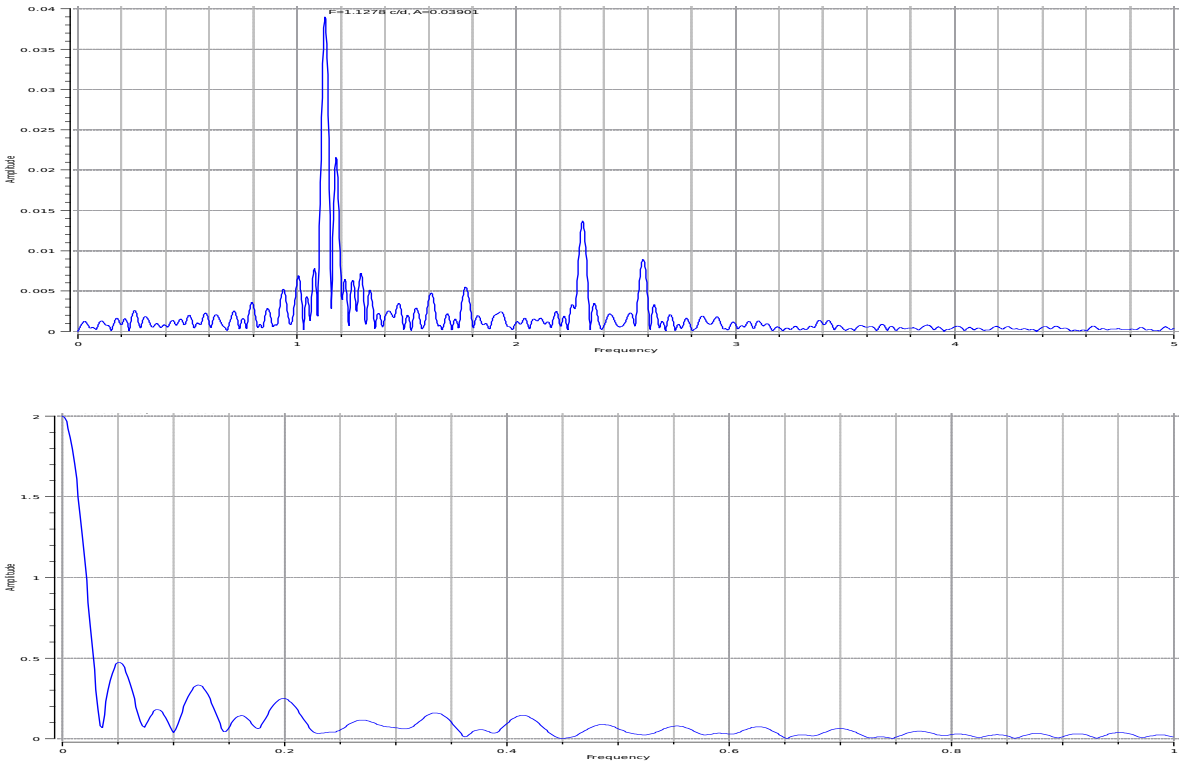

Figure A.3: Fourier spectrum from FAMIAS for the HD 209295 light curve for 0–5 d^{-1} (top) and (b) the spectral window from 0–1 d^{-1} (bottom).

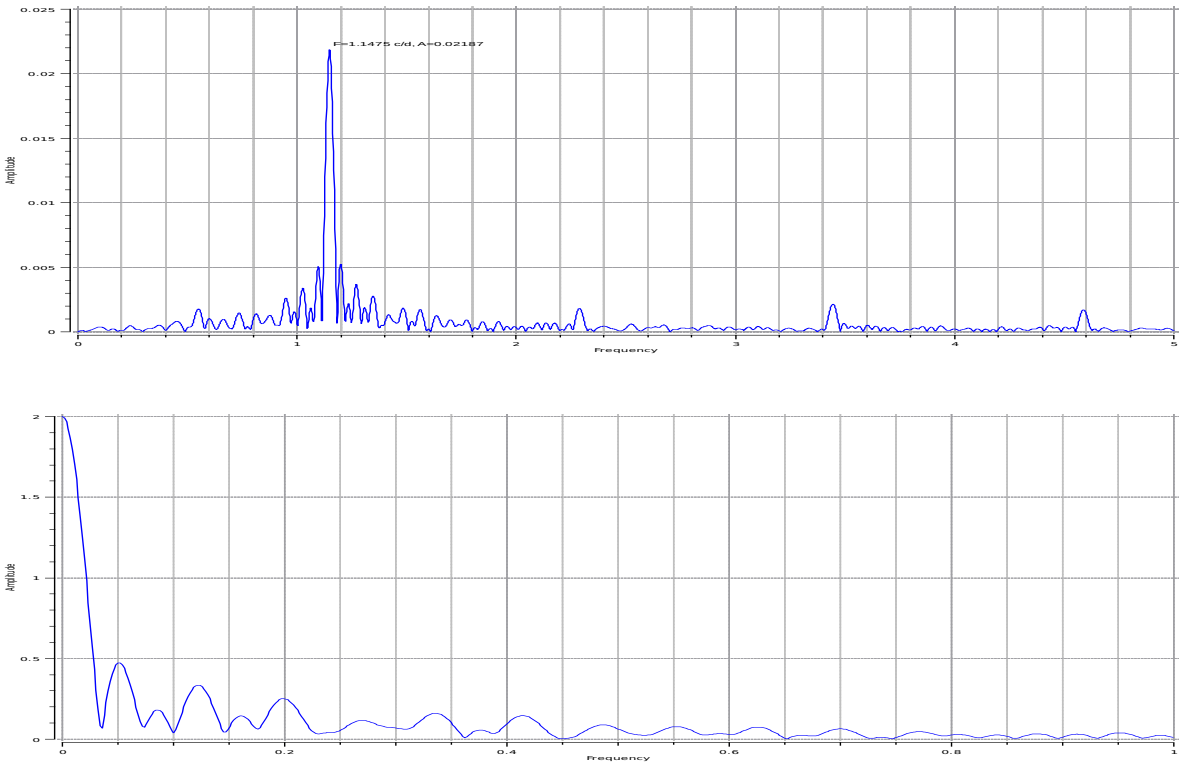

Figure A.4: Fourier spectrum from FAMIAS for the HD 214291 light curve for 0–5 d^{-1} (top) and the spectral window from 0–1 d^{-1} (bottom).

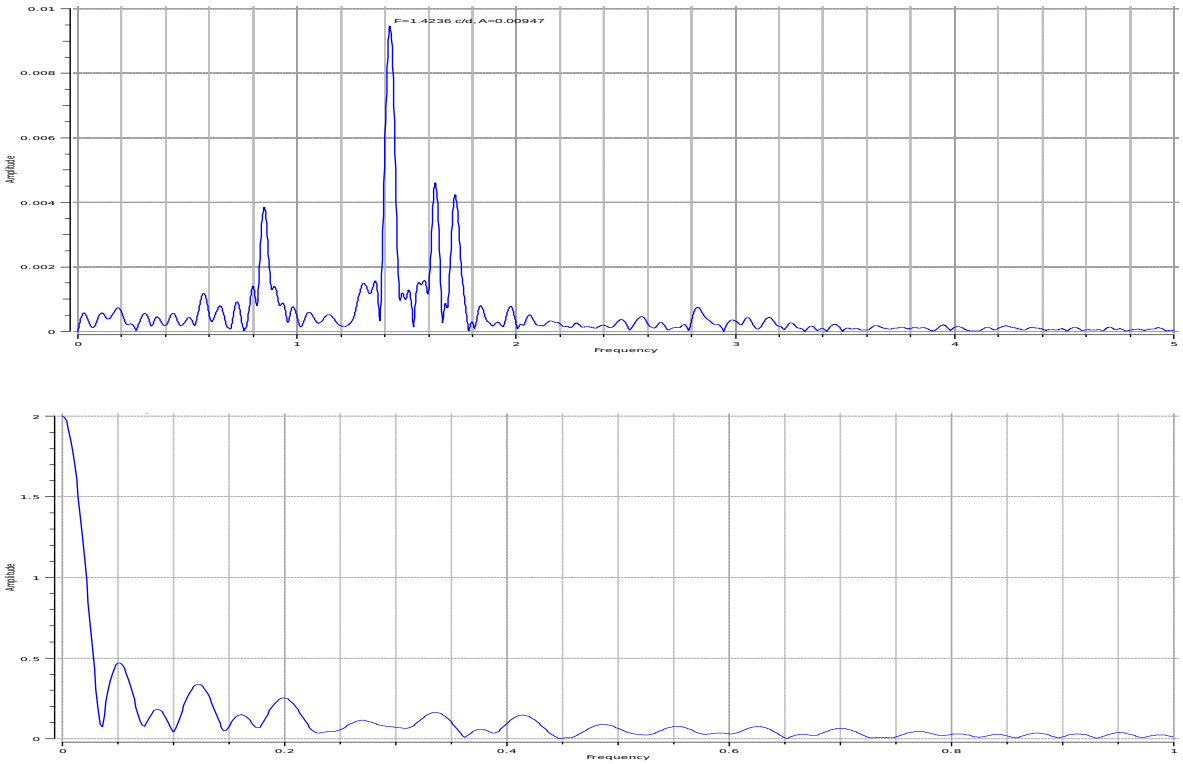

Figure A.5: Fourier spectrum from FAMIAS for the HD 216910 light curve for 0–5 d^{-1} (top) and the spectral window from 0–1 d^{-1} (bottom).

Appendix B. Frequencies Detected in TASOC Light Curves

Table B.1: Frequencies detected by SigSpec in the TASOC light curve for HD 10167. Values have been rounded to 6 s.f., 2 s.f. and 3 s.f. respectively

	Frequency (d^{-1})	Amplitude (mag)	S/N	Coupling
f_1	0.509943	0.0039	635	
f_2	0.413458	0.0021	696	
f_3	0.0825661	0.0018	744	
f_4	0.00531304	0.018	1510	
f_5	1.573600	0.00089	390	
f_6	0.151233	0.0013	388	
f_7	0.633000	0.00078	372	
f_8	0.498590	0.0029	328	
f_9	1.65555	0.00087	342	
f_{10}	0.885482	0.0010	336	$f_7 + f_{13}$ $f_{41} + f_{49}$
f_{11}	0.794767	0.0011	323	
f_{12}	1.91823	0.00070	3267	
f_{13}	0.252400	0.00058	310	
f_{14}	1.00048	0.00097	277	
f_{15}	0.729185	0.00085	277	
f_{16}	1.80564	0.00062	233	
f_{17}	0.941741	0.00088	229	
f_{18}	1.29916	0.00043	166	
f_{19}	0.336157	0.0068	165	
f_{20}	2.54512	0.00036	167	
f_{21}	1.35678	0.00031	117	
f_{22}	0.668612	0.00089	101	
f_{23}	1.53329	0.00032	113	$f_{13} + f_{39}$
f_{24}	1.14893	0.00018	56.4	
f_{25}	2.44727	0.00019	54.7	$f_{29} + f_{41}$ $f_{18} + f_{24}$
f_{26}	1.72627	0.00030	48.2	
f_{27}	2.61071	0.00013	35.5	$f_{24} + f_{28}$

Table B.1: (Continued) Frequencies detected by SigSpec in the TASOC light curve for HD 10167. Values have been rounded to 6 s.f., 2 s.f. and 3 s.f. respectively.

	Frequency (d^{-1})	Amplitude (mag)	S/N	Coupling
f_{28}	1.46098	0.00021	35.4	
f_{29}	2.12211	0.00022	36.2	
f_{30}	2.01310	0.00014	28.6	
f_{31}	3.57657	0.00010	25.7	
f_{32}	1.05612	0.00015	25.6	
f_{33}	3.15139	0.000094	23.7	
f_{34}	2.49672	0.00014	24.1	
f_{35}	1.70035	0.00027	18.0	
f_{36}	0.970106	0.00042	18.7	
f_{37}	3.24260	0.000090	15.6	
f_{38}	3.02670	0.000098	17.0	
f_{39}	1.28189	0.00029	15.6	
f_{40}	2.06970	0.00019	15.3	$f_{13} + f_{47}$
f_{41}	0.324994	0.00032	13.7	
f_{42}	2.76893	0.00011	13.8	
f_{43}	2.37074	0.000095	12.1	
f_{44}	3.49296	0.000077	11.2	
f_{45}	27.3001	0.000090	10.9	
f_{46}	3.39086	0.000086	10.4	$f_{18} + f_{53}$
f_{47}	1.81773	0.00028	9.14	$f_{22} + f_{24}$
f_{48}	27.3161	0.000084	8.24	
f_{49}	0.560215	0.00011	7.68	
f_{50}	3.33513	0.000068	7.43	
f_{51}	2.89705	0.000064	6.88	
f_{52}	4.20414	0.000059	6.46	
f_{53}	2.09123	0.00014	6.24	$f_{17} + f_{24}$
f_{54}	4.13853	0.000060	5.97	$2f_{40}$
f_{55}	2.24589	0.000060	5.66	
f_{56}	26.6459	0.000057	5.42	
f_{57}	4.42508	0.000049	5.17	$f_9 + f_{42}$
f_{58}	26.8133	0.000081	4.79	
f_{59}	26.9212	0.000055	4.63	
f_{60}	26.7971	0.000087	5.97	
f_{61}	2.71992	0.000051	4.28	

Table B.2: Frequencies detected by SigSpec in the TASOC light curve for HD 206481. Values have been rounded to 6 s.f., 2 s.f. and 3 s.f. respectively

	Frequency (d^{-1})	Amplitude (mag)	S/N	Coupling
f_1	1.60809	0.0089	2150	
f_2	1.34846	0.0062	2280	
f_3	0.810707	0.0023	622	
f_4	0.259740	0.0025	577	
f_5	1.40896	0.0020	671	
f_6	0.833739	0.0020	484	
f_7	3.21179	0.0013	381	
f_8	0.0599715	0.0020	379	
f_9	1.50450	0.00097	395	
f_{10}	1.86176	0.00096	340	
f_{11}	0.763312	0.00097	310	
f_{12}	1.57057	0.0048	318	
f_{13}	1.56066	0.0042	306	
f_{14}	0.0461664	0.0015	345	
f_{15}	0.192413	0.00098	341	
f_{16}	1.31737	0.00091	388	
f_{17}	2.94889	0.00072	348	
f_{18}	1.70883	0.00050	345	
f_{19}	0.530432	0.00080	346	
f_{20}	1.77311	0.00055	279	
f_{21}	1.20531	0.00049	282	
f_{22}	0.425605	0.00050	259	
f_{23}	1.24793	0.00069	254	
f_{24}	0.556687	0.00054	258	
f_{25}	2.704295	0.00058	270	
f_{26}	3.11677	0.00022	230	
f_{27}	0.162889	0.00037	213	
f_{28}	1.06277	0.00054	223	
f_{29}	0.650736	0.00070	182	
f_{30}	2.47878	0.00029	170	
f_{31}	0.255330	0.0019	167	
f_{32}	3.17576	0.00047	176	
f_{33}	2.40286	0.00028	169	
f_{34}	2.53456	0.00030	157	
f_{35}	0.384464	0.00033	156	
f_{36}	3.46964	0.0023	160	
f_{37}	2.99271	0.00026	166	
f_{38}	2.76740	0.00028	153	
f_{39}	0.486657	0.00028	148	
f_{40}	2.11861	0.00050	162	
f_{41}	3.39201	0.00026	148	
f_{42}	0.940152	0.00026	156	
f_{43}	2.30975	0.00020	129	
f_{44}	1.13318	0.00035	130	
f_{45}	2.19861	0.00022	136	

Table B.2: (Continued) Frequencies detected by SigSpec in the TASOC light curve for HD 206481. Values have been rounded to 6 s.f., 2 s.f. and 3 s.f. respectively.

	Frequency (d^{-1})	Amplitude (mag)	S/N	Coupling
f_{46}	2.12861	0.00051	143	
f_{47}	1.81114	0.00041	123	
f_{48}	2.04799	0.00024	141	
f_{49}	3.02793	0.00023	131	
f_{50}	3.30951	0.00018	124	
f_{51}	1.47310	0.00082	127	
f_{52}	0.986184	0.00028	143	
f_{53}	2.64316	0.00015	120	
f_{54}	0.637651	0.00042	63.3	
f_{55}	3.87091	0.00017	64.5	
f_{56}	2.03183	0.00018	50.8	
f_{57}	4.07098	0.000082	42.6	
f_{58}	3.97435	0.000079	40.1	
f_{59}	0.318948	0.00014	40.3	
f_{60}	6.39247	0.000068	34.9	
f_{61}	6.23855	0.000073	32.0	
f_{62}	3.58992	0.000059	31.4	
f_{63}	3.67676	0.000073	30.1	
f_{64}	6.32414	0.000047	29.5	
f_{65}	2.35932	0.00016	28.1	
f_{66}	6.10666	0.000038	26.3	
f_{67}	4.24672	0.000066	26.1	
f_{68}	5.85714	0.000063	23.2	
f_{69}	3.70680	0.000087	22.4	
f_{70}	6.16903	0.000067	22.3	
f_{71}	4.74697	0.000046	21.6	
f_{72}	2.71718	0.00028	21.3	
f_{73}	5.74346	0.00011	21.5	
f_{74}	4.12098	0.000050	20.0	
f_{75}	5.88763	0.000048	17.1	
f_{76}	3.54904	0.000064	16.5	
f_{77}	5.07174	0.000034	16.0	
f_{78}	9.36866	0.000047	14.8	
f_{79}	3.37906	0.00011	15.0	
f_{80}	7.14763	0.000040	13.3	
f_{81}	3.85560	0.00014	13.5	
f_{82}	5.15261	0.000042	13.2	
f_{83}	4.51254	0.000038	13.2	
f_{84}	6.00092	0.000045	12.8	
f_{85}	8.63506	0.000034	12.5	
f_{86}	6.79676	0.000029	10.9	
f_{87}	13.2018	0.000033	10.3	
f_{88}	0.921048	0.00012	10.1	
f_{89}	9.42817	0.000029	9.59	
f_{90}	3.90612	0.000062	9.62	

Table B.2: (Continued) Frequencies detected by SigSpec in the TASOC light curve for HD 206481. Values have been rounded to 6 s.f., 2 s.f. and 3 s.f. respectively.

	Frequency (d^{-1})	Amplitude (mag)	S/N	Coupling
f_{91}	2.45929	0.00011	9.44	
f_{92}	5.38958	0.000032	8.68	
f_{93}	6.51354	0.000042	8.34	
f_{94}	6.82251	0.000040	8.44	
f_{95}	7.38556	0.000031	8.38	
f_{96}	7.03785	0.000031	9.04	
f_{97}	4.22604	0.000045	8.27	
f_{98}	4.42475	0.000028	8.29	
f_{99}	7.82469	0.000032	8.08	
f_{100}	4.88068	0.000032	7.84	
f_{101}	9.26912	0.000026	7.80	
f_{102}	8.92992	0.000027	8.80	
f_{103}	5.72972	0.00012	7.64	
f_{104}	6.67495	0.000033	7.53	
f_{105}	13.0534	0.000027	7.34	
f_{106}	10.7827	0.000030	7.28	
f_{107}	8.41096	0.000029	6.95	
f_{108}	8.16922	0.000024	7.02	
f_{109}	5.44876	0.000040	6.91	
f_{110}	8.85208	0.000024	6.63	
f_{111}	5.65454	0.000038	6.49	
f_{112}	2.80726	0.000045	6.39	
f_{113}	4.69197	0.000027	6.41	
f_{114}	11.7589	0.000027	6.09	
f_{115}	5.58939	0.000035	6.06	
f_{116}	7.62728	0.000024	5.74	
f_{117}	20.9719	0.000024	5.63	
f_{118}	11.3374	0.000025	5.59	
f_{119}	10.4673	0.000021	5.70	
f_{120}	23.8777	0.000022	5.20	
f_{121}	33.2447	0.000022	4.97	
f_{122}	11.8727	0.000035	4.91	
f_{123}	11.8870	0.000035	5.02	
f_{124}	14.9988	0.000021	5.08	
f_{125}	17.0764	0.000023	4.95	
f_{126}	17.1612	0.000022	5.07	
f_{127}	9.21417	0.000025	4.89	
f_{128}	11.5877	0.000025	5.00	
f_{129}	12.1425	0.000021	4.82	
f_{130}	6.64787	0.000037	4.77	
f_{131}	6.58581	0.000033	6.45	
f_{132}	10.0228	0.000038	4.85	
f_{133}	1.09142	0.000051	4.78	
f_{134}	10.0381	0.000037	4.54	
f_{135}	8.49779	0.000022	4.55	

Table B.2: (Continued) Frequencies detected by SigSpec in the TASOC light curve for HD 206481. Values have been rounded to 6 s.f., 2 s.f. and 3 s.f. respectively.

	Frequency (d^{-1})	Amplitude (mag)	S/N	Coupling
f_{136}	10.7338	0.000023	4.48	
f_{137}	13.9609	0.000020	4.42	
f_{138}	19.8949	0.000020	4.32	
f_{139}	8.22316	0.000022	4.18	
f_{140}	11.3792	0.000021	4.28	
f_{141}	14.4097	0.000021	4.13	
f_{142}	14.7451	0.000020	4.14	
f_{143}	21.8996	0.000020	4.08	
f_{144}	1.96309	0.000032	4.10	
f_{145}	4.35046	0.000025	4.22	
f_{146}	12.6838	0.000019	4.01	

Table B.3: Frequencies detected by SigSpec in the TASOC light curve for HD 209295. Values have been rounded to 6 s.f., 2 s.f. and 3 s.f. respectively

	Frequency (d^{-1})	Amplitude (mag)	S/N	Coupling
f_1	1.12808	0.036	2880	
f_2	2.30455	0.013	1200	
f_3	1.17509	0.013	1600	
f_4	2.57642	0.0093	1550	
f_5	1.76732	0.0050	846	
f_6	0.966525	0.0041	672	
f_7	1.60881	0.0037	667	
f_8	1.28657	0.0036	582	
f_9	2.27029	0.0035	609	
f_{10}	0.642626	0.0030	653	
f_{11}	0.322664	0.0023	467	
f_{12}	1.93125	0.0021	455	
f_{13}	1.21871	0.0020	363	
f_{14}	2.14867	0.0015	354	
f_{15}	1.43098	0.0017	353	
f_{16}	2.90454	0.0017	303	
f_{17}	1.07090	0.0015	316	
f_{18}	2.41198	0.0012	262	
f_{19}	2.37476	0.00097	265	
f_{20}	0.264987	0.00095	225	
f_{21}	3.41002	0.0011	178	
f_{22}	3.11178	0.00081	147	
f_{23}	0.849449	0.0011	148	
f_{24}	2.19230	0.00081	148	
f_{25}	27.2521	0.00061	132	
f_{26}	2.85745	0.00069	117	
f_{27}	1.02525	0.0011	122	
f_{28}	3.39367	0.0013	107	
f_{29}	2.22894	0.00097	103	
f_{30}	1.69363	0.00064	112	
f_{31}	0.476438	0.00019	108	
f_{32}	13.6890	0.00045	106	
f_{33}	1.33313	0.00064	107	
f_{34}	16.4793	0.00053	108	
f_{35}	0.0296504	0.00059	109	
f_{36}	29.9929	0.00046	107	
f_{37}	3.69469	0.00080	110	
f_{38}	0.738560	0.00088	107	
f_{39}	1.41503	0.0013	104	
f_{40}	1.98093	0.00055	111	
f_{41}	3.48659	0.00054	85.0	
f_{42}	2.53554	0.00045	89.8	
f_{43}	2.74167	0.0010	114	
f_{44}	22.0214	0.00053	93.9	
f_{45}	12.8194	0.00050	86.0	

Table B.3: (Continued) Frequencies detected by SigSpec in the TASOC light curve for HD 209295. Values have been rounded to 6 s.f., 2 s.f. and 3 s.f. respectively.

	Frequency (d^{-1})	Amplitude (mag)	S/N	Coupling
f_{46}	16.0380	0.00029	79.1	
f_{47}	0.435664	0.00058	79.2	
f_{48}	1.64716	0.00053	82.3	
f_{49}	0.537249	0.00071	81.8	
f_{50}	12.5227	0.00036	81.3	
f_{51}	4.00867	0.00027	82.9	
f_{52}	21.8803	0.00061	84.1	
f_{53}	28.2653	0.00070	80.4	
f_{54}	0.182077	0.00038	78.4	
f_{55}	0.105597	0.00047	81.5	
f_{56}	4.18633	0.00025	76.5	
f_{57}	2.48276	0.00044	78.0	
f_{58}	20.2148	0.00060	77.6	
f_{59}	16.6965	0.00025	78.0	
f_{60}	29.1229	0.00014	77.1	
f_{61}	2.08854	0.00051	78.0	
f_{62}	3.86406	0.00045	79.2	
f_{63}	17.4950	0.00034	78.3	
f_{64}	0.670731	0.00074	76.6	
f_{65}	25.5607	0.00026	77.5	
f_{66}	19.4871	0.00028	79.3	
f_{67}	4.57753	0.00096	75.7	
f_{68}	15.9798	0.00065	65.4	
f_{69}	3.21452	0.00032	66.1	
f_{70}	27.6684	0.00024	65.6	$f_{270} + f_{395}$
f_{71}	23.5668	0.0012	66.8	
f_{72}	3.32623	0.00027	65.6	
f_{73}	24.3793	0.00025	65.6	
f_{74}	28.5357	0.00028	65.6	
f_{75}	15.1381	0.00018	62.0	$f_{347} + f_{449}$
f_{76}	0.791445	0.00049	61.8	
f_{77}	31.0737	0.00023	61.4	
f_{78}	21.9483	0.00026	59.5	
f_{79}	25.9400	0.00035	59.8	
f_{80}	4.87768	0.00022	51.6	
f_{81}	29.9951	0.00024	51.2	
f_{82}	15.6642	0.00022	51.8	
f_{83}	0.598951	0.00044	52.2	
f_{84}	2.67955	0.00029	53.5	
f_{85}	0.222367	0.00026	55.7	
f_{86}	23.6375	0.00018	52.3	$f_{396} + f_{502}$
f_{87}	19.4167	0.00035	53.4	
f_{88}	22.6621	0.00026	50.8	
f_{89}	3.06449	0.00021	51.7	
f_{90}	3.67993	0.00059	46.0	

Table B.3: (Continued) Frequencies detected by SigSpec in the TASOC light curve for HD 209295. Values have been rounded to 6 s.f., 2 s.f. and 3 s.f. respectively.

	Frequency (d^{-1})	Amplitude (mag)	S/N	Coupling
f_{91}	17.0772	0.00014	45.1	
f_{92}	23.8479	0.00021	45.3	$f_{99} + f_{197}$
f_{93}	34.0303	0.00014	44.3	
f_{94}	21.2966	0.00019	44.0	
f_{95}	17.5539	0.00021	43.7	
f_{96}	24.3056	0.00050	44.7	
f_{97}	5.14459	0.00022	45.0	
f_{98}	31.0245	0.00020	44.5	
f_{99}	19.0016	0.00021	42.0	
f_{100}	25.2748	0.00046	40.3	
f_{101}	21.4393	0.00021	40.3	
f_{102}	26.1261	0.00013	40.7	$f_{269} + f_{414}$
f_{103}	20.9624	0.00017	39.8	
f_{104}	19.9371	0.00050	40.5	
f_{105}	29.8871	0.00013	39.1	
f_{106}	4.58504	0.000872	39.2	
f_{107}	4.26148	0.00034	41.4	
f_{108}	15.7335	0.00014	39.8	
f_{109}	17.0189	0.00051	39.9	
f_{110}	34.9363	0.00012	40.4	$f_{287} + f_{602}$
f_{111}	14.5890	0.00017	40.3	
f_{112}	27.1621	0.00016	37.9	
f_{113}	19.6349	0.00042	34.4	
f_{114}	12.6387	0.00010	33.7	
f_{115}	13.9445	0.00014	34.7	
f_{116}	2.92166	0.00052	33.7	
f_{117}	29.7184	0.00013	33.9	
f_{118}	23.5555	0.00063	34.0	
f_{119}	23.8265	0.00018	37.1	
f_{120}	22.2339	0.00015	35.4	
f_{121}	20.2955	0.000080	34.8	
f_{122}	20.6818	0.00027	35.3	
f_{123}	25.7227	0.00012	32.5	$f_{91} + f_{489}$
f_{124}	22.1131	0.00012	33.1	
f_{125}	25.2831	0.00041	33.0	
f_{126}	31.1359	0.00017	31.3	
f_{127}	28.2250	0.00017	30.8	
f_{128}	3.75093	0.00016	30.7	
f_{129}	28.9738	0.00014	30.6	
f_{130}	1.89994	0.00025	30.1	
f_{131}	34.9894	0.00014	30.3	
f_{132}	24.5303	0.00015	30.5	
f_{133}	24.7257	0.00012	33.2	
f_{134}	21.6884	0.00013	29.9	
f_{135}	20.8140	0.000068	29.7	

Table B.3: (Continued) Frequencies detected by SigSpec in the TASOC light curve for HD 209295. Values have been rounded to 6 s.f., 2 s.f. and 3 s.f. respectively.

	Frequency (d^{-1})	Amplitude (mag)	S/N	Coupling
f_{136}	18.3820	0.00029	30.8	
f_{137}	17.0060	0.00061	29.5	
f_{138}	13.9991	0.00017	28.9	
f_{139}	30.0304	0.00010	28.2	$f_{273} + f_{388}$ $f_{520} + f_{581}$
f_{140}	32.1672	0.00028	28.4	
f_{141}	19.5501	0.00016	28.1	
f_{142}	26.6948	0.00011	28.3	$f_{367} + f_{472}$
f_{143}	0.886036	0.00022	27.7	
f_{144}	15.1820	0.00012	28.7	
f_{145}	12.2637	0.000094	27.6	
f_{146}	3.54154	0.00010	27.5	
f_{147}	30.7786	0.00010	27.2	
f_{148}	20.1225	0.00010	27.5	
f_{149}	29.1595	0.00033	27.7	$f_{150} + f_{264}$
f_{150}	1.83182	0.00021	27.9	
f_{151}	23.2989	0.00014	28.0	
f_{152}	23.2053	0.00047	28.9	
f_{153}	19.9470	0.00060	28.2	
f_{154}	22.7883	0.000056	28.6	
f_{155}	2.74732	0.00071	28.6	
f_{156}	18.9103	0.000082	28.5	
f_{157}	17.2017	0.000055	28.7	
f_{158}	21.6302	0.00012	28.0	
f_{159}	4.34448	0.00010	27.9	
f_{160}	19.1887	0.00012	27.6	
f_{161}	4.45042	0.00013	27.5	
f_{162}	27.7194	0.000095	27.7	
f_{163}	19.6857	0.00013	27.6	
f_{164}	27.9746	0.00010	27.1	$f_{280} + f_{602}$
f_{165}	23.4158	0.000087	27.2	$f_{346} + f_{635}$
f_{166}	34.1643	0.00011	26.9	
f_{167}	18.3394	0.000097	26.5	
f_{168}	33.1192	0.000097	26.2	
f_{169}	28.1915	0.000076	26.1	
f_{170}	24.4791	0.00012	26.3	
f_{171}	31.6803	0.000094	26.5	$f_{280} + f_{445}$
f_{172}	15.9726	0.00049	26.8	
f_{173}	17.5974	0.00012	25.9	
f_{174}	16.7822	0.00011	25.5	
f_{175}	15.4789	0.000086	25.6	
f_{176}	27.5952	0.000097	25.4	
f_{177}	13.4895	0.000087	25.0	
f_{178}	27.4298	0.000082	25.1	$f_{312} + f_{413}$

Table B.3: (Continued) Frequencies detected by SigSpec in the TASOC light curve for HD 209295. Values have been rounded to 6 s.f., 2 s.f. and 3 s.f. respectively.

	Frequency (d^{-1})	Amplitude (mag)	S/N	Coupling
f_{179}	14.6803	0.00011	24.9	$f_{213} + f_{379}$
f_{180}	20.0384	0.00015	25.1	
f_{181}	3.13387	0.00021	25.0	
f_{182}	14.4287	0.00024	25.2	
f_{183}	35.9333	0.000082	25.4	
f_{184}	6.37538	0.000064	25.1	
f_{185}	33.0663	0.00011	25.1	$f_{176} + f_{216}$ $f_{159} + f_{415}$
f_{186}	30.3758	0.000098	24.7	
f_{187}	16.5613	0.000073	24.7	
f_{188}	22.9518	0.00012	24.0	
f_{189}	26.5553	0.00022	23.9	
f_{190}	18.0177	0.000084	23.7	
f_{191}	20.8660	0.000087	23.1	
f_{192}	35.0383	0.000078	23.3	$f_{247} + f_{520}$
f_{193}	22.4391	0.000065	23.0	
f_{194}	18.4453	0.000068	23.0	
f_{195}	26.8526	0.000054	22.2	
f_{196}	28.5794	0.000089	22.8	
f_{197}	4.84638	0.000091	22.3	
f_{198}	31.2365	0.000094	22.1	
f_{199}	25.0162	0.000065	21.6	
f_{200}	29.2102	0.000094	21.7	
f_{201}	29.4176	0.000078	22.3	
f_{202}	17.3996	0.000090	21.5	
f_{203}	13.7929	0.00023	21.3	
f_{204}	24.2979	0.00044	20.8	
f_{205}	31.8164	0.000085	20.9	
f_{206}	1.45757	0.00073	20.2	
f_{207}	23.5824	0.00053	20.6	
f_{208}	23.0451	0.000051	21.9	
f_{209}	19.8550	0.00011	21.7	
f_{210}	29.5001	0.000077	20.7	
f_{211}	35.8526	0.00084	21.1	$f_{478} + f_{621}$
f_{212}	32.5289	0.000036	21.0	
f_{213}	4.15286	0.00013	20.7	
f_{214}	4.08185	0.00016	28.8	
f_{215}	31.5977	0.000099	21.0	
f_{216}	5.47117	0.000083	20.9	
f_{217}	16.1048	0.00014	21.1	
f_{218}	3.94205	0.00012	21.0	
f_{219}	24.5870	0.000077	21.1	
f_{220}	25.9269	0.00029	21.2	
f_{221}	27.8424	0.000084	21.5	

Table B.3: (Continued) Frequencies detected by SigSpec in the TASOC light curve for HD 209295. Values have been rounded to 6 s.f., 2 s.f. and 3 s.f. respectively.

	Frequency (d^{-1})	Amplitude (mag)	S/N	Coupling
f_{222}	15.8931	0.000078	21.7	
f_{223}	28.4168	0.00011	21.6	
f_{224}	25.4945	0.00013	21.9	
f_{225}	14.7844	0.00021	21.5	
f_{226}	21.0444	0.00011	21.4	
f_{227}	13.8045	0.00041	21.1	
f_{228}	18.2656	0.000085	21.1	
f_{229}	30.9219	0.000066	20.6	
f_{230}	5.28881	0.000071	20.4	
f_{231}	32.8689	0.000080	20.4	
f_{232}	33.2617	0.000065	21.0	$f_{284} + f_{515}$
f_{233}	28.2717	0.00052	20.8	
f_{234}	13.2254	0.00011	20.9	
f_{235}	20.4077	0.000071	21.0	
f_{236}	17.4328	0.000089	20.9	
f_{237}	36.3398	0.000058	21.0	
f_{238}	22.5933	0.00011	20.6	
f_{239}	22.5331	0.00010	21.2	
f_{240}	37.0906	0.00011	20.6	
f_{241}	24.7994	0.00018	20.3	
f_{242}	23.7758	0.000093	20.4	$f_{333} + f_{385}$
f_{243}	21.8751	0.00039	20.4	
f_{244}	21.5486	0.000086	20.6	
f_{245}	28.6547	0.000059	20.4	$f_{156} + f_{508}$
f_{246}	21.3391	0.000095	20.2	
f_{247}	11.1084	0.000062	19.3	
f_{248}	11.2506	0.00011	20.8	
f_{249}	7.67756	0.000058	19.9	
f_{250}	10.9804	0.000042	19.5	
f_{251}	21.2515	0.00010	19.6	
f_{252}	14.8507	0.00012	19.7	
f_{253}	32.1855	0.00019	19.3	
f_{254}	13.8219	0.00020	19.2	
f_{255}	19.7564	0.000076	19.3	
f_{256}	4.65905	0.00010	19.2	
f_{257}	15.5730	0.000059	19.3	
f_{258}	4.27390	0.00027	18.9	
f_{259}	12.8944	0.000088	18.7	
f_{260}	13.3216	0.000068	18.8	
f_{261}	36.1104	0.000065	18.9	$f_{520} + f_{565}$
f_{262}	35.7111	0.000067	20.7	
f_{263}	27.1393	0.00011	19.0	$f_{574} + f_{629}$
f_{264}	27.3277	0.000069	23.0	$f_{346} + f_{460}$
f_{265}	25.6010	0.00020	19.6	
f_{266}	16.6277	0.000080	19.1	

Table B.3: (Continued) Frequencies detected by SigSpec in the TASOC light curve for HD 209295. Values have been rounded to 6 s.f., 2 s.f. and 3 s.f. respectively.

	Frequency (d^{-1})	Amplitude (mag)	S/N	Coupling
f_{267}	20.5130	0.000082	19.2	$f_{230} + f_{575}$
f_{268}	11.5833	0.000081	19.2	$f_{486} + f_{633}$
f_{269}	14.1253	0.000076	19.4	$f_{475} + f_{577}$
f_{270}	20.6925	0.00027	19.3	
f_{271}	16.3910	0.00015	19.2	
f_{272}	33.0055	0.000060	18.8	
f_{273}	17.8156	0.000057	18.9	
f_{274}	35.0722	0.000078	18.8	
f_{275}	18.1720	0.00016	18.4	
f_{276}	22.3032	0.000077	19.0	
f_{277}	23.2017	0.00048	18.6	
f_{278}	10.0908	0.000036	17.7	
f_{279}	6.80852	0.00019	18.0	
f_{280}	21.7970	0.000088	17.7	
f_{281}	19.3652	0.000080	17.3	
f_{282}	16.9005	0.00022	17.2	
f_{283}	36.1536	0.000053	17.1	
f_{284}	17.8406	0.000058	17.2	$f_{249} + f_{630}$
f_{285}	31.4506	0.000083	17.3	
f_{286}	11.7612	0.000057	17.4	
f_{287}	28.7586	0.000045	17.2	
f_{288}	33.2057	0.000044	17.6	$f_{465} + f_{571}$
f_{289}	32.3299	0.00020	17.5	
f_{290}	32.4158	0.000056	17.6	
f_{291}	13.5544	0.000053	17.6	
f_{292}	13.2985	0.000088	17.4	
f_{293}	13.6325	0.000047	19.0	$f_{146} + f_{278}$
f_{294}	5.12235	0.000098	17.7	
f_{295}	27.8143	0.000071	17.0	$f_{199} + f_{635}$
f_{296}	32.5948	0.000058	17.2	
f_{297}	31.3725	0.000077	16.9	
f_{298}	22.8474	0.000089	17.4	
f_{299}	30.2752	0.000069	17.0	
f_{300}	30.3278	0.000057	17.0	
f_{301}	5.36577	0.000051	16.8	$8f_{64}$
f_{302}	11.1570	0.000052	16.9	
f_{303}	33.6283	0.000047	16.8	$f_{560} + f_{631}$
f_{304}	33.9682	0.00016	17.4	
f_{305}	26.7252	0.000076	16.5	
f_{306}	18.5956	0.00022	16.5	
f_{307}	6.56219	0.000034	16.5	
f_{308}	34.6677	0.000051	16.7	
f_{309}	10.2230	0.000057	16.1	
f_{310}	23.7034	0.000053	16.0	
f_{311}	11.2359	0.00012	16.0	

Table B.3: (Continued) Frequencies detected by SigSpec in the TASOC light curve for HD 209295. Values have been rounded to 6 s.f., 2 s.f. and 3 s.f. respectively.

	Frequency (d^{-1})	Amplitude (mag)	S/N	Coupling
f_{312}	12.3829	0.000081	16.6	
f_{313}	14.3862	0.000069	16.3	
f_{314}	19.1357	0.00013	16.4	$f_{356} + f_{504}$ $f_{359} + f_{384}$
f_{315}	7.90906	0.000063	16.5	
f_{316}	21.1544	0.000064	16.2	
f_{317}	18.6881	0.000058	16.6	
f_{318}	4.80183	0.000066	16.0	
f_{319}	37.4503	0.000050	15.8	
f_{320}	17.3174	0.000075	15.7	
f_{321}	25.6150	0.00018	16.1	
f_{322}	18.3906	0.00028	15.7	
f_{323}	25.1776	0.00027	16.1	$f_{89} + f_{124}$
f_{324}	19.2431	0.00082	16.7	
f_{325}	18.9515	0.000072	19.2	
f_{326}	25.3256	0.000067	17.0	
f_{327}	36.5942	0.00014	16.4	
f_{328}	26.0203	0.000072	16.6	
f_{329}	33.8232	0.000073	16.3	
f_{330}	33.9562	0.00023	17.4	
f_{331}	33.4756	0.000052	16.6	$f_{418} + f_{460}$
f_{332}	18.8380	0.000043	16.1	
f_{333}	6.07430	0.000060	16.2	
f_{334}	34.7695	0.000048	15.9	
f_{335}	3.62592	0.00012	15.7	
f_{336}	3.26459	0.00010	16.6	
f_{337}	11.8028	0.000060	16.3	
f_{338}	30.1646	0.000063	15.5	
f_{339}	26.2970	0.00027	15.0	
f_{340}	35.5208	0.000056	14.8	$f_{424} + f_{565}$
f_{341}	35.6643	0.000050	15.2	
f_{342}	32.1504	0.00017	15.0	
f_{343}	32.8918	0.000099	15.2	
f_{344}	40.6459	0.000038	14.2	
f_{345}	26.9408	0.000058	14.1	
f_{346}	20.6176	0.000058	14.3	
f_{347}	8.32157	0.000045	14.2	
f_{348}	12.5981	0.00011	14.2	
f_{349}	20.2252	0.00040	14.4	
f_{350}	27.8976	0.000064	14.6	
f_{351}	27.0517	0.000035	14.8	
f_{352}	28.1253	0.000062	14.8	
f_{353}	24.1091	0.00017	14.8	$f_{396} + f_{558}$
f_{354}	10.9271	0.000038	14.5	

Table B.3: (Continued) Frequencies detected by SigSpec in the TASOC light curve for HD 209295. Values have been rounded to 6 s.f., 2 s.f. and 3 s.f. respectively.

	Frequency (d^{-1})	Amplitude (mag)	S/N	Coupling
f_{355}	24.9444	0.000045	14.3	
f_{356}	8.84734	0.000039	14.1	
f_{357}	31.9487	0.000040	14.1	
f_{358}	5.93886	0.000025	13.9	
f_{359}	6.41333	0.000065	14.1	
f_{360}	14.7751	0.00016	14.0	$f_{404} + f_{546}$
f_{361}	26.2920	0.00025	13.8	
f_{362}	32.3357	0.00018	13.6	$f_{456} + f_{577}$
f_{363}	19.4200	0.00031	13.6	
f_{364}	22.4759	0.000067	14.3	$f_{413} + f_{446}$
f_{365}	5.75523	0.000039	13.8	
f_{366}	5.57948	0.000029	14.1	
f_{367}	10.4430	0.000041	13.4	
f_{368}	5.24393	0.00012	13.5	
f_{369}	21.3832	0.000060	13.3	
f_{370}	32.7635	0.000053	13.3	$f_{184} + f_{462}$
f_{371}	28.3571	0.000056	13.4	
f_{372}	38.8339	0.000034	13.3	$f_{381} + f_{626}$
f_{373}	15.6218	0.000050	13.5	
f_{374}	36.0033	0.000089	13.5	
f_{375}	37.0805	0.000094	13.4	
f_{376}	35.2027	0.000045	13.6	
f_{377}	19.6290	0.00034	13.1	
f_{378}	18.1013	0.000032	13.2	
f_{379}	10.5275	0.000026	13.4	
f_{380}	13.0451	0.000047	13.0	
f_{381}	7.98889	0.000026	12.9	
f_{382}	16.0849	0.00014	12.8	
f_{383}	14.4367	0.00022	12.9	
f_{384}	12.7224	0.000067	12.8	
f_{385}	17.7015	0.000039	12.8	
f_{386}	20.8816	0.000097	13.3	
f_{387}	16.7363	0.000036	13.4	
f_{388}	12.2149	0.000073	13.2	
f_{289}	17.9278	0.000039	13.1	
f_{390}	10.7705	0.000040	13.5	
f_{391}	10.6343	0.000034	15.8	
f_{392}	27.2216	0.000047	13.5	
f_{393}	36.7622	0.000045	13.3	$f_{487} + f_{587}$
f_{394}	8.49393	0.000038	13.2	
f_{395}	6.97595	0.000037	12.7	
f_{396}	16.3831	0.00014	12.7	
f_{397}	31.5366	0.000049	12.6	
f_{398}	25.1838	0.00028	12.5	
f_{399}	18.5896	0.00020	12.3	

Table B.3: (Continued) Frequencies detected by SigSpec in the TASOC light curve for HD 209295. Values have been rounded to 6 s.f., 2 s.f. and 3 s.f. respectively.

	Frequency (d^{-1})	Amplitude (mag)	S/N	Coupling
f_{400}	33.3948	0.000048	12.5	
f_{401}	37.1714	0.000047	12.5	$f_{242} + f_{429}$
f_{402}	31.3209	0.000068	12.2	
f_{403}	30.9814	0.000051	13.0	
f_{404}	9.15537	0.000036	11.8	
f_{405}	9.50087	0.000037	11.9	
f_{406}	6.59780	0.000040	11.9	
f_{407}	12.6295	0.00020	11.7	
f_{408}	24.8054	0.00016	12.0	$f_{337} + f_{482}$
f_{409}	41.5644	0.000068	12.1	
f_{410}	28.8322	0.00017	11.9	$f_{278} + f_{610}$
f_{411}	24.6426	0.000071	12.0	
f_{412}	34.4859	0.000023	11.9	
f_{413}	15.0469	0.000064	11.9	$f_{404} + f_{475}$
f_{414}	12.0008	0.000053	11.8	
f_{415}	28.7219	0.000048	11.5	
f_{416}	29.0492	0.000047	11.8	
f_{417}	11.8653	0.000048	11.8	
f_{418}	26.7656	0.000038	11.4	
f_{419}	7.51733	0.000037	11.4	
f_{420}	38.0324	0.000028	11.3	
f_{421}	32.9834	0.000068	11.3	$f_{165} + f_{459}$
f_{422}	32.2495	0.000078	11.7	$f_{266} + f_{373}$
f_{423}	16.9913	0.00020	11.5	
f_{424}	23.3404	0.000038	11.5	
f_{425}	39.0089	0.000028	11.4	
f_{426}	41.7536	0.000073	11.2	
f_{427}	22.0099	0.00021	11.0	
f_{428}	11.3937	0.000064	10.9	
f_{429}	13.3956	0.000043	10.9	
f_{430}	17.1460	0.000041	10.8	$f_{390} + f_{184}$
f_{431}	24.2461	0.000036	10.9	
f_{432}	41.4926	0.000029	11.0	
f_{433}	41.2857	0.000030	11.1	
f_{434}	41.0317	0.000033	11.1	
f_{435}	22.8899	0.000053	10.9	
f_{436}	9.94436	0.000043	10.9	
f_{437}	42.3226	0.000031	10.8	
f_{438}	19.9637	0.00018	10.8	
f_{439}	33.6710	0.000048	11.2	
f_{440}	30.0979	0.000060	11.1	
f_{441}	29.7548	0.000046	12.9	
f_{442}	30.4256	0.000044	12.3	

Table B.3: (Continued) Frequencies detected by SigSpec in the TASOC light curve for HD 209295. Values have been rounded to 6 s.f., 2 s.f. and 3 s.f. respectively.

	Frequency (d^{-1})	Amplitude (mag)	S/N	Coupling
f_{443}	35.5357	0.000082	10.8	$f_{239} + f_{482}$ $f_{200} + f_{633}$ $f_{146} + f_{593}$
f_{444}	8.53180	0.000034	10.6	
f_{445}	9.88337	0.000033	10.8	
f_{446}	7.42913	0.000026	10.6	
f_{447}	14.2262	0.000057	10.5	
f_{448}	13.8715	0.000073	11.4	$f_{333} + f_{479}$
f_{449}	6.81657	0.00016	10.5	
f_{450}	31.1881	0.000069	10.7	
f_{451}	22.7635	0.000087	10.7	
f_{452}	37.0024	0.000029	10.8	$f_{371} + f_{489}$
f_{453}	36.4570	0.000035	11.1	
f_{454}	35.4207	0.000050	10.6	
f_{455}	35.2835	0.000043	10.1	$3f_{286}$
f_{456}	24.1018	0.00019	10.1	
f_{457}	24.0268	0.000048	12.1	
f_{458}	25.4116	0.000051	10.1	
f_{459}	9.56758	0.000033	10.0	
f_{460}	6.71008	0.000030	9.91	
f_{461}	14.3068	0.000048	9.78	
f_{462}	26.3881	0.000044	9.89	$f_{461} + f_{493}$
f_{463}	38.3047	0.000034	9.97	
f_{464}	34.3683	0.000032	9.96	$f_{135} + f_{291}$
f_{465}	11.0182	0.000047	9.76	
f_{466}	36.5868	0.00014	9.68	$f_{197} + f_{487}$
f_{467}	22.3604	0.000041	9.56	
f_{468}	42.9460	0.000031	9.41	
f_{469}	26.1735	0.000048	9.36	
f_{470}	26.5626	0.00019	9.94	
f_{471}	29.3637	0.000031	9.41	
f_{472}	16.2517	0.000049	9.50	
f_{473}	16.1857	0.000049	10.2	
f_{474}	3.86950	0.00032	9.85	
f_{475}	5.89141	0.000044	10.2	
f_{476}	4.04499	0.00015	10.2	
f_{477}	8.90642	0.000032	10.4	
f_{478}	8.20398	0.000082	10.4	
f_{479}	7.79725	0.000038	10.7	
f_{480}	8.76769	0.00011	10.3	
f_{481}	12.8055	0.00021	10.2	
f_{482}	13.0025	0.000043	13.6	
f_{483}	25.7519	0.000033	10.0	$f_{379} + f_{575}$
f_{484}	33.1821	0.000048	10.2	$f_{404} + f_{457}$

Table B.3: (Continued) Frequencies detected by SigSpec in the TASOC light curve for HD 209295. Values have been rounded to 6 s.f., 2 s.f. and 3 s.f. respectively.

	Frequency (d^{-1})	Amplitude (mag)	S/N	Coupling
f_{485}	14.6522	0.000082	10.1	
f_{486}	5.25768	0.00016	10.0	
f_{487}	31.7405	0.000046	9.88	
f_{488}	31.8721	0.000036	10.1	$f_{424} + f_{444}$
f_{489}	8.64538	0.000031	9.83	
f_{490}	40.1830	0.000094	9.80	$f_{443} + f_{607}$ $f_{542} + f_{635}$
f_{491}	40.4246	0.000076	9.76	
f_{492}	38.1881	0.000031	9.85	$f_{483} + f_{618}$
f_{493}	12.0813	0.000032	9.61	
f_{494}	12.3248	0.000036	10.2	
f_{495}	30.6712	0.000033	9.49	
f_{496}	30.2326	0.000035	9.96	
f_{497}	30.5900	0.000028	9.90	
f_{498}	39.1999	0.000031	9.64	
f_{499}	38.9436	0.000033	10.2	
f_{500}	44.9215	0.000027	9.20	$f_{405} + f_{454}$
f_{501}	16.8950	0.00019	9.13	
f_{502}	7.25435	0.000043	9.20	
f_{503}	44.0649	0.000025	9.20	
f_{504}	10.2884	0.000033	9.15	
f_{505}	49.8327	0.000022	8.82	
f_{506}	19.3363	0.000060	8.94	
f_{507}	44.7888	0.000025	8.64	
f_{508}	9.74429	0.000026	8.65	
f_{509}	14.2080	0.000050	8.70	
f_{510}	13.6085	0.000056	9.31	$f_{381} + f_{546}$
f_{511}	41.2464	0.000023	8.91	
f_{512}	41.8810	0.0000093	9.15	
f_{513}	41.1140	0.000025	9.25	
f_{514}	4.48252	0.000043	8.84	
f_{515}	15.4211	0.000027	8.85	
f_{516}	27.4614	0.000046	9.00	
f_{517}	28.8227	0.00014	9.37	
f_{518}	10.3847	0.000026	9.04	
f_{519}	37.9364	0.000028	8.88	
f_{520}	23.9300	0.000041	8.95	
f_{521}	39.4027	0.000026	8.65	$f_{329} + f_{366}$
f_{522}	25.6816	0.000054	8.71	
f_{523}	37.8112	0.000025	8.61	
f_{524}	37.6467	0.000022	8.72	
f_{525}	38.7590	0.000033	8.37	
f_{526}	34.2180	0.000031	8.24	
f_{527}	33.9372	0.00011	9.23	$f_{246} + f_{348}$

Table B.3: (Continued) Frequencies detected by SigSpec in the TASOC light curve for HD 209295. Values have been rounded to 6 s.f., 2 s.f. and 3 s.f. respectively.

	Frequency (d^{-1})	Amplitude (mag)	S/N	Coupling
f_{528}	36.8971	0.000028	8.66	
f_{529}	42.1615	0.000029	8.51	
f_{530}	39.5918	0.000021	8.19	
f_{531}	11.4514	0.000036	8.20	
f_{532}	14.7242	0.000066	7.89	
f_{533}	14.9785	0.000044	8.93	$f_{565} + f_{635}$
f_{534}	14.5225	0.000047	7.90	$f_{405} + f_{587}$
f_{535}	39.2682	0.000022	7.95	$f_{520} + f_{576}$
f_{536}	38.6432	0.000088	8.29	
f_{537}	13.2428	0.000065	7.94	
f_{538}	34.1105	0.000028	7.58	
f_{539}	45.8331	0.000020	7.67	
f_{540}	35.8285	0.000043	7.63	
f_{541}	40.5675	0.000022	7.76	
f_{542}	37.3850	0.000027	7.39	
f_{543}	43.0769	0.000023	7.47	
f_{544}	8.76141	0.00010	7.47	
f_{545}	6.18861	0.000069	7.25	
f_{546}	5.61966	0.000030	7.91	
f_{547}	9.27853	0.000026	7.33	
f_{548}	42.7318	0.000021	7.30	
f_{549}	44.1547	0.000020	7.26	
f_{550}	7.23743	0.000044	7.13	
f_{551}	32.4779	0.000023	7.07	
f_{552}	31.7787	0.000026	7.20	
f_{553}	40.7899	0.000022	6.96	
f_{554}	29.5881	0.000028	6.97	$f_{581} + f_{640}$
f_{555}	38.4573	0.000028	6.94	
f_{556}	46.5268	0.000020	6.86	$4f_{572}$
f_{557}	49.1486	0.000019	6.69	$f_{417} + f_{608}$
f_{558}	7.72602	0.000028	6.63	
f_{559}	27.5400	0.000031	6.59	
f_{560}	24.6297	0.000055	6.71	
f_{561}	42.6408	0.000018	6.64	
f_{562}	33.7214	0.000021	6.62	
f_{563}	47.4713	0.000020	6.49	
f_{564}	43.8410	0.000019	6.54	$f_{496} + f_{510}$
f_{565}	12.1804	0.000051	6.55	
f_{566}	40.1887	0.000087	6.55	$f_{440} + f_{278}$
f_{567}	39.6534	0.000018	6.42	
f_{568}	13.1386	0.000036	6.38	
f_{569}	38.6512	0.000090	6.35	$f_{565} + f_{636}$
f_{570}	38.3762	0.000026	6.43	
f_{571}	22.1875	0.000029	6.31	$f_{337} + f_{518}$
f_{572}	11.6317	0.000068	6.35	

Table B.3: (Continued) Frequencies detected by SigSpec in the TASOC light curve for HD 209295. Values have been rounded to 6 s.f., 2 s.f. and 3 s.f. respectively.

	Frequency (d^{-1})	Amplitude (mag)	S/N	Coupling
f_{573}	11.3741	0.000048	7.42	
f_{574}	15.5254	0.000037	6.40	
f_{575}	15.2243	0.000029	7.77	
f_{576}	15.3382	0.000033	6.65	$f_{315} + f_{446}$
f_{577}	8.23383	0.000083	6.42	
f_{578}	41.6547	0.000028	6.33	
f_{579}	41.5510	0.000074	7.96	
f_{580}	41.7428	0.000075	8.13	
f_{581}	6.10033	0.000037	6.28	
f_{582}	47.1165	0.000020	6.02	
f_{583}	7.60187	0.000025	6.10	
f_{584}	25.8288	0.000041	6.09	
f_{585}	45.1712	0.000019	6.13	$f_{366} + f_{530}$
f_{586}	7.28848	0.000025	6.04	
f_{587}	5.02169	0.000028	6.56	
f_{588}	8.11536	0.000027	6.07	
f_{589}	8.21987	0.00013	8.21	
f_{590}	40.4179	0.000065	6.06	
f_{591}	34.8113	0.000021	6.01	
f_{592}	18.1817	0.000099	5.93	$f_{493} + f_{581}$
f_{593}	31.9941	0.000024	5.98	
f_{594}	36.5031	0.000020	5.93	
f_{595}	38.7821	0.000037	5.92	
f_{596}	19.0686	0.000045	5.92	
f_{597}	46.9032	0.000019	5.80	
f_{598}	45.5087	0.000017	5.89	
f_{599}	49.4247	0.000017	5.64	
f_{600}	46.3637	0.000016	5.66	
f_{601}	35.9940	0.000078	5.58	
f_{602}	6.17763	0.000057	5.50	
f_{603}	34.5302	0.000020	5.44	$f_{195} + f_{249}$
f_{604}	47.5747	0.000026	5.46	
f_{605}	47.6921	0.000023	6.12	
f_{606}	47.6291	0.000018	5.77	
f_{607}	4.64721	0.000094	5.35	
f_{608}	37.2834	0.000016	5.40	
f_{609}	29.2394	0.000024	5.33	
f_{610}	18.7413	0.000035	5.32	
f_{611}	41.9244	0.000019	5.32	
f_{612}	39.8770	0.000017	5.37	
f_{613}	10.0477	0.000028	5.23	
f_{614}	36.8311	0.000031	5.21	$f_{367} + f_{462}$
f_{615}	35.3491	0.000026	5.13	
f_{616}	44.5798	0.000016	5.00	$f_{288} + f_{573}$
f_{617}	21.5841	0.000045	4.89	

Table B.3: (Continued) Frequencies detected by SigSpec in the TASOC light curve for HD 209295. Values have been rounded to 6 s.f., 2 s.f. and 3 s.f. respectively.

	Frequency (d^{-1})	Amplitude (mag)	S/N	Coupling
f_{618}	12.4362	0.000026	5.10	
f_{619}	29.8645	0.000062	4.74	$f_{191} + f_{631}$
f_{620}	35.2279	0.000024	4.67	
f_{621}	27.6487	0.000048	4.62	
f_{622}	47.8604	0.000016	4.63	
f_{623}	48.0760	0.000018	5.10	
f_{624}	46.1112	0.000015	4.77	$f_{414} + f_{538}$
f_{625}	49.2432	0.000016	4.79	
f_{626}	30.8451	0.000021	4.68	
f_{627}	39.1267	0.000018	4.43	$f_{212} + f_{406}$
f_{628}	48.7516	0.000015	4.46	
f_{629}	11.6139	0.000072	4.46	
f_{630}	10.1631	0.000026	4.68	
f_{631}	8.99853	0.000017	5.05	
f_{632}	43.3361	0.000015	4.39	
f_{633}	6.32558	0.000019	4.39	
f_{634}	43.7877	0.000015	4.29	$f_{365} + f_{420}$
f_{635}	2.79808	0.000029	4.24	
f_{636}	26.4707	0.000021	4.23	
f_{637}	48.0031	0.000016	4.20	$4f_{414}$
f_{638}	47.7934	0.000015	4.26	
f_{639}	49.3131	0.000014	4.23	
f_{640}	23.4878	0.000021	4.21	
f_{641}	36.8153	0.000029	4.18	
f_{642}	32.5734	0.000026	4.09	
f_{643}	45.0665	0.000014	4.03	

Table B.4: Frequencies detected by SigSpec in the TASOC light curve for HD 214291. Values have been rounded to 6 s.f., 2 s.f. and 3 s.f. respectively

	Frequency (d^{-1})	Amplitude (mag)	S/N	Coupling
f_1	1.14784	0.022	3790	
f_2	3.44369	0.0020	954	
f_3	2.29506	0.0018	1010	
f_4	4.59119	0.0017	1200	
f_5	0.545761	0.0016	1540	
f_6	5.73890	0.0013	1730	
f_7	6.88683	0.00094	1600	
f_8	8.03438	0.00061	1080	
f_9	0.587965	0.00049	1120	
f_{10}	9.18244	0.00034	656	$2f_4$
f_{11}	0.0598837	0.00062	529	
f_{12}	0.628093	0.00037	420	
f_{13}	1.09697	0.00016	214	
f_{14}	0.288845	0.00050	216	
f_{15}	0.439002	0.00025	236	
f_{16}	1.72588	0.00016	229	
f_{17}	0.278116	0.00054	199	
f_{18}	13.7731	0.00013	207	
f_{19}	1.21725	0.00014	184	
f_{20}	0.139584	0.00027	169	
f_{21}	0.457496	0.00025	189	
f_{22}	0.710173	0.00013	190	
f_{23}	10.3293	0.00011	201	
f_{24}	12.6264	0.00010	207	
f_{25}	14.9218	0.00010	206	
f_{26}	1.64503	0.000088	130	
f_{27}	0.831180	0.000096	121	
f_{28}	0.962231	0.000082	130	
f_{29}	16.0695	0.000069	118	
f_{30}	0.0461604	0.00040	94.6	
f_{31}	0.241896	0.000099	116	
f_{32}	1.03477	0.000067	72.4	
f_{33}	1.92408	0.000048	56.2	
f_{34}	1.38776	0.00011	48.0	
f_{35}	0.649537	0.00012	47.1	
f_{36}	20.6606	0.000042	46.2	
f_{37}	1.16833	0.000079	44.8	
f_{38}	1.66943	0.000062	48.1	
f_{39}	1.80504	0.000088	45.4	
f_{40}	11.4740	0.000037	44.4	
f_{41}	4.01305	0.000038	42.0	
f_{42}	1.33336	0.000042	41.8	
f_{43}	0.156477	0.00015	43.3	
f_{44}	19.5142	0.000036	41.7	
f_{45}	2.93727	0.000081	39.3	

Table B.4: (Continued) Frequencies detected by SigSpec in the TASOC light curve for HD 214291. Values have been rounded to 6 s.f., 2 s.f. and 3 s.f. respectively.

	Frequency (d^{-1})	Amplitude (mag)	S/N	Coupling
f_{46}	21.8133	0.000034	35.0	
f_{47}	17.2122	0.000031	33.1	
f_{48}	2.27783	0.000064	30.9	
f_{49}	2.07390	0.00010	30.7	
f_{50}	1.79789	0.000091	27.4	
f_{51}	22.9555	0.000026	23.7	
f_{52}	5.16533	0.000026	21.7	
f_{53}	27.5514	0.000024	19.6	
f_{54}	2.06761	0.000094	18.8	
f_{55}	0.355844	0.000046	18.8	
f_{56}	2.87666	0.000026	18.3	
f_{57}	1.87529	0.000022	17.6	
f_{58}	0.915348	0.000029	16.6	
f_{59}	2.75400	0.000029	15.3	
f_{60}	2.95065	0.000080	16.7	
f_{61}	1.50951	0.000026	14.9	
f_{62}	1.40149	0.000083	14.4	
f_{63}	2.23258	0.000033	12.3	
f_{64}	3.12870	0.000024	12.3	
f_{65}	2.37841	0.000046	11.3	
f_{66}	2.69305	0.000017	11.2	
f_{67}	24.0116	0.000017	9.92	
f_{68}	3.27419	0.000027	9.70	
f_{69}	3.47899	0.000034	11.0	
f_{70}	3.06413	0.000023	10.5	$f_{32} + f_{93}$
f_{71}	1.46380	0.000025	9.48	
f_{72}	28.6895	0.000016	9.32	
f_{73}	26.4065	0.000016	8.74	
f_{74}	2.59577	0.000019	8.58	
f_{75}	34.4283	0.000014	8.45	
f_{76}	5.45576	0.000019	8.32	
f_{77}	5.33935	0.000048	8.35	
f_{78}	4.10837	0.000021	8.22	
f_{79}	4.81339	0.000012	7.92	
f_{80}	9.31830	0.000014	8.02	
f_{81}	5.67433	0.000016	7.46	
f_{82}	7.58683	0.000017	7.32	$f_{61} + f_{99}$
f_{83}	7.19521	0.000065	7.23	
f_{84}	7.33763	0.000026	7.68	
f_{85}	7.20372	0.000063	8.62	
f_{86}	3.63888	0.000018	7.05	
f_{87}	14.0371	0.000015	7.17	
f_{88}	13.9753	0.000016	7.64	
f_{89}	4.28412	0.000039	7.03	
f_{90}	3.54875	0.000017	6.22	

Table B.4: (Continued) Frequencies detected by SigSpec in the TASOC light curve for HD 214291. Values have been rounded to 6 s.f., 2 s.f. and 3 s.f. respectively.

	Frequency (d^{-1})	Amplitude (mag)	S/N	Coupling
f_{91}	13.4875	0.000013	6.35	
f_{92}	2.46003	0.000017	6.27	
f_{93}	2.02933	0.000021	6.16	
f_{94}	25.1311	0.000021	5.98	
f_{95}	9.99584	0.000014	5.82	
f_{96}	6.98580	0.000043	5.80	
f_{97}	5.20291	0.000017	5.79	
f_{98}	6.20123	0.000018	5.64	$f_{34} + f_{79}$
f_{99}	6.07735	0.000023	6.54	
f_{100}	5.94634	0.000012	5.63	
f_{101}	6.99516	0.000041	5.54	
f_{102}	7.69350	0.000012	5.49	$f_{55} + f_{84}$
f_{103}	41.3240	0.000012	5.47	
f_{104}	5.34772	0.000043	5.25	
f_{105}	4.66627	0.000014	5.32	
f_{106}	4.50755	0.000015	5.88	
f_{107}	4.29455	0.000040	5.92	
f_{108}	3.86620	0.000013	5.24	
f_{109}	3.34917	0.000015	5.19	
f_{110}	2.98462	0.000020	5.49	
f_{111}	5.85780	0.000012	5.25	
f_{112}	9.10369	0.000012	5.01	
f_{113}	21.6295	0.000011	4.78	
f_{114}	8.26566	0.000010	4.79	
f_{115}	2.36886	0.000039	4.60	
f_{116}	7.43615	0.000016	4.57	
f_{117}	7.09382	0.000013	4.52	
f_{118}	7.31940	0.000021	4.64	$f_{26} + f_{81}$
f_{119}	7.46455	0.000015	5.41	
f_{120}	12.1026	0.000010	4.42	
f_{121}	8.84021	0.000011	4.35	
f_{122}	25.1146	0.000020	4.37	
f_{123}	10.2076	0.000011	4.37	
f_{124}	42.4679	0.000010	4.32	
f_{125}	6.09531	0.000017	4.19	
f_{126}	6.31658	0.000012	4.48	
f_{127}	5.53704	0.000012	4.26	
f_{128}	2.82993	0.000013	4.26	
f_{129}	4.88870	0.000011	4.33	
f_{130}	13.0966	0.000011	4.26	
f_{131}	12.9830	0.000011	4.06	
f_{132}	16.4849	0.000010	4.07	
f_{133}	24.9811	0.000010	4.03	
f_{134}	29.8351	0.0000099	4.06	

Table B.5: Frequencies detected by SigSpec in the TASOC light curve for HD 216910. Values have been rounded to 6 s.f., 2 s.f. and 3 s.f. respectively

	Frequency (d^{-1})	Amplitude (mag)	S/N	Coupling
f_1	1.40590	0.0082	2170	
f_2	1.72431	0.0039	931	
f_3	0.855471	0.0045	1030	
f_4	1.62917	0.0041	1420	
f_5	1.44129	0.0065	700	
f_6	1.57015	0.0023	1070	
f_7	0.875457	0.0016	421	
f_8	1.31019	0.0011	413	
f_9	0.534482	0.00043	418	
f_{10}	0.292131	0.00066	327	
f_{11}	0.186481	0.0010	244	
f_{12}	0.133938	0.00095	291	
f_{13}	0.0895862	0.00097	263	
f_{14}	0.806445	0.00070	274	
f_{15}	2.83679	0.00072	287	
f_{16}	1.21209	0.00093	249	
f_{17}	0.939599	0.00087	293	
f_{18}	0.960926	0.00071	281	
f_{19}	1.88140	0.00080	260	$6f_{59}$
f_{20}	0.0256447	0.0011	251	
f_{21}	1.82023	0.00078	264	
f_{22}	1.52533	0.00077	267	
f_{23}	3.14132	0.00050	232	
f_{24}	3.03387	0.00044	242	
f_{25}	2.03480	0.00043	248	
f_{26}	2.88867	0.00035	237	
f_{27}	0.576510	0.0012	240	
f_{28}	2.56504	0.00037	240	
f_{29}	1.38750	0.0016	232	
f_{30}	0.229897	0.00068	228	
f_{31}	2.97571	0.00035	251	
f_{32}	0.629326	0.00039	222	
f_{33}	2.21160	0.00039	169	
f_{34}	2.09373	0.00043	185	
f_{35}	2.15713	0.00044	243	
f_{36}	2.31444	0.00021	206	
f_{37}	0.773378	0.00057	171	
f_{38}	2.75325	0.00033	191	
f_{39}	2.46426	0.00020	162	
f_{40}	1.74497	0.00038	171	
f_{41}	1.92324	0.00029	183	
f_{42}	3.078013	0.00035	189	
f_{43}	0.703613	0.00038	209	
f_{44}	3.26832	0.00016	206	
f_{45}	3.19372	0.00022	238	

Table B.5: (Continued) Frequencies detected by SigSpec in the TASOC light curve for HD 216910. Values have been rounded to 6 s.f., 2 s.f. and 3 s.f. respectively.

	Frequency (d^{-1})	Amplitude (mag)	S/N	Coupling
f_{46}	1.03975	0.00028	206	
f_{47}	2.70288	0.00016	173	
f_{48}	3.45562	0.00017	180	
f_{49}	1.08021	0.00015	172	
f_{50}	3.33832	0.00013	187	
f_{51}	1.99708	0.00040	184	
f_{52}	2.55757	0.00048	174	
f_{53}	0.479019	0.00017	134	
f_{54}	1.24245	0.00027	117	
f_{55}	2.35749	0.00017	123	
f_{56}	3.37323	0.00011	93.0	
f_{57}	4.03629	0.000059	85.78	
f_{58}	2.65173	0.000081	77.9	
f_{59}	0.313559	0.00064	71.8	
f_{60}	4.22937	0.000078	71.9	
f_{61}	3.51316	0.000055	67.7	
f_{62}	3.96784	0.000065	52.8	
f_{63}	0.37878	0.000099	45.3	
f_{64}	2.94602	0.000092	36.0	
f_{65}	3.66938	0.000061	32.8	
f_{66}	2.77478	0.000093	33.5	
f_{67}	3.83993	0.000048	31.0	
f_{68}	3.58717	0.000048	27.9	
f_{69}	1.28191	0.000074	26.4	
f_{70}	2.17083	0.00015	27.1	
f_{71}	4.27527	0.000061	25.9	
f_{72}	5.68039	0.000047	24.8	
f_{73}	6.23982	0.000035	22.9	
f_{74}	5.45431	0.000036	21.6	
f_{75}	5.15696	0.000033	22.1	
f_{76}	6.54554	0.000034	18.6	
f_{77}	2.42491	0.000070	17.7	
f_{78}	5.06405	0.000028	17.5	
f_{79}	5.80279	0.000088	15.9	
f_{80}	4.04582	0.000088	15.2	
f_{81}	4.38852	0.000046	13.2	
f_{82}	4.33257	0.000046	13.2	
f_{83}	4.11332	0.000038	16.9	
f_{84}	3.71681	0.000037	13.0	
f_{85}	4.77046	0.000021	13.1	
f_{86}	6.15634	0.000033	13.1	
f_{87}	6.81718	0.000026	12.0	
f_{88}	5.87831	0.000035	10.9	
f_{89}	5.99592	0.000024	10.8	
f_{90}	8.60364	0.000027	10.8	

Table B.5: (Continued) Frequencies detected by SigSpec in the TASOC light curve for HD 216910. Values have been rounded to 6 s.f., 2 s.f. and 3 s.f. respectively.

	Frequency (d^{-1})	Amplitude (mag)	S/N	Coupling
f_{91}	8.76467	0.000016	9.79	
f_{92}	4.58149	0.000030	9.63	
f_{93}	7.73347	0.000019	9.58	
f_{94}	6.28487	0.000030	9.08	
f_{95}	6.71752	0.000020	8.34	
f_{96}	6.48261	0.000022	7.99	
f_{97}	6.09663	0.000023	7.92	
f_{98}	5.53694	0.000016	7.71	
f_{99}	7.16120	0.000022	7.63	
f_{100}	6.85716	0.000021	8.07	
f_{101}	7.02910	0.000020	8.94	
f_{102}	4.69187	0.000021	7.55	
f_{103}	8.72287	0.000022	6.54	
f_{104}	42.2561	0.000016	6.50	
f_{105}	4.16400	0.000040	6.38	
f_{106}	3.98406	0.000087	6.55	
f_{107}	5.35820	0.000016	6.30	
f_{108}	10.1002	0.000015	6.03	
f_{109}	8.84870	0.000021	6.15	
f_{110}	8.92586	0.000018	6.07	
f_{111}	9.65900	0.000015	5.63	
f_{112}	5.61548	0.000017	5.77	
f_{113}	12.5727	0.000014	5.69	
f_{114}	1.51097	0.000060	5.25	
f_{115}	8.47720	0.000015	5.15	
f_{116}	4.46000	0.000019	5.02	
f_{117}	5.10644	0.000016	4.74	
f_{118}	10.4848	0.000013	4.62	
f_{119}	23.8645	0.000013	4.58	
f_{120}	47.3879	0.000013	4.43	
f_{121}	13.2171	0.000013	4.43	
f_{122}	40.9416	0.000013	4.37	
f_{123}	12.1029	0.000012	4.28	
f_{124}	12.4117	0.000013	4.33	
f_{125}	9.04169	0.000013	4.05	
f_{126}	8.14524	0.000012	4.04	

Appendix C. Frequency Aliasing and Combinations

Table C.1: Combinations of frequencies determined from the detected photometric frequencies for HD 206481.

Combinations	
$2f_{116} + 1 \approx 8f_{56}$	$f_{104} - 1 \approx 7f_3$
$-f_2 + 2 \approx 4f_{27}$	$3f_9 + 2 \approx f_{93}$
$f_{19} + 4 \approx f_{36}$	$-f_{115} + 8 \approx 2f_{21}$

Table C.2: Aliasing of detected photometric frequencies for HD 209295.

$f_{455} + 2 \approx f_{608}$	$f_{538} + 2 \approx f_{261}$	$f_{48} + 3 \approx f_{607}$	$f_{110} + 3 \approx f_{519}$	$f_{591} + 3 \approx f_{523}$
$f_{586} + 3 \approx f_{504}$	$f_{347} + 5 \approx f_{260}$	$f_{396} + 5 \approx f_{369}$	$f_{157} + 6 \approx f_{277}$	$f_{450} + 7 \approx f_{492}$
$f_{74} + 7 \approx f_{443}$	$f_{28} + 8 \approx f_{428}$	$f_{388} + 8 \approx f_{58}$	$f_{491} + 9 \approx f_{599}$	$f_{165} + 9 \approx f_{290}$
$f_{195} + 9 \approx f_{211}$	$f_{476} + 9 \approx f_{380}$	$f_{380} + 10 \approx f_{208}$	$f_{451} + 10 \approx f_{370}$	$f_{115} + 11 \approx f_{355}$
$f_{245} + 13 \approx f_{578}$	$f_{356} + 14 \approx f_{298}$	$f_{269} + 14 \approx f_{352}$	$f_{436} + 15 \approx f_{355}$	$f_{471} + 17 \approx f_{600}$
$f_{179} + 17 \approx f_{171}$	$f_{633} + 19 \approx f_{326}$	$f_{602} + 19 \approx f_{323}$	$f_{82} + 20 \approx f_{341}$	$f_{160} + 21 \approx f_{566}$
$f_{174} + 22 \approx f_{595}$	$f_{37} + 23 \approx f_{142}$	$f_{10} + 24 \approx f_{411}$	$f_{406} + 25 \approx f_{215}$	$f_{377} + 28 \approx f_{606}$
$f_{459} + 31 \approx f_{541}$	$f_{54} + 33 \approx f_{484}$	$f_{545} + 34 \approx f_{566}$	$f_{11} + 42 \approx f_{437}$	$f_{14} + 47 \approx f_{557}$

Table C.3: Combinations of detected photometric frequencies for HD 209295.

$2f_{141} \approx 9f_{159}$	$f_{568} + 1 \approx 8f_5$	$7f_{248} + 1 \approx 2f_{612}$	$f_{202} + 1 \approx 5f_{90}$
$2f_{419} + 1 \approx 4f_{51}$	$f_{605} + 1 \approx 6f_{588}$	$6f_{84} + 1 \approx f_{91}$	$3f_{414} + 1 \approx f_{452}$
$3f_{335} + 1 \approx 2f_{358}$	$f_{213} + 1 \approx 2f_4$	$2f_{317} + 1 \approx f_{570}$	$2f_{69} + 1 \approx f_{446}$
$5f_2 + 1 \approx f_{50}$	$f_{584} + 1 \approx 5f_{301}$	$4f_{250} + 1 \approx f_{500}$	$3f_{474} + 2 \approx f_{510}$
$3f_{286} + 2 \approx f_{608}$	$6f_9 + 2 \approx f_{373}$	$9f_7 + 2 \approx f_{34}$	$2f_{638} + 2 \approx 3f_{212}$
$5f_{85} + 2 \approx f_{22}$	$2f_{165} + 2 \approx 7f_{395}$	$f_{104} + 2 \approx 7f_{181}$	$f_{374} + 2 \approx 2f_{99}$
$f_{50} + 2 \approx 5f_{16}$	$f_{592} + 2 \approx 2f_{278}$	$3f_{107} + 2 \approx f_{225}$	$f_{319} + 3 \approx 2f_{349}$
$2f_{388} + 3 \approx f_{178}$	$2f_{180} + 3 \approx f_{543}$	$f_{542} + 4 \approx 2f_{270}$	$2f_{578} + 5 \approx 2f_{549}$
$2f_{247} + 5 \approx 2f_{510}$	$2f_{159} + 5 \approx f_{32}$	$-f_{38} + 5 \approx f_{107}$	$2f_{473} + 7 \approx 2f_{163}$
$2f_{11} + 8 \approx f_{489}$	$2f_{174} + 8 \approx f_{409}$	$f_{361} + 8 \approx 2f_{430}$	$2f_{356} + 9 \approx f_{142}$
$2f_{335} + 9 \approx f_{472}$	$2f_{395} + 9 \approx f_{188}$	$2f_{280} + 9 \approx 2f_{339}$	$2f_{88} + 9 \approx 2f_{112}$
$f_{14} + 10 \approx 2f_{333}$	$f_{141} + 10 \approx 2f_{360}$	$-f_{57} + 10 \approx f_{419}$	$-f_{294} + 10 \approx f_{80}$
$2f_{122} + 5 \approx f_{600}$	$f_{99} + 5 \approx 2f_{414}$	$f_{67} + 6 \approx 2f_{230}$	$-f_{39} + 6 \approx f_{106}$
$f_{80} + 7 \approx 2f_{358}$			

Table C.4: Combinations of frequencies determined from the detected photometric frequencies for HD 214291.

Combinations				
$4f_{105} \approx 9f_{49}$	$2f_{12} \approx 9f_{20}$	$3f_{10} \approx 4f_{7}$	$3f_{4} \approx 2f_{7}$	$f_{74} + 1 \approx 2f_{50}$
$f_{97} + 1 \approx 3f_{54}$	$3f_{55} + 1 \approx f_{54}$	$4f_{21} + 1 \approx f_{128}$	$f_{1} + 3 \approx 2f_{49}$	$-f_{2} + 4 \approx 2f_{17}$
$f_{48} + 5 \approx 2f_{86}$	$-f_{16} + 5 \approx f_{68}$	$-f_{84} + 9 \approx 2f_{27}$		

Table C.5: Combinations of frequencies determined from the detected photometric frequencies for HD 216910.

Combinations				
$2f_{5} \approx 5f_{27}$	$2f_{59} \approx 7f_{13}$	$2f_{36} + 1 \approx 8f_{43}$	$-2f_{11} + 1 \approx 7f_{13}$	$f_{4} + 1 \approx 9f_{10}$
$-2f_{63} + 2 \approx f_{54}$	$f_{82} + 2 \approx 9f_{43}$	$f_{29} + 5 \approx 2f_{45}$	$-2f_{83} + 9 \approx f_{37}$	